Computational modeling and analysis of viscoelastic multiphase flows

by

Hafiz Usman Naseer

A Dissertation Submitted to the
Graduate School of Sciences and Engineering
in Partial Fulfillment of the Requirements for
the Degree of

Doctor of Philosophy

in

Mechanical Engineering

KOÇ ÜNİVERSİTESİ

July 2025

Computational modeling and analysis of viscoelastic multiphase flows

Koç University

Graduate School of Sciences and Engineering

This is to certify that I have examined this copy of a doctoral dissertation by

Hafiz Usman Naseer

and have found that it is complete and satisfactory in all respects,

and that any and all revisions required by the final

examining committee have been made.

Committee Members:

Prof. Metin Muradoğlu (Advisor)

Assoc. Prof. Savaş Taşoğlu

Assist. Prof. Erkan Şenses

Prof. Mehmet Şahin

Assoc. Prof. Kerem Uğuz

Date:

Dedicated to my wife for her patience and support throughout this long journey

ABSTRACT

Computational modeling and analysis of viscoelastic multiphase flows
Hafiz Usman Naseer
Doctor of Philosophy in Mechanical Engineering
July 2025

Interface-resolved direct numerical simulations of multiphase viscoelastic fluid flows have been performed by using a high fidelity finite-difference/front-tracking method to explore some of the most complex dynamics of these intricate flow regimes. Surfactant contamination is also considered. The flow equations are solved fully coupled with the viscoelastic model equations and the equations governing interfacial and bulk surfactant concentrations. The latter coupling is accomplished by a nonlinear equation of state that relates the surface tension to the surfactant concentration.

Simulations are first performed to study the phenomenon of negative wakes generated behind a pair of bubbles rising in an otherwise quiescent viscoelastic fluid under buoyancy. It is found that, in addition to the formation of long tails that tilt towards each other, the lateral symmetry is also broken in the two-bubble system. The rise velocity of the parallel bubbles remains slightly smaller than that of the single bubble due to bubble-bubble interactions. Symmetry observed in the case of parallel bubble pairs is broken when bubbles are initialized by an initial offset in vertical direction.

Next, lateral migration of a deformable bubble in a viscoelastic pressure driven channel flow is studied. It is found that the forces induced by fluid inertia push a bubble towards wall while elasticity and deformability pull it towards channel center. This interplay between fluid inertia, elasticity, and bubble deformability determines the orientation of bubble migration in the channel and its final equilibrium position. It is shown that secondary flow velocity induced by a bubble migrating towards wall is an order of magnitude higher than the one induced by a solid particle under similar flow conditions. This behavior is attributed to the slip condition on the bubble surface.

Then, a novel mechanism of achieving an elasto-inertial turbulent (EIT) state

by injecting bubbles into a pressure-driven viscoelastic channel flow under the conditions for which a single-phase flow remains laminar is demonstrated even for the Reynolds number as low as $Re = 10$ and a Weissenberg number as low as $Wi = 1$. It is found that curved streamlines across the bubble interfaces provide the necessary condition to trigger an elastic instability that leads to a fully chaotic motion even at very low Reynolds and Weissenberg numbers for which the single-phase flow remains completely laminar. The energy spectra shows a scaling of -2 for this multiphase EIT regime. It is also found that bubbles move towards the channel centerline and form a string-shaped alignment pattern in the core region at lower values of $Re = 10$ and $Wi = 1$. Unlike solid particles, increasing shear-thinning effect tends to break up alignment of bubbles.

Finally, interface-resolved direct numerical simulations are performed to investigate drag reduction by polymer additives in a bubbly turbulent channel flow in the presence of surfactant contamination for a fixed Reynolds number of $Re = 5600$. Simulations are carried out for the high-drag-reduction (HDR) and maximum-drag-reduction (MDR) regimes. It is shown that, once flow is made viscoelastic by polymer additives, an HDR regime is achieved with a drag reduction of 49%. It is found that Reynolds stress is reduced in this HDR regime but still remains higher than polymer stress. Injection of contaminated bubbles reduces Reynolds stress even further and drag is not increased. Reynolds stress in single-phase flow of maximum MDR regime reduces below the value of polymer stress with a drag reduction of 68% and flow is dominated by elastic effects. Injection of bubbles in this MDR regime produces non-monotonic effect. A small concentration of contaminated bubbles increases Reynolds stress, turbulence production by mean flow and turbulent kinetic energy whereas a higher concentration of bubbles in the MDR regime reduces all these quantities. However, these effects remain restricted to core region of the channel and do not increase drag. It is found that turbulent kinetic energy spectrum shows a scaling of -2 in both of these multiphase HDR and MDR regimes and this scaling is not affected by a change in bubble concentration.

ÖZETÇE

Viskoelastik Çok-Fazlı Akışlarının Hesaplamalı Modellemesi ve Analizi
Hafiz Usman Naseer
Makine Mühendisliği, Doktora
Temmuz 2025

Sonlu-farklar/arayüz-izleme yöntemi kullanılarak çok fazlı viskoelastik akışların arayüz çözümlü doğrudan sayısal simülasyonları yapılmış ve bu karmaşık akış rejimlerinin en girift dinamikleri araştırılmıştır. Simülasyonlarda sürfaktan (yüzey-aktif maddesi) etkileri de göz önünde bulundurulmuştur. Akış denklemleri, viskoelastik model denklemleri ve sürfaktan evolüsyon denklemleriyle birlikte tamamıyla bağlaşık bir şekilde çözülmüştür. Bu bağlaşımda yüzey gerilmesi ara-yüzeydeki sürfaktan konsantrasyonuna doğrusal olmayan bir hâl denklemiyle bağlanmıştır.

İlk olarak, kaldırma kuvveti etkisiyle durgun bir viskoelastik akışkanda içerisinde yükselen iki kabarcığın ardında oluşan negatif girdap fenomenini incelenmiştir. Birbirine doğru eğilen uzun girdapların oluşumuna ek olarak, iki kabarcıklı sistemde yanal simetrinin de bozulduğu gösterilmiştir. Paralel kabarcıkların yükselme hızının kabarcık-kabarcık etkileşimleri nedeniyle tek bir kabarcığa kıyasla biraz daha düşük kaldığı gözlenmiştir. Kabarcıklar başlangıçta düşey yönde bir ofset ile konumlandırıldığında ise simetrinin bozulduğu tespit edilmiştir.

Daha sonra ise basınç tahrikli viskoelastik kanal akışında deforme olabilen bir kabarcığın yanal hareketi araştırılmıştır. Atalet kaynaklı kuvvetler kabarcığı kanal duvarına doğru iterken, elastik kuvvetler ve deformasyonun kabarcığı kanal merkezine doğru sevk ettiği gösterilmiştir. Atalet kuvveti, elastik kuvvet ve kabarcık deformabilitesi arasındaki bu etkileşim kabarcığın yanal hareketinin yönünü ve nihai denge konumunu belirlediği bulunmuştur. Duvara doğru hareket eden bir kabarcığın indüklediği ikincil akış hızının benzer akış koşullarında küresel bir katı parçacığın indüklediğinden bir mertebe daha yüksek olduğu tespit edilmiştir. Bu davranışın nedeni ise kabarcık yüzeyindeki kayma sınır koşulunun varlığına atfedilmiştir.

Kabarcığın basınç tahrikli kanaldaki yanal hareketi incelendikten sonra yine aynı kanalda kabarcık enjeksiyonu ile laminer akıştan türbülanslı akışa geçişi sağlayacak

yeni bir mekanizma ve yöntem bulunmuştur. Bu yöntemde, tek fazlı viskoelastik laminer akışa ani olarak kabarcıklar enjekte edilmekte ve bu sayede laminer akıştan Elasto-Ataletsel Türbülans (EIT) akış rejimine çok düşük Reynolds sayısı ($Re = 10$) ve çok düşük Weissenberg sayısı ($Wi = 1$) değerlerinde bile geçiş sağlanabilmektedir. Bunun nedeni kabarcık arayüzleri boyunca eğrisel akım çizgilerinin oluşması ve bu eğriliğin akış kararsızlığını tetikleyerek türbülanslı akışa geçişi sağlamasıdır. Enerji spektrumu bu düşük Weissenberg sayılı çok-fazlı EIT akış rejimi için -2 ölçeklenmesini göstermektedir. Bu ölçeklenme kabarcık boyutundan veya sayısından etkilenmemekte olup evrensel bir enerji transfer mekanizmasına delalet etmektedir. Ayrıca, belli koşullar altında kabarcıkların kanal merkezinde sicim şeklinde hizalandıkları tespit edilmiştir. Katı parçacıklar için literatürde yapılan gözlemlerin aksine, kayma-incelmesi etkisinin artmasının kabarcık hizalanmasının bozulmasına neden olduğu tespit edilmiştir.

Son olarak, çok-fazlı türbülanslı akışa polimer eklenmesinin sürtünme kaynaklı sürükleme kuvveti üzerindeki etkileri incelenmiştir. Simülasyonlar yüksek sürükleme azalması (high-drag-reduction (HDR)) ve maksimum sürükleme azalması (maximum-drag-reduction (MDR)) rejimleri için yapılmıştır. Kabarcıkların kanal duvarında birikmesini önlemek için akışa sürfaktan ilave edilmiştir. Simülasyonlarda Reynolds sayısı $Re = 5600$ değerinde sabit tutulmuştur. Basınç-tahrikli bir kanaldaki Newtonsal türbülanslı akışa az miktarda polimer eklenerek viskoelastik hâle getirildiğinde sürüklemede %49'luk bir azalma olduğu gözlenmiş olup bu HDR rejimine delalet etmektedir. Bu HDR rejiminde Reynolds gerilmesi azalmış olmasına rağmen hala polimer gerilmesinden daha yüksektir. MDR rejiminde ise, tek-fazlı akışın Reynolds gerilmesi polimer gerilmesinin altına düşerek %68'lik bir sürükleme azaltımı elde edilmiş ve akışın elastik etkiler tarafından domine edildiği gözlemlenmiştir. Bu rejimde, kabarcık enjeksiyonu kabarcık konsantrasyonuna bağlı olarak tekdüze olmayan etkiler yaratmıştır: Düşük kabarcık konsantrasyonu durumunda Reynolds gerilmesi, ortalama akım kaynaklı türbülans üretimi ve türbülans kinetik enerjisi artırırken, daha yüksek konsantrasyon durumunda bu büyüklüklerin azaldığı tespit edilmiştir. Ancak, bu etkiler kanalın orta bölgesiyle sınırlı kalmış ve sürükleme artışına neden olmamıştır. Ayrıca, çok-fazlı HDR ve MDR rejimlerinde türbülans kinetik enerjisi spektrumunun -2 ölçeklenmesi gösterdiği ve Weissenberg sayısından bağımsız olduğu bulunmuştur.

ACKNOWLEDGMENTS

I am really grateful to my thesis advisor Prof. Dr. Metin Muradoglu for granting me the opportunity to work on such an interesting topic. His guidance, motivation, expert advice and innovative ideas made my journey smoother and joyful. I am also thankful to Dr. Daulet Izbassarov for his guidance, motivation and expert advice. I am grateful to the thesis monitoring committee members Prof. Mehmet Şahin, Assoc. Prof. Kerem Uğuz and Asst. Prof. Erkan Şenses for their valuable inputs for presentation improvement, constructive ideas during the progress meetings and critical reading of the thesis draft. I would also like to thank the jury members for sparing their precious time and valuable comments for improving the thesis. I really enjoyed working with exceptional people in our research group.

I would like to thank my parents and family for encouraging me during the toughest times and their understanding when I was not able to spare time for them. It was their unending support that helped me turning my dream into a reality.

TABLE OF CONTENTS

LIST OF TABLES

LIST OF FIGURES

Chapter 1

INTRODUCTION

A Newtonian fluid becomes viscoelastic and its properties are transformed dramatically once a small amount of polymers is added to it. Development of first (N_1) and second (N_2) normal stress differences in such a flow leads to some exotic phenomena which remain absent in a Newtonian fluid flow. The exact mechanism behind many of these phenomena exhibited by viscoelastic fluids are yet to be fully explored. A few examples of these complex and often counter-intuitive phenomena include rod climbing, elastic recoil, negative wakes behind the bubbles, drag reduction in turbulent flows at high Reynolds number and sustaining a chaotic, turbulent like state at a very low Reynolds number [5]. Researchers have long been fascinated by these type of flows which are widely used in many industrial processes these days. Drilling of oil and gas fields [6], food processing [7], pharmaceuticals [8], paints and coatings [9], cosmetics [10] are just few such examples. Even more importantly, the unique properties of viscoelastic fluids are used to understand many biological processes such as blood flow [11], lungs airways [12], synovial fluid [13], bioprinting [14], cell mechanics [15] and drug delivery [16].

Direct numerical simulation (DNS) has become a powerful tool in recent years to understand these complex fluid flows with the development of advanced numerical methods and availability of rapidly increasing computational resources. However, DNS of a viscoelastic flow requires handling of additional non-linear elastic stresses which arise due to the presence of polymers. Addition of bubbles into such a flow complicates the problem even further. DNS of multiphase viscoelastic flow involves not only accurate modeling of viscoelastic stresses but also ever evolving interface which can undergo large deformations including topological change as well. Discontinuous variation of material properties across the interface is to be handled carefully while resolving the interface. If surfactants (surface active agents) are also present in the flow in the form of an impurity or added deliberately to manipulate the flow, as is the case in many natural processes and industrial applications, the DNS of such a flow becomes a formidable task and is the topic of many current research activities.

1.1 Front-Tracking Method

Over the years, various numerical methods have been developed to tackle the complex challenge of simulating multiphase flows. In the 1960s, the Marker and Cell (MAC) method was pioneered to study interfacial instabilities, gravity currents, waves and the droplet collisions with walls. This method uses Lagrangian virtual particles that move with the local fluid velocity on an Eulerian staggered grid to define the interface's shape and position. Later, Hirt et al. [17] introduced the Volume of Fluid (VOF) method, a memory-efficient approach that tracks the volume fraction of each fluid in every cell of an Eulerian grid. Another technique, the level set method [18], maintains a continuous signed distance function to ensure a well-resolved interface throughout the simulation. Jacqmin [19] demonstrated the phase field method's effectiveness in simulating two-phase flows through critical test cases. These approaches are collectively known as 'interface capturing' methods. In contrast, 'interface tracking' methods, such as the front-tracking method developed by Tryggvason et al. [20, 21], use a separate Lagrangian grid to represent the interface while solving governing equations on a background Eulerian mesh. This front-tracking method is employed in the current thesis to track the interface.

In the Front-Tracking Method (FTM), two separate grids are used i.e., an Eulerian grid and a Lagrangian grid. Boundary between fluids (interface) is represented by connected marker points that are moved with the local flow velocity. The equations governing the fluid flow are solved on the fixed Eulerian grid while the Lagrangian grid is used to track the interface. The term 'front' is used to refer to the complete set of computational objects which represent the interface. Figure 1.1

shows the result of a simulation of a buoyant bubble at one time instant. The Lagrangian grid is clearly visible with a cross-sectional plane of the regular structured fluid grid, where the velocity field is plotted. The Lagrangian grid is used for the accurate advection of the fluid interface and the computations of surface tension.

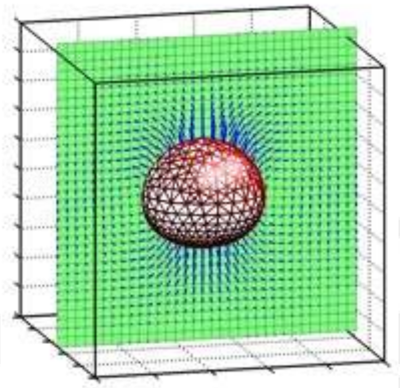

Figure 1.1: Front-tracking simulation of a buoyant bubble. The bubble surface is tracked by an unstructured triangular grid, but the fluid equations are solved on a regular structured grid.

Three-dimensional interfaces are represented by a triangular mesh as shown in Fig. 1.2. The marker points are located at the vertices of the triangular elements. Triangulation is done in such a way that an edge is shared only by two neighboring elements. Linked lists are created and maintained so that each element knows its corner marker points and neighboring elements. The corners of each element and the edges are numbered counterclockwise. The front points are moved with the local flow velocity interpolated from the fixed Eulerian grid. By using a first-order explicit Euler scheme, the new location of the marker points is given by

$$x_f^{n+1} = x_f^n + v_f^n \Delta t, \tag{1.1}$$

where x_f is the front position, v_f is the front velocity, and Δt is the time step. Superscript n denotes time step. After the front is moved/advected, it is essential to perform the restructuring of the front as it will stretch and deform due to the fluid motion. Stretching and compression causes long and short separation distance between the marker points, respectively. Thus, it is important to restructure the Lagrangian grid by splitting, deleting or reshaping the front elements to maintain good resolution. The decision for the addition and deletion of an element is based on the the size of each element, the length of its edges or its shape. The shape is monitored by aspect ratio and is compared with that of an equilateral triangle. Thus, the restructuring is controlled by the length of the edges and aspect ratio of an element. The details of restructuring scheme can be found in the book by Tryggvason et al. [21].

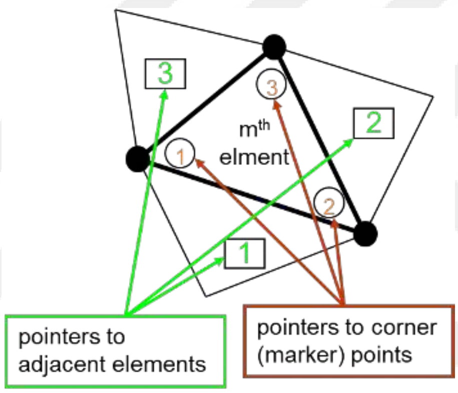

Figure 1.2: Structure of a three-dimensional front element

Accurate computation of surface tension is one of the most critical aspects of any method designed to follow motion of the boundary between immiscible fluids. In the front tracking method, surface tension force is determined on the Lagrangian grid and distributed conservatively onto the Eulerian grid. In the presence of surfactant, the surface tension on a surface segment is given by

$$\delta f_e = \oint_{\Delta C} \sigma(\Gamma)\mathbf{p}dl, \tag{1.2}$$

where $\sigma(\Gamma)$ is surface tension coefficient evaluated as a function of interfacial surfactant concentration (Γ) by using the equation of state

$$\sigma = \sigma_s[1 + \beta_s \ln{(1 - \frac{\Gamma}{\Gamma_\infty})}], \tag{1.3}$$

where $\beta_s = \frac{RT\Gamma_\infty}{\sigma_s}$ is the elasticity number. The surface segment can be selected in different ways and here we select a surface segment consisting of a third of all the elements connected to a given point. The surface segment for the point with coordinates x_1 is the cross-hatched area, bounded by a thick line, in the left side of Fig. 1.3. The area contributing to each point is found by identifying the centroid of the element and drawing lines from the centroid to the midpoints of the edges of the element that connect to the point in the middle. The centroid of element e is at

$$\mathbf{x_c} = \frac{1}{3}(\mathbf{x_1} + \mathbf{x_2} + \mathbf{x_3}). \tag{1.4}$$

The midpoints of the sides are

$$\mathbf{x_{12}} = \frac{1}{2}(\mathbf{x_1} + \mathbf{x_2}), \mathbf{x_{23}} = \frac{1}{2}(\mathbf{x_2} + \mathbf{x_3}), \mathbf{x_{13}} = \frac{1}{2}(\mathbf{x_1} + \mathbf{x_3}). \tag{1.5}$$

The normal to the element is found by

$$\mathbf{n_e} = \frac{\Delta\mathbf{x_{12}} \times \Delta\mathbf{x_{13}}}{|\Delta\mathbf{x_{12}} \times \Delta\mathbf{x_{13}}|} \tag{1.6}$$

where $\Delta\mathbf{x_{12}} = (\mathbf{x_1} - \mathbf{x_2})$ and so on. Since the force on the side connecting $\mathbf{x_1}$ and $\mathbf{x_{12}}$ is canceled by the force from the other element bordering that side, and the same is true for the side connecting $\mathbf{x_1}$ and $\mathbf{x_{31}}$, we only need to consider the lines connecting $\mathbf{x_{12}}$ to $\mathbf{x_c}$ and $\mathbf{x_c}$ to $\mathbf{x_{31}}$. The integral over the first line segment is

$$\oint_{\Delta C} \sigma(\Gamma)\mathbf{p}dl \approx \sigma(\Gamma_1)\mathbf{p_1}\Delta s_1 = \sigma(\Gamma_1)\mathbf{n_e} \times \frac{\mathbf{x_c} - \mathbf{x_{12}}}{\Delta s_1}\Delta s_1 = \\ \sigma(\Gamma_1)\mathbf{n_e} \times (\mathbf{x_c} - \mathbf{x_{12}}). \tag{1.7}$$

The net contribution to the force on the area segment surrounding point 1, from element e, is the integral over both line segments. Thus, we can write

$$\delta f_{1e} = \oint_{\Delta C} \sigma(\Gamma)\mathbf{p}dl \approx \sigma(\Gamma_1)\mathbf{p_1}\Delta s_1 + \sigma(\Gamma_2)\mathbf{p_2}\Delta s_2, \tag{1.8}$$

where $\Gamma_1 = (\Gamma_e + \Gamma_{er})/2$ and $\Gamma_2 = (\Gamma_e + \Gamma_{e1})/2$. The contributions from the other elements sharing node 1 are computed in a similar fashion and summed up to find

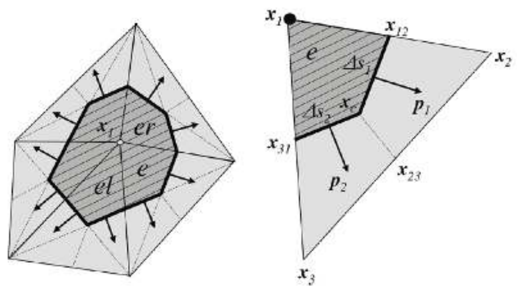

Figure 1.3: Computations of surface gradient, surface Laplacian and surface tension force of the 3D front. The surface gradient and surface tension forces are computed at the nodes by adding up contributions from the adjacent elements. The surface Laplacian is computed at cell centers.

the net force. The surface tension forces computed at the nodes as described above are then distributed onto neighboring Eulerian grid points as a body force in a conservative manner using Peskin's distribution. Details of the distribution can be found in the book by Tryggvason et al. [21].

In presence of surfactant, during refining of the front as discussed above, special attention is paid to conserve the total surfactant mass during the addition and deletion of front elements. The details of this treatment can be found in the paper by Muradoglu and Tryggvason [22].

1.2 Viscoelastic Fluid Models

Viscoelastic fluids are materials that display both viscous and elastic behaviors in response to applied stresses. The earliest attempts to capture the characteristics of such a fluid flow were made by the linear combination of viscous and elastic effects. As illustrated in Fig. 1.4, 1D Maxwell model is the example of a linear viscoelastic model. The shear stress Σ created in an elastic solid obeys Hooke's law and can be written as $\Sigma = \gamma G$, where G is the elastic constant of the material, or shear modulus and γ is the deformation or displacement gradient. Similarly, the constitutive equation for a Newtonian viscous fluid is a linear relationship between the stress and shear rate, i.e.; $\Sigma = \eta\dot{\gamma}$, where η is the viscosity of the fluid, and the dot denotes a time derivative. Following the analogy of an electric circuit, $\gamma = \gamma_s + \gamma_d$ and $\Sigma = \Sigma_s = \Sigma_d$ for the serialized connection in the Maxwell model, where the subscripts 's' and 'd' denote the spring and dashpot, respectively. Thus, it can be written as

$$\Sigma + \frac{\eta}{G}\dot{\Sigma} = \eta\dot{\gamma}. \tag{1.9}$$

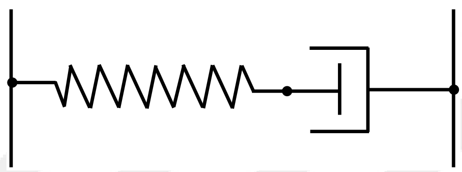

Figure 1.4: Representation of the Maxwell model with a spring (elastic behavior) and a dashpot (viscous behavior)

The Maxwell model, Eq. (1.9) can be formally solved [23] to yield

$$\Sigma(t) = \frac{1}{\lambda}\int_{-\infty}^{t} e^{-\frac{t-t'}{\lambda}} \eta\dot{\gamma}(t')dt', \tag{1.10}$$

where $\lambda = \eta/G$ is the Maxwell relaxation time. As can be seen from the solution, the stress created by a steplike deformation relaxes exponentially on the time scale λ indicating viscous-fluid-like properties, while at short times, $\Sigma(t) \sim \eta\gamma(t)/\lambda$, the Maxwell material is solid-like.

Linear viscoelastic materials exhibit stress that is directly proportional to their strain history but this behavior typically applies only to small deformations, low strain rates, low stress and inherently linear materials. In contrast, approximately 90% of fluids display nonlinear behavior, characterized by large deformations and complex responses. Nonlinear viscoelasticity becomes prominent when materials undergo significant deformation, often altering their properties in the process. To address this, sophisticated mathematical models incorporating elastic, viscous and inertial nonlinear effects have been developed to describe these behaviors [24].

Many of these differential constitutive models originate from the kinetic theory of dilute polymer solutions where polymer molecules are represented as dumbbells—two beads connected by a massless spring. These models account for interactions between polymer molecules and the surrounding Newtonian fluid but neglect interactions among the polymers themselves. Simple models like the Upper Convected Maxwell (UCM) and Oldroyd-B [25] are effective for viscoelastic shear flows. However, in extensional flows, these models predict infinite stretching of the dumbbells leading to nonphysical singularities. To address this limitation, Finitely Extensible Nonlinear Elastic (FENE) models restrict polymer chain extensibility, capturing the shear-thinning effect. Similarly, the Giesekus model [26] limits extensibility, predicts shear-thinning and accounts for non-zero second normal stress differences, enhancing its applicability to complex viscoelastic flows.

In this thesis, three viscoelastic models are used; Oldroyd-B, FENE-P and the Giesekus depending upon the nature of the problem. In these models, the generic form of viscoelastic stress tensor $\boldsymbol{\tau}$ is given by

$$\boldsymbol{\tau} = \frac{\mu_p}{\lambda}(F\boldsymbol{B} - \boldsymbol{I}), \tag{1.11}$$

where μ_p, $\boldsymbol{B}$, λ and $\boldsymbol{I}$ are the polymeric viscosity, polymer conformation tensor, polymer relaxation time and the identity tensor, respectively. The conformation tensor evolves by

$$\frac{\partial \boldsymbol{B}}{\partial t} + \boldsymbol{\nabla} \cdot (\boldsymbol{u}\boldsymbol{B}) - (\boldsymbol{\nabla}\boldsymbol{u})^T \cdot \boldsymbol{B} - \boldsymbol{B} \cdot \boldsymbol{\nabla}\boldsymbol{u} = \chi(\boldsymbol{B}). \tag{1.12}$$

The function $\chi(\boldsymbol{B})$ for the three viscoelastic models is defined as

$$\chi(\boldsymbol{B}) = \begin{cases} -\frac{1}{\lambda}(F\boldsymbol{B} - \boldsymbol{I}), F = \boldsymbol{I} & \text{Oldroyd-B} \\ -\frac{1}{\lambda}(F\boldsymbol{B} - \boldsymbol{I}), F = \frac{L^2}{L^2 - \mathrm{tr}(\boldsymbol{B})} & \text{FENE-P} \\ \frac{1}{\lambda}[(1-\alpha)\boldsymbol{I} + (2\alpha - 1)\boldsymbol{B} - \alpha\boldsymbol{B^2}] & \text{Giesekus} \end{cases} \tag{1.13}$$

where L is the maximum extensibility of polymer molecules and α is the mobility factor, representing the anisotropy of the hydrodynamic drag exerted on the polymer molecules.

1.3 Outline and contribution of thesis

This thesis contributes to the existing body of knowledge by investigating the complex flow regimes of multiphase viscoelastic fluid flows. The primary objective is to examine two notable phenomena in viscoelastic fluid flows: elasto-inertial turbulence at low Reynolds numbers and drag reduction at high Reynolds numbers, both in the presence of bubbles. Prior to conducting large-scale Direct Numerical Simulations (DNS) to explore these inertial regimes in a multiphase context, two preliminary studies are undertaken to analyze the dynamics of individual bubbles in viscoelastic flows under the influence of buoyancy and pressure-driven conditions. Interface resolved direct numerical simulations have been performed by using a high fidelity finite-difference/front-tracking method. The details of governing equations used under the framework of front tracking method are described in each chapter separately depending upon the flow conditions and the presence of surfactant. The dissertation is organized as follows:

In Chapter 2, dynamics and interactions of two parallel bubbles rising in a viscoelastic fluid under buoyancy is analyzed in detail. The interaction of negative wake regions generated behind these bubbles is examined and different forces acting on the bubbles are quantified. It is observed that in addition to the formation of long tails behind the bubbles that tilt towards each other, the lateral symmetry is also broken in the two bubble system.

In Chapter 3, lateral migration of a bubble in a viscoelastic pressure driven channel flow is examined in detail. A square-shaped duct is used as the computational domain and a highly concentrated polymer solution is simulated using the Giesekus model. It is observed that the secondary flow velocity induced by a bubble migrating towards the wall is an order of magnitude higher than the one induced by a solid particle under similar flow conditions. At a high Weissenberg number, elastic instability occurs due to curvature of streamlines across bubble interface, which motivates the study conducted in Chapter 4.

In Chapter 4, the ability of viscoelastic flow to sustain a chaotic flow state even at a very low Reynolds number is explored in the presence of bubbles. A novel mechanism of achieving the EIT state by injecting the bubbles into a pressure-driven viscoelastic flow under the conditions for which a single-phase flow remains laminar is tested and verified at a Reynolds number as low as 10 and a Weissenberg number as low as 5. The curved streamlines across the bubbles interfaces provide the necessary condition to trigger an instability even when the viscoelastic stresses are not very high and the single-phase flow remains completely laminar. The energy spectra shows a scaling of -2 for this low Wi multiphase EIT regime.

In Chapter 5, the drag reducing phenomenon of viscoelastic flows at high Reynolds number is explored in its extreme limits. Large scale DNS are performed to achieve drag reduction up to 49% (HDR regime) and 68% (MDR regime) at the corresponding Weissenberg numbers of 7 and 24, respectively. Subsequently, contaminated bubbles are injected into these flow regimes with a volume fraction of 3% and 9%. The effects of bubbles on the turbulent dynamics of the flow under these extreme flow conditions are studied in detail.

Finally, conclusions are drawn in Chapter 6.

Chapter 2

DYNAMICS AND INTERACTIONS OF PARALLEL BUBBLES RISING IN A VISCOELASTIC FLUID UNDER BUOYANCY[1]

2.1 Introduction

The buoyancy-driven motion of bubbles rising through a viscoelastic liquid is markedly different from that in a Newtonian fluid. Due to its relevance in many natural processes and industrial applications such as pharmaceutical and medicine [27], bubble column reactors [28, 29] and water aeration and waste treatment [30], it has been an active subject of research especially since the pioneering work of Astarita and Apuzzo [31] who demonstrated some exotic behaviors of bubbles in a viscoelastic liquid. As many of fluids encountered in real life are non-Newtonian [32] exhibiting viscoelastic behavior, studying their multiphase dynamics is of great scientific and practical importance. In particular, bubbles ascending in a viscoelastic medium under buoyancy have significant prominence due to their peculiar dynamics. While a vast amount of literature is available which covers the flow dynamics and interaction of gas bubbles in Newtonian fluids [33, 34], many aspects of the bubble dynamics in viscoelastic fluids are yet to be fully explored. Many attempts have been made in the recent past to understand the complex flow field and dynamics of bubble rise in this particular class of non-Newtonian fluids [1, 35, 36]. The previous studies have largely focused on single bubble dynamics [37]. In spite of their fundamental importance in bubbly flows of practical interest, less attention has been paid to understand the effects of viscoelasticity on bubble-bubble interactions, which is the

[1]PUBLISHED AS A PAPER UNDER THE SAME TITLE IN JOURNAL OF NON-NEWTONIAN FLUID MECHANICS 313 (2023): 105000

subject of the present study.

One important difference between a bubble rising in a viscoelastic fluid compared to that in a Newtonian fluid is the appearance of a 'negative wake' behind the trailing edge of the bubble [38]. This phenomenon was first observed by Hassage [39] and later confirmed by many experimental [40, 41] and computational works [38, 42, 43]. The second interesting difference is the appearance of 'velocity jump' discontinuity in the bubble rise velocity once its volume exceeds a critical limit. This phenomena was first observed experimentally by Astarita and Apuzzo [31]. Both 'negative wake' and 'velocity jump' are mainly associated with the viscoelasticity of the ambient fluid and the bubble volume. As the bubble volume is increased, first a negative wake starts to appear in a transition region with no noticeable velocity jump. When the bubble volume is increased further beyond the critical value, its terminal velocity undergoes a rather abrupt increase by as much as an order of magnitude. Based on their own experimental data and using the dimensional analysis, Pilz and Brenn [44] showed that the critical volume depends on the ratio of the polymer relaxation time to the convective time scale and the capillary length. Once the bubble volume is increased beyond its critical value, the negative wake gains further strength, and the terminal rise velocity is further increased abruptly. A recent study by Bothe et al. [45] provides a convincing explanation for this velocity discontinuity through experimental measurements and extensive computational simulations. They showed that the interplay of convective time scale and relaxation time scale of polymer molecules plays a critical role in the discontinuous increase of the rise velocity. The third major difference occurs in the bubble shape. The fore-aft symmetry of bubble shape is lost in a viscoelastic liquid caused by non-zero viscoelastic normal stress difference at the interface. Depending upon the flow parameters, a range of different bubble shapes have been reported from a slightly ellipsoidal to a more 'eye drop', 'cusp' or a bubble with a long thin tail.

Several studies are available describing the interaction of parallel bubbles in Newtonian fluids due to their relevance in many industrial and medical applications such as microbubble aerator for water treatment [30], medical ultrasound imaging [27], algae farming at a large scale [46], to name a few. Legendre et al. [47] studied the hydrodynamic interactions between two initially spherical bubbles rising side by side in a Newtonian liquid. The interactions were studied under a wide range of Reynolds numbers for both viscous and nearly inviscid cases. They found that, in contrast to the potential theory, the lateral force between bubbles becomes repulsive in the low Reynolds number limit due to the interactions of vorticity fields produced at respective bubble interfaces. Bunner and Tryggvason [48] computationally studied the effects of bubble deformation on the properties of the bubbly flow. They found that deformed bubbles interacts much more strongly than the spherical bubbles, and thus induce higher fluctuations of velocity in their vicinity. Zhang et al. [49] studied vortex interactions between parallel bubbles rising in a silicon oil and reported that wake interactions produced by parallel bubbles can induce strong fluctuations in the surrounding bulk fluid.

Similarly, several experimental studies have been conducted to study the dynamics of a gas bubble rising in a viscoelastic medium as this situation is encountered frequently in many processing industries. Kee et al. [50] experimentally studied bubble motion and coalescence in polymer solutions but did not observe any velocity discontinuity. More recently, experimental result [51] showed that two parallel bubbles rising in a non-Newtonian fluid of carboxymethylcellulose (CMC) solution attract each other when the initial gap between their centers is small. However, parallel bubbles with the same volume repel each other when their initial separation is large. Li [52] and Frank [53] used particle image velocimetry (PIV) technique to investigate the rise velocity of bubble chain in a viscoelastic medium with respect to their volumes. They reported that during the dynamic process of bubble-bubble interactions, there was a temporary decrease in the local viscosity which facilitated the rise of following bubble in a highly viscoelastic fluid.

Despite these experimental studies, complex dynamics of bubble-bubble interactions in a viscoelastic medium have not been explored completely. Advances made in the last few decades in interface-resolved simulations of multiphase flows allow to overcome the limitations faced in the experimental methods. Fully three-dimensional interface-resolved simulations can be used to describe this dynamic process in great detail and reveal complex physics of strongly interacting bubbles in a viscoelastic ambient fluid in the regime where the intriguing phenomenon of negative wake occurs. To the best of authors' knowledge, there has been no computational study which describes the interactions of parallel bubbles in a viscoelastic fluid. Yuan et al. [54] have recently studied important aspects of coalescence and interactions of inline bubbles in a shear thinning viscoelastic fluid using a volume-of-fluid (VOF) method with an adaptive mesh refinement technique. They examined the interactions of inline bubbles for a range of different volume combinations in the subcritical, critical and supercritical regimes. However, they have not considered the case of parallel bubbles that interact very differently than the inline bubbles.

In the present study, interface-resolved numerical simulations of 3D bubbles have been performed to examine the interactions of buoyancy-driven parallel bubbles rising in an otherwise quiescent viscoelastic fluid. Extensive simulations have been performed for a range of non-dimensional parameters to observe the flow field around these bubbles and a particular attention is paid to the interactions between the bubbles with negative wakes. In section 2.2, the mathematical model is described in the framework of the front-tracking method. Section 2.3 contains detailed information regarding the computational domain and the numerical set up used in the present study. The calculation of 3D forces acting on the surface of bubbles and the effects of Galilei and Weissenberg numbers on the interactions of parallel bubbles have been presented in section 2.4.1. The effects of Eötvös number, solvent viscosity ratio and the initial distance between the bubble centers have been described in detail in the supplementary material due to space considerations. Some details of the grid convergence are also provided in the supplementary material, which can be accessed in the online version of the paper.

2.2 Mathematical Model and Numerical Method

The flow and viscoelastic model equations are briefly described here in the context of the front-tracking method. Following the work of Muradoglu and Tryggvason [21, 22], a single set of flow equations can be written for the entire computational domain of a multiphase flow field as long as the effects of surface tension are appropriately modelled and the discontinuities in material properties are correctly accounted for. In the present one-field formulation, the Navier-Stokes equations are written as:

$$\frac{\partial \rho \boldsymbol{u}}{\partial t} + \boldsymbol{\nabla} \cdot (\rho \boldsymbol{u}\boldsymbol{u}) = -\boldsymbol{\nabla} p + \boldsymbol{\nabla} \cdot \boldsymbol{\tau} + \boldsymbol{\nabla} \cdot \mu_s(\boldsymbol{\nabla}\boldsymbol{u} + \boldsymbol{\nabla}\boldsymbol{u}^T) + \boldsymbol{g}\Delta\rho + \int_A \sigma\kappa\boldsymbol{n}\delta(\boldsymbol{x} - \boldsymbol{x}_f)dA \tag{2.1}$$

where $\boldsymbol{u}$, p, ρ, μ_s are the velocity vector field, pressure field, discontinuous density and discontinuous solvent viscosity fields, respectively. The effect of surface tension is added as a body force term on the right-hand side of the momentum equation where σ is the surface tension coefficient, κ is twice the mean curvature and $\boldsymbol{n}$ is a unit vector normal to the interface. As the surface tension acts only on the interface, δ represents a three-dimensional delta function with the arguments $\boldsymbol{x}$ and $\boldsymbol{x}_f$ being a point at which the equation is evaluated and a point at the interface, respectively. The momentum equation is supplemented by the incompressibility condition:

$$\boldsymbol{\nabla} \cdot \boldsymbol{u} = 0. \tag{2.2}$$

It is assumed that the material properties remain constant following a fluid particle, i.e.,

$$\frac{D\rho}{Dt} = 0, \frac{D\mu_s}{Dt} = 0, \frac{D\mu_p}{Dt} = 0, \frac{D\lambda}{Dt} = 0, \tag{2.3}$$

where $\frac{D}{Dt} = \frac{\partial}{\partial t} + \boldsymbol{u} \cdot \boldsymbol{\nabla}$ is the material derivative. For a viscoelastic fluid, μ_p is the polymeric viscosity and λ is the polymer relaxation time.

Viscoelasticity of bulk liquid is modeled using the FENE-P model [55]. In this model, the conformation tensor $\mathbf{B}$ evolves by

$$\begin{aligned} \frac{\partial \boldsymbol{B}}{\partial t} + \nabla \cdot (\boldsymbol{u}\boldsymbol{B}) - (\nabla \boldsymbol{u})^T \cdot \boldsymbol{B} - \boldsymbol{B} \cdot \nabla \boldsymbol{u} &= -\frac{1}{\lambda}\left(F\boldsymbol{B} - \boldsymbol{I}\right), \\ F &= \frac{L^2}{L^2 - \mathrm{trace}(\boldsymbol{B})}, \end{aligned} \tag{2.4}$$

where $\boldsymbol{B}$, L, λ, and $\boldsymbol{I}$ are the conformation tensor, the maximum polymer extensibility, polymer relaxation time and the identity tensor, respectively. The polymeric stress tensor is then calculated as

$$\boldsymbol{\tau} = \frac{\mu_p}{\lambda}(F\boldsymbol{B} - \boldsymbol{I}), \tag{2.5}$$

where μ_p is the polymeric viscosity. The log-conformation method [56] is used to solve the FENE-P model equations to overcome the well-known numerical difficulties due to stiffness at high Weissenberg numbers.

A finite-difference/front-tracking (FD/FT) [21, 22] method is used to solve the flow equations [Eqs. (2.2) and (2.2)] fully coupled with the FENE-P model [Eq. (2.4)]. A fixed Eulerian grid is used to solve field equations on a staggered grid. The velocity nodes are located at the cell faces of this Eulerian grid while the material properties, pressure and the extra stresses are all located at the cell centers. A QUICK scheme is used to discretize convective terms in the momentum equations while second-order central differences are used to discretize the diffusive terms. For the convective terms in the viscoelastic equations, a 5th order WENO-Z [57] scheme is used. A second-order predictor-corrector method is used for the time integration. In this method, the first-order solution (Euler method) acts as a predictor which is then corrected by the trapezoidal rule. The details of the present front-tracking method can be found in the book by Tryggvason [21] and in the review paper [20]. An FFT based solver is used for the Poisson equation. Since the pressure equation is not separable due to variable density in the present multiphase flow, the FFT-based solvers cannot be used directly. To overcome this challenge, a pressure-splitting technique is employed [58, 59]. In the present front-tracking method, the Eulerian quantities are advanced from the time step n to the time step $n+1$ as

$$\begin{aligned}\frac{\rho^{n+1}\boldsymbol{u}^t - \rho^n\boldsymbol{u}^n}{\Delta t} = \big[&-\boldsymbol{\nabla_h}\cdot(\rho\boldsymbol{u}\boldsymbol{u}) + \boldsymbol{\nabla_h}\cdot(\mu_s(\boldsymbol{\nabla_h}\boldsymbol{u} + \boldsymbol{\nabla_h^T}\boldsymbol{u})) + (\rho - \rho_{av})\boldsymbol{g} \\ &+ \boldsymbol{\nabla_h}\cdot\boldsymbol{\tau} + \int_A \sigma\kappa\mathbf{n}\delta(\mathbf{x} - \mathbf{x_f})dA\Big]^n,\end{aligned} \tag{2.6}$$

$$\boldsymbol{\nabla_h}^2 p^{n+1} = \boldsymbol{\nabla_h}\cdot\left[\left(1 - \frac{\rho_0}{\rho^{n+1}}\right)\boldsymbol{\nabla_h}\left(2p^n - p^{n-1}\right)\right] + \frac{\rho_0}{\Delta t}\boldsymbol{\nabla_h}\cdot\boldsymbol{u}^t, \tag{2.7}$$

$$\boldsymbol{u}^{n+1} = \boldsymbol{u}^{t} - \Delta t \left[\frac{1}{\rho_0} \boldsymbol{\nabla_h} p^{n+1} + \left(\frac{1}{\rho^{n+1}} - \frac{1}{\rho_0} \right) \boldsymbol{\nabla_h} \left(2p^{n} - p^{n-1} \right) \right], \tag{2.8}$$

where ∇_{h} is the discrete version of the Nabla operator, $\rho_0 = min(\rho_i, \rho_o)$ and $\mathbf{u}^t$ is the temporary velocity. The solution obtained by Eqs. (2.6-2.8) is only first order accurate in time. For a second order temporal accuracy, this solution is used as a predictor to compute the solution at the time level $n+2$. Then, a second order solution at time level $n+1$ is recovered by averaging the solutions at n and $n+2$. We note that this time integration scheme is equivalent to the trapezoidal rule for a linear problem.

2.3 Numerical Setup and Validation

Simulations are first performed to validate the numerical method for a buoyancy-driven single bubble rising in an otherwise quiescent viscoelastic liquid and the results are compared with the computational results of Yuan et al. [1]. Although the present method has already been rigorously tested and utilized in several studies [60, 61, 62] involving multiphase flows, a baseline case from Yuan et al. [1] is selected to check its accuracy for the case with a negative wake. To facilitate a direct comparison, the Oldroyd-B model [25] is used in the validation simulations.

The buoyancy-driven flow in a viscoelastic medium is characterized by several non-dimensional numbers. Four of these numbers are of primary importance [1, 63]. These are the Galilei number (Ga), the Eötvös number (Eo), the Weissenberg number (Wi) and solvent to total viscosity ratio (β). The Galilei number represents the ratio of gravitational force to viscous force, the Eötvös number represents the ratio of gravitational force to surface tension force and the Weissenberg number represents the ratio of polymer relaxation time to convective time scale. Using the initial bubble radius R as the length scale, $U_g = \sqrt{gR}$ as the velocity scale and $\frac{R}{U_g}$ as the time scale, these non-dimensional parameters are defined as

$$Ga = \frac{\rho_o U_g R}{\mu_s + \mu_p}, Eo = \frac{\rho_o g R^2}{\sigma}, Wi = \frac{\lambda U_g}{R}, \beta = \frac{\mu_s}{\mu_s + \mu_p}. \tag{2.9}$$

For all the simulations, the density (ρ_o/ρ_i) and viscosity (μ_o/μ_i) ratios are set to 40. Although, in a typical liquid-air system, density ratio is an order of magnitude higher than the one used here, it has been previously demonstrated [64, 65] that the results are not affected significantly at higher ratios for these kind of flows. A smaller property ratio enhances numerical stability, relaxes the time step restrictions and hence reduces the computational cost. Note that, although not shown here due to space consideration, simulations have been performed for the density and viscosity ratios of 80 and the results are found to be essentially the same as those computed for $\rho_o/\rho_i = \mu_o/\mu_i = 40$, i.e., the difference is less than 1% in all the quantities.

To duplicate the results of Yuan et al. [1] for two selected cases, the same rectangular domain is generated with the size of $L_y = 40R$ in the streamwise direction and $L_x = L_z = 8R$ in the other two directions. The bubble is positioned initially at the centerline of the channel with a distance of $3R$ from the bottom of domain (Fig. 2.1). The bubble rise velocity is normalized using the gravitational velocity ($U_g = \sqrt{gR}$) and time is normalized by the convective time scale ($\frac{R}{U_g}$) throughout this study. The grid size and the flow parameters for these two validation cases are presented in Table 2.1. With this combination of non-dimensional numbers, a negative wake is observed behind the trailing edge of the bubble for the case-I and a semi-circular cusp shaped bubble is obtained without a negative wake for the case-II (Fig. 2.1).

Figure 2.1a shows the evolution of bubble shape until it reaches its terminal velocity. Figure 2.1b shows the average elongation of polymer molecules around the bubble quantified by the trace of the conformation tensor $\boldsymbol{B}$ contours in a vertical cutting plane at the center of computational domain. The region of negative wake is clearly indicated by the contours of velocity in the bottom part of Fig. 2.1c. The velocity vectors are also plotted in the top portion of Fig. 2.1c to better show the negative wake region. As seen in this figure, the velocity vectors reverse their direction in the wake region behind the trailing edge of the bubble. Figure 2.1d shows the comparison of bubble rise velocities for the two selected validation cases. The Weissenberg number and solvent to total viscosity ratio are ($Wi = 10, \beta = 0.2$) and ($Wi = 1, \beta = 0.8$) for Case-I and Case-II, respectively. The other parameters for these two validation cases are $Eo = 100$ and $Ga = 3.91$. The comparison of bubble shapes for the validation Case-II ($Wi = 1, \beta = 0.8$) for which the negative wake is not generated behind the bubble is also shown in the inset. The evolution of bubble rise velocities for both the cases show a good agreement with the results of Yuan et al. [1].

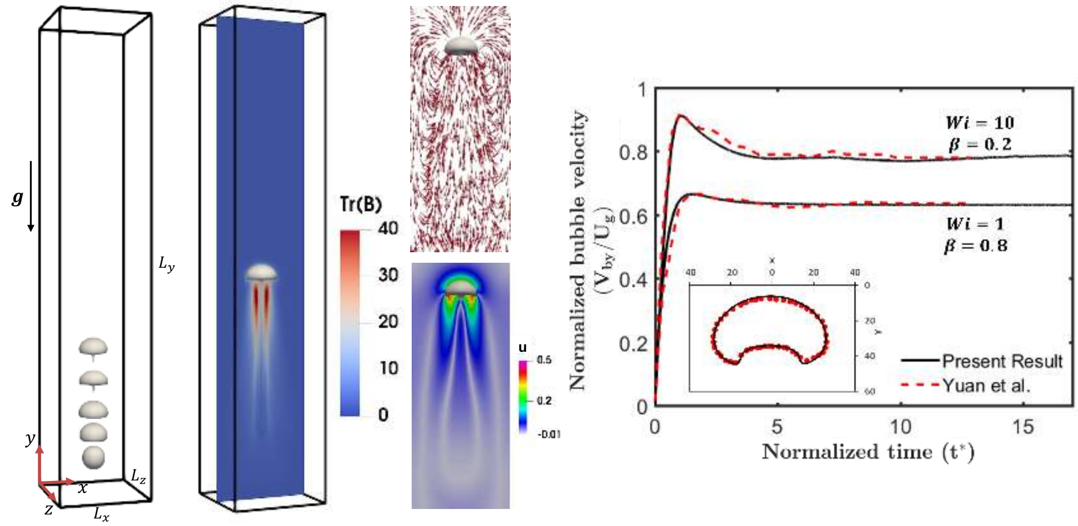

Figure 2.1: (a) The computational domain and the evolution of a 3D bubble rising in a viscoelastic fluid under buoyancy ($Eo = 100, Wi = 10, Ga = 3.91, \beta = 0.2$). (b) The average elongation of polymer molecules around the bubble indicated by the trace of the conformation tensor $\boldsymbol{B}$ is shown in a vertical cutting plane at the center of domain. (c) The region of negative wake is shown by constant contours of velocity in a plane (bottom portion). The velocity vectors around 3D bubble are also shown in the same plane to better show the region of the negative wake (top portion). (d) The present numerical results are compared with the results of Yuan et al. [1] for the two validation cases. A comparison of steady bubble shapes is shown in the inset for $Wi = 1, \beta = 0.8$.

2.4 *Results and Discussion*

After validating the numerical method for a single bubble case and observing a strong negative wake for this combination of non-dimensional numbers, the study is expanded further for the two parallel bubble cases. The validation Case-I ($Eo = 100, Ga = 3.91, Wi = 10, \beta = 0.2$) is selected as the baseline case and the non-

Table 2.1: Geometric and flow parameters for the two validation cases

Parameter	Symbol	Input Value
Galilei Number	Ga	3.91
Eötvös Number	Eo	100
Domain Size	$L_x \times L_y \times L_z$	$8R \times 40R \times 8R$
Grid Size	$N_x \times N_y \times N_z$	$120 \times 1200 \times 120$
Validation Case-I		
Weissenberg Number	Wi	10
Viscosity Ratio	β	0.2
Validation Case-II		
Weissenberg Number	Wi	1
Viscosity Ratio	β	0.8

dimensional parameters are varied one by one around this baseline case for the two parallel bubble system to observe how bubble-bubble interactions vary over a range of critical flow parameters. This set of non-dimensional parameters is selected as the baseline case since the single bubble produces a strong negative wake at these values without undergoing a breakup. It is important to note that the bubble volume is in the super-critical range and its terminal velocity is an order of magnitude higher than that of the corresponding sub-critical bubble. However, the rise velocity does not decrease sharply after attaining its peak value and quickly settles down to its terminal velocity. Thus, the velocity jump discontinuity is not apparently visible. The main reason is an oblate shape of the bubble which ensures a quick force balance between the viscous and viscoelastic forces as recently pointed out by Yuan et al. [1, 36].

Figure 2.2a shows the computational domain with two parallel bubbles of unequal sizes at their initial locations. In yz-plane, the bubbles are positioned exactly at the center. The geometric parameters used in the parallel bubble system are listed in Table 2.2. In the validation cases, it is observed that the transient region of rise velocity of a single bubble remains less than $5R$ in the streamwise (y) direction. The bubble quickly reaches its terminal velocity in this buoyancy driven flow. The effect of the domain size is checked for the baseline two-bubble system by performing simulations for the vertical domain size of $L_y = 20R$ and $L_y = 40R$, and the results are found to be nearly identical (Fig. 2.2b). Therefore, the domain size is reduced to $20R$ in the vertical direction with the periodic boundary conditions for the subsequent parallel bubble cases to facilitate extensive simulations. In the simulations, the periodic boundary conditions are applied in the x and y directions whereas the no-slip boundary conditions are applied in the z direction. Instead of the Oldroyd-B model used earlier for the validation cases, a more realistic shear-thinning viscoelastic FENE-P model [66] is used for the simulations of the parallel bubbles. The other non-dimensional numbers are the same as those of the single bubble case (validation case-I, see Table 2.1).

Table 2.2: Geometric parameters for parallel bubbles

Parameter description	Symbol	Input value
Radius of the small bubble	r	$0.5R - R$
Initial horizontal distance between bubble centers	d_i	$2.5R$ - $4R$
Initial vertical distance between bubble centers	d_y	0 - R
Steady distance between bubble centers	d_f	-
Initial distance from side wall	l_{xi}	$2.75R$
Initial distance from bottom of domain	l_{y_i}	$3R$

Simulations are first performed for the baseline case with two parallel bubbles of equal size having perfect initial alignment in the horizontal direction ($d_y = 0$). The results are presented only for the left bubble since both bubbles are identical in the two-bubble system. Figure 2.2c shows the evolution of the bubble rise velocity compared to the rise velocity of the single bubble case. It is observed that the terminal velocity of parallel bubbles remains slightly less than that of the single bubble case due to the bubble-bubble interactions. In the inset of Fig. 2.2c, the constant contours of velocity at steady-state are shown in a vertical cutting plane at the center of the domain for both cases. Thin extended tails appear behind the bubbles in the two-bubble system and they bend towards each other due to strong interactions of the negative wakes. In the case of the two parallel bubbles, the region of the negative wake appears only in a thin region adjacent to the long bubble tails whereas, in the case of a single bubble, the region of negative wake extends downwards behind the trailing edge of the bubble.

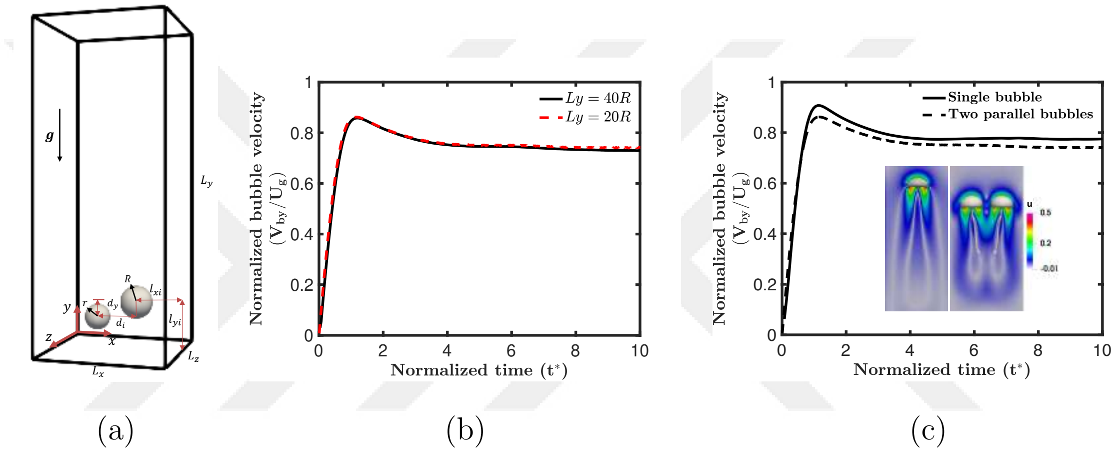

Figure 2.2: (a) The computational domain is shown with two parallel bubbles at their initial locations. (b) Effects of computational domain size in the streamwise (y) direction for $L_y = 20R$ and $L_y = 40R$. (c) Rise velocity of a single bubble is compared with the rise velocity of two parallel bubbles ($d_y = 0$) having an initial distance of $2.5R$ between their centers. The contours of velocity in a 2D plane at the center of computational domain are shown in the inset for both the cases at steady state. ($Eo = 100, Wi = 10, Ga = 3.91, \beta = 0.2$)

Figure 2.3 shows the comparison of bubble shapes at five different times between the parallel-bubble and single bubble cases under the same parametric settings. At their terminal velocity, the parallel bubbles appear to have much longer tails tilted towards each other. The strong interactions of negative wakes in the two-bubble system result in non-symmetric deformation of bubbles as seen in the bottom view plots in Fig. 2.3b. It is interesting to observe that, although the bottom parts of the bubbles attract each other, the overall net force is repelling as quantified and discussed below. As a result, the distance between parallel bubbles increases and reaches the approximate steady distance of $3.45R$ from an initial value of $2.5R$ between their centers. These changes in the bubble shapes and flow dynamics around the bubbles can be better understood by computing various forces acting on the bubbles as discussed below.

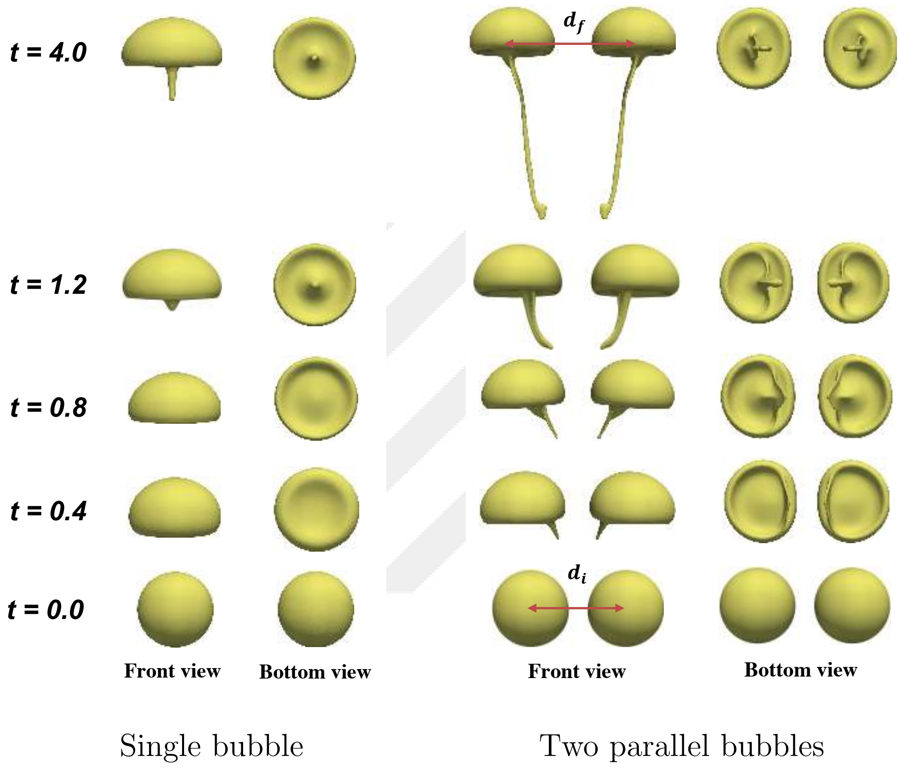

Figure 2.3: A comparison of 3D bubble shapes between a single bubble and a two parallel bubble systems at various time intervals. In the parallel bubble system, bubble tails are tilted towards each other due to their interactions in the viscoleastic medium. $(Eo = 100, Wi = 10, Ga = 3.91, \beta = 0.2)$

2.4.1 Forces acting on the bubbles

There are primarily four surface forces acting on the bubble during its rise in a viscoelastic liquid under buoyancy. These are viscous force, viscoelastic force, pressure force, and the force due to surface tension. Once the bubble reaches its steady motion, the net surface force becomes equal to the buoyancy force and the bubble attains its terminal velocity.

The total force acting on a bubble surface due to viscoelastic stresses is computed using the divergence theorem as

$$\mathbf{F}_\tau = \iint_A (\boldsymbol{\tau} \cdot \boldsymbol{n}) dA = \iiint_V (\boldsymbol{\nabla} \cdot \boldsymbol{\tau}) dV, \tag{2.10}$$

where $\boldsymbol{\tau}$ is the viscoelastic stress tensor and $\boldsymbol{n}$ is the unit normal vector. The viscoelastic stresses exist only in the ambient fluid and vanish in the bubble but the variation across the interface is smoothed in the present one-field formulation. Therefore the total viscoelastic force acting on a bubble surface is computed numerically utilizing the indicator function as

$$\boldsymbol{F_\tau} \cong \sum_{I_{ijk} \leq I_{th}} (\boldsymbol{\nabla}_h \cdot \boldsymbol{\tau})_{ijk} \Delta V_{ijk}, \tag{2.11}$$

where $(\boldsymbol{\nabla}_h \cdot \boldsymbol{\tau})ijk$ is the discrete divergence of the stress tensor evaluated using central differences, ΔV_{ijk} is the volume of the cell, I_{ijk} is the indicator function in the cell and I_{th} is the threshold value taken as 0.95 in the present results. The viscous force is calculated exactly the same way by using the viscous stress tensor. The force due to pressure is also calculated similarly as

$$\boldsymbol{F_p} = -\iint_A (p\boldsymbol{n}) dA = -\iiint_V (\boldsymbol{\nabla} p) dV \cong -\sum_{I_{ijk} \leq I_{th}} (\boldsymbol{\nabla}_h p)_{ijk} \Delta V_{ijk}, \tag{2.12}$$

where the central differences are used to evaluate the pressure gradient. In the front-tracking method, the force due to surface tension is already computed to be added to the momentum equation as

$$\boldsymbol{F_\sigma} = \iint_A \sigma \kappa \boldsymbol{n} \delta(\boldsymbol{x} - \boldsymbol{x_f}) dA. \tag{2.13}$$

Equation (2.13) is evaluated numerically using the standard procedure as described by Tryggvason et al. [20].

These forces are normalized by the buoyant body force which remains constant due to the incompressibility condition. Figure 2.4 shows the evolution of vertical components of all four forces acting on a single bubble for two different values of the Eötvös number. Note that the Eötvös number is varied by changing the surface tension coefficient (σ) to keep the Galilei number constant. The buoyancy force pushes the bubble in the upward direction while the surface forces oppose to this upward motion. The force due to surface tension on the upper and lower hemispheres of the bubble nearly cancel out and its net magnitude becomes negligibly small compared to the other forces. However, the surface tension influences the bubble shape that transforms from the 'teardrop' shape for $Eo = 1$ into a 'mushroom' shape for $Eo = 100$. In both cases, the lower pole has a peculiar cusped shape. The magnitude of pressure force decreases while the magnitude of viscous force increases rapidly during the transient period ($t^* < 8$) and eventually both forces reach their steady state values. In the case of $Eo = 100$, a large wake region forms behind the mushroom shape bubble, which creates a low pressure region and thus increases the pressure-induced drag force. The magnitude of viscoelastic force also shows a smooth increase during this transient period but it does not reach a steady value and exhibits an oscillatory behavior. This interesting behavior is attributed to the polymer molecules which stretch and relax along the curvature of the bubble surface during its convection and the frequency is determined by the interplay between convective and polymer relaxation time scales. Once the bubble attains its terminal velocity, the combined effect of all the surface forces becomes equal to buoyancy force, which is verified in the insets of Figs. 2.4a and 2.4b. It is seen that the computed net surface force is slightly smaller than the buoyancy force, which is mainly attributed to the cut-off used for the indicator function in computing surface forces in Eqs. (2.11) and (2.12). The normalized terminal velocity of the bubbles decreases with an increase in the Eötvös number, as seen in Fig. 2.4c. A similar behavior is also observed in the two-bubble system as elaborated more in the Supplementary Material. The bumpy feature of the elastic force may be explained by the recent theory of Bothe et al. [45]. As the polymer molecules pass over the bubble, they are stretched by the flow and this stored elastic energy is released on the lower hemisphere of the bubble giving an additional push to the bubble in the present cases. The oscillatory behavior of viscoleastic force is a persistent feature as will be elaborated more later. The constant contours of velocity vectors indicate the region of negative wake behind the trailing edges of the bubbles for these two values of Eötvös number, as shown in the inset of Fig. 2.4c.

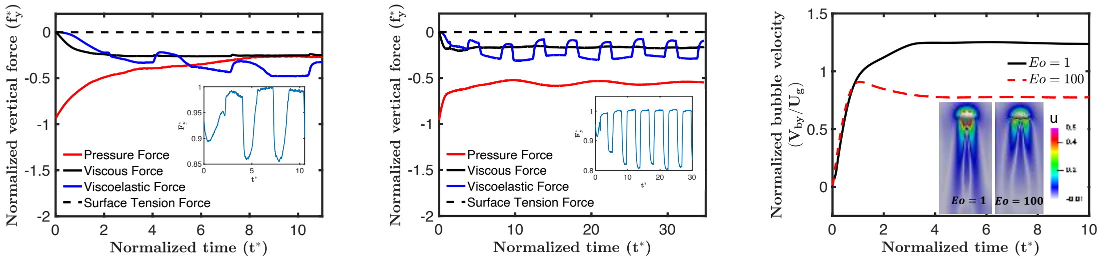

(a) (b) (c)

Figure 2.4: Evolution of vertical forces acting on a single bubble for (a) $Eo = 1$ and (b) $Eo = 100$. The sum of the surface forces is shown in the insets, which is the total force opposing the buoyant body force. (c) Evolution of bubble rise velocities is shown for two different values of Eötvös number. The contours of velocity around these bubbles in a vertical cutting plane are shown in the inset. $(Wi = 10, Ga = 3.91, \beta = 0.2)$

2.4.2 Effects of Galilei number

Simulations are performed to study the effects of Galilei number on the bubble-bubble interactions. For this purpose, the Galilei number is reduced by half successively in each of the four simulations while keeping all the other parameters constant at the baseline case. The bubbles are positioned initially in such a way that they have perfect horizontal alignment ($d_y = 0$) and the distance between their centers is $2.5R$. Figure 2.5 depicts 3D bubble shapes at their approximate steady state velocities for different values of the Galilei number. Since the tail becomes extremely thin and tends to breakup for $Ga > 3.91$, and the topology change is not implemented in the present numerical method, the simulations are restricted to $Ga \leq 3.91$. The constant contours of the average elongation of polymer molecules ($tr(\mathbf{B})/L^2$) are also plotted in Fig. 2.5. The contours and the velocity vectors are shown in a vertical cutting plane at the center of the computational domain. It is observed that, as the Galilei number decreases, lower hemisphere of both bubbles changes from a 'mushroom' to a more 'eye drop' shape. The elongation of polymer molecules on the surface and around the bubbles decreases with decreasing the Galilei number. The tails of bubbles become thicker by decreasing the Galilei number and at $Ga = 0.9775$, the region of negative wake (reversed flow) is entrapped in between the long bubble tails. At $Ga = 0.48875$, the entire region just below the trailing edges of the bubbles shows a reversed flow (negative wake region) whereas at $Ga = 3.91$, this region of negative wake almost disappears and the reversed flow remains confined to a very thin region adjacent to bubble tails.

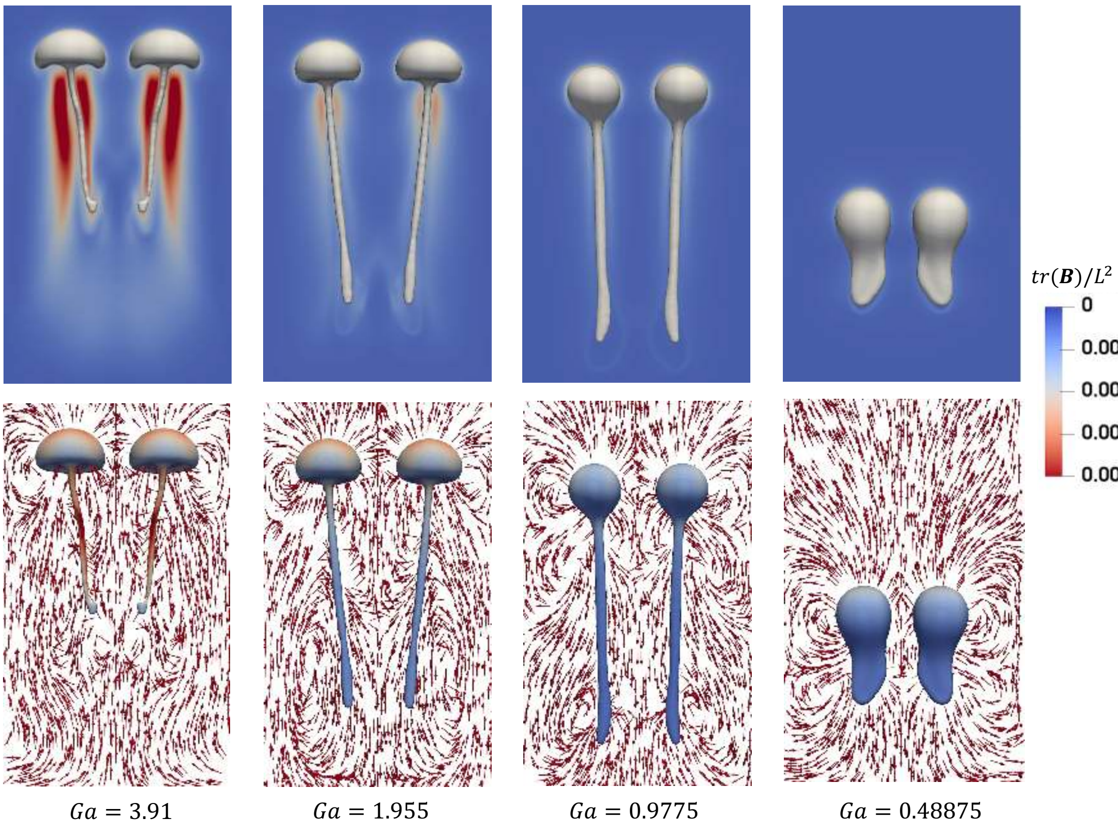

Figure 2.5: (top row) The average elongation of polymer molecules quantified by the contours of $tr(\mathbf{B})/L^2$ in a vertical cutting plane at the center of the domain for different values of Ga. (bottom row) The constant contours of $tr(\mathbf{B})/L^2$ on the surface of 3D bubbles for various values of Ga. The velocity vectors are shown around these bubbles in a vertical cutting plane at the center of the domain. ($Eo = 100, Wi = 10, \beta = 0.2$)

Figure 2.6a shows the evolution of the rise velocity of the left bubble for various values of the Galilei number. As the Galilei number is reduced, the rise velocity of the bubbles decreases and the bubbles reach their approximate steady state velocities in a comparatively shorter distance. In the simulations, the initial distance between the bubble centers is kept constant at $d_i = 2.5R$. Figure 2.6b shows the distance between bubble centers once they reach their approximate steady state motion for various values of the Galilei number. It is seen that the distance between the bubble centers also decreases as the Galilei number decreases, and for $Ga = 0.48875$, the distance is less than the initial value. Figure 2.6c shows the percentage contribution of various forces acting on the left bubble in the vertical (y) direction at its steady motion. As Ga increases, the contribution of pressure force in the total vertical force acting on the bubble increases whereas the contributions of viscous and viscoelatsic forces decrease. The contribution of force due to surface tension remains negligible. The increase in the pressure force is mainly due to the deformation of the bubble into a mushroom shape that causes a reduced pressure wake zone behind the bubble. The reduction in the viscoelastic force is interesting and deserves more elaboration. As indicated by the contours of $tr(\mathbf{B})/L^2$ in Fig. 2.5, the largest elongation of polymer molecules occurs on the upper hemisphere at a lower Ga. As Ga increases, this region moves towards the lower pole and eventually the largest elongation occurs along the bubble tails at $Ga = 3.91$. As explained by Bothe et al. [45], the polymers molecules are stretched resulting in an extra stress (hoop stress) as they pass over the bubble surface and they relax on the upper hemisphere before reaching the bubble equator inducing an enhanced drag force on the bubble when the relaxation time is smaller than the convective time scale, which is the case at low Ga. As Ga is increased, the convection is enhanced so that the polymer relaxation occurs on the lower hemisphere resulting in a reduction in the total elastic force and creation of a long tail behind the bubbles. Due to a lower viscoelastic stress concentration on the lower hemisphere of the bubbles at $Ga = 0.48875$, the long tails of the bubbles are vanished and the region of negative wake is shifted in the downward direction. These observations are in line with the findings of Bothe et al. [45].

Evolution of vertical and lateral components of surface forces acting on the bubbles are plotted in Fig. 2.7 for $Ga = 0.9775$, $Ga = 1.955$, and $Ga = 3.91$ cases. The total surface forces are also plotted in the insets of Fig. 2.7. In the vertical (y)

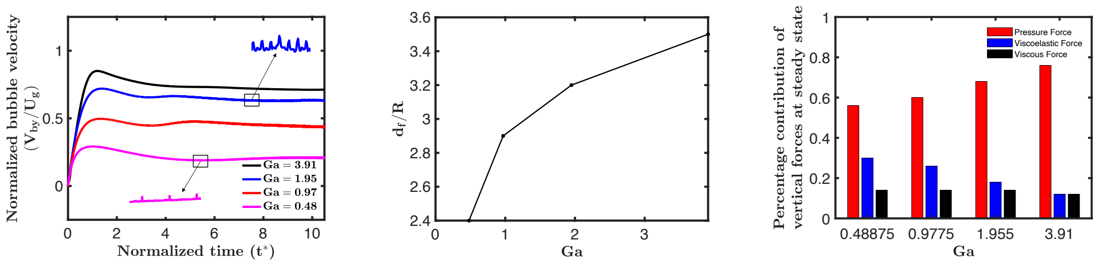

(a) (b) (c)

Figure 2.6: (a) Rise velocity of the left bubble in a parallel bubble system for different values of Ga. (b) Distances between the bubble centers at approximate steady state velocities for different values of Ga. (c) The percentage contribution of each of the surface forces acting on the bubble in the vertical direction for different values of Ga once the bubble attains its terminal velocity. ($Eo = 100, Wi = 10, \beta = 0.2$)

direction, it is interesting to observe that the frequency and the amplitude of the viscoelastic force oscillation increase with increasing Ga. In addition, the net share of the elastic force increases in the expense of the pressure force as Ga is reduced. The oscillations in the elastic force also induce oscillations in the viscous force but with a much smaller amplitude. This oscillating behavior of the viscoelastic force is caused by the ongoing stretching and relaxation of polymer molecules along the bubble curvature as discussed above. The combined oscillatory effect of viscous and viscoelastic forces is visible in the rise velocities as well (Fig. 2.6a). As the magnitude of these oscillations is very small, the rise velocity of the bubble apparently remains smooth. In the lateral (x) direction, the combined effect of all these forces pushes the bubbles away from each other. At $Ga = 0.9775$, as the bubbles approach their steady state velocity, viscoelastic force is balanced by the pressure force. At $Ga = 1.955$, all these individual forces acting on the surface of bubble approach zero as the bubble attains its terminal velocity. As inertia increases with increasing Ga, e.g., $Ga = 3.91$, the pressure force reverses its direction and cancels out the combined effect of viscous and viscoelastic forces at the steady state. We note that, in addition to the numerical discretization error, the apparent discrepancy between the total surface force and the buoyancy force seen in the insets of Fig. 2.7 is partly attributed to the crude approximation of total surface forces utilizing a cut-off for the indicator function in Eqs. (2.11,2.12).

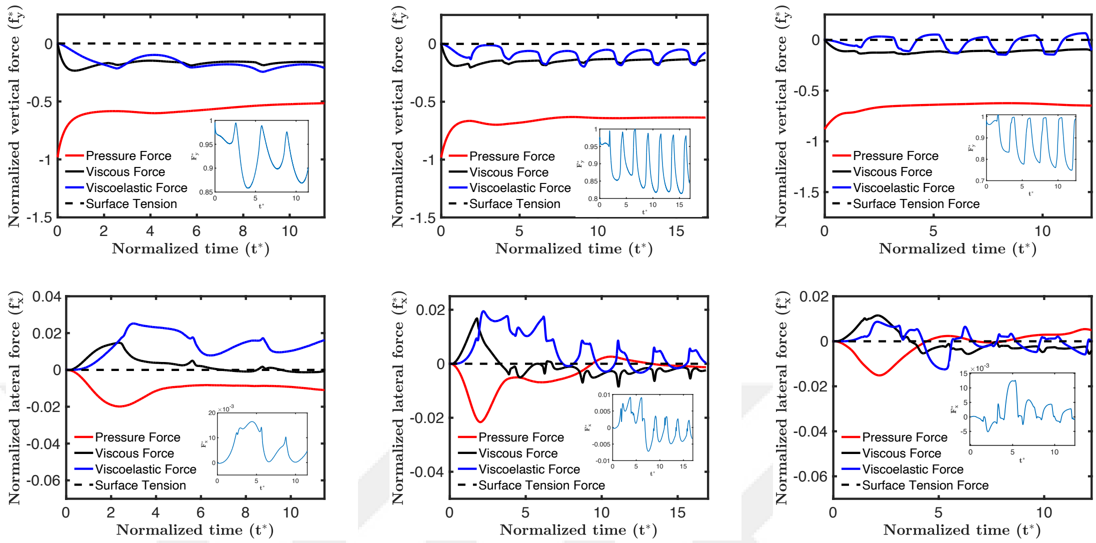

$Ga = 0.9775$ $\quad$ $Ga = 1.955$ $\quad$ $Ga = 3.91$

Figure 2.7: (top row) Evolution of vertical component of surface forces acting on the left bubble in parallel bubble system for different values of Ga. (bottom row) Evolution of lateral component of surface forces acting on the left bubble for different values of Ga. ($Eo = 100, Wi = 10, \beta = 0.2$)

Simulations are also performed to highlight the differences between flow fields for the Newtonian and viscoelastic cases at $Ga = 0.9775$ and $Ga = 3.91$. Figure 2.8 shows that the flow fields and the bubble shapes are markedly different in the Newtonian and viscoelastic cases. The reversed flow is visible in the viscoelastic cases not only in the wake region but also in between the bubbles, which can also be seen in the inset of Fig. 2.8d where the constant contours of the vertical velocity component are plotted. It is interesting to see a diamond shaped reversed flow region in between the bubbles in the viscoealstic case (Fig. 2.8d). The flow is in the upward direction in the wake region as well as in between the bubbles in the Newtonian case (Fig. 2.8a). The vertical velocity is plotted along the mid-planes (indicated by the vertical blue lines in Figs. 2.8a,c) in Figs. 2.8b and 2.8d for the Newtonian and viscoelastic cases, respectively. In these figures, the shaded region indicates the region occupied by the bubbles. As seen, the vertical velocity is always positive in the Newtonian case while it becomes negative in the wake region and in the middle of the bubbles in the viscoelastic cases. The steady rise velocity, Reynolds number ($Re = \frac{\rho_o V_{by} R}{\mu_o}$) and the distance between bubble centers are summarized in Table 2.3 for the Newtonian and viscoelastic cases. As seen in this table, both the rise velocity and the distance are significantly larger in the viscoelastic case and the increase is enhanced as Ga is reduced. In the case of a Newtonian fluid, Legendre et al. [47] have demonstrated that the attractive interaction force between two spherical bubbles in the potential flow limit becomes repulsive in the viscous dominated low-Reynolds-number flow since the vorticity generated at the bubble surfaces induces upward velocities resulting in vertical velocities in the gap smaller than the rising velocity of the bubbles. As seen in the shaded region in Figs. 2.8b,d, the flow velocity between the bubbles becomes smaller than the rise velocity of the bubbles. Since the Reynolds number is small, the lateral force is expected to be repulsive [47], which is verified as the separation distance between bubbles increases from the initial value of $2.5R$ to the steady value of $2.53R$ and $3.2R$ for $Ga = 0.9775$ and $Ga = 3.91$, respectively (Table 2.3).

The long tails appear primarily due to viscoelastic stresses generated by the relaxing polymer molecules along the lower hemisphere of the bubble and the resulting normal stress difference, enhanced by the shear-thinning behavior of the outer fluid [67]. If the bubbles are allowed to ascend for a considerably longer period of time, the long tails behind the bubbles may eventually start to break up into satellite bubbles. In the case of a viscoelastic droplet rising in a viscoelastic medium, Ortiz et al. [67] argued that the balance between elongational stress and shear stress along the tail determines the type of breakup of the tail. A similar phenomenon may arise in the present scenario of air bubbles as well. However, the Galilei number is restricted to a lower range in the present study where the break-up of tails is not expected to occur at least until the bubbles reach their approximate terminal velocities.

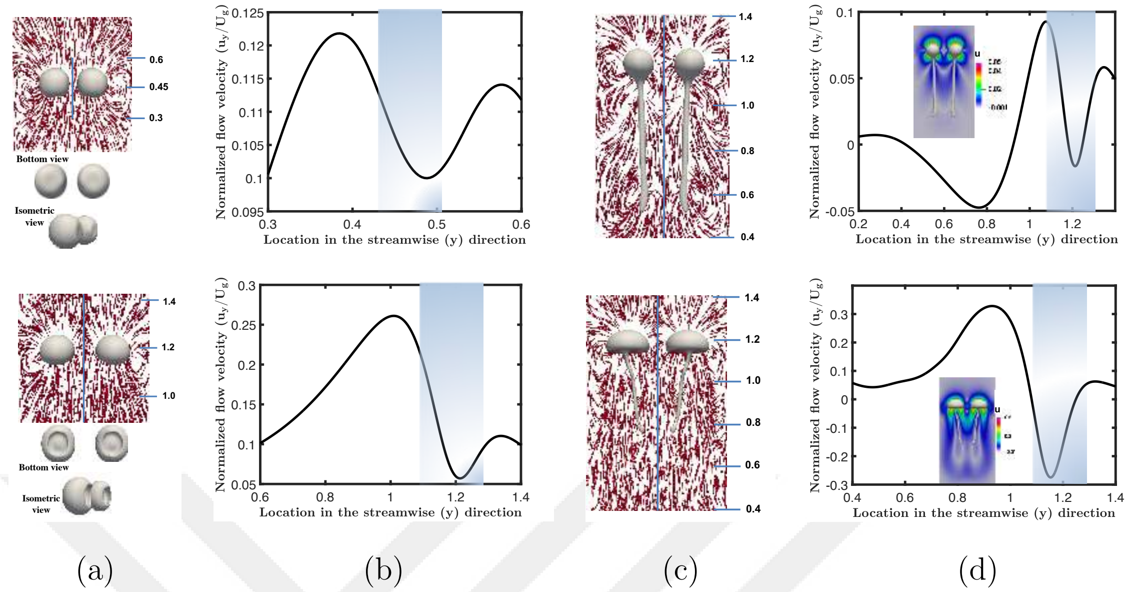

Figure 2.8: Flow fields and bubbles shapes for the Newtonian (a,b) and viscoelastic (c,d) cases are shown at $Ga = 0.9775$ (top) and $Ga = 3.91$ (bottom). The velocity vectors around two parallel bubbles are shown in a 2D plane at the center of the domain. 3D bubble shapes are also shown at their steady state velocities for the Newtonian (a) and the viscoelastic (c) cases. Vertical flow velocities along the vertical lines in between the bubbles indicated by blue lines in (a) and (c) are shown for the Newtonian (b) and the viscoelastic (d) cases, indicating a significant reduction of flow velocity in between the two parallel bubbles. The shaded area shows the region in between the bubbles. ($Eo = 100, Wi = 10, \beta = 0.2$)

2.4.3 Effects of Weissenberg number

Simulations are then performed to investigate the effects of Weissenberg number (Wi) on the flow dynamics and interactions of the bubbles. The bubbles are initially aligned horizontally ($d_y = 0$) with an initial distance of $2.5R$ between their centers. The Weissenberg number is reduced by half successively in each of the six simulations while keeping all the other parameters constant at the baseline case. Figure 2.9 shows the shapes of 3D bubbles at their approximate steady state velocities for different values of Weissenberg number. As seen, there are long tails that tilt towards each other in all the viscoelastic cases, which is in contrast with the corresponding Newtonian case where no tail appears as shown in Figure 2.9i. As the Weissenberg number increases, the viscoelastic stresses dominate and the bub-

Table 2.3: The Newtonian and viscoelastic cases at $Ga = 0.9775$ and $Ga = 3.91$

Cases	V_{by}/U_g	Re	d_f/R
Newtonian ($Ga = 0.9775$)	0.22	0.21	2.53
Viscoelastic ($Ga = 0.9775$)	0.42	0.41	2.9
Newtonian ($Ga = 3.91$)	0.56	2.19	3.2
Viscoelastic ($Ga = 3.91$)	0.71	2.78	3.5

bles take a more mushroom like shape. The contours of $tr(\mathbf{B})/L^2$, representing the average elongation of polymer molecules, are shown on the surface of the bubbles and in a vertical cutting plane at the center of the computational domain. It is observed that the average elongation of polymer molecules is reduced around the bubbles as the Weissenberg number is decreased. As indicated by the velocity vectors, there is no apparent region of negative wake (reversed flow) behind the bubbles or in between them in this range of Wi. It is interesting to observe that the tails are first pushed away from each other in the outward direction breaking the symmetry and they then move back towards the middle of the bubble as Wi increases. The bubbles are essentially symmetric without any tail in the Newtonian case as seen in Fig. 2.9i. The tails of the bubbles start to shrink at the higher values of Wi due to large polymer relaxation time. The polymer molecules tend to relax after passing through the lower hemisphere of the bubble at higher value of Wi which starts to change its shape, as shown in Fig. 2.10. The bottom views of the bubbles show an interesting double-layered asymmetric shape at these higher values of Wi.

Figure 2.11a shows the evolution of bubble rise velocities for different values of the Weissenberg number. As the Weissenberg number is increased, terminal velocities of the bubbles are also increased. These results suggest that the extra push by the polymers-induced hoop stress is also at play in the present scenario and this effect is amplified as Wi increases [45]. The steady distance between bubble centers is plotted in Fig. 2.11b as a function of Wi. Since the initial distance is $2.5R$, this figure shows that the lateral force between bubbles is repulsive that decays faster as the

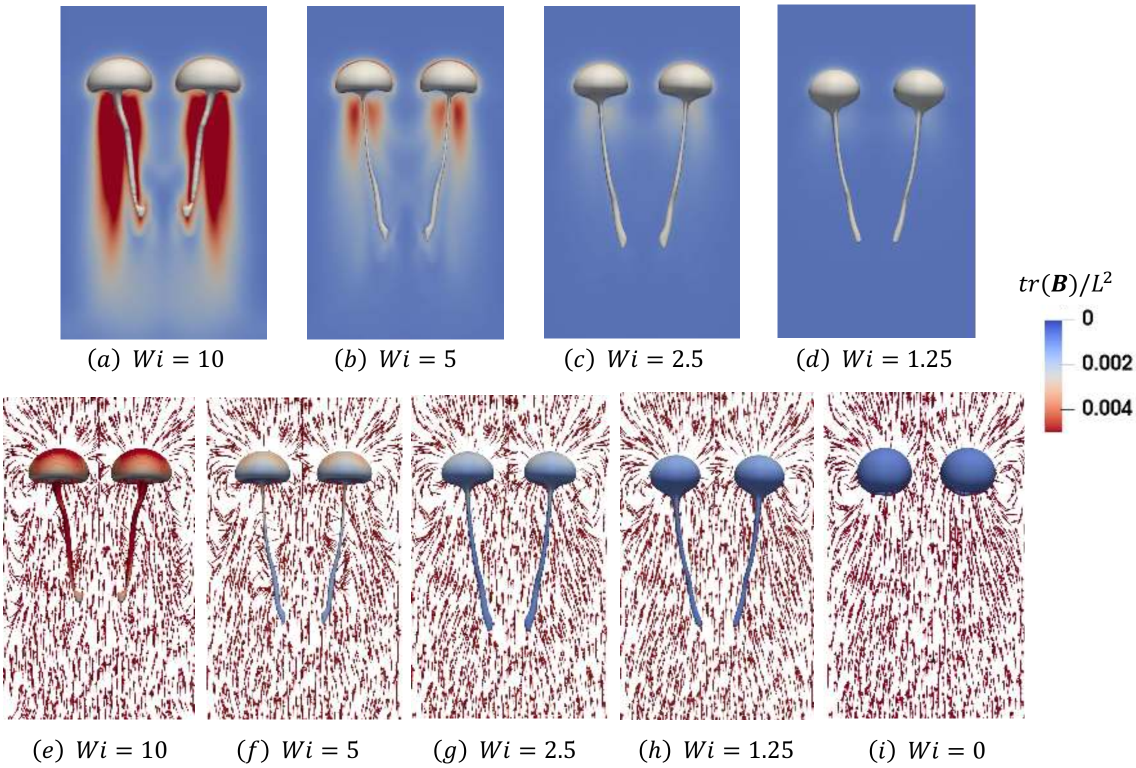

Figure 2.9: $(a-d)$ The average elongation of polymer molecules indicated by the contours of $tr(\boldsymbol{B})/L^2$ in a vertical cutting plane at the center of domain for different values of Wi. $(e-h)$ The contours of $tr(\boldsymbol{B})/L^2$ on the surface of 3D bubbles for different values of Wi. The velocity vectors are shown around these bubbles in a vertical cutting plane at the center of domain $(Eo = 100, Ga = 3.91, \beta = 0.2)$. (i) The bubble shapes and velocity vectors are shown for the Newtonian case $(Wi = 0, Eo = 100, Ga = 3.91, \beta = 1.0)$.

Weissenberg number increases. Figure 2.11c shows the percentage contribution of various surface forces acting on the bubble in the vertical direction (y) at its steady state velocity. As Wi increases, the contribution of pressure and viscous forces increases while the contribution of the viscoelastic force decreases. The decrease in the viscoelastic force with Wi also explains the increase in the terminal velocity seen in Fig. 2.11a. The terminal velocity of the bubbles increases with increasing Wi due to the enhanced extra 'push' provided by the relaxing polymer molecules [45].

Figure 2.12 shows the evolution of vertical and lateral component of surface forces for different values of the Weissenberg number. As seen in Figs. 2.12 (top row), the

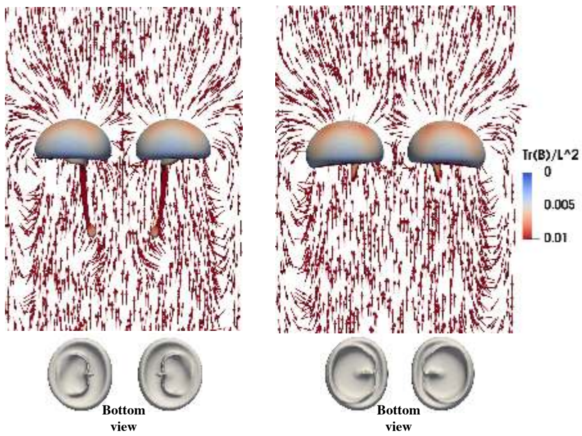

(a) $Wi = 20$ (b) $Wi = 40$

Figure 2.10: Bubble shapes at higher Weissenberg numbers. The contours of $tr(\boldsymbol{B})/L^2$ are shown on the surface of 3D bubbles for (a) $Wi = 20$ and (b) $Wi = 40$. The velocity vectors are shown around these bubbles in a vertical cutting plane at the center of domain $(Eo = 100, Ga = 3.91, \beta = 0.2)$.

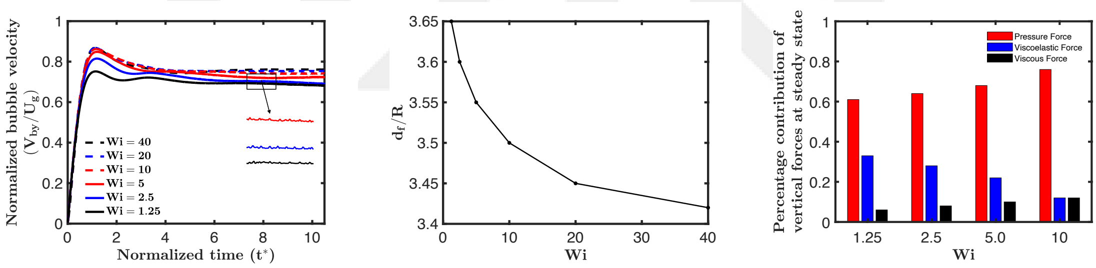

(a) (b) (c)

Figure 2.11: (a) Rise velocities of the left bubble in a parallel bubble system for various values of Wi. (b) Distances between the bubble centers at approximate steady state velocities for various values of Wi. (c) Percentage contribution of each of the surface forces acting on the bubble in the vertical direction for different values of Wi once the bubble attains its terminal velocity. $(Eo = 100, Ga = 3.91, \beta = 0.2)$

vertical component of the viscoelastic force oscillates and the oscillation amplitude increases with Wi. The magnitude of the viscoelastic force slightly decreases as Wi increases. The magnitude of the vertical pressure force increases mainly due the enhanced deformation of the bubbles as Wi increases while the viscous force seems to be less sensitive to the change in Wi. As seen previously, the oscillatory behavior of viscous and viscoleastic forces induce pulsations in the rise velocity of the bubble as well, as shown in the inset of Fig. 2.11a. The steady distance between the bubble centers increases as Wi decreases as seen in Fig. 2.11b. As mentioned previously, the separation distance increases for all the values of the Weissenberg number suggesting that the lateral force is generally repulsive (positive). This is verified in Fig. 2.12 (bottom row) where the time evolution of the lateral components of surface forces acting on the left bubble are plotted. As seen, the net lateral force is repulsive in the transient period and approaches zero when the bubbles are pushed sufficiently far from each other reaching an approximately steady distance. The viscous force is significantly smaller than the other forces for the smaller values of the Weissenberg number, i.e., $Wi \leq 2.5$. The viscoelastic and pressure forces mostly act in the opposite direction. In the steady motion, the viscoelastic and the viscous forces are balanced by the pressure force in the lateral direction.

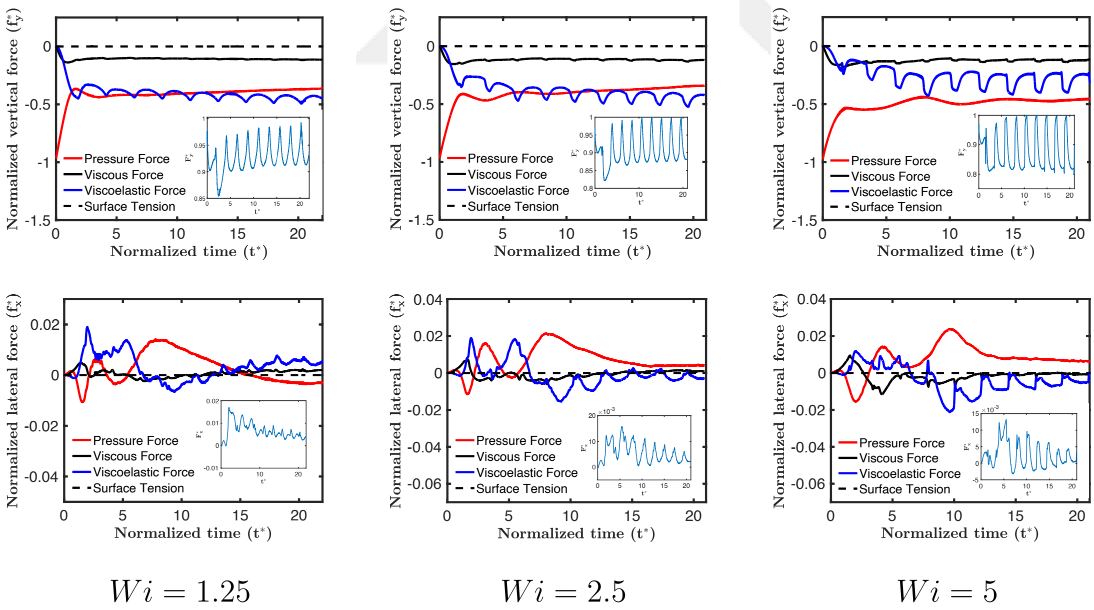

Figure 2.12: (top row) Evolution of vertical component of surface forces acting on the left bubble in the parallel bubble system for different values of Wi. (bottom row) Evolution of lateral component of surface forces acting on the left bubble for different values of Wi. $(Eo = 100, Ga = 3.91, \beta = 0.2)$

2.4.4 Effects of vertical offset and unequal bubble size

Finally, the effects of an initial offset in the vertical position of bubble pairs are investigated for both equal and unequal-sized bubble pairs. For this purpose, simulations are performed by changing the initial vertical alignment of bubbles and their sizes while keeping all the other parameters constant at the baseline case. Figure 2.13 shows five such situations. In all the cases presented in this section, the initial horizontal distance between bubble centers is kept constant at $2.5R$, where R is the the radius of the larger bubble in the case of unequal bubbles.

We first examine the effects of the offset on the interactions of the equal-sized bubble pairs. When one of the bubbles is initialized behind the other one by an offset of the bubble radius, i.e., $d_y = R$, the upper hemispheres of the bubbles also start tilting towards each other during their rise under buoyancy (Fig. 2.13a). As the rise velocity of both bubbles are nearly the same, thanks to their equal size, they maintain their initial offset alignment as seen in Fig. 2.13a. The symmetric shape of bubble tails observed in the case of aligned bubbles (Fig. 2.5a) under the same parametric settings is broken for the case of offset bubbles as the trailing bubble rises in the wake region of the leading one and the interactions are not symmetric anymore.

We next simulate unequal-sized bubble pairs. When volume of one bubble is made a half of the other one and they are initially placed side by side ($d_y = 0$), the larger bubble moves faster and takes the lead due to the larger magnitude of the buoyancy force it experiences as shown in Fig. 2.13b. The shapes of bubble tails are significantly different than those of the corresponding equal-sized bubble pairs mainly due to the modified stress distribution around the tails (Fig. 2.13b). When the smaller bubble is placed behind the larger one with an offset of the radius of the larger bubble ($d_y = R$), its upper hemisphere is transformed into a 'cap' like shape as it directly comes under the wake region of the larger bubble (Fig. 2.13c). It is interesting to observe the striking influence of the initial conditions on the bubble shapes, the stress distribution and overall flow field as seen from comparison of Figs. 2.13b and c.

When one bubble is made much smaller than the other one, i.e., its radius is one-half the radius of the larger bubble, the bubble-bubble interactions are significantly reduced and the effects of the initial offset virtually disappears as seen in Figs. 2.13d and e. The larger bubble rises faster than the smaller one leaving it behind quickly whether they are placed side by side or with a vertical offset. The larger bubble tends to retain its nearly symmetric shape while the smaller one is tilted as it is entrapped into the negative wake region of the larger one.

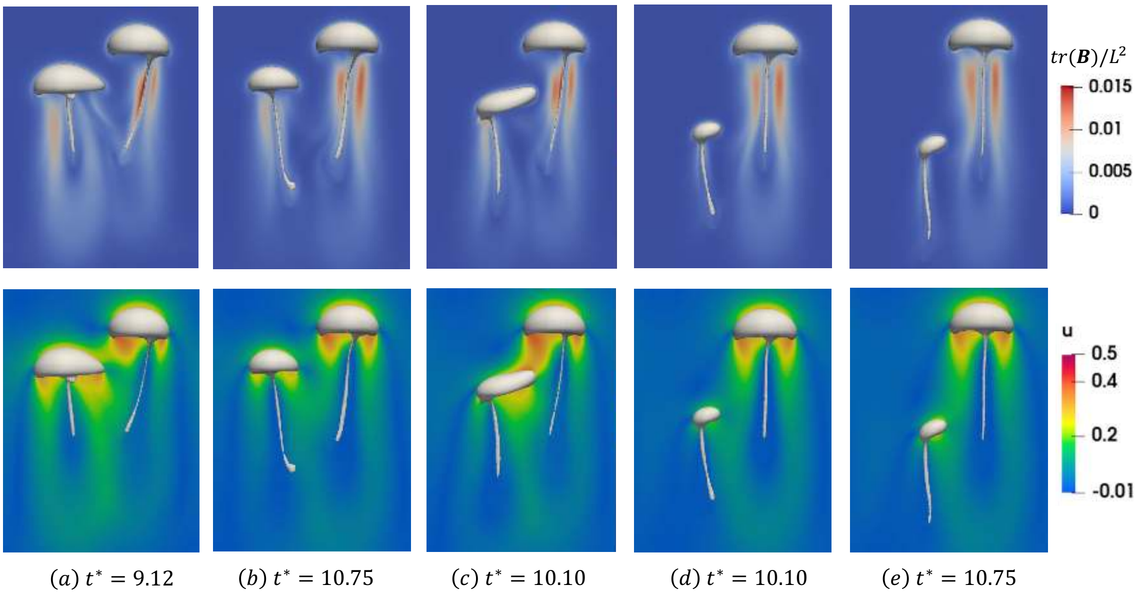

Figure 2.13: The effects of a initial vertical offset and unequal bubble size on the bubble-bubble interactions. The trace of conformation tensor $\boldsymbol{B}$ and the contours of the vertical flow velocity around the bubbles in a vertical cutting plane at the center of computational domain. (a) The bubbles are of equal size with an initial vertical offset of R in the vertical direction. (b) The volume of the left bubble is one-half the volume of the right bubble with no initial offset. (c) The same as (b) but with an initial offset of R in the vertical direction. (d) The radius of left bubble is one-half the radius of the right bubble with no initial offset in the vertical direction. (e) The same as (d) but with an initial offset of R in the vertical direction. $(Ga = 3.91, Eo = 100, Wi = 10, \beta = 0.2)$

2.5 Conclusion

Fully three-dimensional interface-resolved simulations are performed to examine the interactions of buoyancy-driven parallel bubbles in a viscoelastic ambient fluid. In addition to the evolution of the flow field and bubble shapes, various statistics are computed to reveal complicated flow physics and bubble dynamics. In particular, surface forces acting on the bubbles due to pressure, viscous and viscoelastic stresses and surface tension are quantified in the transient and steady state conditions.

The bubbles and their wakes interact strongly as they rise and long tails form behind the bubbles due to viscoelastic stress difference at the interface. The bubble shapes are markedly different in the two bubble system compared to that in the single bubble case. In addition to the formation of long tails that tilt toward each other, the lateral symmetry is also broken in the two bubble system. The rise velocity of the parallel bubbles remains slightly smaller than that of the single bubble due to the bubble-bubble interactions.

The net surface tension force acting on the bubble is generally found to be negligibly small compared to the other surface forces. The pressure force dominates over the viscous and viscoelastic forces in the initial period and its magnitude reduces as the viscous and viscoelastic stresses develop. It is interesting to find that the viscoelastic force oscillates and never reaches a steady value even when the bubbles attain their steady motion. The amplitude and frequency of the oscillations are determined by the intricate interplay of the convective and polymer relaxation time scales. Some oscillations are also observed in the viscous force but with a much smaller amplitude. No apparent oscillations are detected in the pressure force acting on the bubble. This oscillatory behavior is observed in the terminal velocity of the bubble as well and is argued to support the recent theory by Bothe et al. [45].

The bubble shapes are strongly influenced by the the Galilei number (Ga). As Ga reduces, the bubbles transform from a mushroom shape into a tear drop shape in the steady motion. The flow between bubbles is found to be slower than the rise velocity of bubbles in both the Newtonian and viscoelastic cases but a reversed flow is observed in between the bubbles in the viscoelastic case similar to the negative wake region that occurs behind the bubble.

The steady distance between the bubble is found to be strongly influenced by the Weissenberg number (Wi). The relative contribution of the viscoelastic force in the vertical direction is enhanced as Wi is reduced, as the stretched polymer molecules relax on the upper hemisphere due to shorter relaxation time at lower Wi inducing a larger drag force as explained by Bothe et al. [45].

The Eötvös number is found to have a non-monotonic effect on the normalized terminal velocity of the bubbles. As Eötvös number decreases, the terminal velocity slightly decreases in the range $25 \leq Eo \leq 100$ and then starts to increase rapidly for $Eo \leq 12.5$. A detailed description of the effects of Eötvös number, solvent viscosity ratio (β) and the initial distance between the bubble centers can be found in the supplementary material.

The symmetry observed in the case of the parallel bubble pairs is broken when the bubbles are initialized by an initial offset in the vertical direction. It is found that equal-sized bubble pairs maintain their initial orientation. In the case of unequal-sized bubble pairs, the larger bubble moves faster leaving the smaller one behind and then maintain their orientation regardless of an initial offset in the vertical direction.

The results reported in the present study demonstrate the benefits of the interface-resolved/front-tracking method. However, the front tracking method used in the present work is not capable of handling the break-up and coalescence of bubbles. The mechanism behind the break-up of bubble tails will be explored in the future work after implementation of a topology change algorithm into the present code to expand the scope of the study. Furthermore, in the present paper, we have only considered the bubbles with relatively large volumes to produce negative wakes. Further research is required to analyse the interaction of bubbles in a viscoelastic medium with different sizes and orientations.

Chapter 3

LATERAL MIGRATION OF A DEFORMABLE FLUID PARTICLE IN A SQUARE CHANNEL FLOW OF VISCOELASTIC FLUID[2]

3.1 Introduction

Cross-stream or lateral migration of particles in a pressure-driven flow has been an active area of research due to its relevance in many industrial [68, 69] and biological [70] applications. The phenomenon of lateral migration is specifically used for the manipulation of biological cells and particles in various microfluidic applications [71, 72]. The wall normal component of force acting on the particle is responsible for its lateral migration and it is usually called the lift force. The lift force which is often relatively small in magnitude plays a central role in determining the final position of an individual particle and the particle distribution in particulate flows [73].

The lateral motion of a particle was first investigated experimentally by Segre and Silberberg [74] in a tube flow. Their observation was later confirmed by many experimental [75, 76] and numerical [77, 78]. The same observation was made in rectangular channels where particles move towards or away from the channel wall in the cross-streamwise direction [79, 80, 81, 82]. The situation becomes more involved when the ambient fluid is viscoelastic as the fluid elasticity plays its role in pushing the particle towards the center of the channel [83]. In the case of viscoelastic fluids, most of the existing literature is primarily focused on solid particles suspended in a viscoelastic fluid [84]. In the absence of inertia, the cross-stream migration of

[2]PUBLISHED AS A PAPER UNDER THE SAME TITLE IN JOURNAL OF FLUID MECHANICS 996:A31 (2024)

a non-deformable particle is not possible to occur in a confined Newtonian fluid flow due to the inherent reversibility of Stokes flow. On the other hand, the non-linear characteristics of viscoelasticity provide the required irreversibility making the lateral migration possible in a complex fluid even with negligible inertia. The lateral migration of particles in complex fluids and their application in manipulating the particles in various microfluidic devices have been summarized in the review paper by D'Avino et al. [85].

In the presence of both inertia and viscoelasticity, several factors determine the orientation of particle migration in a pressure-driven channel flow. Some of these factors reported in numerous studies so far include shear-induced lift force [86], wall-induced lift force [87], fluid elasticity [75, 88], initial position of the particle [89], geometry of the channel [90], the shear-thinning of the ambient fluid [2] and particle rotation rate (the Magnus effect). The effects of one or more of these factors determine the migration of a particle towards or away from the channel wall. Moreover, the deformability of an object adds further complexity to this phenomenon, and therefore, complex dynamics of lateral migration of deformable particles in viscoelastic fluids are yet to be fully explored. As a result of this migration, some interesting secondary flow features also emerge in the vicinity of the particle. One of them is a secondary flow which is perpendicular to the primary flow (streamwise) direction and may have a velocity as large as the order of the particle migration velocity. However, this secondary flow is generated in non-circular channels only by the viscoelastic fluids having non-zero second normal stress difference [91].

When a spherical particle moves with a relative velocity in a shear flow, a force is exerted on the particle by the surrounding fluid in a direction perpendicular to its relative motion. This force is known as the shear-induced lift force, first calculated analytically by Saffman [86] for a solid sphere. This force pushes the particle towards the channel wall until it is balanced by the wall-induced lift force [77, 92]. The flow field around the particle is significantly influenced by the presence of the wall. The wall decelerates the motion of the particle in the streamwise direction due to extra drag and repels it away from the wall if the characteristic length of the particle is much smaller than the channel size. If the characteristic length of the particle is comparable to the channel size, like the motion of bubbles in capillaries, the channel walls constrain the motion of the immersed object, as explained by Michaelides [93].

The well-known Magnus effect (rotation-induced lift force) is another factor influencing the migration of an object in the channel flow. For a solid particle having the no-slip condition on its surface, the difference in the relative fluid velocity on its sides may cause it to rotate. This shear-induced rotation generates an additional transverse pressure difference and the resulting lift force is referred to as the 'Magnus effect' [94]. Instead of a solid particle, if the object is deformable, the deformability induces yet another lateral migration directed toward the channel center [95]. Similarly, the initial position of the particle in the channel has a direct impact on its lateral migration as dictated by the gradient of velocity at that initial location. The size of the particle as compared to the channel is another important variable to be considered while analyzing the lateral migration in a pressure-driven flow. It is generally characterized by the blockage ratio [96] defined as $b = d/H$, where d is the particle size (e.g., diameter) and H is the channel width. It has been observed in both experimental [97] and numerical [98] works that a deformable object with a diameter beyond a certain limit migrates towards the channel center due to deformation-induced lift force while a smaller one migrates towards the wall due to inertial lift force. This feature is used in many microfluidic devices for sorting particles of different sizes [99].

The Magnus effect, shear-induced lift force, and wall-induced lift force may be referred to as the 'inertial effects' as all these forces primarily originate due to fluid inertia. If the ambient fluid is viscoelastic, the elastic effects tend to push the object toward the center [83] while the inertial effects tend to move it toward the channel wall. The relative strength of inertia and elasticity determines the final equilibrium position of a non-deformable particle in a channel. This interplay between inertia and elasticity is quantified by the elasticity number, defined as $El = Wi/Re$, where Wi and Re are the Weissenberg number and the Reynolds number, respectively. Furthermore, if the ambient fluid exhibits a shear-thinning behavior as well, it has been reported by Li et al. [2] that the shear-thinning amplifies inertial effects and thus promotes particle migration towards the wall. Hazra et al. [100] experimentally studied the role of shear thinning on the cross-stream migration of droplets in a confined shear flow for $Re < 1$. They observed that larger droplets followed their original steamlines while the smaller ones migrated towards the center. Similarly, in order to predict the role of elasticity, Mukherjee and Sarkar [101] performed computational simulations of a viscoelastic drop in a Newtonian fluid for a linear shear flow with negligible inertia. They found a non-monotonic impact of elasticity on the migration velocity of the droplet.

The above-mentioned list of factors affecting the migration dynamics of a deformable object is still not exhaustive. In the presence of surfactant contamination, the surfactant-induced Marangoni stresses oppose the inertial lift force and can completely alter the migration dynamics of an object. In our earlier work [102, 103], it was observed that, in the pressure-driven channel flow of a Newtonian fluid, clean spherical bubbles move towards the wall while the deformable ones migrate away from it. On the other hand, even the spherical bubbles can move away from the wall in the presence of a strong enough surfactant.

Although there are a large number of experimental and numerical works devoted to solid particle migration, much less attention has been paid to the combined effects of inertia, viscoelasticity, and shear-thinning on the lateral migration of a deformable fluid particle and only a few details are available in the existing literature, which motivates the present study. The main focus here is to explore the combined effects of fluid inertia, viscoelasticity, and particle deformability on its lateral migration in a shear-thinning viscoelastic fluid. For this purpose, fully interface-resolved numerical simulations are performed using an Eulerian-Lagrangian method [104] for a wide range of relevant flow parameters to explore the features of this complex flow field. In addition to the lateral migration, the particle-induced elastic instability and its impact on the onset of a path instability, the effect of shear-thinning, and the resulting flow are investigated computationally. The secondary flow field developed due to the second normal stress difference in the flow is also examined and quantified.

The rest of the paper is organized as follows. The problem statement and the computational setup are described in the next section. The governing equations and the numerical method are briefly described in §3.3. The results are presented and discussed in §3.4 followed by the conclusions in §3.5. A grid convergence study is conducted and the results are presented in the Appendix.

3.2 Problem Statement and Computational Setup

Microfluidic devices usually use channels with rectangular cross-sections due to their relative ease of fabrication. If the aspect ratio of the channel is reduced, the relative influence of channel walls on the flow field becomes more pronounced [84]. The limiting case is obtained for a square-shaped cross-section, which is selected in the present study. Figure 4.1a shows the computational domain which is a square channel with the dimensions of H, L, and H in the x, y, and z directions, respectively. Periodic boundary conditions are applied in the streamwise (y) direction whereas the other two directions (x and z) have no-slip/no-penetration boundary conditions. The centroid of the particle is denoted by (x_b, y_b, z_b) and a spherical fluid particle of diameter d is initially located at $(x_{bi}, y_{bi}, z_{bi}) = (0.5H, H, 0.25H)$ unless specified otherwise. The value of H is set to $4d$. After performing the simulations by gradually increasing the length of the channel in the streamwise (y) direction to check the effects of periodicity, the channel length is set to $L = 4H$, which is found to be sufficient to eliminate any significant effects of periodicity.

The deformable particle is at rest initially at $t = 0$ and a constant pressure gradient $dp_0/dy = -U_o\mu_o\pi^3/4kH^2$ is applied in the y-direction to drive the flow, where U_o is the flow velocity at the centerline of the channel in the case of a fully-developed single-phase laminar flow and k is a geometric constant. For a square channel, $k \approx 0.571$ [105]. It is important to note that U_o is the centerline velocity in the channel for the Newtonian and Oldroyd-B fluids. In a Giesekus fluid, the centerline velocity becomes greater than U_o due to the shear-thinning effect. However, throughout this paper, all the non-dimensional numbers are defined based on U_o corresponding to the applied pressure gradient in the Newtonian fluid unless stated otherwise. H, U_o, and H/U_o are used as the length, velocity, and time scales, respectively. The stresses are normalized by $\mu_o U_o/H$. The normalized non-dimensional quantities are denoted by the superscript (*). The blockage ratio ($b = d/H$) is fixed at 0.25. The density (ρ_o/ρ_i) and the viscosity (μ_o/μ_i) ratios are set to 10 in this study where the subscripts i and o denote the dispersed and continuous phases, respectively. These comparatively smaller ratios are used to reduce the spatial error exacerbated by sudden jumps in material properties across the interface and enhance numerical stability, and thus relax the excessive grid resolution requirement and time step restrictions. Tasoglu [64] and Olgac et al. [65] have demonstrated that the results are not affected significantly for these types of flows at higher ratios. In the present case of pressure-driven viscoelastic channel flow, although not shown here, simulations have been performed for the density and viscosity ratios of 20, 40 and 80 as well, and the results are found to be not very sensitive to the increase in the density ratio, i.e., the difference is less than 1% but more sensitive to the viscosity ratio due to higher contribution of polymeric viscosity in a concentrated polymer solution. It is observed that at a higher viscosity ratio, the secondary flow velocity induced by the fluid particle once it attains its equilibrium position (as will be discussed in detail in §3.4.4) is not much affected but the lateral displacement of the fluid particle is still significantly influenced by this higher viscosity ratio. As the viscosity ratio in the liquid-air system of a complex fluid flow can be as high as 10^8 depending upon the molecular weight and concentration of the polymer molecules, the term 'deformable fluid particle' is used instead of a bubble in the present study.

In addition to the density and viscosity ratios, the flow conditions are characterized by the following non-dimensional numbers defined as

$$Re = \frac{\rho_o U_o H}{\mu_o}, Wi = \frac{\lambda U_o}{H}, Eo = \frac{g \Delta\rho d^2}{\sigma}, Mo = \frac{g\mu_o^4}{\rho_o \sigma^3}, Ca = \frac{\mu_o U_o}{\sigma}, \beta = \frac{\mu_s}{\mu_o}, \quad (3.1)$$

where Re, Wi, Eo, Mo, and Ca denote the Reynolds, Weissenberg, Eötvös, Morton, and capillary numbers, respectively. Note that the Morton number is not an independent parameter. β is the ratio of solvent viscosity to zero shear viscosity of

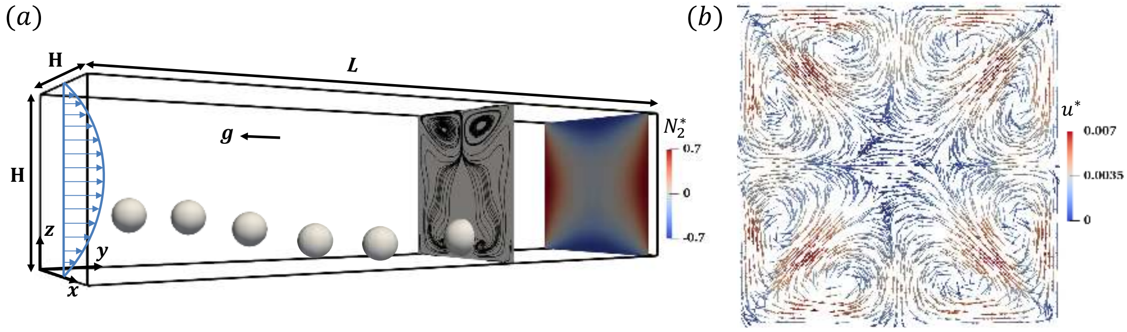

Figure 3.1: (a) The computational domain is shown with the schematic representation of a deformable fluid particle migrating toward the wall of the channel. The streamlines of the flow are shown above the particle in the xz-plane once the particle reaches its equilibrium position closer to the wall. The distribution of the second normal stress difference (N_2) is shown in the xz-plane upstream of the particle at $y = 3.95$. (b) Eight vortices showing the secondary flow field in the same xz-plane away from the particle at $y = 3.95$ are shown. The velocity vectors are colored by the magnitude of flow velocity in that plane. $(Re = 18.9, El = 0.05, Eo = 0, Ca = 0.01, \alpha = 0.1)$

the viscoelastic fluid. The density difference is defined as $\Delta\rho = \rho_o - \rho_i$. The particle deformation (χ) is quantified as

$$\chi = \sqrt{I_{\max}/I_{\min}} \ , \tag{3.2}$$

where $I_{\max}$ and $I_{\min}$ are the maximum and minimum eigenvalues of the second moment of inertia tensor defined as

$$I_{ij} = \frac{1}{\mathcal{V}_b} \int_V (x_i - x_{io})(x_j - x_{jo}) dV, \tag{3.3}$$

where $\mathcal{V}_b$ is the volume of the particle and x_{io} and x_{jo} are the coordinates of the particle centroid in the i^{th} and j^{th} directions, respectively. Bunner and Tryggvason [48] have shown that deformation quantified by this method is approximately equal to the ratio of the shortest to the longest axis for modestly deformed ellipsoids. However, for complex particle shapes, this definition of deformation gives a more general measure for the particle deformation and eliminates uncertainty in identifying the longest and the shortest axes.

3.3 Governing Equations and Numerical Method

The flow and the Giesekus model equations are described here in the context of the Eulerian-Lagrangian method that utilizes a one-field formulation. As discussed by Tryggvason et al. [106, 107, 108], one set of governing equations can be written for the entire multiphase computational domain. In this approach, the effect of surface tension is taken into account by adding a distributed body force term to the momentum equations near the interface, and the discontinuities in material properties are handled by defining an indicator function. The Navier-Stokes equations are thus written as

$$\rho\frac{\partial \boldsymbol{u}}{\partial t} + \rho\boldsymbol{\nabla}\cdot(\boldsymbol{u}\boldsymbol{u}) = -\boldsymbol{\nabla}p - \frac{dp_0}{dy}\boldsymbol{j} + \boldsymbol{\nabla}\cdot\boldsymbol{\tau} + \boldsymbol{\nabla}\cdot\mu_s(\boldsymbol{\nabla}\boldsymbol{u} + \boldsymbol{\nabla}\boldsymbol{u}^T) + \boldsymbol{g}\,(\rho - \rho_{ave}) + \int_A \sigma\kappa\boldsymbol{n}\delta(\boldsymbol{x} - \boldsymbol{x}_f)dA \tag{3.4}$$

where $\mathbf{u}$, $\boldsymbol{\tau}$, p, ρ, μ_s are the velocity vector, polymer stress tensor, pressure, discontinuous density, and solvent viscosity fields, respectively. A constant pressure gradient $-\frac{dp_0}{dy}\mathbf{j}$ is applied to drive the flow where $\mathbf{j}$ is the unit vector in the y-direction. The buoyancy term consists of the gravitational acceleration $\mathbf{g}$ and the density difference $\rho - \rho_{ave}$, where ρ_{ave} is the average density in the computational domain. The effect of surface tension is added as a body force term on the right-hand side of the momentum equation where σ is the surface tension coefficient, κ is twice the mean curvature and $\mathbf{n}$ is a unit vector normal to the interface. As the surface tension acts only on the interface, δ represents a three-dimensional Dirac delta function with the arguments $\mathbf{x}$ and $\mathbf{x}_f$ being a point at which the equation is evaluated and a point at the interface, respectively. The momentum equation is supplemented by the continuity equation

$$\boldsymbol{\nabla}\cdot\boldsymbol{u} = 0. \tag{3.5}$$

It is assumed that the material properties remain constant following a fluid particle, i.e.,

$$\frac{D\rho}{Dt} = 0, \frac{D\mu_s}{Dt} = 0, \frac{D\mu_p}{Dt} = 0, \frac{D\lambda}{Dt} = 0, \tag{3.6}$$

where $\frac{D}{Dt} = \frac{\partial}{\partial t} + \boldsymbol{u} \cdot \nabla$ is the material derivative. For a viscoelastic fluid, μ_p is the polymeric viscosity and λ is the polymer relaxation time.

Using an indicator function (I), the material properties are set in the entire computational domain as

$$\left.\begin{aligned}
\rho &= \rho_o I(\mathbf{x}, t) + \rho_i \left(1 - I(\mathbf{x}, t)\right), \\
\mu_s &= \mu_{s,o} I(\mathbf{x}, t) + \mu_{s,i} \left(1 - I(\mathbf{x}, t)\right), \\
\mu_p &= \mu_{p,o} I(\mathbf{x}, t) + \mu_{p,i} \left(1 - I(\mathbf{x}, t)\right), \\
\lambda &= \lambda_o I(\mathbf{x}, t) + \lambda_i \left(1 - I(\mathbf{x}, t)\right),
\end{aligned}\right\} \tag{3.7}$$

where the subscripts "i" and "o" denote the properties of the particle and the bulk fluid, respectively. Since the fluid in the dispersed phase is Newtonian, the values of $\mu_{p,i}$ and λ_i are set to zero. The indicator function is defined as

$$I(\mathbf{x}, t) = \begin{cases} 1 & \text{in the bulk fluid,} \\ 0 & \text{in the particle.} \end{cases} \tag{3.8}$$

Viscoelasticity of bulk liquid is modeled using the Giesekus model ([26]). This model is capable of capturing the elongation of individual polymer chains and the resulting shear-thinning behavior of the viscoelastic fluid. In the Giesekus model, the polymer stress tensor $\boldsymbol{\tau}$ evolves by

$$\boldsymbol{\tau} = \frac{\mu_p}{\lambda}(\boldsymbol{B} - \boldsymbol{I}), \tag{3.9}$$

where $\boldsymbol{B}$ and $\boldsymbol{I}$ are the conformation and the identity tensors, respectively. The conformation tensor evolves by

$$\frac{\partial \boldsymbol{B}}{\partial t} + \boldsymbol{u} \cdot \boldsymbol{\nabla B} - \boldsymbol{\nabla u}^T \cdot \boldsymbol{B} - \boldsymbol{B} \cdot \boldsymbol{\nabla u} = \frac{1}{\lambda}[(1 - \alpha)\boldsymbol{I} + (2\alpha - 1)\boldsymbol{B} - \alpha \boldsymbol{B^2}], \tag{3.10}$$

where α is the mobility factor representing the anisotropy of the hydrodynamic drag exerted on the polymer molecules. Due to the thermodynamic considerations, α is restricted to $0 \leq \alpha \leq 0.5$ [109]. When $\alpha = 0$, the Giesekus model reduces to the Oldroyd-B model.

The flow equations (Eqs. (3.4) and (3.5)) are solved fully coupled with the Giesekus model equation (Eq. (3.9)). The momentum, continuity and viscoelastic constitutive equations are solved on a stationary staggered Eulerian grid. A QUICK scheme is used to discretize the convective terms in the momentum equations while second-order central differences are used for the diffusive terms. For the convective terms in the viscoelastic equations, a 5th-order WENO-Z scheme [110] is used. An FFT-based solver is used for the pressure Poisson equation. Since the pressure equation is not separable due to variable density in the present multiphase flow, the FFT-based solvers cannot be used directly. To overcome this challenge, a pressure-splitting technique presented by Dodd and Dong [59, 111] is employed. The fluid-fluid interface is tracked by using the Lagrangian marker points located at the vertices of a triangular surface mesh. The marker points move with the local flow velocity interpolated from the Eulerian grid. The surface tension is computed on the Lagrangian grid and transferred to the Eulerian grid to be added to the momentum equation as a body force in a conservative manner. The Lagrangian grid is restructured at every time step to maintain the surface mesh nearly uniform, smooth and comparable to the Eulerian grid. The indicator function is computed based on the location of the interface using the standard procedure as described by Tryggvason [106], which requires a solution of a separable Poisson equation. The same FFT-based solver is used to compute the indicator function. Once the indicator function is computed, the material properties are set in each phase using Eq. (3.7), which results in a smooth transition of material properties across the interface. A predictor-corrector scheme is used to achieve second-order time accuracy.

3.4 Results and Discussions

We first examine the dynamics of a nearly spherical fluid particle under similar conditions as used by Li et al. [2] for a solid particle, i.e., $Re = 18.9, El = 0.05, Ca = 0.01, \alpha = 0$. The main difference in the present case is the slip at the particle interface. Note that this set of parameters is also designated as the *baseline* case in the present study to facilitate direct comparison with the results obtained for a solid particle by Li et al. [2].

A peculiar feature of a viscoelastic fluid flow is the presence of normal stress differences, which are given by $N_1 = \tau_{yy} - \tau_{zz}$ and $N_2 = \tau_{zz} - \tau_{xx}$ in the present scenario. In the absence of the shear-thinning effect ($\alpha = 0$), the Giesekus model reduces to the Oldroyd-B model and the second normal stress difference (N_2) becomes zero. Thus, $\alpha > 0$ is an essential condition to model a viscoelastic fluid that exhibits a non-zero second normal stress difference. The geometry of the channel also plays a significant role in the development of these stresses. N_1 is found to be maximum in the highest shear region near the walls and its value becomes minimum in the corners and at the center. Ho and Leal [112] argued that this particular distribution of N_1 in a four-wall channel is the primary reason for the accumulation of solid particles in the corner and centerline regions. When the second normal stress difference develops in a shear-thinning viscoelastic fluid, not only does the distribution of N_1 in the channel change but its magnitude is also reduced due to enhanced inertial effects [2]. Figure 4.1a shows the distribution of N_2 in the channel cross-section when there is a strong shear-thinning effect present in the flow, i.e., $\alpha = 0.1$. Eight vortices generated due to this distribution of N_2 away from the particle are also depicted in Fig. 4.1b. This particular distribution of N_2 affects the orientation of particle migration and the development of a secondary flow field around the particle. An asymmetric pattern of streamlines is shown in Fig. 4.1a above the particle once the particle reaches its equilibrium position near the wall. These effects on the lateral migration of a deformable particle are explored one by one in the subsequent sections.

3.4.1 Dynamics of Particle Migration

Simulations are first performed to examine the effects of the Weissenberg number, the capillary number, the initial position and the mobility factor on the lateral migration of a non-buoyant particle in the channel flow at the nominal Reynolds

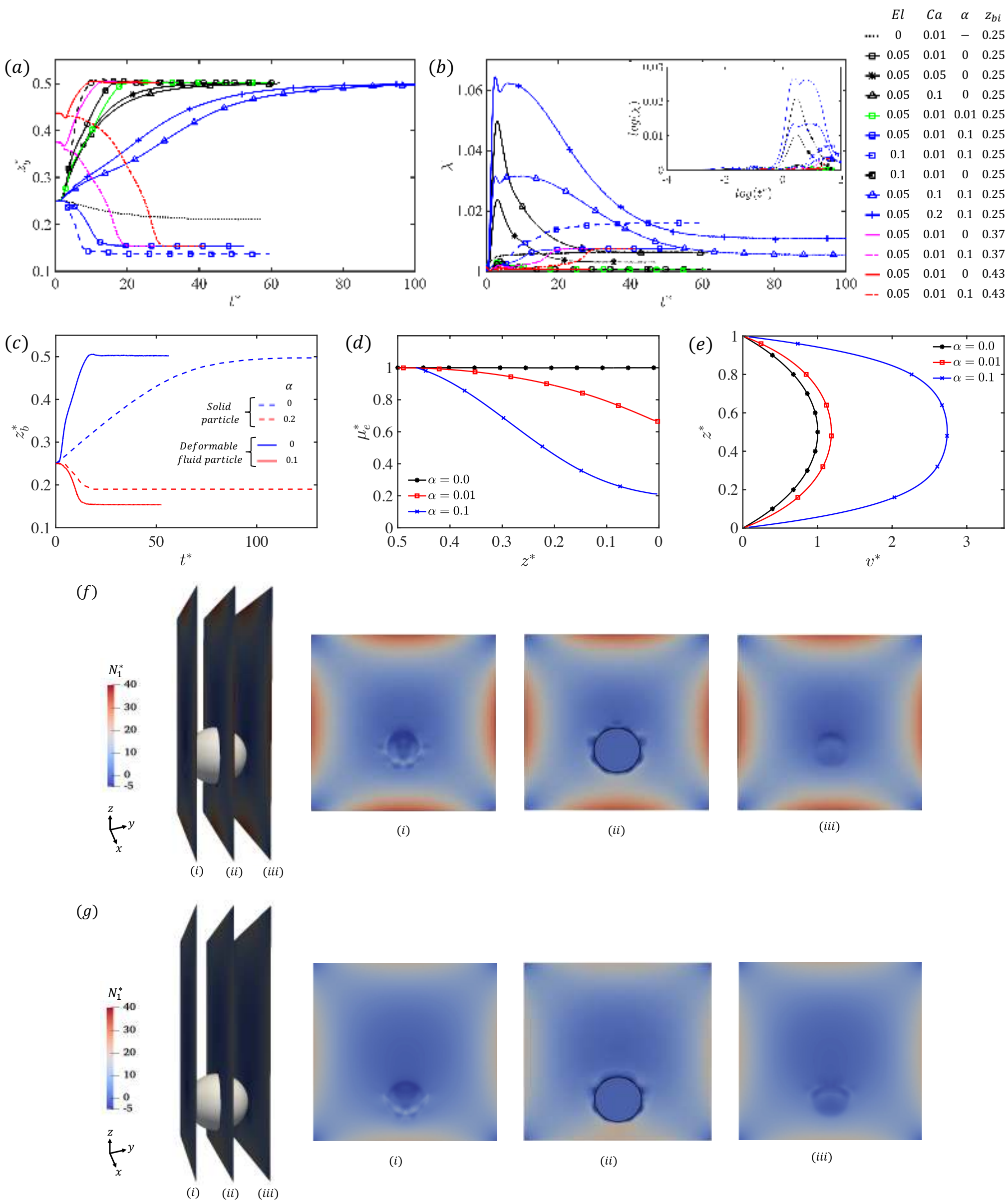

Figure 3.2: (a) Evolution of fluid particle displacement in the wall-normal (z) direction under non-buoyant conditions for different initial positions and flow conditions. (b) The corresponding change in the particle deformation is shown as the particle moves towards or away from the wall. The same plot is shown in the inset on a log-scale. (c) The evolution of fluid particle displacement is compared with a solid particle studied by [2] under similar flow conditions. (d) The reduction in the effective viscosity of the fluid due to shear-thinning is quantified in a vertical cutting xz-plane away from the particle. (e) The flow velocity profiles in the same xz-plane are shown for different values of α. The distributions of the first normal stress difference (N_1) around the particle are shown in vertical cutting planes of (i), (ii), and (iii) as indicated on the left for (f) $\alpha = 0.01$ and for (g) $\alpha = 0.1$. For (c), (d), (e), (f) & (g) $El = 0.05, Ca = 0.01$. $Re = 18.9$ for all the cases presented in this figure.

number $Re = 18.9$ and $\beta = 0.1$. Figures 3.2a and 3.2b show the evolution of particle displacement in the lateral (z) direction and the corresponding change in the particle deformation during its migration, respectively. In a Newtonian fluid, a nearly spherical particle slightly moves towards the channel wall under the effects of inertia and stabilizes near the wall where wall-induced repulsive force balances the lift force. When the ambient fluid is viscoelastic, modeled by Oldroyd-B ($\alpha = 0$), the same spherical particle moves towards the center of the channel under the elastic effects just like a solid particle [2]. It is observed that, although the overall trend of fluid particle displacement in the Oldroyd-B fluid is similar to that of a solid particle, the fluid particle moves towards the center of the channel at a much higher rate as shown in Fig. 3.2c. Compared to a solid particle, a fluid particle experiences a smaller drag due to slip at the interface, which makes it more sensitive to the inertial and elastic effects. When the particle deformability is increased gradually by increasing the capillary number to $Ca = 0.05$ and $Ca = 0.1$ for the same Oldroyd-B fluid, the rate of particle migration towards the channel center is slightly reduced. As the particle moves towards the low shear region (towards the center), its deformability starts to reduce and the same effect is observed in its lateral velocity as well. The effects on particle velocity will be discussed in detail later in Section 3.4.5. It is interesting to observe that, although the deformability-induced lift force is expected to push the particle towards the center, it acts in the opposite direction at this Reynolds number and slows down the particle migration towards the center of the channel. Evolution of streamwise and wall normal velocities of the spherical and the slightly deformable particle are shown in Fig. 3.3 where the constant contours of viscoelastic stress components of τ_{yz} and τ_{zz} are also plotted in the insets in the yz-cutting plane. As seen, not only the wall normal velocity but also the streamwise velocity is reduced when the particle is made slightly deformed by increasing the capillary number to $Ca = 0.1$, although the deformation is still modest, i.e., $\chi \approx 1.05$. The viscoelastic stress distribution is also markedly different in both cases. This extreme sensitivity is attributed to a similar mechanism that is responsible for a jump discontinuity in the rise velocity of a buoyancy-driven bubble

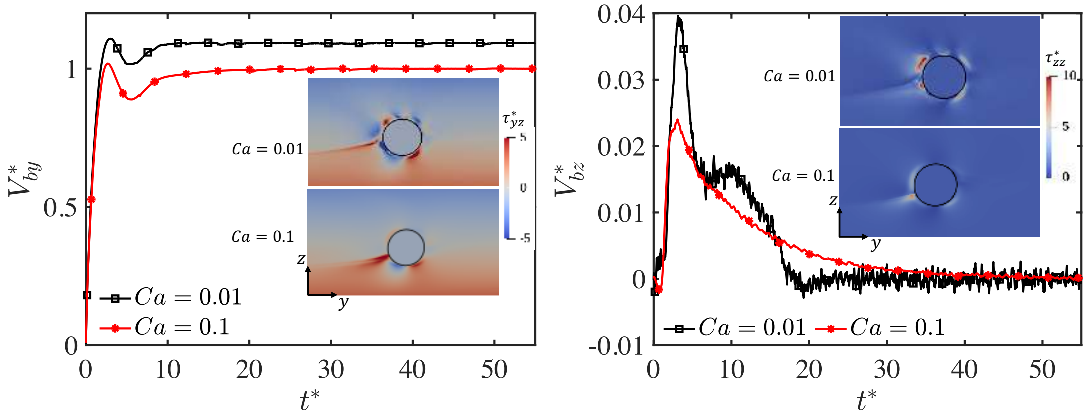

Figure 3.3: Evolution of migration velocity of a nearly spherical ($Ca = 0.01$) and a slightly deformed ($Ca = 0.1$) fluid particle in the streamwise (*left*) and in the wall normal (*right*) directions. The contours of viscoelastic stress components τ_{yz} and τ_{zz} are shown in the insets around the particles in the yz-cutting plane at $t^* = 5.53$ ($Re = 18.9, El = 0.05, \alpha = 0$).

[45]. A different manifestation of the same mechanism has also been observed in our earlier work [113] as well. According to the theory proposed by Bothe et al. [45], polymer molecules are stretched by the flow as they pass over the particle and this stored elastic energy is released on its front/back hemisphere giving an additional pull/push to the particle depending on the flow conditions. The transition is expected to occur when the convective time scale is equal to the polymer relaxation time, i.e., the effective Weissenberg number is unity. In the present scenario, the effective Weissenberg number can be defined as $Wi_{\text{eff}} = \frac{\lambda}{(R/u_{\text{rel}})}$, where R is the particle radius and u_{rel} is the slip velocity. For the nearly spherical particle, the effective Weissenberg number is computed as $Wi_{\text{eff}} = 0.92$ at $t^* = 5.53$ which is close to the critical value of unity. As the particle is elongated in the streamwise direction in the deformable case, the effective radius (minor axis) becomes larger so the polymer molecules relax on the front part of the particle before reaching the equator, which thus increases the drag and slows down particle the migration velocity.

When the shear-thinning effects are enhanced by increasing the mobility parameter (α) in the Giesekus model, the orientation of particle migration changes due to an increase in the relative importance of the fluid inertia. At a very small value of $\alpha = 0.01$, a spherical particle still moves towards the center but it takes a comparatively longer time than that in the Oldroyd-B fluid to reach its equilibrium position. Once α is increased further to 0.1, the orientation of particle migration changes completely, i.e., instead of moving towards the center, it starts moving towards the wall. Again, although the trend is similar to that of a solid particle in a shear-thinning fluid under the same parametric settings, the migration of fluid particle is significantly more sensitive to the shear-thinning parameter than the corresponding solid particle. For example, while $\alpha = 0.2$ is required by the solid particle to reverse its orientation from the channel center towards the wall [2], $\alpha = 0.1$ is sufficient for the fluid particle to reverse its orientation. The shear-thinning effect is quantified by the reduction in the effective viscosity (μ_e) of the fluid defined as

$$\mu_e/\mu_o = \frac{\mu_s(\frac{\partial v}{\partial z} + \frac{\partial w}{\partial y}) + \tau_{yz}}{\mu_o(\frac{\partial v}{\partial z} + \frac{\partial w}{\partial y})}. \tag{3.11}$$

The variation of the effective viscosity and the corresponding flow velocity profiles are shown in Figs. 3.2d and 3.2e, respectively, for $\alpha = 0$, 0.01 and 0.1. As seen, for $\alpha = 0$, the effective viscosity remains constant in the channel as expected. In a shear-thinning fluid ($\alpha > 0$), the viscosity of the fluid decreases significantly in the high shear region near the wall and becomes as low as 20% of its value in the channel center for $\alpha = 0.1$. As a result, the centerline flow velocity becomes approximately 2.8 times larger than that of the non-shear-thinning fluid (Fig. 3.2e). This enhanced inertia helps the quick migration of the particle towards the wall as seen in Fig. 3.2a. It is observed that this shear thinning effect is strong enough to reverse the migration of fluid particle from the center towards the wall even when the initial position of the particle is shifted gradually towards the channel center, i.e., a low shear region (Fig. 3.2a). The shear-thinning also changes the distribution of the first normal stress difference (N_1) in the channel. The distribution of N_1 is shown in three vertical cutting planes in the vicinity of the particle for $\alpha = 0.01$ and $\alpha = 0.1$ in Figs. 3.2f and 3.2g, respectively, at the same time instant $t^* = 5.71$. The higher magnitude of N_1 for $\alpha = 0.01$ explains why the particle is pushed towards the channel center. It is important to note that in the present study, as the channel aspect ratio is fixed (square duct only) and the initial position of the fluid particle is varied along one wall normal direction (z) only while the initial position of the particle is fixed at $x = 0.5H$ in the second wall normal direction, the equilibrium positions of the fluid particle along the channel diagonals or in the corner regions are not observed [90].

When the elasticity number is increased to $El = 0.1$ by increasing the Weissenberg number in the presence of a strong shear-thinning effect ($\alpha = 0.1$) for a spherical particle ($Ca = 0.01$), the viscoelastic stresses take more time to develop due to a higher relaxation time (λ) of polymer molecules. Therefore, the enhanced inertia due to the shear-thinning quickly moves the particle towards the wall while the viscoelastic stresses are not yet fully developed in the flow. The particle reaches its equilibrium position closer to the wall and its deformation also increases due to a higher shear region there. However, this higher deformability and higher elasticity are not strong enough to reverse the particle migration back towards the channel center. In the absence of the shear-thinning ($\alpha = 0$) with the same high elasticity number, the particle quickly moves towards the center due to relatively lower inertia.

When the fluid particle is made more deformable by increasing the capillary number to $Ca = 0.1$ (Fig. 3.2b) in this shear-thinning fluid ($\alpha = 0.1$), the deformability-induced lift force resists the pronounced effects of shear-thinning on the fluid inertia. This higher particle deformation is sufficient enough to push the particle back toward the channel center. However, due to the resistance by the higher inertial force, the rate of particle migration is much slower in this fluid than in the non-shear-thinning fluid. When the capillary number is increased even further to $Ca = 0.2$, the effect is found to be more pronounced and the rate of particle migration towards the center of the channel is slightly increased. The enhanced fluid inertia due to the shear-thinning effect also makes the particle more deformable in a shear-thinning fluid due to an effective high capillary number.

For all the simulations shown in Fig. 3.2, the nominal Reynolds number is kept constant. It can be observed that in this non-buoyant situation, the orientation of particle migration can be controlled with the shear-thinning effect of the viscoelastic fluid. With a strong shear-thinning effect ($\alpha = 0.1$), the particle moves towards the wall and higher elasticity (e.g., $El = 0.1$) is not able to reverse its orientation. The higher particle deformability, however, resists this shear-thinning effect on particle migration and moves it back towards the center. Interestingly, the particle deformation increases only by 6% in the case of the maximum capillary number of $Ca = 0.2$ in this viscoelastic fluid. However, even this modest deformation makes a significant impact on the dynamics of particle migration and reverses its orientation towards the center. In the absence of shear-thinning, the particle migrates towards the center even with a weak elastic effect or with a little deformability.

3.4.2 Path Instability

Path instability of a freely rising bubble in a Newtonian fluid has been thoroughly studied and well documented in the existing literature. For instance, Zenit et al. [114] experimentally observed that the path instability of a bubble does not depend on the Reynolds number and it is rather governed by the aspect ratio of bubble shape, i.e., its deformation. When the aspect ratio increases beyond $\chi > 2$, vortices generated on the free-slip surface of the bubble give rise to a wake instability behind the trailing edge, forcing its path to become unstable. In the case of a viscoelastic ambient fluid, Shew et al. [115] observed that the flow structure in the wake region becomes more intense leading to path instability even at a much lower deformability.

Simulations are first performed for $Re = 100$, 500, and 1000 to examine the effects of the Reynolds number on the path instability of the deformable fluid particle in the present pressure-driven viscoelastic flow in the absence of buoyancy. To isolate the effects of the Reynolds number, the shear-thinning effect is eliminated by setting $\alpha = 0$, and the capillary number is fixed at $Ca = 0.01$ to keep the particle nearly spherical. Simulations are repeated by keeping either the elasticity number or the Weissenberg number constant as the Reynolds number is increased. The results are summarized in Figs. 3.4a & c and 3.4b & d for the fixed elasticity number and

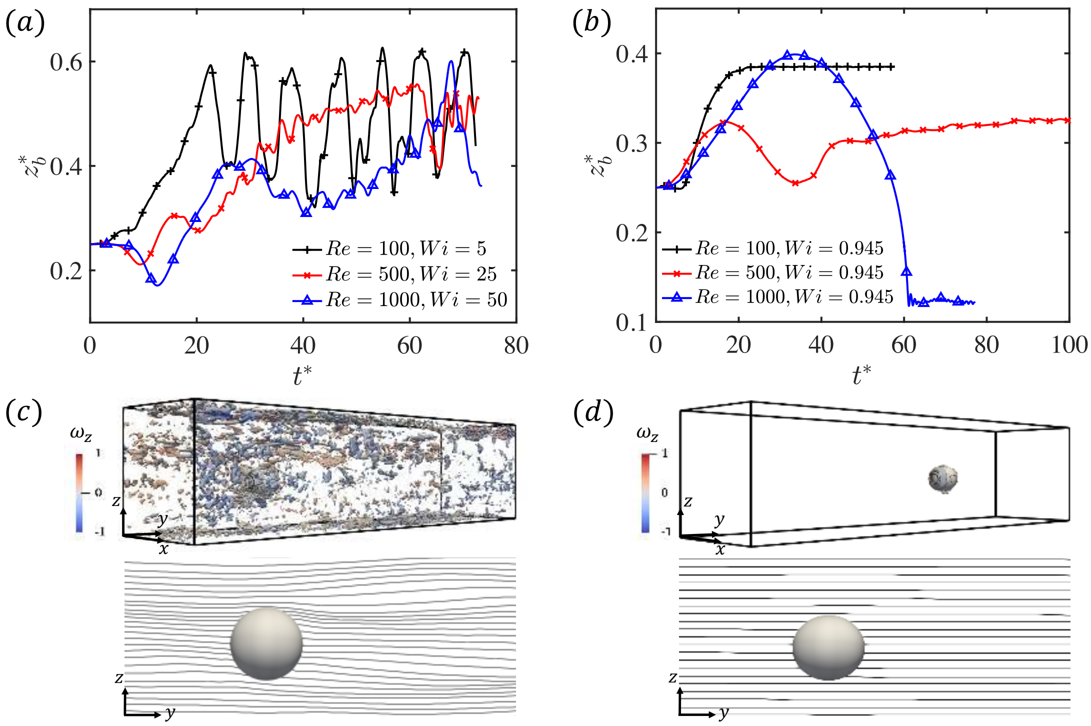

Figure 3.4: Evolution of lateral migration of the fluid particle at constant $El = 0.05$ (a) and at constant $Wi = 0.945$ (b) are shown for different values of Reynolds number. (c) The constant contours of Q-criterion at 0.001 colored by the vorticity component (ω_z) are shown for $Re = 500, Wi = 25$ as the flow becomes elastically unstable due to the curvature of streamlines across the particle. (d) The contours of Q-criterion plotted at the same value of 0.001 for $Re = 500, Wi = 0.945$ show a negligible presence, confirming a stable flow. This is also confirmed by the straight streamlines across the fluid particle.

the fixed Weissenberg number cases, respectively. When the elasticity number is kept constant at $El = 0.05$ (Fig. 3.4a), the Weissenberg number increases as the Reynolds number is increased. The particle path becomes unstable at $Re = 100$ (the corresponding $Wi = 5$). However, the particle deformation remains negligible due to a low value of the capillary number. The path instability observed in this case of a nearly spherical particle at $Re = 100$ occurs mainly due to the onset of an elastic flow instability caused by the curved streamlines along the particle interface. Mckinley et al. [116] determined a critical parameter for the onset of an elastic instability as

$$M^2 = \frac{\lambda U}{R} \frac{N_1}{|\tau_t|} \geq M_{crit}^2, \tag{3.12}$$

where U is the flow velocity along the streamline, N_1 is the first normal stress difference, R is the radius of curvature of the streamline and τ_t is the total shear stress. Mckinley [116] calculated the critical value for a 2D cylinder as $M_{crit} \approx 6.08$. In the present scenario of a spherical fluid particle, the critical value turns out to be $M_{crit} \approx 5.59$ at $Re = 100$. The constant contours of the Q-criterion (second invariant of velocity gradient tensor) at 0.001 and the streamlines are also plotted around the particle in Fig. 3.4c for $Re = 500$ to show the overall flow structure. The contours are colored by the magnitude of vorticity in the z-direction. The curvature of streamlines across the particle and the contours of the Q-criterion confirm that the flow is no longer stable. As a result, the particle path shows an oscillatory pattern around the channel center for $Re = 100$. When the Weissenberg number is increased further by increasing the Reynolds number at the fixed value of $El = 0.05$, Fig. 3.4a shows that the particle path becomes more irregular and unpredictable as the flow gets closer to the onset of elastic turbulence stemming from the elastic instability. The exact mechanism behind this probable transition is still elusive [5].

On the other hand, when the Weissenberg number is kept constant at $Wi = 0.945$ as Re is increased, the particle path remains stable even for the Reynolds number as high as $Re = 1000$. As shown in Fig. 3.4d, the streamlines remain straight across the particle and no significant contours of Q-criterion are observed in the flow, unlike the fixed elasticity number case. It is interesting to observe that the particle initially moves towards the channel centerline and then reverses its direction towards the channel wall at higher Reynolds numbers. The final position is determined by the interplay of inertial and viscoelastic effects. The equilibrium position of the particle shifts from the channel center towards the wall as the Reynolds number is increased (Fig. 3.4b). At $Re = 1000$, the particle reaches the wall under the influence of strong inertia, which results in an increase in its deformation as well due to the high shear region near the wall.

3.4.3 Effect of Buoyancy

The buoyancy is significant in many natural processes and practical applications. A commonly encountered situation is an upward flow where the gravity acts in the opposite direction of the fluid flow such as in bubble column reactors and in crude oil extraction. Simulations are next performed for a range of Eötvös number to examine the effects of buoyancy in an upward flow while keeping the other parameters fixed at their baseline values of $Re = 18.9$, $Ca = 0.01$ and $El = 0.05$. Note that the Morton number is $M = 4.97 \times 10^{-6}$ for $Eo = 1$ in this viscoelastic fluid. For reference, this value is much higher than the Morton number of 2.52×10^{-11} for an air particle in water at 20°C but can be matched by using a water-glycerin solution [117].

Simulations are performed by gradually increasing the Eötvös number from $Eo = 0$ (neutrally buoyant) to $Eo = 1$ without and with the shear-thinning effect. The case of $Eo = 0$ is simulated by setting $\mathbf{g} = 0$, which can be realistic only in a microgravity environment. This condition is used here to isolate the sole effects of the other parameters from buoyancy. The results are shown in Figs. 3.5(a),(c),(e),(g) and 3.5(b),(d),(f),(h) in terms of the evolution of particle deformation, its three-dimensional displacement, the wake structure behind the particle, and the pressure distribution on the particle surface for an Oldroyd-B ($\alpha = 0$) and a Giesekus ($\alpha = 0.1$) fluid cases, respectively. In the Oldroyd-B fluid, the particle moves toward the channel wall without any sign of path instability at $Eo = 0.25$. We note that the same particle moves toward the channel center in the absence of buoyancy. This change in the orientation occurs due to the additional buoyancy-induced lift force [118]. At $Eo = 0.5$, the particle still migrates towards a channel wall (interestingly not to the same wall as in the $Eo = 0.25$ case) but small oscillations start to appear in its path with a regular zigzag pattern indicating the onset of a path instability. A similar oscillatory pattern is also visible in the particle deformation (χ) as seen in Fig. 3.5(a). When Eo is further increased to 0.75, the particle deformation also increases and the particle path shifts from a zigzag to a helical pattern. The particle moves laterally to eventually settle near the other side of the channel and its motion becomes more chaotic with a significant velocity component in the wall normal

(x) direction. At $Eo = 1$, the particle path becomes completely unstable with a deformation parameter (χ) exceeding 1.6 (Fig. 3.5a).

It is worth noting that the deformation parameter is only about $\chi = 1.1$ when the deformed particle undergoes path instability at $Eo = 0.5$ in the present setting. This value is much smaller than the condition $\chi \geq 2$ required for the onset of a path instability in the case of a freely rising bubble in a Newtonian fluid [114]. This result confirms that the viscoelasticity facilitates the earlier onset of path instability as also pointed out by Shew et al. [115]. The wake region is much more intense in the viscoelastic fluid than in the Newtonian fluid due to the additional viscoelastic stresses, forcing its path to become unstable at a relatively small deformation. The evolution of the wake region and the corresponding pressure distribution on the particle surface is depicted for the $Eo = 1$ case in Figs. 3.5e and 3.5g, respectively, to qualitatively show the mechanism for the path instability. As seen, the structure of the wake is highly complex and transient, and the pressure distribution changes accordingly, indicating the footprint of the instability.

Next, a strong shear-thinning effect is added ($\alpha = 0.1$), and the simulations are repeated for the same values of Eo by keeping the other parameters fixed at their baseline values of $Re = 18.9$, $El = 0.05$, and $Ca = 0.01$. The results are summarized on the right side of Fig. 3.5. As seen in Fig. 3.5d, the particle migrates towards a wall for all the cases but interestingly not to the same wall. The path of the fluid particle remains stable for $Eo = 0.25$ but it migrates towards the wall at a much higher rate than that for the non-buoyant case of $Eo = 0$. This behavior is attributed to the same enhanced lift force due to the buoyancy as in the non-shear-thinning case. Some oscillations appear in the particle trajectory for $Eo = 0.5$ but they are damped very quickly as the particle stabilizes near a wall. As Eo is increased beyond $Eo = 0.5$, the oscillations are amplified leading to path instability. For $Eo = 0.75$, the particle migrates laterally and settles near the other wall similar to the Oldroyd-B fluid case. In this case, the particle initially follows a helical path but, interestingly, its path is stabilized after some time (Fig. 3.5*d*). The corresponding oscillatory pattern observed in the deformation also vanishes once the particle path

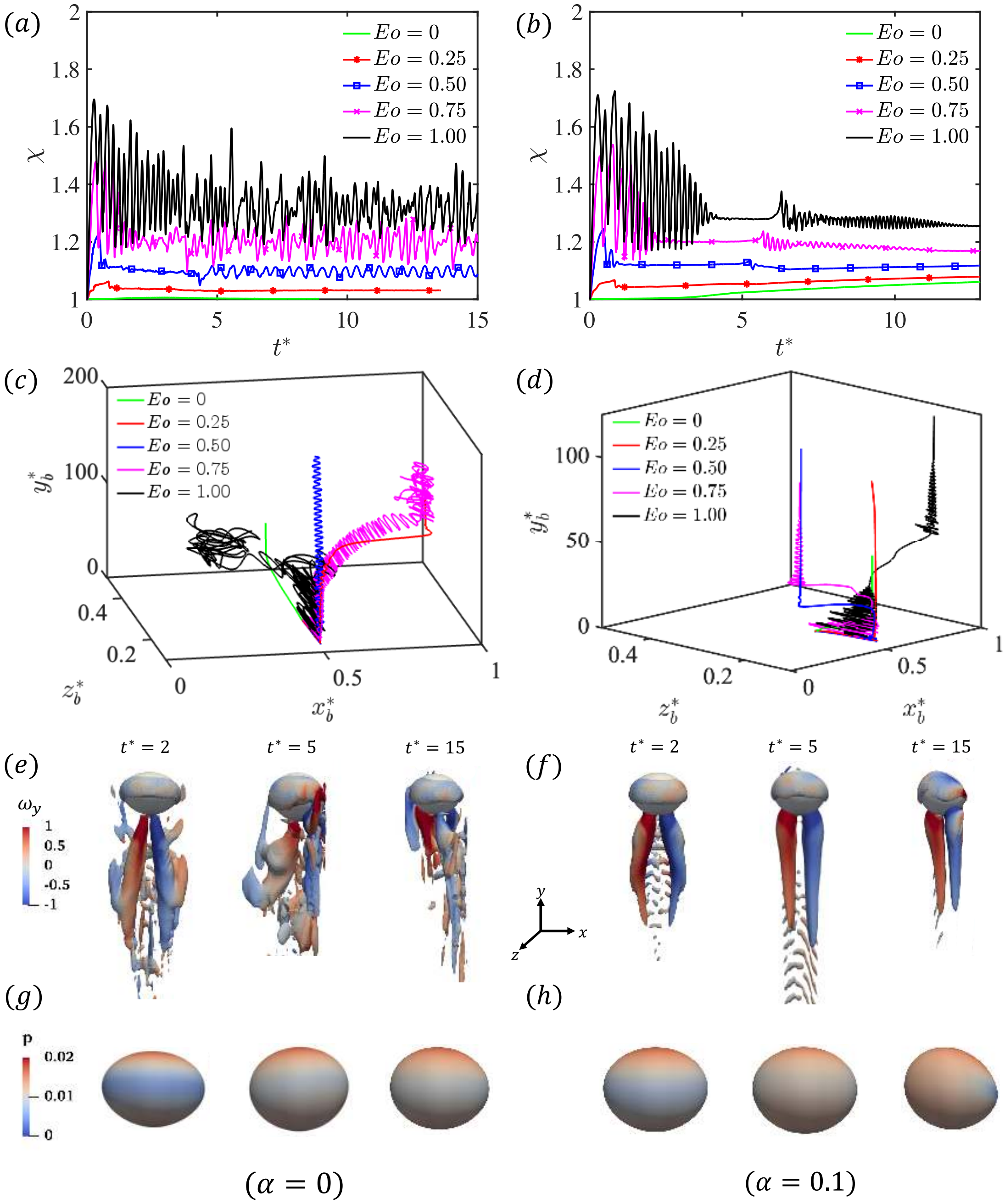

Figure 3.5: Evolution of particle deformation and its 3D displacement at different values of Eötvös number are shown for (a,c) $\alpha = 0$ and for (b,d) $\alpha = 0.1$. For the $Eo = 1$ case, the constant contours of the Q criterion at 0.05 are shown to visualize the complex flow pattern in the wake region behind the particle for (e) $\alpha = 0$ and for (f) $\alpha = 0.1$. The contours are colored by vorticity (ω_y) in the range of ± 1. For the same $Eo = 1$ case, the pressure distribution on the particle surface are shown at the same times for (g) $\alpha = 0$ and for (h) $\alpha = 0.1$. $(Re = 18.9, Ca = 0.01, El = 0.05, \beta = 0.1)$

is stabilized (Fig. 3.5*b*). The stabilized particle path is also observed for $Eo = 1$. The stabilization mechanism is visualized in Fig. 3.5f where the evolution of the wake structure is depicted for the $Eo = 1$ case. As seen, the wake behind the particle is not symmetric initially but it later evolves into a symmetric two counter-rotating vortex structures indicating that the path is stabilized. Two contributory factors are speculated to be the main reason for this stabilization mechanism. First, with a decrease in fluid viscosity in the vicinity of the particle due to the shear-thinning effect, the vortices generated on the surface of the deformed particle are not strong enough to make the wake region unstable. Secondly, due to the shear-thinning of the fluid, the first normal stress difference N_1 decreases in this viscoelastic fluid, which reduces the destabilization effect of viscoelasticity. Thus, the intense flow structures observed in the wake region in the case of the Oldroyd-B fluid (Fig. 3.5e) are damped out in this shear-thinning fluid (Fig. 3.5f). Although an addition of shear-thinning makes the particle path more stable, it cannot maintain path stability indefinitely. For instance, although not shown here due to space consideration, once the particle deformation exceeds $\chi > 2$ at $Eo = 2$, the path remains unstable even for the mobility factor as high as $\alpha = 0.1$.

All the simulations have heretofore been performed for a small value of the viscosity ratio, $\beta = 0.1$, representing highly concentrated polymer solutions. Thus, the fluid exhibited a strong viscoelastic behavior and the particle path remained stable only up to $Eo = 0.25$ and $Eo = 1$ without and with the shear-thinning effect, respectively. To examine the particle migration dynamics in dilute polymer solutions, simulations are now performed for another extreme value of $\beta = 0.9$ without and with the shear-thinning effect. It is important to note that $\beta = 0.9$ represents a very rare case that can be achieved only with specially designed fluids. Figures 3.6a and 3.6b show the evolution of lateral displacement of a particle and its deformation for the range of $2 \leq Eo \leq 8$. We note that, at the lower values of Eo up to $Eo = 2$, there is not much difference observed in the particle deformation and its equilibrium position compared to the case of $Eo = 2$ in Fig. 3.6a. As Eo increases, the difference in the equilibrium position of the particle becomes more and more pronounced without and with the shear-thinning effect. For the smaller values of Eötvös number up to $Eo = 2$, the shear-thinning effect does not play a dominant role due to a lower value of particle deformation. As the contribution of polymeric viscosity towards the total viscosity of the fluid is already very low at $\beta = 0.9$, a further decrease in the viscosity due to shear-thinning starts to show its effect only at a higher value of particle deformation. Beyond $Eo = 2$ and with $\alpha = 0.1$, the particle reaches the channel center for all the values of Eo up to $Eo = 8$, whereas, without the shear-thinning effect, the equilibrium position of the particles occurs slightly away from the center depending upon its deformation. The most interesting feature is the persistent stability of the particle path even when the deformation exceeds 2.3 for the $Eo = 8$ case (Fig. 3.6b-inset). Zenit et al. [114] have shown that for a freely rising bubble, the path becomes unstable when the deformation value exceeds 2. They argued that for such a buoyancy-driven bubble, path instability depends upon the bubble deformation rather than the Reynolds number. On the other hand, Haberman et al. [119] and Kelley et al. [120] had earlier demonstrated that the path instability of an air bubble in a viscous fluid of a Hele-Shaw cell did depend on the Reynolds number. It is found that the criterion, $\chi > 2$, for triggering path instability does not apply in the present case of a pressure-driven viscoelastic channel flow at this low Reynolds number.

In order to verify the dependence of path instability of the fluid particle on the Reynolds number, simulations are next performed by increasing the Reynolds number to 47.25 while keeping the Weissenberg number fixed at $Wi = 0.945$. As a result, the elasticity number is reduced to 0.02. Simulations are repeated for $\alpha = 0$ (no shear-thinning) and $\alpha = 0.1$ (significant shear-thinning) cases for the range of Eötvös number $1 \leq Eo \leq 4$. Figures 3.6c and 3.6d depict the evolution of particle displacement in the lateral direction and its deformation. As Eo increases, the particle deformation also increases and its equilibrium position gradually shifts away from the wall. At $Eo = 3$, as the fluid viscosity decreases in the vicinity of the particle, the elastic effect becomes dominant and the particle migrates towards the channel center. The particle crosses the channel center under the combined effects of

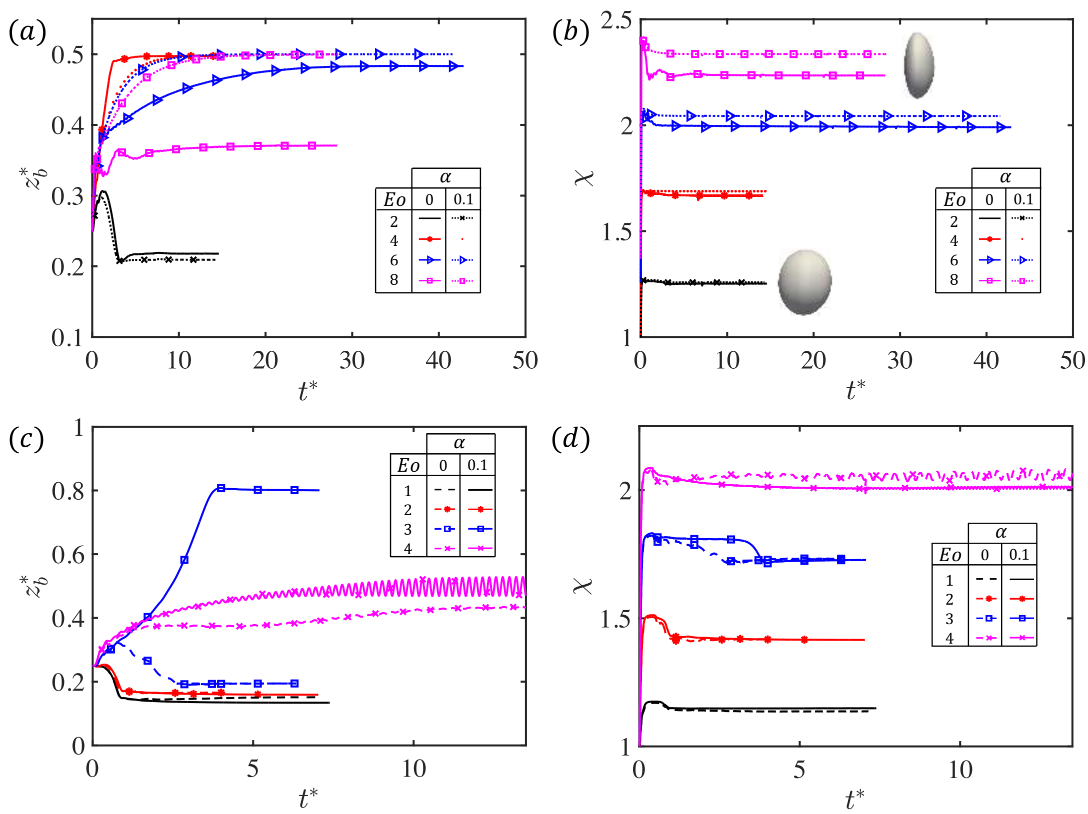

Figure 3.6: (a) Evolution of particle displacement in the lateral (z) direction and (b) its deformation for different values of Eötvös number. For (a) and (b), $Re = 18.9$, $Ca = 0.01$, $El = 0.05$, $\beta = 0.9$. For (c) and (d), $Re = 47.25$, $Ca = 0.01$, $El = 0.02$, $\beta = 0.9$. The shapes of the deformed fluid particles are shown in the inset of (b) for $\alpha = 0$ case at $Eo = 2$ and $Eo = 8$.

deformation-induced lift force and the fluid elasticity and settles at an equilibrium position closer to the wall on the other side of the channel as the inertial effects eventually dominate (Fig. 3.6c). On the other hand, without shear-thinning, the particle migrates towards the wall as the deformation and elasticity are not strong enough to counter high inertial lift force at $Eo = 3$. Interestingly, both the particles settle at the same equilibrium position closer to the wall but on the opposite sides of the channel.

At $Eo = 4$, when the particle deformation exceeds 2 and the shear-thinning effect is present, small oscillations start to appear in its path indicating the onset of a path instability. It shows that path instability of the fluid particle in this pressure-driven viscoelastic flow is a function of Reynolds number as well along with the particle deformation. It is also observed that the particle path remains stable in the absence of shear-thinning ($\alpha = 0$) at the same value of $Eo = 4$. Interestingly, this role of shear-thinning is opposite to what was observed in the case of $\beta = 0.1$, i.e., the shear-thinning damps out the path instability at low values of β (high polymer concentration) whereas it promotes the path instability of the particle at high β values (dilute polymer concentration). This interesting behavior is attributed to the local change in the effective elasticity number (El) due to the shear-thinning effect. Ray et al. [121] have shown that, for larger values of El, there is an asymptotic limit of stabilization observed in the Oldroyd-B model. We find that this role of elasticity number in stabilizing or destabilizing the particle path is further dependent upon the value of β. At lower β, a decrease in the local value of El stabilizes the particle path while, at the higher value of β, the same decrease in El is found to be destabilizing.

3.4.4 Particle-Induced Secondary Flow

The presence of the second normal stress difference (N_2) and the geometry of the square-shaped channel induces a secondary flow field in a direction perpendicular to the primary flow. The dynamics of this secondary flow field are significantly influenced by the presence of a fluid particle. Moreover, the orientation of particle migration also affects the magnitude of the secondary flow velocity. The secondary flow velocity has been analyzed by varying the particle deformability (Ca), the shear-thinning (α), the fluid elasticity (Wi), and the fluid inertia (Re). Figure 3.7 shows complex flow patterns in vertical cutting planes at the downstream, the center, and upstream of the particle under different flow conditions. The upstream and downstream planes are located at $+0.75$ and -0.75 from the particle center, respectively. The velocity vectors are colored by the magnitude of flow velocity in the $xz-$plane. In an Oldroyd-B fluid, the particular distribution of N_1 in the channel far away from the particle builds up a weak secondary flow oriented towards the corners of the channel from its center. It generates a 'flower-shaped' flow pattern as shown in Fig. 3.7a. The presence of N_2 due to the shear-thinning effect (Giesekus fluid)

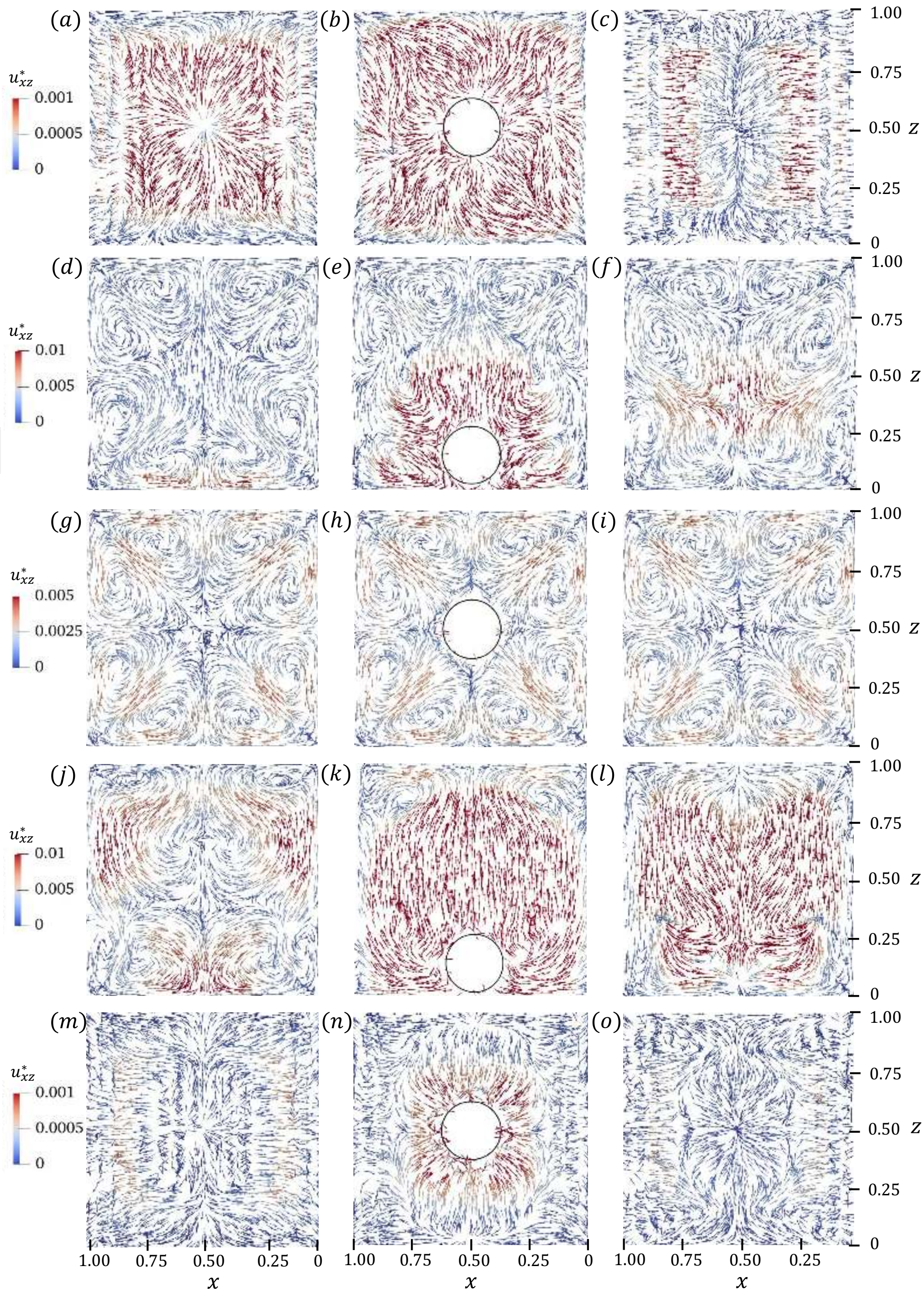

Figure 3.7: Velocity vectors representing the complex flow patterns of secondary flow field in vertical cutting planes at a downstream (a,d,g,j,m), the center (b,e,h,k,n) and at upstream (c,f,i,l,o) of the particle. (a,b,c) $Re = 18.9, Ca = 0.01, El = 0.05, \alpha = 0$. ($d$,$e$,$f$) $Re = 18.9, Ca = 0.01, El = 0.05, \alpha = 0.1$. ($g$,$h$,$i$) $Re = 18.9, Ca = 0.2, El = 0.05, \alpha = 0.1$. ($j$,$k$,$l$) $Re = 18.9, Ca = 0.01, El = 0.1, \alpha = 0.1$. ($m$,$n$,$o$) $Re = 18.9, Ca = 0.1, El = 0.05, \alpha = 0$.

generates an additional eight vortices at the corners of the channel (Fig. 3.7d). Once the particle passes through this plane and migrates towards the center (Fig. 3.7g and 3.7h), this flow pattern gets disturbed but becomes symmetric again above and below the particle once the particle attains its steady state position. On the other hand, if the particle migrates towards a channel wall, the flow pattern becomes highly asymmetric away from the wall resulting in a strong secondary flow with a velocity as high as the order of particle migration velocity (Fig. 3.7k).

The quantitative comparison of secondary flow velocities is summarized in Fig. 3.8 for different flow conditions. The z-component of flow velocity is numerically integrated in the region ± 0.75 upstream and downstream of the particle in the streamwise (y) direction and the integration is performed in the entire domain $[0, 1]$ in the z-direction, i.e.,

$$\langle u_z \rangle_{y,z} = \frac{1}{A_{yz}} \int_0^1 \int_{-0.75}^{+0.75} u_z dz dy \cong \frac{1}{(j_{\max} - j_{\min} + 1)\, N_z} \sum_{k=1}^{N_z} \sum_{j=j_{\min}}^{j_{\max}} (u_z)_{jk}, \quad (3.13)$$

where A_{yz} is the area of the yz-plane, and $j_{\min} = (y_b - 0.75)N_y/L$ and $j_{\max} = (y_b + 0.75)N_y/L$ with N_y and N_z being the number of grid points in the y and z directions, respectively. The average secondary velocity, $\langle u_z \rangle_{y,z}$, in the y and z directions is plotted along x in Fig. 3.8 once the particle reaches its equilibrium position closer to a wall or towards the center of the channel. Figures 3.8a and 3.8b show the average secondary flow velocity for $Re = 18.9$ while the results for higher Reynolds numbers are shown in Figs. 3.8c and 3.8d.

At $Re = 18.9$, the magnitude of the secondary flow velocity remains negligible for all the situations where the particle migrates towards the channel center (Fig. 3.8a). In an Oldroyd-B fluid, the particle migrates towards the center of the channel under the effect of elasticity, as shown in Fig. 3.2. As the particle migrates in the z-direction and reaches the center, the flow pattern becomes symmetric above and below the particle (Fig. 3.7b). In a Giesekus fluid, when the shear-thinning effect is sufficient enough to move the particle towards a wall ($\alpha = 0.1$), a strong secondary flow pattern is observed as shown in Fig. 3.8b. When the elasticity number is increased in this shear-thinning fluid, the maximum magnitude of the secondary flow velocity is attained. This is the same combination of parameters for which the particle equilibrium position is closest to the channel wall in Fig. 3.2a. The flow pattern above the particle for this situation is depicted in Fig. 3.7k. When the Reynolds

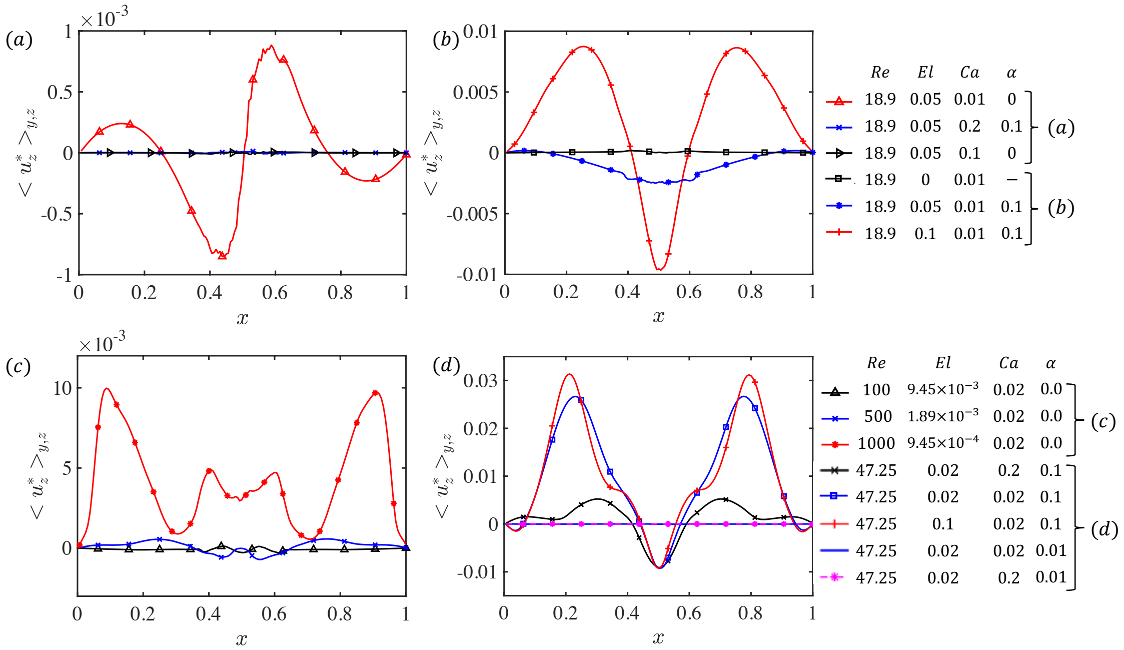

Figure 3.8: The averaged secondary flow velocity under the flow conditions (a) where the fluid particle migrates towards the channel center and (b) where the particle migrates towards a wall at Re = 18.9. The averaged secondary flow velocity is plotted for higher Reynolds numbers in the range $47.25 \leq Re \leq 1000$ for (c) an Oldroyd-B fluid and (d) a Giesekus fluid.

number is increased in an Oldroyd-B fluid, the equilibrium position of the particle moves closer to the channel wall. When the Weissenberg number is kept constant while increasing the Reynolds number to avoid elastic instability, as discussed in Section 3.4.2, the magnitude of the secondary flow velocity keeps increasing with the Reynolds number and becomes as high as 1% of the maximum flow velocity in the channel (Fig. 3.8c). A small asymmetry observed in the secondary flow pattern for the Re = 1000 case is attributed to the slight migration of particle in the x-direction due to onset of an inertial path instability.

At Re = 47.25, when the shear-thinning effect is small (α = 0.01), the particle moves towards the center of the channel whether it is spherical ($Ca = 0.01$) or highly deformable ($Ca = 0.1$). The secondary flow velocity remains negligible for both of these situations (Fig. 3.8d). However, this time the magnitude of the secondary flow velocity depends on the particle deformability along with the fluid elasticity. When the particle deformability is increased, the magnitude of the secondary flow velocity is reduced whereas an increase in the fluid elasticity (Wi) further increases its magnitude. Thus, a nearly spherical particle migrating towards the channel wall induces maximum secondary flow due to the maximum asymmetric area of influence above. This area reduces with the particle deformability and hence a reduction in the induced secondary flow is observed. Similarly, a higher magnitude of viscoelastic stresses due to higher Wi generates a complex flow pattern in the direction normal to the primary flow. This flow pattern becomes more and more asymmetric with increasing Wi and as a result, the secondary flow velocity becomes as high as 3% of the maximum flow velocity in this square channel (Fig. 3.8d).

It can be summarized that an increase in the fluid elasticity (Wi) or inertia (Re) increases the magnitude of the secondary flow velocity as long as the particle moves towards a wall. If the flow conditions are such that the particle moves towards the channel center, an increase in the inertia or elasticity of the fluid makes negligible impact on the velocity of the secondary flow once the particle reaches its steady state position. However, during the transient period while the particle is still migrating towards the center, the inertia and fluid elasticity do make an impact on the velocity of the secondary flow but its magnitude during this transient period remains two orders of magnitude lower than the corresponding cases where the particle migrates towards the wall.

It is important to note that the secondary flow velocity induced by a fluid particle is at least an order of magnitude higher than the velocity induced by the solid particle under the similar flow conditions as reported by Li et al. [2]. The primary reason is the higher drag experienced by the solid particle due to the no-slip condition on its surface. This attribute of fluid particle-induced secondary flow can be exploited in the situations where mixing, heat transfer or other transport phenomena are of importance.

3.4.5 Flow Start-up

It is a well-known aspect that stress waves propagate [122] and cause velocity fluctuations during flow build-up in a channel flow. The elasticity of the fluid affects these fluctuations depending upon the relaxation time of its polymer molecules. In our earlier work [113], these velocity fluctuations were also observed in the rise velocities of freely rising bubbles in a viscoelastic fluid. Similarly, these velocity fluctuations affect the migration velocity of the solid particle as well during the flow build-up ([123]). Goyal et al. [124] have shown that a solid particle settling down during these fluctuations often rebounds after the first oscillation. In the present study, we explore the same effects for a fluid particle in this viscoelastic channel flow.

Figure 3.9a shows the migration velocity of the particle in the wall-normal direction (z) under various flow conditions. The two cases are shown in the inset where the particle is highly deformable ($Ca = 0.1$ and $Ca = 0.2$) and it takes a comparatively longer time to reach a steady state. Figure 3.9b shows the evolution of the average streamwise component of flow velocity in the channel for the same nine situations. In the case of a nearly spherical particle (low Ca) migrating in an Oldroyd-B fluid ($\alpha = 0$), the elastic stresses develop quickly in the flow and take the particle towards the center. As N_1 decreases in the low shear region near the center, the particle reaches its peak velocity at $t^* \approx 4$ and then starts to decelerate while continuing its migration towards the center. The minor fluctuations in the particle velocity are attributed to the extension/relaxation of polymer molecules across its surface as recently explained by Bothe et al. [45] and verified in our earlier work [113]. A minor decline in the flow velocity is observed after an initial peak once the viscoelastic stresses are developed in the flow (Fig. 3.9b). When the particle deformability is increased ($Ca = 0.05$ and $Ca = 0.1$), the particle starts migrating towards the channel center. However, due to a slight increase in its deformability, the peak velocity of the particle migration remains lower than that of the nearly spherical particle. When a spherical particle ($Ca = 0.01$) migrates in the Giesekus

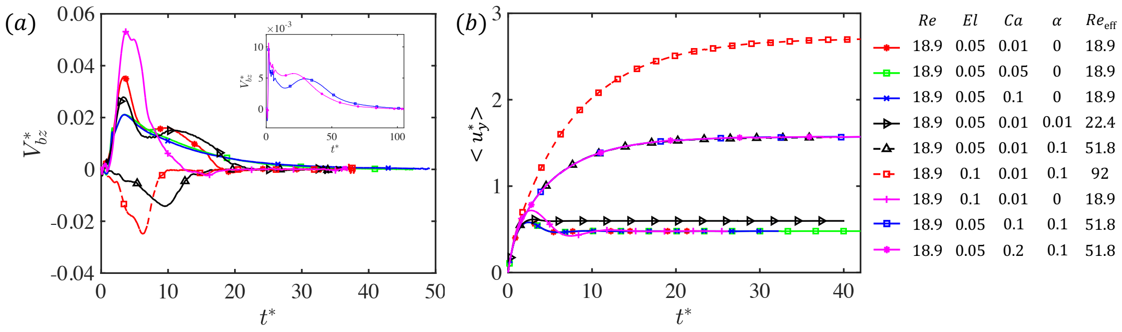

Figure 3.9: (a) Evolution of particle migration velocity in the wall normal (z) direction during flow start-up. (b) Evolution of average steamwise component of flow velocity in the channel.

fluid having a very low shear-thinning ($\alpha = 0.01$), migration towards the channel center occurs primarily due to the elastic effects and similar fluctuations are observed in the migration velocity as in the case of Oldroyd-B fluid. As the shear-thinning promotes the relative importance of fluid inertia which acts to pull the particle back towards the wall, the peak velocity of the particle remains lower than that in the Oldroyd-B fluid. The average flow velocity is slightly increased in the channel due to the shear-thinning effect and the actual effective Reynolds number becomes $Re_{\text{eff}} = 22.4$. When the shear-thinning effect is high enough ($\alpha = 0.1$), the enhanced fluid inertia overcomes the elastic effects and causes the particle to migrate towards the wall, as indicated by the opposite direction of particle velocity in Fig. 3.9a. The flow velocity in the channel increases further and the effective Reynolds number reaches 51.8 with the same value of an applied pressure gradient. When the elasticity number is increased ($El = 0.1$) by increasing the polymer relaxation time in this shear-thinning viscoelastic fluid, the inertial effects still dominate and push the particle towards a wall at a higher rate. With increased viscoelastic stresses at higher El and a strong shear-thinning effect, the effective Reynolds number reaches 92. With the same high elasticity number ($El = 0.1$) but without shear-thinning ($\alpha = 0$), the particle migrates towards the center under the elastic effects. Due to a higher Weissenberg number, the viscoelastic stresses become comparatively stronger and the particle reaches a higher value of its migration velocity. As there is no shear-thinning effect, the flow Reynolds number remains at the baseline value of $Re = 18.9$.

Once the particle is made highly deformable ($Ca = 0.1$ and $Ca = 0.2$) and the fluid is strongly shear-thinning ($\alpha = 0.1$), the 'deformability-induced' lift force overcomes the shear-thinning enhanced inertial effects and the particle moves towards the channel center. As the particle gets closer to the center, its deformability starts reducing due to low shear (as shown in Fig. 3.2b) resulting in a deceleration in its lateral migration velocity. It is worth noting that the effective flow Reynolds number becomes $Re_{\text{eff}} = 51.8$ due to a strong shear-thinning effect in this case.

3.5 Conclusions

Interface-resolved numerical simulations are performed to explore the complex dynamics of cross-stream migration of a fluid particle in a viscoelastic pressure-driven channel flow for a wide range of flow parameters. Unlike the solid particle, the deformability of the fluid particle, the slip condition at the interface, and the particle-induced elastic flow instability at a higher Weissenberg number add further complexity to this phenomenon. The particle deformability (Ca), shear-thinning of the ambient fluid (α), fluid elasticity (Wi), buoyancy (Eo) and concentration of polymers (β) are varied one by one to isolate their sole effects. The conditions for triggering a path instability of a deformable particle in this pressure-driven viscoelastic flow are investigated and the particle-induced secondary flow is quantified.

It is observed that the forces induced by fluid inertia push the particle towards the wall while elasticity and deformability pull it towards the channel center. This interplay between fluid inertia, elasticity, and particle deformability determines the orientation of particle migration in the channel and its final equilibrium position. As shear-thinning increases the relative importance of the fluid inertia, it is found to promote migration towards a wall. At a high Weissenberg number, elastic instability occurs due to the curvature of streamlines across the particle. When the Reynolds number is increased while keeping the Weissenberg number fixed at a low value, the particle path remains stable even for the Reynolds number as high as $Re = 1000$.

In the case of a high polymer concentration (e.g., $\beta = 0.1$), it is found that strong viscoelastic effects make the particle path unstable even when the particle is nearly spherical. This path instability occurs as the flow itself becomes elastically unstable at a higher value of Wi. In the absence of strong viscoelastic stresses (low Wi), the path of the particle becomes unstable when its deformation becomes high due to high Eo. However, the shear-thinning acts as a stabilizing factor and can make the particle path stable even for the particle deformation as large as $\chi = 2$. The stabilizing role of shear-thinning is reversed at higher values of β. When the Reynolds number is small and $\beta = 0.9$, the particle path remains stable even for the Eötvös number as large as $Eo = 8$ and its deformation exceeds $\chi > 2.3$. Thus, the path instability of a deformable particle in a viscoelastic pressure-driven channel flow can occur when the flow itself becomes elastically unstable at high Wi or when its deformation exceeds a threshold value under buoyant conditions. If the path instability is triggered by the later mechanism, i.e., when the particle deformation exceeds a critical value, the shear-thinning suppresses the path instability at higher polymer concentration (lower β) while it reverses its role and promotes the path instability at lower polymer concentration (higher β).

It is shown that the secondary flow velocity induced by a fluid particle migrating towards the wall is an order of magnitude higher than the one induced by a solid particle under similar flow conditions. This behavior is attributed to the slip condition on the particle surface and the internal flow. For all the situations where the fluid particle migrates towards the center, the secondary flow velocity becomes negligible due to the symmetric flow pattern above and below the particle when viewed in its migrating plane.

During the flow build-up in this square-shaped channel, the maximum value of flow velocity depends upon the shear-thinning property of the fluid. The particle migration velocity is dictated by the inertial effects and the rate at which the viscoelastic stresses are built up in the flow.

Chapter 4

BUBBLE-INDUCED TRANSITION TO ELASTO-INERTIAL TURBULENCE[3]

4.1 Introduction

Adding a minute amount of long-chain flexible polymers can drastically change mechanical properties of an otherwise Newtonian fluid and makes it viscoelastic. Stretching of polymer molecules causes elastic stresses and gives a memory to the fluid flow, resulting in a range of exotic and often counter-intuitive behaviours such as rod climbing, elastic recoil and drag reduction in turbulent flows [5]. The exact mechanism behind many of the exotic phenomena exhibited by the viscoelastic fluids are yet to be fully explored. A striking example of such phenomena is sustaining a chaotic, turbulent like fluid motion observed at a low Reynolds number [125, 126, 5, 127]. In case of a classical Newtonian turbulent flow, the flow instabilities arise from the non-linear convective terms of the Navier-Stokes equations and therefore, a very high Reynolds number is always required to sustain a turbulent flow field. In case of a viscoelastic fluid flow, however, the non-linear coupling between viscous and viscoelastic stresses are capable of sustaining the required instabilities in the flow even in the absence of inertia [5]. This turbulent flow state at a Reynolds number below the threshold value of inertial turbulence (IT) is often referred as the "elasto-inertial turbulence" (EIT). When the Reynolds number is further reduced to a negligibly smaller value, it turns out that high enough viscoelastic stresses are still capable of sustaining a chaotic turbulent-like state, referred as the elastic turbulence (ET), which is purely dominated by the elastic effects [126]. The present

[3]SUBMITTED AS A PAPER UNDER THE SAME TITLE IN JOURNAL OF FLUID MECHANICS

study mainly focuses on the elasto-inertial instability and transition to the elasto-inertial turbulence where, as the name implies, the chaotic flow state is caused and sustained by both elastic and inertial effects.

In the inertialess limit, only nonlinearity arises from the elastic stress that becomes anisotropic in a shear flow and results in the hoop stress acting on the fluid in the direction of the streamline curvature. This hoop stress provides the driving force for the elastic instability and triggers a transition to the elastic turbulent (ET) state even in the absence of inertia [126]. Since the discovery of ET in inertialess flows with curved streamlines by Groisman and Steinberg [125], a non-linear instability leading to a similar kind of chaotic state in planar shear flows was suspected and investigated by Morozov et al. [128, 129]. These studies suggested that a non-linear instability can also be triggered in a planar shear flow when a sufficient flow curvature is induced via external perturbations. To realize this, the initial perturbations have been usually induced in the form of blowing/suction at the wall or by placing an obstacle in the channel to trigger the instability and attain an EIT state [130].

There are different pathways which can be followed to achieve the EIT state in a wall bounded flow. Samanta et al. [131] have demonstrated that the transition threshold to inertial turbulence can be controlled by varying the polymer concentration. They computed the puff lifetimes to examine the effects of viscoelasticity on transition and differentiate the EIT states from the Newtonian turbulence in a pipe flow. They found that polymer additives delay the subcritical transition to IT conforming to their drag reducing effects in turbulent channel flows. They also demonstrated that, as the shear rate is increased, a separate instability occurs at a much lower Reynolds number than the inertial turbulence and triggers a very different type of disordered motion of elasto-inertial turbulence. Rota et al. [132] showed that a reverse pathway can also be followed to achieve the EIT state. That is, polymer molecules are added into an already turbulent Newtonian flow and then the Reynolds number is reduced gradually. Unlike the Newtonian flow, which would immediately re-laminarize below a certain threshold value of Re, the viscoelastic flow is capable of maintaining its turbulent state even at a Reynolds number as low as $Re = 0.5$ in a rectilinear channel. Moreover, at a low Reynolds number, if some external perturbations are superimposed on a laminar viscoelastic flow field, these instabilities can grow and achieve the EIT state under a certain parametric setting [133, 134].

The dynamic features of EIT differ greatly from the inertial turbulence, which is the focus of many contemporary investigations. Sid et al. [135] have demonstrated that the essential dynamic structures of EIT exist even in a two-dimensional (2D) flow. More recently, Dubief et al. [136] have identified four distinct regimes of the stress field in a 2D channel flow by using the FENE-P viscoelastic model. These regimes were named as chaotic, chaotic arrowhead, intermittent arrowhead and stable arrowhead regimes based on constant contours of first normal stress difference (N_1) and pressure field. A sharp pressure gradient was observed within the flow field, similar to the one across a shock wave, promoting the shape of an arrowhead. In this 2D flow field, it was reported that an increase in the polymer concentration promoted stability while an increase in the domain length promoted chaos, indicating the role of large scales in the dynamics of EIT. The drag was found to be increasing in all these EIT regimes when compared to the corresponding laminar states. In a 3D periodic channel flow, Dubief et al. [137] observed an alternating train of positive and negative Q-iso-surfaces (second invariant of velocity gradient tensor) near the channel wall during transition to the EIT state. Interestingly, these patterns sustained on a smaller scale unlike the inertial turbulence even when the viscoelastic flow got fully developed. These patterns were interpreted as the regions of local rotation ($Q > 0$) and dissipation of turbulent kinetic energy ($Q < 0$), and were found to change their alignment from streamwise to spanwise direction during low-drag events. Another striking difference between IT and EIT is the reversed energy cascade. Unlike the inertial turbulence where the energy transfer occurs from large to small scales, energy transfer of turbulent elastic energy to turbulent kinetic energy is observed to be from smaller to larger scales in EIT [138].

Despite an ever increasing interest in this area in recent years, many fundamental aspects related to EIT are still elusive. In the present study, we focus on two such aspects. First, instead of providing any external perturbations to the flow, direct numerical simulations of concentrated viscoleastic flows are performed in a square-shaped channel by gradually increasing the fluid elasticity while keeping the Reynolds number fixed at a low value for which the corresponding Newtonian flow is fully laminar to examine the conditions for attaining the EIT state. Secondly, a novel mechanism of injecting bubbles into a laminar viscoelastic flow is investigated to ascertain whether the presence of bubbles can trigger a transition to a EIT state in this straight channel. For this purpose, extensive interface-resolved direct numerical simulations are performed using a finite-difference/front-tracking method. The log-conformation method is employed to handle the stiff constitutive equations of the viscoelastic model (Giesekus) at high Weissenberg numbers.

The numerical method and the computational setup used in this paper are described in §4.2 & §4.3, respectively. The results are presented and discussed for a single-phase and then for the multiphase flow in §4.4, followed by the conclusions in §4.5.

4.2 Governing Equations and Numerical Method

The flow equations and the Giesekus model are presented within the framework of the finite-difference/front-tracking (FT) method. The front-tracking method used in the present study was originally developed by Unverdi and Tryggvason [139]. Izbassarov and Muradoglu [108] added a capability to this FT method to simulate viscoelastic two-phase systems in which one or both phases could be viscoelastic. This robust and high fidelity method has been extensively used in our several previous works involving laminar (e.g., [140], [60], [113], [141]) as well as turbulent multiphase flows (e.g., [103], [107]). Referring to the coordinate system shown in Fig. 4.1 and employing the one-field formulation, the Navier-Stokes equations are written as

$$\rho\frac{\partial \mathbf{u}}{\partial t} + \rho\boldsymbol{\nabla}\cdot(\mathbf{u}\mathbf{u}) = -\boldsymbol{\nabla}p - \frac{dp_o}{dy}\mathbf{j} + \boldsymbol{\nabla}\cdot\boldsymbol{\tau} + \boldsymbol{\nabla}\cdot\mu_s(\boldsymbol{\nabla}\mathbf{u} + \boldsymbol{\nabla}\mathbf{u}^T) + \int_A \sigma\kappa\mathbf{n}\delta(\mathbf{x}-\mathbf{x}_f)dA, \tag{4.1}$$

where $\mathbf{u}$, $\boldsymbol{\tau}$, p, ρ and μ_s are the velocity vector, the polymer stress tensor, the pressure, and the discontinuous density and solvent viscosity fields, respectively. A pressure gradient $-\frac{dp_o}{dy}\mathbf{j}$ is applied to drive the flow and it is adjusted dynamically to keep the flow rate constant, where $\mathbf{j}$ is the unit vector in the y-direction. The effect of surface tension is added as a body force term on the right-hand side of the momentum equation where σ is the surface tension coefficient, κ is twice the mean curvature and $\mathbf{n}$ is a unit vector normal to the interface. As the surface tension acts only on the interface, δ represents a three-dimensional Dirac delta function with the arguments $\mathbf{x}$ and $\mathbf{x}_f$ being a point at which the equation is evaluated and a point at the interface, respectively. The momentum equation is supplemented by the incompressibility condition

$$\boldsymbol{\nabla}\cdot\mathbf{u} = 0. \tag{4.2}$$

The viscoelasticity of the bulk liquid is modelled using the Giesekus model [26]. Since this model accounts for the polymer–polymer interactions, it is a suitable choice to simulate concentrated polymer solutions [142]. In the Giesekus model, the polymer stress tensor $\boldsymbol{\tau}$ evolves by

$$\boldsymbol{\tau} = \frac{\mu_p}{\lambda}(\boldsymbol{B} - \boldsymbol{I}), \tag{4.3}$$

where μ_p is the polymer viscosity, λ is the polymer relaxation time, $\boldsymbol{B}$ is the conformation tensor and $\boldsymbol{I}$ is the identity tensor. The conformation tensor evolves by

$$\frac{\partial \boldsymbol{B}}{\partial t} + \mathbf{u}\cdot\boldsymbol{\nabla}\boldsymbol{B} - \boldsymbol{\nabla}\mathbf{u}^T\cdot\boldsymbol{B} - \boldsymbol{B}\cdot\boldsymbol{\nabla}\mathbf{u} = \frac{1}{\lambda}[(1-\alpha)\boldsymbol{I} + (2\alpha-1)\boldsymbol{B} - \alpha\boldsymbol{B}^{\mathbf{2}}], \tag{4.4}$$

where α is the mobility factor representing the anisotropy of the hydrodynamic drag exerted on the polymer molecules. Due to the thermodynamic considerations, α is restricted to $0 \leq \alpha \leq 0.5$ [109]. When $\alpha = 0$, the Giesekus model reduces to the Oldroyd-B model.

At high Weissenberg numbers, these highly non-linear viscoelastic constitutive equations become extremely stiff, which makes their numerical solution a challenging task. Artificial diffusion terms may be added to the discretize viscoelastic model equations to alleviate this problem. However, it has been found that, when the model equations are discretized using the conventional numerical schemes, this artificial diffusion method may alter the mathematical nature of the constitutive equations from hyperbolic to parabolic, affecting the integrity of the simulated EIT physics, especially at high Weissenberg numbers [130]. The log-conformation method offers an alternative solution to this problem and it is used in the present study. In this approach, an eigen decomposition is employed to re-write the constitutive equation of the conformation tensor [108, 143]. It is found that, although it is computationally more expensive than the artificial diffusion method, the log-conformation retains the hyperbolic nature and thus removes the stiffness of the viscoelastic model equations, allowing robust and accurate numerical solutions by preserving large-scale features in the simulations of elastic turbulence as shown recently by Yerasi et al. [144]. The interested readers are referred to [56] for the detailed procedure.

The flow equations (Eqs. (4.1) and (4.2)) are solved fully coupled with the Giesekus model equation (Eq. (2.4)). A QUICK scheme is used to discretize the convective terms in the momentum equations while second-order central differences are used for the diffusive terms. For the convective terms in the viscoelastic equations, a 5^{th}-order WENO-Z [110] scheme is used. An FFT-based solver is employed to solve the pressure Poisson equation. Since the pressure equation is not separable due to variable density in the present multiphase flow, the FFT-based solvers cannot be used directly. To overcome this challenge, a pressure-splitting technique presented by Dong et al. [111, 59] is employed. A predictor-corrector scheme is used to achieve second-order time accuracy as described by Tryggvason [104]. The details of the front-tracking method can be found in the book by Tryggvason [106] and in the review paper by Tryggvason et al. [104], and the treatment of the viscoelastic

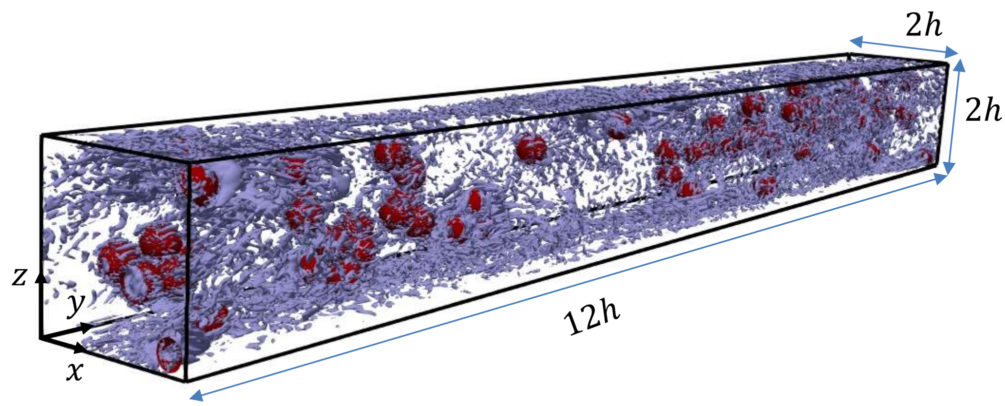

Figure 4.1: The computational domain and the coordinate system considered in the present study. The constant contours of Q-criterion are shown around the bubbles (red colour) at a value of $Q = 25$ ($Re = 1000, Wi = 10, Ca = 0.01, \beta = 0.1$).

model equations in the paper by Izbassarov and Muradoglu [108, 143]. The present numerical scheme is second order accurate both in space and time.

4.3 Computational setup

Figure 4.1 shows the computational domain which is a square channel with the dimensions of $2h$, $12h$ and $2h$ in the x, y and z directions respectively, where h is half of the channel width. Periodic boundary conditions are applied in the streamwise (y) direction whereas the other two directions (x and z) have no-slip/no-penetration boundary conditions. The length of the channel is set to $12h$ so that a sufficient length is available for the bubbles to exhibit their effects in this viscoelastic flow field.

The flow conditions are characterized by the following non-dimensional numbers defined as

$$Re = \frac{\rho_o u_o h}{\mu_o}, \; Wi = \frac{\lambda u_o}{h}, \; Ca = \frac{\mu_o u_o}{\sigma}, \; \beta = \frac{\mu_s}{\mu_o}, \tag{4.5}$$

where Re, Wi and Ca are the Reynolds, Weissenberg and capillary numbers, respectively. Further, β is the ratio of the solvent viscosity (μ_s) to the zero shear viscosity

(μ_o) of the viscoelastic fluid. In Eq. (4.5), ρ_o is the density of the of bulk fluid and u_o is the average velocity in the channel. The value of β is fixed at 0.1, representing a highly concentrated polymer solution, for all the results presented in this paper.

The present study covers the Reynolds and the Weissenberg numbers spanning in the ranges of $10 \leq Re \leq 1000$ and $1 \leq Wi \leq 1000$. Note that the highest value of $Re = 1000$ is still less than the minimum value required to sustain inertial turbulence in a channel flow [145]. For these low values of Re, the grid resolution near the wall cannot be determined by the classical wall criterion of $x^+ < 1$ and $z^+ < 1$. As the bubbles are also injected into the flow, despite a low Re, a sufficiently fine grid is required to resolve the bubble interfaces and to capture the essential flow features of this chaotic viscoelastic flow regime. Therefore, a grid size of $320 \times 960 \times 320$ is used in the x, y and z directions even for $Re = 10$ case. For a reference, this grid resolution is sufficient to achieve $x^+ < 0.6$ and $z^+ < 0.6$ in an inertial turbulent channel flow at $Re = 5600$ ($Re_\tau = 180$). For the multiphase cases, there are 64 grid cells per equivalent bubble diameter with this selected grid size.

The flow is driven by applying dp_0/dy in the negative y-direction. This external pressure gradient is varied dynamically at each time step to keep the flow rate (and thus the bulk Reynolds number) constant in the channel. To normalize various quantities reported in this study, h is used as the length scale, u_o as the velocity scale and h/u_o as the time scale. The normalized quantities are denoted by the superscript *. The stresses are normalized by $\rho_o v_\tau^2$, where $v_\tau = \sqrt{\bar{\tau}_w/\rho_o}$ with $\bar{\tau}_w$ being the average total wall shear stress. Once the flow reaches a statistically steady state, the combined force due to the shear stresses at the four walls of the channel is balanced by the force due to the applied pressure gradient dp_0/dy. In this multiphase flow, the density and viscosity of the bubble are denoted by ρ_i and μ_i, respectively. The density and the viscosity ratios are set to $\rho_o/\rho_i = 10$ and $\mu_o/\mu_i = 80$, respectively. These comparatively smaller ratios are used to enhance numerical stability and thus relaxing the time step restrictions due to the numerical stability. Apparently, this low density ratio may seem unrealistic when compared to a liquid-air system. However, a higher density ratio does not affect the bubble dynamics as has been reported by Bunner and Tryggvason [146] for a Newtonian flow. Simulations are also performed to check the effects of the density and viscosity ratios on the viscoelastic multiphase flows considered in this study. As documented in the Appendix, the results are not very sensitive to a further increase in the density and viscosity ratios beyond $\rho_o/\rho_i = 10$ and $\mu_o/\mu_i = 80$.

4.4 Results and discussion

Simulations are first performed for a single-phase flow by gradually increasing the Reynolds number from $Re = 10$ to $Re = 1000$. Subsequently, the flow is made viscoelastic by gradually increasing the Weissenberg number in the range of $1 \leq Wi \leq 1000$ at a fixed Reynolds number to ascertain whether the flow attains an EIT state without introducing any explicit external perturbations. To facilitate the development of second normal stress difference (N_2), a square-channel (duct) is used and a small shear thinning effect is also incorporated by setting $\alpha = 0.001$ for the Giesekus model. A concentrated polymer solution ($\beta = 0.1$) is selected to follow the pathway identified by Samanta et al. [131] for the earlier possible transition to the EIT regime. After identifying the range of Wi for which the single-phase flow remains essentially laminar, bubbles are subsequently injected into fully developed viscoelastic laminar flows at $Wi = 1, 5$ and 10 while keeping Re constant to ascertain whether the presence of bubbles can trigger a flow instability. The bubble volume fraction is kept constant at 3% for all the cases. The value of capillary number is fixed at a low value of $Ca = 0.01$ to maintain approximately spherical bubble shapes. The resultant single-phase and multiphase flows are presented and discussed in the following sections.

4.4.1 EIT in a single-phase flow

Figure 4.2 summarizes the flow states in the Re-Wi space. At a low value of $Re = 10$, the single-phase flow remains fully laminar for up to $Wi = 1000$. Two points are selected in the computational domain to collect all the components of velocity and viscoelastic stresses at each time step to monitor their evolution to ascertain the

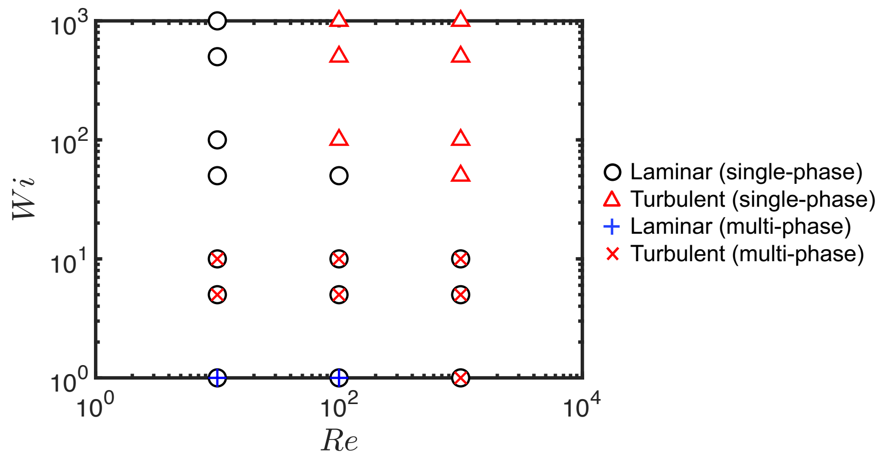

Figure 4.2: Various flow states in the Re-Wi space. $(Ca = 0.01, \beta = 0.1)$

attainment of a statistically steady-state solution. One of the 'numerical probes' is located at the centre of the channel (x^*=1, y^*=6, z^*=1) while the other one at 25% distance (x^*=0.5, y^*=6, z^*=1) from one of the walls. Once the flow reaches a statistically steady state, the simulations are continued at least for another 3λ time units, during which full flow fields are stored for further statistical analysis.

The simulations are then repeated for $Re = 100$. While gradually increasing Wi, it is observed that the flow remains laminar till $Wi = 100$. However, for $Wi \geq 100$, instabilities start to appear in this low Re flow. These instabilities start to grow with time, and fluctuations are observed ultimately in all three components of velocity akin to a typical turbulent signal. Viscoelastic stresses also start to fluctuate in the time domain, as collected by the numerical probes at two different locations of the channel. It is important to emphasize that no explicit perturbations are provided from outside the system to initialize any instabilities in the flow. Only for $Wi \geq 100$, the viscoelastic stresses are high enough to trigger the instability that ultimately leads to a chaotic flow regime. As the flow rate is kept constant for a fixed Re, a sudden increase in the applied pressure gradient is also observed once the flow is transitioned from laminar to this chaotic state, indicating a rapid increase in the drag. The characteristics of this chaotic flow regime for $Wi \geq 100$ will be discussed in detail in the subsequent paragraphs.

When Re is increased further to 1000, the transition to a chaotic flow regime starts to appear at a lower value of $Wi \geq 50$. This Re is still smaller than the minimum $Re \approx 1100$ required for sustaining the inertial turbulence in a channel flow [145]. As Wi is increased further, the turbulent intensity of this chaotic regime increases with a change in statistical quantities as well.

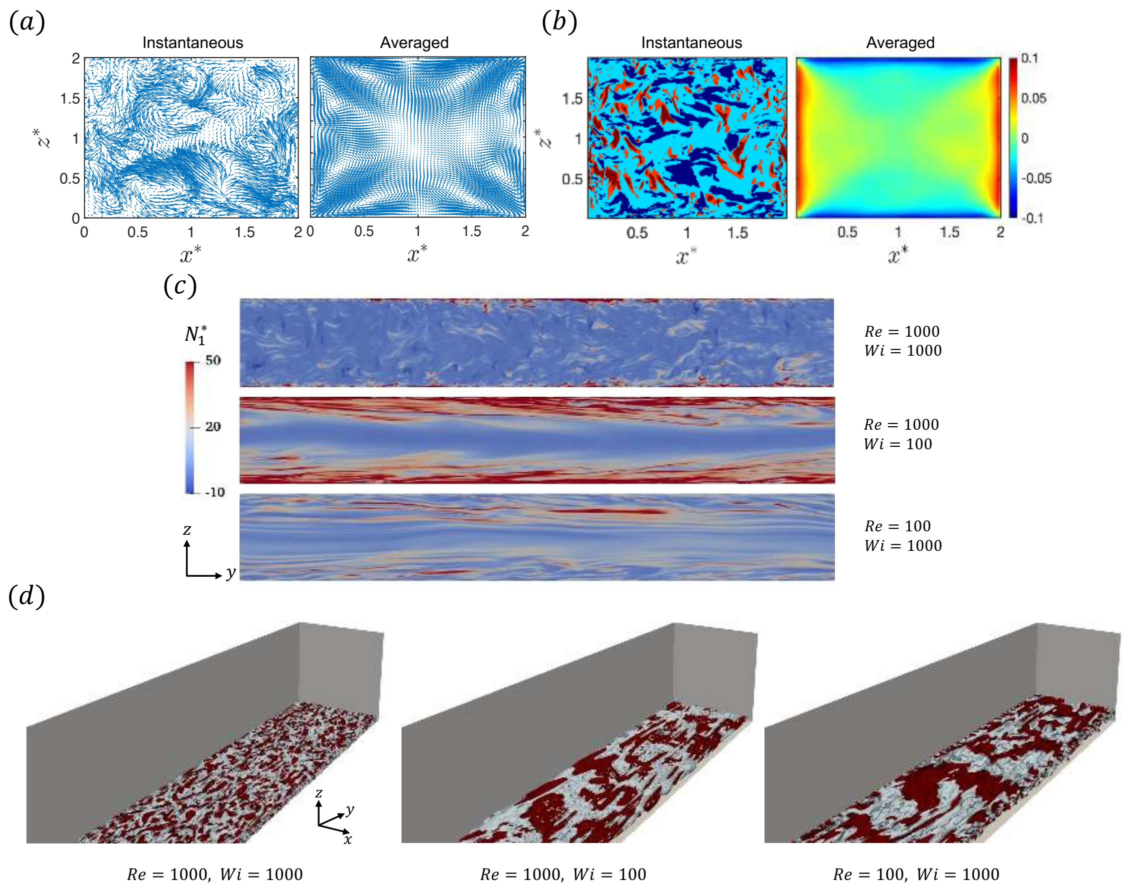

Figure 4.3: *(a)* Instantaneous (*left*) and averaged (*right*) snapshots of velocity vectors showing the secondary flow field at $Re = 1000$ and $Wi = 1000$ *(b)* Instantaneous (*left*) and time-averaged (*right*) snapshots of second normal stress difference (N_2) at $Re = 1000$ and $Wi = 1000$ *(c)*. Contours of first normal stress difference (N_1) are shown in a statistically steady EIT regime for different values of Re and Wi. *(d)* Iso-surfaces of Q-criterion are shown close to the bottom wall of the channel in a statistically steady EIT regime for different values of Re and Wi. The red and gray colours represent the positive and the negative values, respectively. The contours are plotted at ± 5, ± 0.05 and ± 0.005 for $(Re, Wi) = (1000, 1000)$, $(1000, 100)$ and $(100, 1000)$ cases, respectively.

Figure 4.3a shows the velocity vectors in a vertical cutting xz-plane of the viscoelastic duct flow once it reaches a statistically steady state at $Re = 1000$ and $Wi = 1000$ case. The instantaneous and averaged flow fields are plotted in left and right panels of Fig. 4.3a, respectively. As seen, the instantaneous flow field exhibits a chaotic flow regime while the time-averaged velocity field shows a typical secondary flow pattern with eight vortices as also observed in the viscoelastic laminar duct flow with the shear-thinning effect [2, 141]. This secondary flow field is developed in the duct flow primarily due to the presence of a second normal stress difference $N_2 = \bar{\tau}_{zz} - \bar{\tau}_{xx}$. The instantaneous and time-averaged contour plots of N_2 are shown in the left and right panels of Fig. 4.3b, respectively. The instantaneous plot confirms the chaotic flow pattern while the time-averaged one resembles the typical distribution of N_2 in a laminar duct flow. As the EIT regime is associated with long-elongated sheets of the first normal difference (N_1), the distribution of N_1 is also shown in Fig. 4.3c in the yz-plane at the centre of the duct for the various combinations of Re and Wi for which the single-phase flow becomes chaotic. Dubief et al. [130] categorized different EIT regimes based on the structures of N_1 for a 2D channel flow. For a low value of $Re = 100$, a similar 'chaotic regime' is observed in the present 3D duct flow as shown in Fig. 4.3c. At a higher value of $Re = 1000$ but with a moderate value of $Wi = 100$, this regime is shifted to 'chaotic arrowhead' and once the Weissenberg number is increased to a very high value of $Wi = 1000$, the long-elongated sheets of N_1 break down completely and the flow starts to resemble a typical inertial turbulence. The iso-surfaces of the second invariant of velocity gradient tensor (Q-criterion) is depicted in Fig. 4.3d to show the corresponding change in the near-wall vortices for the same combinations of Re and Wi. At a very high values of Re and Wi, the positive and negative contours of the Q-criterion show a chaotic pattern near the wall. With decreasing Re or Wi, the spanwise elongated pattern of positive and negative contours of the Q-criterion starts to appear indicating that the signatures of elastic turbulence become more and more apparent in the EIT regime once the elastic effects dominate over the inertial effects. In the absence of any perturbations from outside the system, the flow is laminar at a lower value of Wi in the present scenario, as shown in Fig. 4.2. Therefore, a clear pattern of alternating contours of Q-criterion is not visible here as observed by Dubief et al. [130].

Figure 4.4 shows various quantities used to evaluate turbulent characteristics of this single-phase chaotic flow regime for various combinations of Re and Wi. The first one is the 1D energy spectrum (Fig. 4.4a). The energy axis is normalized by $\frac{1}{2}\rho_o u_o^2$ and the frequency axis by u_o/h. At the higher values of $(Re, Wi) = (1000, 1000)$, the kinetic energy spectrum shows a typical $-5/3$ scaling at the large scales but it shifts to -4 at the smaller scales (dissipation range). These values are consistent with the results obtained in a single-phase channel flow at lower values of Re by Rota [132] and Mukherjee et al. [147]. The elasticity number, $El = Wi/Re$ provides a measure of the relative strength of elastic to inertial effects. At $(Re, Wi) = (1000, 1000)$, $El = 1$, indicating a balanced elasto-inertial regime. The transition to a -4 slope at smaller scales indicates that viscoelastic effects become significant as the length scale decreases. The steep slope suggests strong suppression of small-scale fluctuations due to elastic stresses in this highly concentrated polymer solution ($\beta = 0.1$). At large scales, the flow behaves like classical turbulence, driven by inertial forces, as seen in Fig. 4.3c. At smaller scales, high Wi and low β cause elastic stresses to dominate, altering the cascade. This dual scaling suggests a crossover frequency where the flow transitions from inertia-dominated to elasticity-dominated dynamics. The exact frequency depends on the balance between Re, Wi and the polymer properties. Once Wi is decreased to $Wi = 100$ while keeping $Re = 1000$, the scaling of energy spectrum shifts from -4 to -3 across the majority portion of the spectrum (Fig. 4.4a). It indicates that lowering Wi reduces the elastic effects, allowing inertial forces to distribute energy more effectively to smaller scales, thus resulting in a less steep spectrum. The -3 slope also suggests a transitional EIT regime where the inertial and the elastic effects are not so balanced ($El = 0.1$), with less suppression of small-scale fluctuations compared to the -4 slope at $Wi = 1000$. This is characterized by 'chaotic arrowhead' regime in Fig. 4.3c. Once Re is reduced to 100 while keeping $Wi = 1000$, the energy spectrum again yields a slope of -3. Here, low Re weakens the inertial effects, increasing the relative importance of viscous and elastic forces ($El = 10$). The -3 slope suggests a regime closer to elastic turbulence (ET) where elastic instabilities drive the flow, modulated by viscous dissipation. The similarity in the -3 slope between $(Re, Wi) = (1000, 100)$ and $(Re, Wi) = (100, 1000)$ indicates that different combinations of inertial and elastic effects can produce similar spectral characteristics. It can be inferred from these scales that once the turbulent flow is entirely governed by inertia (classical inertial turbulence), the energy spectrum assumes a slope of $-5/3$ whereas once the turbulent regime is dominated by the elastic effects with negligible inertia, as in ET, the spectrum exhibits a slope of -4. Any combination of Re and Wi in between these two regimes assumes a slope in between these two limits.

The total mean shear stress in the mid-plane comprises three components: the viscous shear due to mean flow $\bar{\tau}_N$, the Reynolds stress due to velocity fluctuations $\bar{\tau}_R$ and a polymeric stress $\bar{\tau}_P$. Once the flow reaches a statistically steady state, the applied pressure gradient must balance the total shear stress at the four walls of the channel. The three components of shear stress ($\bar{\tau}_N = \mu_o \frac{\partial \bar{v}}{\partial z}$, $\bar{\tau}_R = -\rho_o \overline{v'w'}$, $\bar{\tau}_P = \bar{\tau}_{yz}$) are plotted for the central plane of the duct ($x^* = 1$) for two values of $Wi = 1000$ and $Wi = 100$ at $Re = 1000$ (Figs. 4.4*b*). The fluctuating and the time-averaged quantities are denoted by prime $(.')$ and overbar $(\bar{.})$, respectively. Note that the averaging is performed both in time and in streamwise direction since the flow is expected to be homogeneous in the streamwise direction once a statistically steady state is reached. The stress components are normalized by the local shear stress at the wall of the respective plane. For the high value of $Wi = 1000$, it is observed that the stress balance in the mid-plane of the channel resembles that of a classical inertial turbulence. The viscous stress is maximum at the wall and decays to zero at the channel center whereas the Reynolds stress is zero at the wall, gradually increases to its peak value, and then goes to zero at the channel center. The viscoelastic stress also follows the viscous stress profile and becomes maximum at the wall and zero at the channel center. As a result, the total shear stress decays linearly from the wall towards the channel center (Fig. 4.4*b*). Once

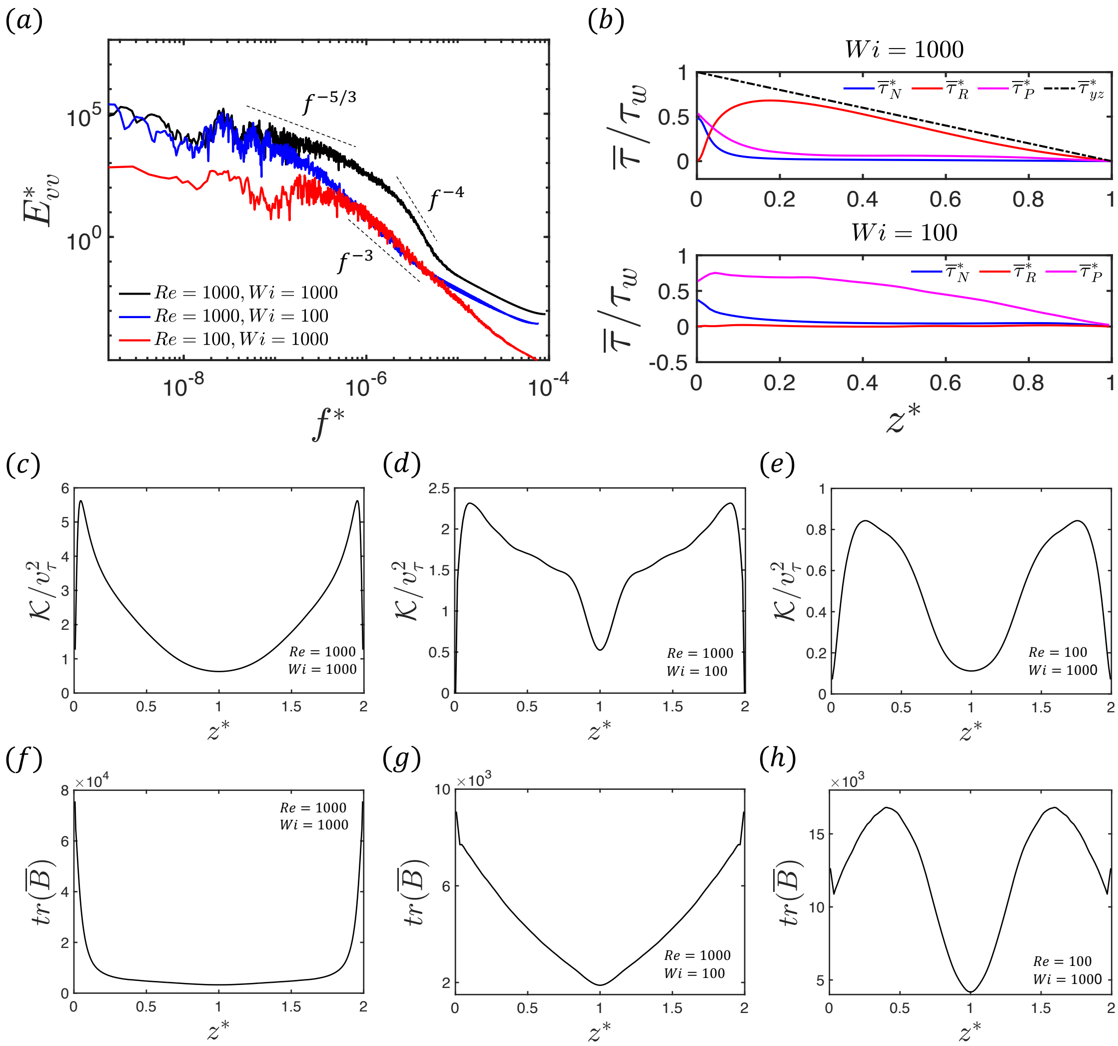

Figure 4.4: *(a)* The 1D energy spectrum for $(Re, Wi) = (1000, 1000)$, $(1000, 100)$ and $(100, 1000)$ cases. *(b)* The distribution of the components of the average shear stress from the channel wall towards the centre in the mid-plane for $(Re, Wi) = (1000, 1000)$ (top panel) & $(Re, Wi) = (1000, 100)$ (bottom panel). *(c, d, e)* The distribution of turbulent kinetic energy in the mid-plane of the channel for different values of Re and Wi. *(f, g, h)* The average elongation of polymer molecules represented by $tr(\bar{B})$ is shown in the same mid-plane.

Wi is reduced to 100 while keeping $Re = 1000$, the magnitude of Reynolds stress becomes negligibly small compared to viscous and polymeric stresses. Although the -3 scaling of the energy spectrum and the turbulent signal are indicative of a turbulent flow field at this comparatively lower value of $Wi = 100$, the Reynolds stress becomes negligibly small compared to the overall shear stress in the mid-plane. These not-so-smooth profiles of different shear stress components indicate a clear departure of the turbulent flow field from the inertial one. The distribution of the turbulent kinetic energy (TKE) $\mathcal{K} = 0.5(\overline{u'^2} + \overline{v'^2} + \overline{w'^2})$ is shown in Figs. 4.4c, d & e at the mid-plane where TKE is found to be maximum near the walls and decays to a minimum value at the centre. Interestingly, the average elongation of polymer molecules quantified by the trace of the conformation tensor $tr(\bar{B})$ shows a similar trend for different values of Wi as shown in Figs. 4.4f, g & h. It is worth mentioning that the value of the applied pressure gradient decreases as Wi increases for a constant value of Re, indicating a decrease in the drag force. As the chaotic flow is driven by elasticity, this unexpected drag reduction with an increase in Wi is attributed to the shear-thinning effect that dominates the drag increase caused by the pronounced chaotic flow.

Garg et al. [133] have shown that for the large Weissenberg numbers, the viscoelastic pipe flow can be linearly unstable to axisymmetric disturbances down to a critical Reynolds number of $Re_{cr} \approx 63$. Buza [148] and Wan et al. [149] later demonstrated that the polymer concentration (β) is the main controlling factor. At a higher polymer concentration, the unstable region shrinks and the transition is mostly supercritical. A similar mechanism seems to be at play in the present single-phase duct flow, where transition occurs even in the absence of any finite perturbation at a high Weissenberg number. The subcritical transition does not occur in a single-phase flow due to the stabilizing role of high polymer concentration ($\beta = 0.1$), as seen for the lower Weissenberg number cases for all the three Reynolds numbers.

Rota et al. [132] have demonstrated that a single-phase viscoelastic flow can sustain a chaotic flow state in a straight channel at a Reynolds number as low as $Re = 0.5$ ($Wi = 50$) if started from a turbulent initial condition for a dilute polymer solution by using the FENE-P model with $\beta = 0.9$. The value of $Wi = 50$ was kept constant in their simulations while bringing down the Reynolds number from $Re = 2800$ to $Re = 0.5$ to keep the polymers in their stretched state. To observe whether the chaotic state is sustained in the present scenario of a duct flow with a concentrated polymer solution, extensive simulations are next performed by keeping the Reynolds number constant at $Re = 1000$ and the Weissenberg number is reduced from $Wi = 1000$ to $[500, 100, 50, 40, 10]$. Each of the lower Wi is started by using the initial conditions of the previous higher Wi case. It is found that the chaotic flow state is sustained till $Wi = 40$. When Wi is further reduced to 10, the single-phase flow is laminarized. Next, the same simulations are repeated by fixing the Reynolds number at $Re = 100$. The Weissenberg number is reduced gradually from $Wi = 1000$ till 10 and it is observed that the chaotic flow is sustained till $Wi \geq 40$. The same limit of $Wi \geq 40$ is observed for $Re = 10$ cases to sustain a chaotic regime in this duct flow if perturbed initially. It can be concluded that if the flow is perturbed initially, the chaotic flow is sustained in this single-phase viscoelastic duct flow only if the value of $Wi \geq 40$. Below this value, the single-phase flow is laminarized. This value is close to $Wi = 50$ used by Rota et al. [132] in their channel flow simulations.

It is important to highlight that exceptionally high Weissenberg numbers required to trigger flow instability in the absence of any discrete external perturbations in this rectilinear channel may seem impractical. However, it should be noted that Wi is defined based on the average flow velocity in the channel. As shear rate decreases significantly towards the channel centre in this duct flow, the effective local Weissenberg number is actually much lower than the nominal value of Wi, which is based on the average flow velocity.

Turbulent kinetic energy

The turbulent kinetic energy ($\mathcal{K} = \frac{1}{2}\overline{u_i' u_i'}$) in a viscoelastic flow evolves by

$$
\begin{aligned}
\frac{\partial \mathcal{K}}{\partial t} \quad &= \overbrace{-\bar{u}_j \frac{\partial \mathcal{K}}{\partial x_j}}^{\mathcal{A}} - \overbrace{\frac{1}{2}\frac{\partial(\overline{u_i' u_i' u_j'})}{\partial x_j}}^{\mathcal{Q}} - \overbrace{\frac{1}{\rho_o}\overline{u_i' \frac{\partial p'}{\partial x_i}}}^{\mathcal{R}} - \overbrace{\left(\overline{u_i' u_j'}\frac{\partial \bar{u}_i}{\partial x_j}\right)}^{\mathcal{P}} + \overbrace{\frac{1}{2}\frac{\partial}{\partial x_j}(\nu_s \frac{\partial \overline{u_i' u_i'}}{\partial x_j})}^{\mathcal{D}} \\
&\quad \underbrace{- \nu_s \overline{\frac{\partial u_i'}{\partial x_j}\frac{\partial u_i'}{\partial x_j}}}_{\epsilon} + \underbrace{\frac{1}{\rho_o}\left(\overline{u_i' \frac{\partial \tau_{ij}'}{\partial x_j}}\right)}_{\mathcal{W}_p} + \underbrace{\overline{u_i' f_i'}}_{\mathcal{B}},
\end{aligned} \tag{4.6}
$$

where $\mathcal{A}$, $\mathcal{Q}$, $\mathcal{R}$, $\mathcal{P}$, $\mathcal{D}$, ϵ, $\mathcal{W}_p$ and $\mathcal{B}$ represent advection by mean flow, transport by velocity fluctuations, transport by pressure, production by mean flow, viscous diffusion, viscous dissipation, polymer work and work done by body force, respectively. In a viscoelastic turbulent flow, $\mathcal{W}_p$ may change its sign and can serve as either dissipation or production depending upon the signs of the polymer stress fluctuations and fluctuating velocity gradients as has been observed in both experimental [150] as well as in numerical [151] works.

To get better insight of the EIT regime in this duct flow, these terms are averaged in time and in the streamwise (y) direction once the flow reaches a statistically steady state. The constant contours of all the terms in Eq. (4.6) normalized by v_τ^2 are shown in Fig. 4.5 at two different values of Re in a vertical cutting xz-plane except for the body force term that is zero for this single-phase flow. For $Re = 1000$, the advection by mean flow (Fig. 4.5a-left) shows small regions of positive peaks at the four corners and towards the centre of the duct. A pattern of four negative peaks is also observed slightly away from the walls at this high Reynolds number EIT flow. However, once the Reynolds number is lowered to $Re = 100$, the magnitude of the advection term becomes negligibly small. Similarly, a symmetric pattern of transport term is observed for the higher Reynolds number (Fig. 4.5b-left) and the same term becomes negligibly small at lower inertia. At $Re = 1000$, the positive and negative peaks of the transport term remain closer to the channel walls except at the corners where it remains approximately zero. An opposite trend is observed for the pressure term (Fig. 4.5c). Once the flow is dominated by the inertial effects ($Re = 1000$), the pressure term remains significant while, in an elastically dominated EIT regime ($Re = 100$), it shows a symmetric pattern of positive and negative zones, however,

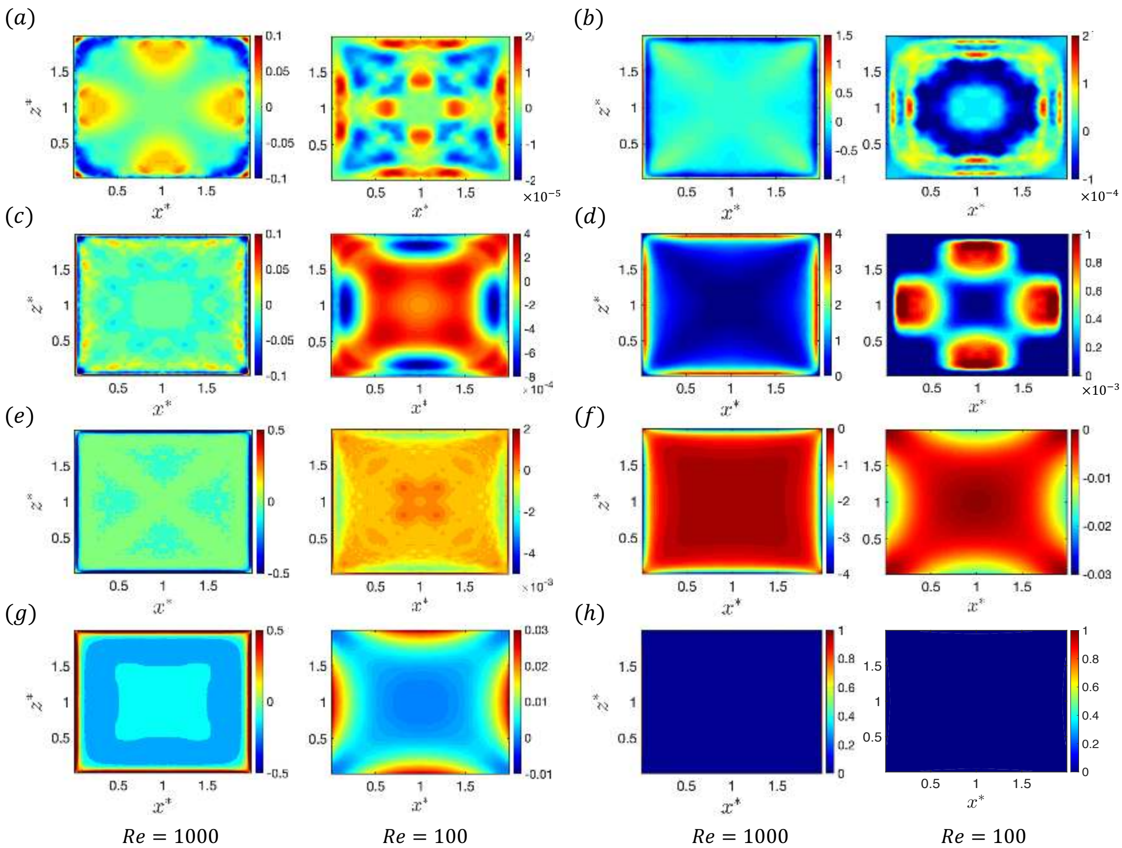

Figure 4.5: Contours of (a) advection by mean flow, (b) transport by velocity fluctuations, (c) transport by pressure, (d) production by mean flow, (e) viscous diffusion, (f) viscous dissipation, (g) polymer work and (h) time derivative of TKE are shown in a vertical cutting xz-plane for (*left*) $Re = 1000, Wi = 1000$ and (*right*) $Re = 100, Wi = 1000$ cases, respectively.

with a negligibly small magnitude. The positive peaks of the pressure term extend from four corners of the duct till the centre with negative peaks in the vicinity of the channel walls. Turbulence production by the mean flow is mainly produced near the walls except at the four corners (Fig. 4.5d) and becomes zero in the most of the central region of the duct with a symmetric pattern at $Re = 1000$. However, in the elastically dominated EIT flow ($Re = 100$), this pattern changes with four regions of positive peaks away from the walls. As the turbulence is mainly produced by the elastic effects at $Re = 100$, the magnitude of the production term also remains negligibly small. Diffusion term (Fig. 4.5e) shows positive peaks adjacent to the walls except at the corners, immediately followed by the negative peaks before decaying to zero for $Re = 1000$ whereas, for the $Re = 100$ case, it is positive near the walls and remains chaotic in the most of the remaining central portions of the duct. The dissipation term shows a similar pattern for both the cases (Fig. 4.5f), i.e., it is maximum at the walls except in the corners and becomes zero towards the duct centre. The most important term in this EIT regime is the work done by the elastic force (Fig. 4.5g) as it can contribute both towards generation or dissipation of turbulence. At higher inertia ($Re = 1000$), the positive peak of the polymer work is observed to be closer to the four walls of the channel. It indicates that the viscoelastic stresses contribute to the turbulence production closer to the walls but act as a dissipating sink away from it. The same term remains negligible at the centre. Interestingly, at lower inertia ($Re = 100$) where the elastic effects dominate, the polymer stresses contribute towards turbulence dissipation at the four corners and towards the central region of the duct. The turbulence production by polymer stresses is concentrated near the walls away from the corners. The viscous dissipation and the pressure terms follow the similar pattern, as seen in Figs. 4.5f & c, respectively. Finally, the summation of all the terms in Eq. (4.4.1) approaches zero confirming that a statistically steady state is reached, as shown in Fig. 4.5h.

Notably, the distribution of various components of TKE in the present EIT regime of a highly concentrated polymer solution at low Re is markedly different than that in a dilute viscoelastic turbulent duct flow at high Re as studied by Shahmardi et al. [152], where the turbulent statistics of the flow were entirely dominated by the inertial effects.

4.4.2 EIT in a multiphase flow

For a given Reynolds number, a significantly high Wi is always required to achieve the EIT state in a single phase flow in the absence of any external perturbations, as has been shown in the previous section. When Re is low (e.g., $Re = 10$), even the Weissenberg number as high as 1000 cannot make the flow unstable (Fig. 4.2). Similarly, the single-phase flow is found to be essentially laminar at the lower values

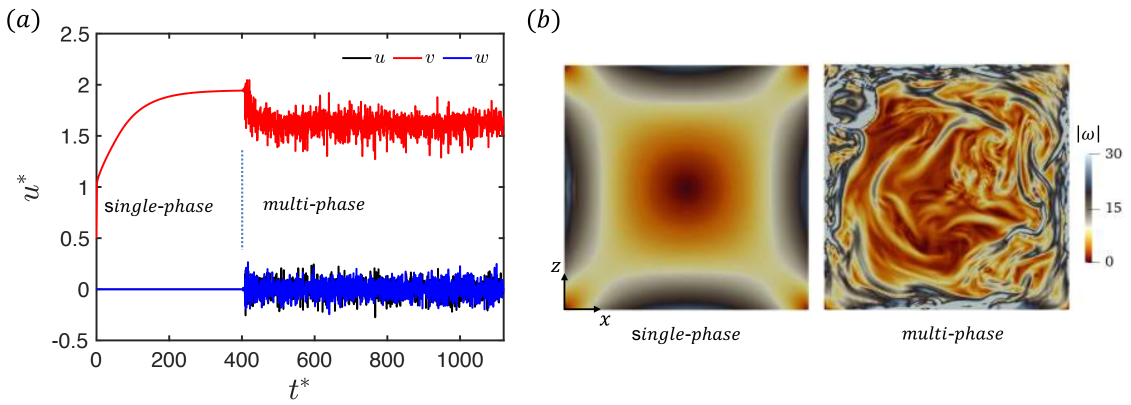

Figure 4.6: (a) Evolution of flow velocity and its transition to turbulent state once bubbles are injected into the flow (b) The contours of vorticity magnitude in an xz-plane at the centre of the domain for the single-phase and multi-phase regimes $(Re = 1000, Wi = 5, \beta = 0.1, Ca = 0.01)$

of Wi even when Reynolds number is as high as $Re = 1000$.

We next examine the effects of bubble injection into the viscoelastic laminar channel flow. For this purpose, simulations are performed for three relatively low values of $Wi = 1$, 5 and 10 at each value of $Re = 10$, 100 and 1000. Note that the single phase flow remains laminar for these combinations of Wi and Re. Calculations are first carried out for the single-phase flow until a statistically steady state is reached. Then, spherical bubbles are injected instantaneously into the flow with a volume fraction of 3% and the relative bubble size of $d_b/2h = 0.2$, where d_b is the bubble diameter. The bubbles are initially injected randomly and uniformly in the entire duct. The capillary number is fixed at $Ca = 0.01$ to keep the bubbles nearly spherical. The state of this multiphase flow field is continuously monitored at each time step using the two numerical probes as for the single-phase case. By introducing the bubbles into the flow, the flow is found to achieve a chaotic state even for the Reynolds and Weissenberg numbers as low as $Re = 10$ and $Wi = 5$. Time histories of instantaneous velocity components are plotted in Fig. 4.6a for the $Re = 1000$ and $Wi = 5$ case to show the transition from a laminar to an EIT state after the injection of bubbles. Bubbles are injected at about $t^* = 400$. As seen, the signals are very smooth until the injection of bubbles indicating a laminar flow. Once the bubbles are injected into the flow, all three components of the velocity exhibit random fluctuations indicating a transition to the EIT state. These fluctuations propagate throughout the domain over time, ultimately leading to a fully chaotic flow field. This chaotic flow state is visualized by plotting constant contours of vorticity ($\boldsymbol{\omega} = \nabla \times \boldsymbol{u}$) magnitude in Fig. 4.6b for the single-phase and multi-phase regimes in a vertical cutting xz-plane at the centre of the duct. Once the flow reaches a statistically steady state after the injection of bubbles, the simulations are continued at least for another 10 flow-through time units ($10 \times 12h/u_o$) to collect data for further statistical analysis.

Although not shown here due to space considerations, further simulations are performed to demonstrate the effect of bubble-induced streamline curvature on the destabilization of the flow. For this purpose, simulations start from a two-phase Newtonian laminar flow at $Re = 100$. Subsequently, the flow is made weakly viscoelastic by setting a small value of $Wi = 0.5$ and the simulation is continued until the viscoelastic stresses are fully developed and no flow destabilization is observed. Then the Weissenberg number is gradually increased first to $Wi = 1$, then to $Wi = 2$ and eventually to $Wi = 5$ while the flow state is continuously monitored. In this process, the simulations are carried out until a statistically steady state is reached before increasing Wi in each step. No transition occurred at low Wi, i.e., $Wi \leq 2$. The flow remained laminar despite the presence of bubbles, confirming that the initial discontinuity (bubble injection) alone is insufficient to trigger transition to turbulence. Transition is finally observed at $Wi = 5$. The transition is governed by the interplay of elasticity and streamline curvature but not the transient discontinuity. The destabilization coincided with the development of strong streamline curvature around bubbles, consistent with prior studies showing that viscoelastic stresses amplify curvature-driven instabilities, as first observed and quantified by Mckinley et al. [116] and has also been confirmed in our earlier work as well [141].

Figure 4.7a shows the distribution of first normal stress difference (N_1) in the mid-plane for three different values of $Re = 10$, $Re = 100$ and $Re = 1000$ at $Wi = 10$. A 'chaotic arrowhead' regime is observed for the all three values of

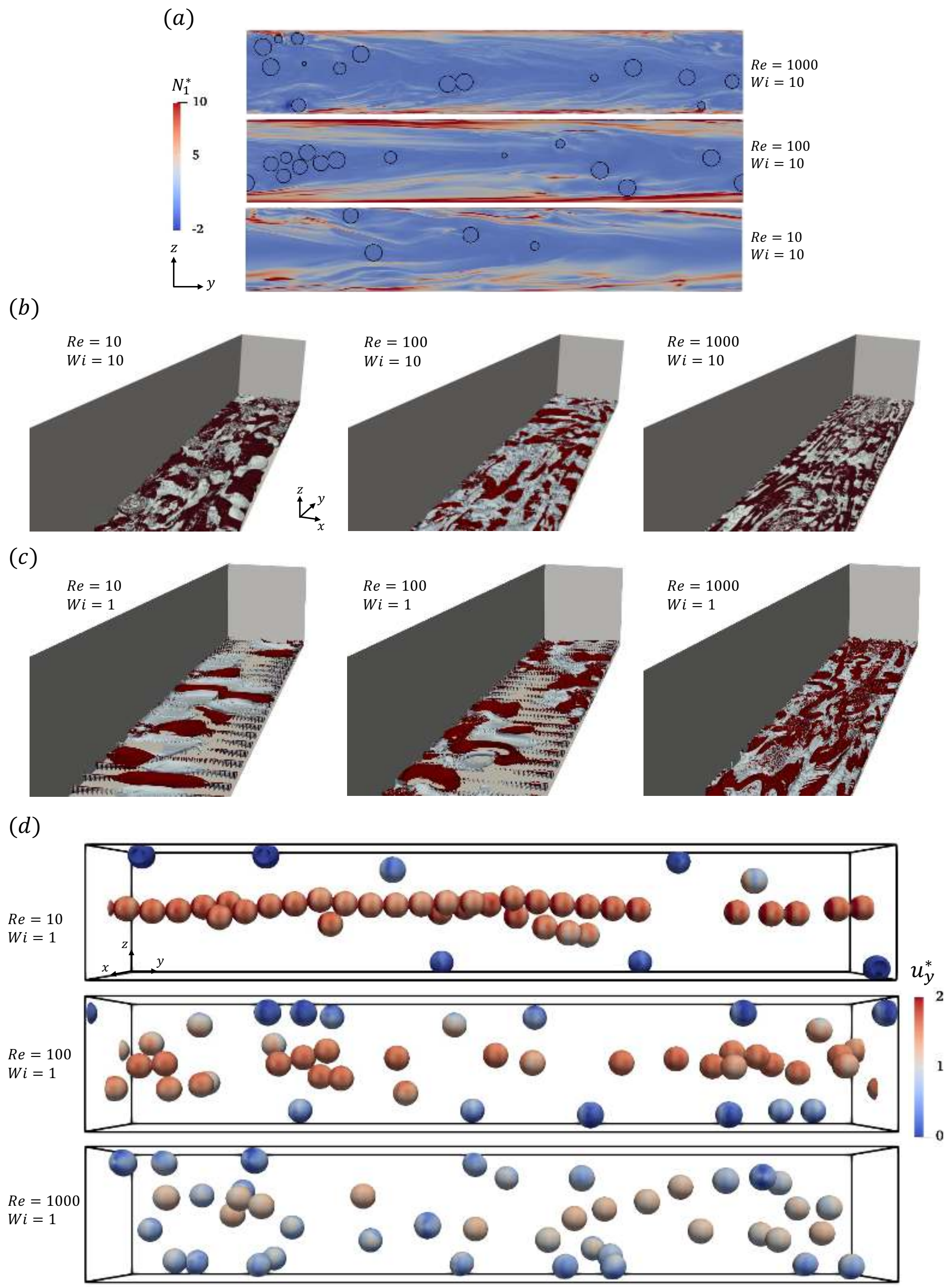

Figure 4.7: (a) Contours of N_1 in the mid-plane for different values of Re at $Wi = 10$. Iso-surfaces of *Q-criterion* at the bottom walls of the channel for the multiphase EIT regime at (b) $Wi = 10$ and at (c) $Wi = 1$ for different values of Re. For (b), the contours are plotted at ± 0.00001, ± 0.001 and ± 0.01 for $Re = 10, 100$ & 1000 cases with red colour (positive) and grey (negative), respectively. For (c), the contours are plotted at ± 0.00001 for $Re = 10, 100$ and at ± 0.1 for $Re = 1000$ case. (d) Distribution of bubbles coloured by the magnitude of streamwise flow velocity in the channel for different values of Re at $Wi = 1$

Re at this relatively low Wi for which the single-phase flow remains fully laminar. Note that all bubbles are of the same size in Fig. 4.7a and the seemingly different appearance of the bubble sizes is simply caused by the out-of-plane bubbles at this particular time instant. The constant contours of Q-criterion at the walls for the same three cases are depicted in Fig. 4.7b, showing a chaotic pattern similar to the one observed in the single-phase cases at low value of Wi (Fig. 4.3d). The contours of Q-criterion at the wall are shown in Fig. 4.7c for Re = 10, 100 and 1000 at $Wi = 1$. It is observed that, for this low $Wi = 1$ case, the flow remains laminar at the walls for $Re = 10$ and $Re = 100$ cases. Small perturbations remain confined to the immediate surroundings of bubbles. The positive and negative structures of Q-criterion are only visible at the walls once plotted at negligibly smaller values (i.e; $\pm 1 \times 10^{-5}$). For $Re = 1000$, however, a chaotic flow regime is observed even at $Wi = 1$ as seen by the contours of Q-criterion (Fig. 4.7c).

The bubble distributions in the duct are depicted in Fig. 4.7d. It is interesting to see that, although the bubble distribution is essentially uniform in the other cases, the majority of the bubbles are aligned in the centre of the duct forming a string-shaped pattern for the lower values of $Re = 10$ and $Wi = 1$, which also explains the reason that the disturbances remain confined to the core region of the duct away from the walls for this case. In the case of non-colloidal spherical solid particles, Won et al. [153] have experimentally shown that although the main driving force for the lateral migration of particles is the first normal stress difference, particle alignment is actually promoted by the shear-thinning effect for a particular rheological setting. In the present case of bubbles, the role of shear-thinning effect in the alignment of bubbles is investigated by performing another simulation at $Re = 10$ and $Wi = 1$ with a higher shear thinning and the results are shown in Fig. 4.8. The change in the effective viscosity (μ_e) of the flow due to shear-thinning effect at different shear rates ($\dot{\gamma}$) is governed by the concentration of polymers (β) and the mobility factor (α) in the Giesekus model. The slope of viscosity versus shear rate plot is controlled by the mobility factor α and the final value of viscosity at a high enough shear rate is determined by the concentration of polymers β ([154]). The vertical line in Fig. 4.8a indicates the shear rate at the wall for the mid-plane of the duct for the $Re = 10$ and $Wi = 1$ case. Once the mobility factor is increased to $\alpha = 0.1$, a random distribution of bubbles is observed instead of the string-shaped aggregation at the centre of the duct Fig. 4.8b. We thus conclude that, unlike the solid particles, a higher shear-thinning effect of the ambient fluid breaks up the alignment of bubbles at least for this particular rheological setting. Further investigation is required to reveal the exact mechanism behind the role of shear-thinning effect on different forces acting on the bubbles and causing them to align in the central region of the duct.

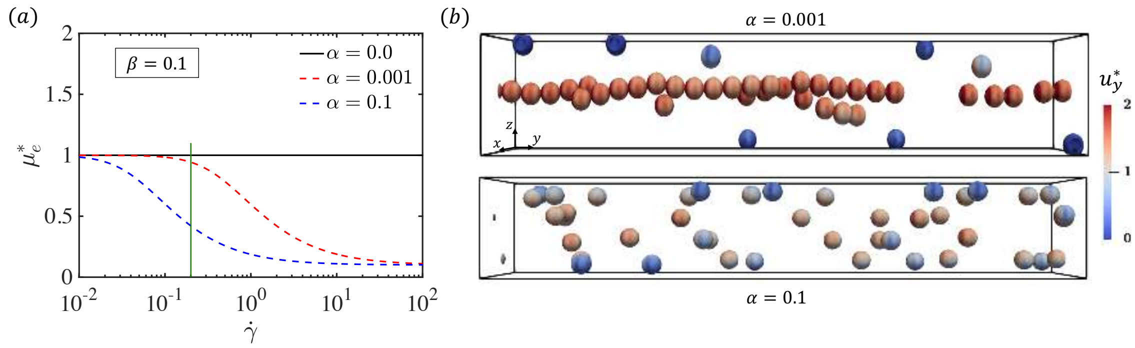

Figure 4.8: (a) The change in the effective viscosity of a Giesekus fluid in a concentrated polymer solution. The vertical line shows the value of shear rate at the wall for the central yz-plane of the present duct flow. (b) The distribution of bubbles in the duct for different values of shear thinning parameter α $(Re = 10, Wi = 1, Ca = 0.01, \beta = 0.1)$.

Figure 4.9a shows that, for the case of $(Re, Wi) = (10, 1)$, majority of the bubbles accumulate in the core region, and the perturbations remain confined to immediate surroundings of the bubbles indicating a laminar flow as shown by the contours of Q-criterion. When the inertia is increased ($Re = 100$) at the same low value of $Wi = 1$, the bubbles become more uniformly distributed but the flow still remains laminar. Finally, once the inertia is sufficiently high ($Re = 1000$), the bubbles become randomly distributed in the entire duct and a fully chaotic flow regime is observed in the entire domain (Fig. 4.9a) with a significant increase in the friction drag. Figure 4.9b shows 1D energy spectrum of the streamwise component of flow velocity for $Wi = 1$, $Wi = 5$ and $Wi = 10$ at $Re = 10$. Once the flow reaches

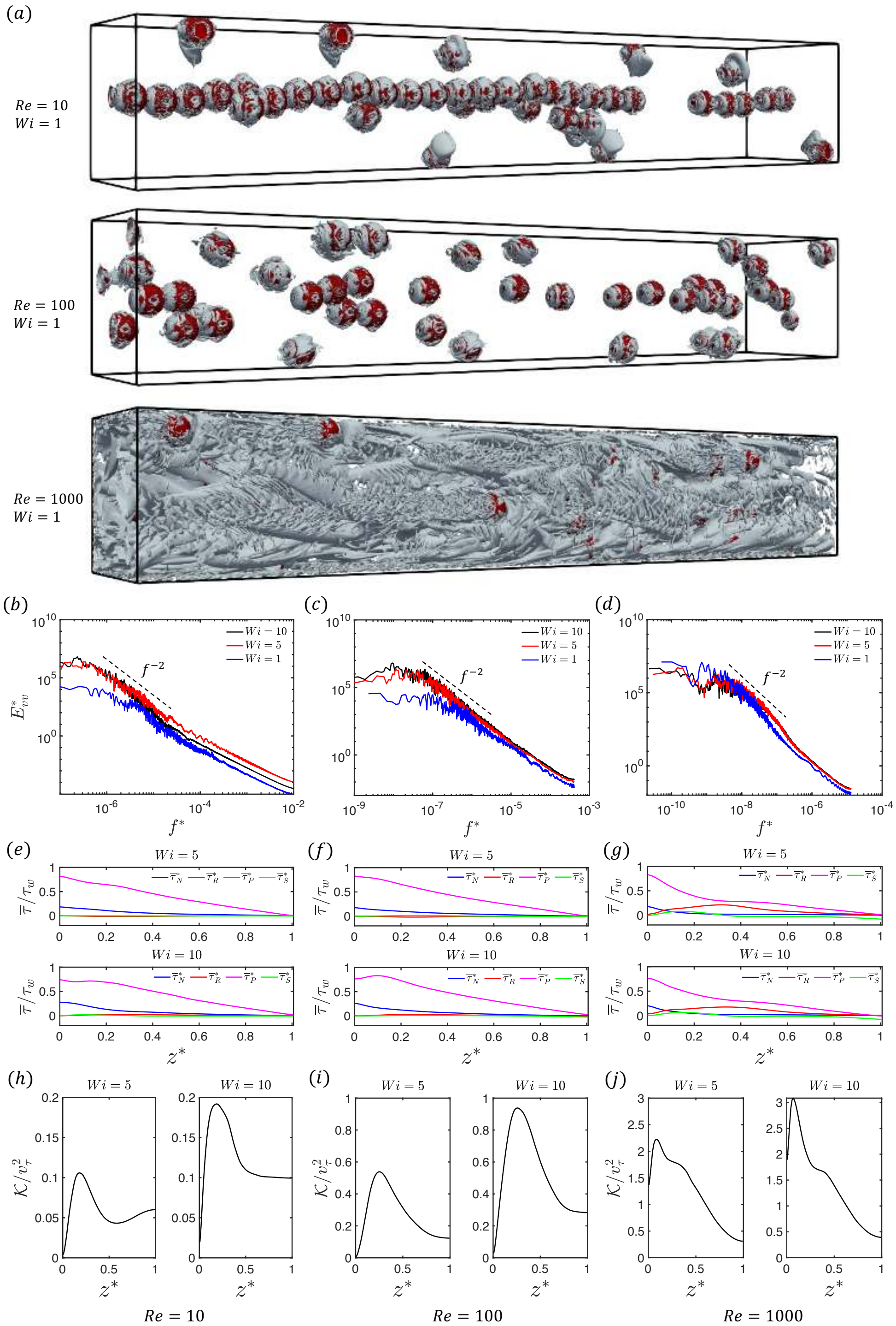

Figure 4.9: *(a)* Iso-surfaces of $Q - criterion$ are shown at different values of Re for $Wi = 1$. The contours are plotted at 0.003, 0.3 and 3 for $Re = 10, 100$ and 1000 cases, respectively. *(b,c,d)* 1D energy spectrum, *(e,f,g)* the distribution of various components of shear stress and *(h,i,j)* turbulent kinetic energy ($\mathcal{K}$) are plotted in the mid-plane for $Re = 10$ (*left*), $Re = 100$ (*middle*) and $Re = 1000$ (*right*) cases, respectively ($\beta = 0.1$ and $Ca = 0.01$).

a statistically steady state, the velocity signal is collected from the point away from the centre ($x^* = 0.5, y^* = 6, z^* = 1$) to avoid the noise due to the bubble cluster. The flow velocity inside the bubbles is filtered out from the signal. A slope of -2 is observed for the $Wi = 5$ & 10 cases when the flow is chaotic in the entire domain. This slope is the same as the temporal spectrum scaling of centreline velocity observed by Lellep et al. [155] indicating a similar chaotic state. The energy spectra of $Wi = 5$ and $Wi = 10$ cases overlap each other, showing a similar flow state for both the cases in the presence of bubbles. As the flow is not fully chaotic at $Wi = 1$ and its signal shows a very high intermittency, the same is manifested in its spectrum where the slope does not match with the slopes of $Wi = 5$ & 10 cases. For the $Re = 100$ cases, the slope for $Wi = 1$ gets closer to the slopes in the $Wi = 5$ & 10 cases and finally at $Re = 1000$, all the three cases show a similar slope of -2 (Fig. 4.9d). This slope of -2 is greater than the classical slope of $-5/3$ in the inertial turbulence but still less than -4 reported for a purely elastic turbulence in the absence of inertia [5] or at a very high value of $Wi = 1000$ observed in the single-phase cases (Fig. 4.4a,c). As this multiphase EIT regime is achieved at the lower values of Wi, it is governed by both inertia and viscoelasticity, and hence the slope remains in between these two limits.

The distribution of different components of shear stress from the channel wall towards the center are shown in Figs. 4.9e, f & g in the mid-plane of the duct for $Re = 10, 100$ & 1000 cases, respectively. As the flow is multiphase, an additional contribution from the surface tension force of the bubbles ($\bar{\tau}_S$) is added towards the total shear stress balance. However, this contribution remains much smaller than the remaining components as the bubble volume fraction is a mere 3%. Similar to the single-phase flow cases, these stress components are normalized by the local shear stress at the wall of the mid-plane. As seen in the figure, the chaotic flow regime is dominated by the viscoelastic stress ($\bar{\tau}_P$) followed by the viscous stress due to the mean flow ($\bar{\tau}_N$). These two stress components are highest at the wall and decay to zero towards the channel centre where the shear rate is minimum. The contribution of the Reynolds stress ($\bar{\tau}_R$) remains negligible for the $Re = 10$ and $Re = 100$ cases.

The Reynolds stress component $\bar{\tau}_R$ starts to show its effect once the inertia becomes high enough in the $Re = 1000$ cases. As the source of flow instability is the curved streamlines around the bubble in this multiphase flow regime [116], the transition to the EIT state greatly depends upon the distribution of bubbles across the channel. The role of viscoelasticity in promoting the bubble migration towards the channel center or towards the wall is governed by the relative change in the convective time scale of the bubbles and the polymer relaxation time as has been explained by Bothe et al. [45]. A similar observation was also made in our earlier work as well [141]. The distribution of turbulent kinetic energy (TKE) for all these three values of Re shows a peak value near the wall and minimum at the channel center, as shown in Figs. 4.9h, i & j. By increasing the value of Wi, the magnitude of TKE also increases following the same qualitative trend in agreement to our previous study of viscoelastic turbulent single phase case [156].

Next, further simulations are performed to examine the effects of size and number of bubbles on the transition and resulting chaotic flow for the $(Re, Wi) = (1000, 1)$ case. First, the number of bubbles are increased from the previous volume fraction of $\Phi = 3\%$ to $\Phi = 9\%$ while keeping the bubble size the same, and then the bubble volume is decreased by 50% while keeping the volume fraction the same at $\Phi = 3\%$. As shown in Fig. 4.10, neither the number of bubbles nor their size has any significant effect on the scaling of energy spectrum except for a slight increase in the energy content at the smaller scales for $\Phi = 9\%$. Moreover, no significant change in transition to a chaotic state is observed by varying the number of bubbles or their size.

Once the flow reaches a steady state, the applied pressure gradient is balanced by the total shear stress at the walls and the average wall shear stress can be simply computed as $\overline{\tau}_w = -\frac{h}{2}\frac{dp_o}{dy}$. The change in the drag is quantified by $\Delta D = (\overline{\tau}_w - \tau_{w_o})/\tau_{w_o}$, where τ_{w_o} is the wall shear stress of the corresponding Newtonian laminar flow for the same Reynolds number. Figure 4.11 summarizes the percentage change in drag for all the multiphase simulations. The single-phase viscoelastic laminar flow has lower drag as compared to the Newtonian laminar flow for the same value

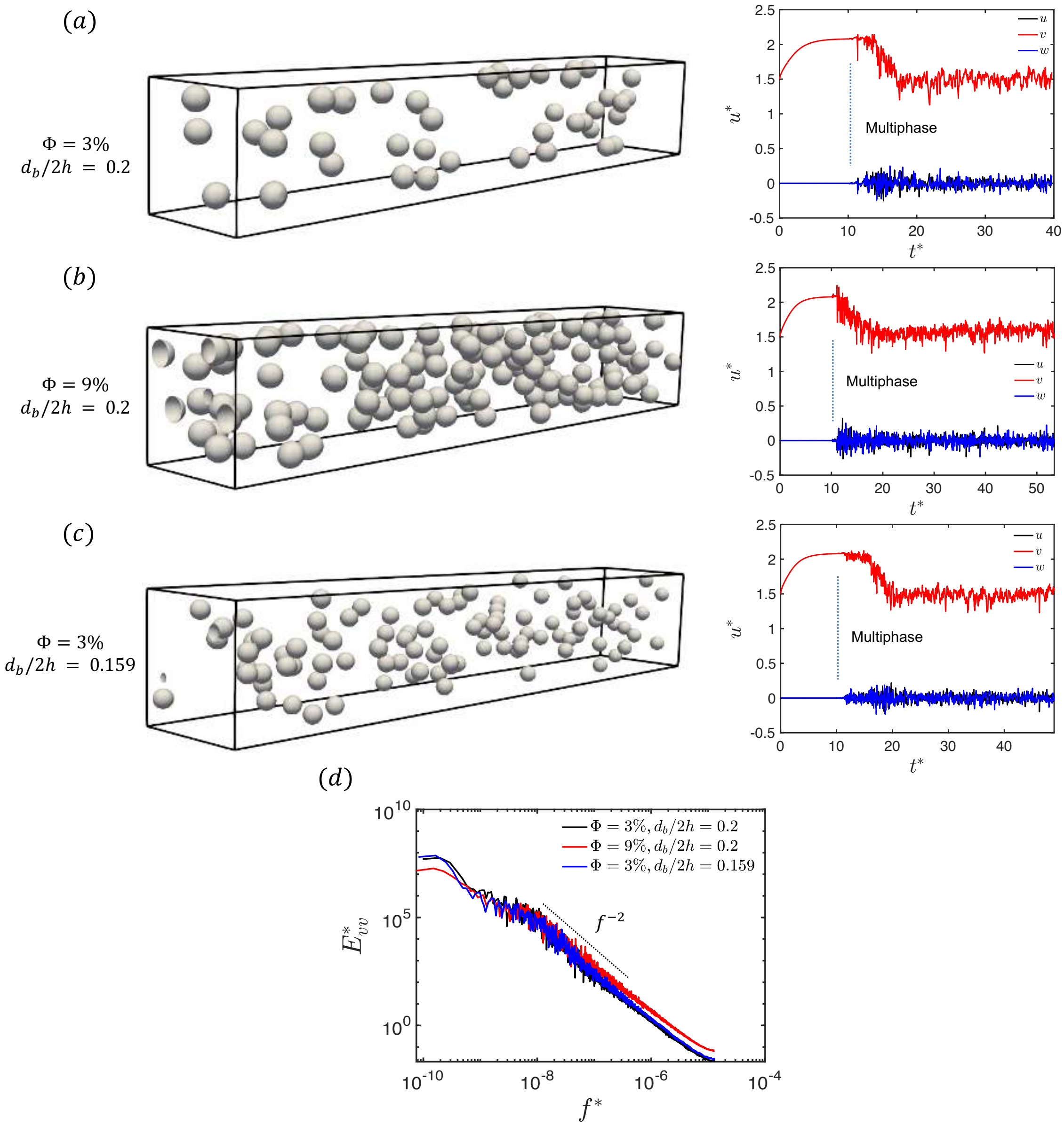

Figure 4.10: Effects of number of bubbles and bubble size. The bubble distribution (left) and the evolution of flow velocity (right) for the void fraction of (a) $\Phi = 3\%$, (b) $\Phi = 9\%$ for the same bubble size of $d_b/2h = 0.2$, and (c) for the bubble size of $d_b/2h = 0.2/\sqrt[3]{2} = 0.159$ with $\Phi = 3\%$. (d) The 1D energy spectra for the same cases $(Re = 1000, Wi = 1, Ca = 0.01, \alpha = 0.001)$.

of Re. Understandably, as the inertia increases in this shear thinning viscoelastic fluid once the flow is made viscoelastic, the drag is reduced. For a particular value of Wi, the percentage reduction in drag is found to be the same for every value of

Re. However, the drag increases significantly once a viscoelastic flow transitions to a chaotic turbulent state after injecting the bubbles (Fig. 4.11). In particular, a rapid increase in the drag is observed at $Re = 1000$ once the flow becomes turbulent for all three values of Wi. It is interesting to observe that, although the drag increases for the $Re = 10$ & 100 cases at $Wi = 5$ & 10 upon transition to the EIT state, it still remains less than that of the respective Newtonian laminar state. Another interesting feature is also observed at $Wi = 1$ for the $Re = 10$ & 100 cases. Once bubbles are injected into the flow, minor fluctuations remain confined to the core region away from the walls where the bubbles collect and form a string-shaped pattern ($Re = 10$) or small clusters ($Re = 100$). The flow remains essentially laminar closer to walls and in the major portion of the duct. In this regime, the drag is reduced as compared to the single-phase laminar state. For this case, the bubbles forming a string-shaped pattern create a low viscosity corridor at the core region where they move faster and thus the streamwise component of flow velocity is slightly increased. As a result, the applied pressure gradient is reduced effectively to maintain the same flow rate. Furthermore, it is important to highlight that the magnitude of drag is small for this laminar flow, so the change is also small. At a higher inertia ($Re = 1000$), the flow becomes fully chaotic in the entire channel, and thus the drag is increased significantly even for the $Wi = 1$ case (Fig. 4.11).

It is interesting to note that for $(Re, Wi) = (10, 10)$ and $(100, 10)$ cases, the flow has become completely chaotic and the EIT state is achieved by injecting the bubbles into the flow, however, the drag is still less than the corresponding Newtonian laminar state, which is primarily attributed to the shear-thinning effect of viscoelastic fluid (Fig. 4.11).

TKE in a multiphase EIT regime

To get further insight into the multiphase EIT regime, all the terms in Eq. 4.6 are integrated in the streamwise direction and averaged in time after the flow reaches a statistically steady state. The results are plotted in Fig. 4.12 for $Re = 100$ and $Re = 1000$ at $Wi = 10$. Compared to the single phase case shown in Fig. 4.5, a

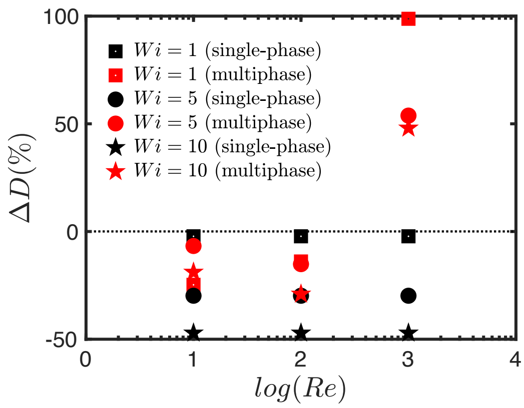

Figure 4.11: The percentage change in drag measured by the change in total shear stress at the wall ($\overline{\tau}_w$) as compared to the Newtonian laminar flow once the flow is made viscoelastic and is subsequently transitioned to turbulent state by injecting the bubbles

prominent effect of bubbles at low Weissenberg number is observed in smoothing sharp gradients near the wall in all the terms that contribute to TKE. We note, however, that comparison between single and multiphase cases should be interpreted only qualitatively since Wi is two orders of magnitude higher in the single phase case. Figure 4.12 shows that the magnitudes of all terms are amplified as Re is increased from 100 to 1000 but the amplification is more pronounced in advection ($\mathcal{A}$), turbulent transport ($\mathcal{Q}$), production by mean flow ($\mathcal{P}$) and viscous diffusion ($\mathcal{D}$) terms. There are also some qualitative differences in these terms in the $Re = 100$ and $Re = 1000$ cases. The peak values of $\mathcal{A}$, $\mathcal{Q}$, P and ϵ occur in the corners and in the middle of the side walls for $Re = 100$ and $Re = 1000$, respectively. In contrast to the single phase case, the maximum value of $\mathcal{R}$ occurs in the central portion of the duct due to presence of bubbles (Fig. 4.12c). Significant viscous dissipation observed in the channel centre is also attributed to the presence of bubbles there. The positive peaks of polymer work for the multiphase case shows that it still contributes towards the production instead of dissipation in some portions of the domain (Fig. 4.12g). The body force term contributes significantly to the TKE budget now due to the work done by the surface tension (Fig. 4.12h).

Notably, the chaotic flow state at these lower values of Weissenberg numbers is

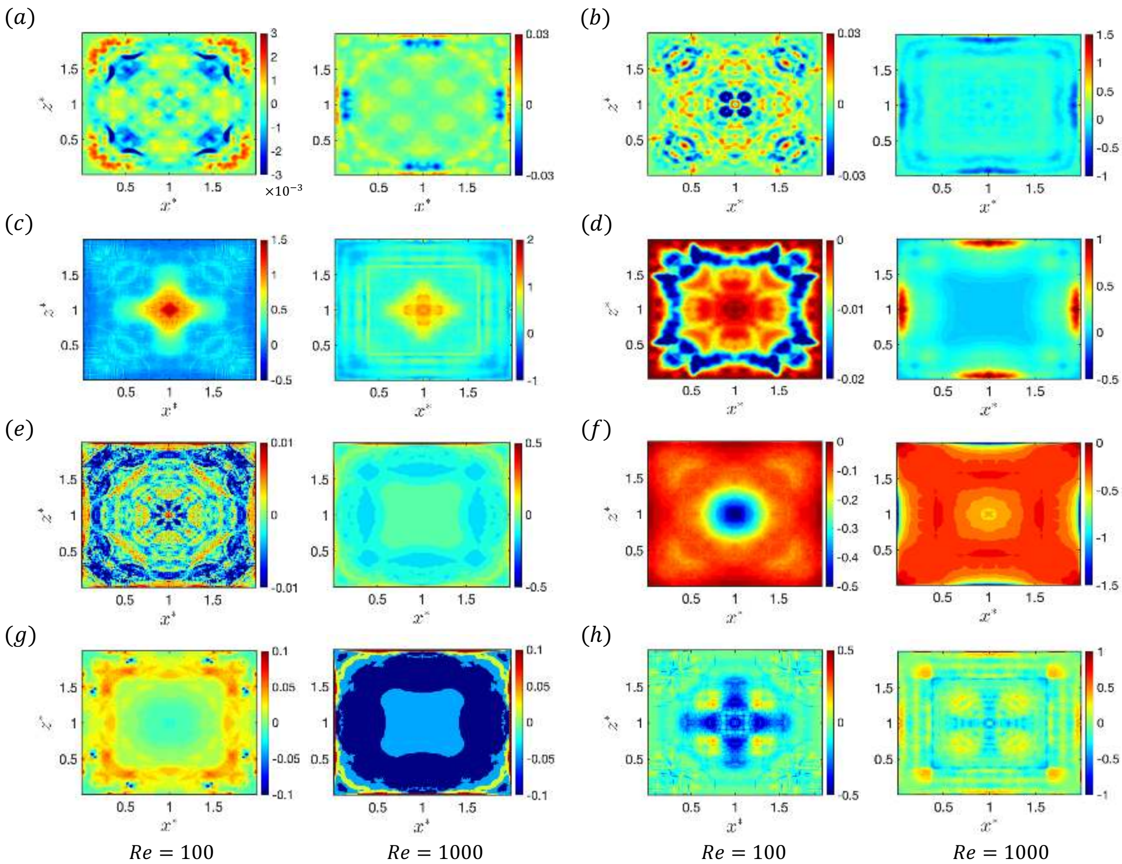

Figure 4.12: Contours of (a) advection by mean flow, (b) transport by velocity fluctuations, (c) transport by pressure, (d) production by mean flow, (e) viscous diffusion, (f) viscous dissipation, (g) polymer work and (h) body force terms are shown in a vertical cutting xz-plane for (*left*) $Re = 100, Wi = 10$ and (*right*) $Re = 1000, Wi = 10$ multiphase cases, respectively.

only sustained in the presence of bubbles. If the bubbles are removed, the single-phase flow would laminarize, as observed in the simulations of single-phase flow where the chaotic flow state could not sustain below $Wi \leq 40$.

In the ET regime (very low Re), it is well established that a sufficiently strong extensional perturbation is required to destabilize the flow and trigger chaos. As inertia increases, the threshold for instability decreases, and the flow becomes more susceptible to a wider range of perturbations—including those introduced by bubbles. In the present simulations, the presence of bubbles provides persistent, finite-amplitude disturbances that can maintain a chaotic state even as inertia becomes more significant. Thus, the bubbly chaotic state observed in the present study at moderate Re can be interpreted as a form of ET that is transitioning towards EIT as inertia increases. This is further supported by the fact that the energy spectra do not yet reach the inertial $-5/3$ scaling, and the flow structures retain characteristic features of ET.

In summary, ET and EIT can be seen as two ends of a spectrum, with present results occupying an intermediate and transitional regime. The bubbly chaotic state in the present scenario likely represents a version of ET influenced by finite inertia and persistent multiphase perturbations, rather than a fully developed EIT state. The spectra and flow localization support this interpretation.

4.5 Conclusions

Direct numerical simulations of single and multiphase viscoelastic fluid flows are performed in a square-shaped channel and the complex dynamics of elasto-inertial turbulent regime are explored without introducing any explicit perturbations from outside the system. The bubble interfaces are fully resolved using a finite-difference/front-tracking method coupled with the Giesekus model equations to simulate chaotic flow regime of a shear-thinning viscoelastic fluid. Instead of using conventional numerical schemes to discretize the constitutive equations by introducing artificial diffusion, a computationally expensive but robust log-conformation method is employed for the present DNS to preserve the integrity of EIT physics [144]. The Reynolds number is varied by two orders of magnitude to cover a vast range below the threshold value of the inertial turbulence in the channel flow. Then the Weissenberg number is varied by three orders of magnitude at each of these values of Reynolds numbers to explore the conditions for triggering transition to a turbulent regime in this rectilinear channel flow. Subsequently, unlike any previously tested methods, bubbles are injected into the flow under the conditions for which a single-phase flow remains fully laminar to check whether the presence of bubbles can trigger an instability to achieve the EIT flow regime. A constant flow rate is maintained corresponding to each Re by dynamically adjusting the applied pressure gradient. As different pathways can be followed in Re-Wi space to achieve EIT [131], a concentrated polymer solution ($\beta = 0.1$) is considered in the present study for which the EIT regime is triggered much earlier than the inertial turbulence as the Reynolds number is increased.

It is observed that beyond $Wi \geq 100$, a single-phase flow becomes unstable when $Re \geq 100$. Fluctuations start to grow in this straight channel even without introducing any discrete external perturbations. These fluctuations propagate throughout the domain over time, ultimately leading to a fully chaotic flow field. The threshold value of Wi to trigger instability in the flow reduces with an increase in Re. For $Re = 1000$, the critical value of Wi to trigger transition from laminar to turbulent state is found to be 50. When the value of Re is low ($Re = 10$), a Weissenberg number as high as 1000 can not make the flow unstable. The energy spectra of this single-phase EIT regime reveal -4 scaling at the higher frequencies (dissipation range) while the classical $-5/3$ scaling is observed at the lower frequencies (inertial range) as the flow is dominated by both inertia as well as the elasticity.

It is found that if perturbed initially, single-phase viscoelastic flow cannot sustain a chaotic state in this rectilinear duct when $Wi \leq 40$ for all the three values of $Re = 1000, 100$ & 10 used in the present study.

A novel mechanism of achieving the EIT state by injecting the bubbles into the flow under the conditions for which a single-phase flow remains laminar is tested and verified at a Reynolds number as low as 10 and a Weissenberg number as low as 5. The curved streamlines across the bubbles interfaces provide the necessary condition to trigger an instability even when the viscoelastic stresses are not very high and the single-phase flow remains completely laminar. The energy spectra shows a scaling of -2 for this low Wi multiphase EIT regime. It is found that this scaling is independent of size and number of bubbles injected into flow. Thus, it is concluded that the scaling of energy spectra varies from -4 to $-5/3$ depending upon the relative dominance of inertia and elasticity, i.e, -4 for a purely elastic turbulence and $-5/3$ for a purely inertial turbulence. All the other values of energy scaling would fall in between these two limits depending upon the relative strength of inertia (Re) and elasticity (Wi). It is also observed that the drag increases for all the situations where the laminar viscoelastic flow is fully transitioned to a turbulent state by injecting the bubbles into the flow. However, at the lower values of $Re = 10$ & 100, this higher value of skin friction drag of the EIT regime still remains lower than that of the corresponding laminar Newtonian flow for the same Reynolds number. Once the inertia and the elasticity are both low, the bubbles are aligned in the core region of the duct forming a string-shaped pattern ($Re = 10$, $Wi = 1$) or clusters ($Re = 100$, $Wi = 1$), and the flow remains laminar. For these cases, the friction drag reduces even further instead of increasing. Unlike the solid particles, it is found that a higher shear-thinning effect breaks up the alignment of bubbles.

The idea of achieving the EIT state at a very low value of Re and Wi just by injecting the bubbles into the flow can find many potential applications involving processes where mixing, heat transfer or other transport phenomena are of primary importance. The present study would intrigue experimental verification as it has been demonstrated that the requirement of Wi to achieve the EIT state in a multi-phase flow is low and realistic.

Chapter 5

POLYMER DRAG REDUCTION IN A TURBULENT BUBBLY CHANNEL FLOW IN THE HDR AND MDR FLOW REGIMES[4]

5.1 Introduction

Once a laminar flow transitions to a turbulent flow regime, a sharp rise in the skin friction drag is observed for the same value of Reynolds number. As the higher friction drag means more power is required to drive the wall-bounded flows and more energy is wasted as heat through dissipation, its reduction has numerous potential applications and benefits. When a small concentration of high molecular-weight polymers is added to an already turbulent wall-bounded Newtonian flow, its drag is reduced significantly. Even after seven decades of its first discovery by Toms [157], the exact mechanism behind this significant decrease in drag is yet to be fully understood. The complex interaction between near-wall turbulent structures and the stretched polymers is still an open question. Researchers have been striving to understand this mechanism offering various explanations, focusing on either viscous effects [158, 159] or elastic effects [160, 161]. Despite experimental observations supporting both explanations, neither of them has been proven unambiguously correct so far.

Viscous explanations of drag reduction (DR) primarily cite the increase in the effective viscosity of the flow due to the presence of polymers as the main reason behind DR. The highest stretching of polymers near the wall due to a higher strain rate in the buffer layer increases the extensional viscosity of the flow which suppresses

[4] TO BE SUBMITTED AS A PAPER UNDER THE SAME TITLE IN PHYSICAL REVIEW FLUIDS

velocity fluctuations, hence the Reynolds stress is decreased. As a result, the thickness of the buffer layer increases, and the mean velocity profile starts to shift away from the log-law of Newtonian flow. This decrease in the Reynolds stress, which is responsible for the increased momentum exchange with the wall in a turbulent flow, results in a decreased skin friction drag [158]. The explanations focusing on the elastic effects, however, argue that although the higher strain rate is associated with the buffer layer, it fluctuates both in space and time. Therefore, the higher strain rate and the vorticity filed in the buffer layer are never sufficient enough to stretch the polymers till their coil-stretched transition state to produce these effects. Rather, once the cumulative elastic energy produced by the partially stretched polymers in the buffer layer becomes comparable with the turbulent kinetic energy of the flow above the Kolmogorov scale, the typical energy cascade gets terminated prematurely at a length scale above the Kolmogorov scale and all the length scales below this are purely dominated by the elastic effects. These effects increase the thickness of the buffer layer and the drag is reduced [160, 161].

Although both these explanations attribute drag reduction to different mechanisms, the common outcome of both the elastic and viscous explanations is the disruption of the self-sustaining cycle of wall turbulence. In classical inertial turbulence, the turbulence cycle is marked with the quasi-streamwise vortices which extract energy from the mean flow and give rise to streamwise velocity streaks [162, 163]. These unstable velocity streaks in turn generate quasi-streamwise vortices and the turbulence cycle is sustained. The addition of polymers or surfactants reduces the strength of these vortices and the streamwise velocity streaks are thickened and found to be stabilized, disrupting the self-sustaining turbulence cycle [164, 165].

The polymer-induced turbulent drag reduction is broadly categorized into low-drag reduction (LDR) and high-drag reduction (HDR) regimes based upon different statistical trends of the turbulent flow field [166]. When DR $\leq 40\%$ (LDR), mean streamwise velocity fluctuations are increased whereas the spanwise and the wall-normal fluctuations are reduced. The Reynolds shear stress decreases monotonically with the increasing DR. The thickness of the buffer layer increases and the mean streamwise velocity profile in the logarithmic region shifts upward but remains parallel to that of a Newtonian flow [167]. These effects on velocity fluctuations are found to be the direct consequence of the large decrease in the mean streamwise component of the pressure-strain term in the Reynolds stress budget [168, 150]. Once DR $> 40\%$ (HDR), the velocity field shows different statistical trends. The slope of the mean velocity profile in the log-region deviates from the Newtonian flow. With a significant reduction in the Reynolds shear stress, polymeric stress starts to play a dominant role in sustaining the turbulence [169, 170]. For a fixed channel size and type of polymer, DR depends mainly on the Reynolds number (Re), the Weissenberg number (Wi) and the concentration of polymers. Once the value of Re is increased for a fixed concentration of polymers or if the concentration is gradually increased for a fixed Re, the maximum achievable DR limit is known as the maximum drag reduction (MDR) asymptote [4, 171]. From the perspective of numerical simulations, it is important to note that achieving DR in the limits of HDR ($40\% <$ DR $\leq 60\%$) or MDR (DR $> 60\%$) requires significantly longer domain lengths of the order of 10^4 wall units [172]. Choueiri et al. [173] have shown that polymers can even reduce drag beyond the suggested asymptotic limit as well due to relaminarization of the flow.

More recently, instead of merely relying on ensemble statistics of turbulent flow fields, a dynamic framework is also suggested to unravel the mechanism behind DR [174]. In wall-bounded inertial turbulence, the instantaneous wall shear stress generally fluctuates around its time-averaged value, but it occasionally experiences significant drops when the flow enters a hibernating phase. It bounces back to the normal level (active phase) after spending some time in hibernation. During these hibernating events, the flow field shows drastically weaker vortex structures. For a Newtonian flow, these hibernating events are quite rare and therefore, the time-averaged flow quantities predominantly represent the characteristics of active turbulence. Once polymers are added to the flow, the frequency of these active intervals are found to be decreasing by an order of magnitude after the onset of DR [175]. Xi and Graham [176] showed that turbulent flow statistics become different during the active and hibernating phases. Mean velocity profile shows a different slope similar to MDR during the hibernating event. Moreover, the Reynolds stress is significantly suppressed, vortices become weaker and velocity streaks are straightened during the hibernation, again similar to MDR. Thus, it is postulated that although the active and hibernation cycles exist in both the Newtonian and viscoelastic turbulent flows, at high Wi, the time scale for active turbulence is drastically reduced and the frequency of hibernation, whose drag is substantially lower, is increased. At sufficiently high Wi, active intervals will be very short so that hibernation becomes predominant. This is when the overall flow converges to MDR. Despite its promising explanation, this theoretical framework still has some gaps to fill. This dynamic theory of drag reduction is till unable to explain quantitative magnitude of MDR, its asymptotic convergence and the dynamics at high Reynolds number. The details can be found in the review paper by Xi [177].

The situation becomes even more involved in a multiphase flow. The existing literature on multiphase viscoelastic turbulent flows are mainly focused on the presence of solid particles in these flows. A dilute suspension of spherical solid particles with a mere volume fraction of 5% in a viscoelastic turbulent flow alters the dynamics of drag reduction and the turbulent statistics of the flow. The presence of particles increases the overall drag more than the corresponding Newtonian flow mainly due to increase in the polymeric stress due to the stretching of polymer chains in the vicinity of particles [178]. In a concentrated suspension of particles with a volume fraction of 20%, Esteghamatian and Zaki [179] found a non-monotonic trend in the total drag. At low Weissenberg numbers, the turbulent shear stress was found to be decreasing along with the total drag. Beyond a critical value of Weissenberg number once the turbulence was nearly eradicated, the drag increased with increasing elasticity.

DNS of turbulent bubbly flows is significantly more challenging than that of single-phase turbulent flows. Beyond the inherent difficulties associated with the wide range of length and time scales in turbulence, multiphase flows involve evolving interfaces that can undergo topological changes as well. The presence of surface tension as well as the discontinuous variation of material properties across the phase boundaries complicate the problem even further. Additionally, complex multiphysics interactions such as the presence of surfactants, add another layer of complexity, making the computational modeling of such flows a highly challenging task. One of our earlier DNS studies showed that after achieving a DR $\approx 38\%$ (LDR regime) in a single-phase viscoelastic turbulent channel flow, once clean bubbles were injected into the flow with a volume fraction of 3%, the drag reduction was completely lost [107]. The clean bubbles accumulated near the channel wall and the drag increased even beyond the level of Newtonian turbulent flow. However, in the presence of surfactant, the wall-layer generated by the clean bubbles became unstable and the bubbles were found to be randomly distributed across the whole channel. Under this condition, DR of a single-phase viscoelastic flow was completely recovered.

As the turbulent dynamics of the flow are extremely sensitive to the flow behavior in the vicinity of the particles, the absence of no-slip condition on the surface of bubbles and the deformation of bubbles in a viscoelastic turbulent flow produce different dynamic effects than the solid particles, as observed in our earlier study of LDR regime [107]. As the turbulent dynamics of the flow are different for the HDR regime than the LDR, the dynamics of bubbles on drag reduction in the HDR regime may be different and are yet to be explored. The aim of the present study is to investigate the dynamics of drag reduction in the HDR and MDR regimes in the presence of contaminated bubbles and to explore the complex interactions of elasticity and turbulence in these extreme limits. Direct numerical simulations are performed by using the front-tracking method to fully resolve the bubbles interfaces. FENE-P model is used to simulate the viscoelastic flow. The properties of an industrial grade surfactant Triton X-100 are used to contaminate the bubbles since it was found to be particularly efficient in our earlier work [107]. These large scale high fidelity simulations are performed on two different domain lengths to achieve the HDR and MDR regimes before injecting the bubbles into the flow.

The remaining part of the paper is organized as follows. In § 5.2, the mathematical formulation and the numerical solution algorithm are briefly described. The problem definition including the computational domain and boundary conditions are given in § 5.3. The results are presented and discussed in § 5.4. Finally, the findings are summarized and some conclusions are drawn in § 5.5.

5.2 Numerical method

The front-tracking method used in the present study was originally developed by Unverdi and Tryggvason [139]. Izbassarov and Muradoglu [108] enhanced this method to simulate viscoelastic two-phase systems in which one or both the phases could be viscoelastic. This robust, high fidelity code has been extensively utilized in our several previous works, including studies on viscoelastic laminar (e.g., [140], [60], [113], [141]) as well as viscoelastic multiphase turbulent channel flows (e.g., [103], [107]). In this finite-difference/front-tracking (FD/FT) method [20], a single set of governing equations can be written for the entire computational domain provided the jumps in the material properties are taken into account and the effects of the interfacial surface tension are treated appropriately [20, 180, 181]. The momentum equation, accounting for interphase coupling, is then given by

$$\rho\frac{\partial \mathbf{u}}{\partial t} + \rho\boldsymbol{\nabla}\cdot(\mathbf{u}\mathbf{u}) = -\boldsymbol{\nabla}p - \frac{dp_o}{dy}\mathbf{j} + \boldsymbol{\nabla}\cdot\boldsymbol{\tau} + \boldsymbol{\nabla}\cdot\mu_s(\boldsymbol{\nabla}\mathbf{u} + \boldsymbol{\nabla}\mathbf{u}^T) + \int_A \big[\sigma(\Gamma)\kappa\mathbf{n} + \nabla_s\sigma(\Gamma)\big]\delta(\mathbf{x}-\mathbf{x_f})dA, \quad (5.1)$$

where ρ, $\mathbf{u}$, p, $\boldsymbol{\tau}$, μ_s and σ are the density, the velocity vector, the pressure, the polymer stress tensor, the solvent viscosity and the surface tension coefficient, respectively. The flow is driven by an applied constant pressure gradient $\frac{dp_o}{dy}\mathbf{j}$, where $\mathbf{j}$ is a unit vector in the streamwise direction . In Eq. (5.1), the last term on the right hand side represents the surface tension where A is the surface area, κ is twice the mean curvature, $\mathbf{n}$ is the unit normal vector and ∇_s is the gradient operator along the interface defined as

$$\nabla_s = \nabla - \mathbf{n}(\mathbf{n}\cdot\nabla). \quad (5.2)$$

It is important to note that the surface tension is a function of the interfacial surfactant concentration Γ and $\nabla_s\sigma(\Gamma)$ represents the surfactant-induced Marangoni stress. The momentum equations are supplemented by the incompressibility condition

$$\boldsymbol{\nabla} \cdot \mathbf{u} = 0. \tag{5.3}$$

The fluid properties remain constant along material lines, i.e.,

$$\frac{D\rho}{Dt} = 0, \frac{D\mu_s}{Dt} = 0, \frac{D\mu_p}{Dt} = 0, \frac{D\lambda}{Dt} = 0, \tag{5.4}$$

where $\frac{D}{Dt} = \frac{\partial}{\partial t} + \mathbf{u} \cdot \nabla$ is the material derivative. The indicator function is used to set the material properties in each phase and is defined as

$$I(\mathbf{x}, t) \;\; = \begin{cases} 1 & \text{in bulk fluid,} \\ 0 & \text{in bubble domain.} \end{cases} \tag{5.5}$$

Then a material property, ϕ, is specified as

$$\phi = \phi_o I(\mathbf{x}, t) + \phi_i \left(1 - I(\mathbf{x}, t)\right), \tag{5.6}$$

where the subscripts "i" and "o" denote the properties of the bubble and bulk fluid, respectively.

The present soluble surfactant methodology is developed in one of our earlier works ([22, 180]) and have been extensively used for various studies [182, 183, 103] so far. The method is briefly described below for completeness. The local value of the surface tension coefficient is related to the local surfactant concentration through the Langmuir equation of state [184] as

$$\sigma = \sigma_s \left[1 + \beta_s \ln\left(1 - \frac{\Gamma}{\Gamma_\infty}\right)\right], \tag{5.7}$$

where σ_s is the surface tension of surfactant-free interface, β_s is the elasticity number, Γ is the concentration of surfactant on the interface and Γ_∞ is the maximum packing concentration. Equation (3.6) is bounded to prevent nonphysical (negative) values of the surface tension:

$$\sigma = \sigma_s \left[\max\left(\epsilon_\sigma, 1 + \beta_s \ln\left(1 - \frac{\Gamma}{\Gamma_\infty}\right)\right)\right], \tag{5.8}$$

where ϵ_σ is taken as 0.05 in the present study. Note that ϵ_σ is typically larger than this value in the common physical systems (e.g., $\epsilon_\sigma \sim 0.2 - 0.3$) but it does not have any influence on the present results since the interfacial surfactant concentration remains much lower than the maximum packing concentration in all the cases considered here. The evolution equation for the interfacial surfactant concentration was derived by Stone [185] and can be expressed as

$$\frac{D\Gamma A}{Dt} = AD_s\nabla_s^2\Gamma + A\dot{S}_\Gamma, \tag{5.9}$$

where A is the surface area of an element of the interface and D_s is the diffusion coefficient along the interface. The source term $\dot{S}_\Gamma$ is given by

$$\dot{S}_\Gamma = k_a C_s(\Gamma_\infty - \Gamma) - k_b\Gamma, \tag{5.10}$$

where k_a and k_b are the adsorption and desorption coefficients and C_s is the bulk surfactant concentration (C) near the interface. The bulk surfactant concentration is governed by an advection-diffusion equation of the form

$$\frac{\partial C}{\partial t} + \nabla\cdot(C\mathbf{u}) = \nabla\cdot(D_{co}\nabla C). \tag{5.11}$$

The coefficient D_{co} is related to the molecular diffusion coefficient D_c and the phase indicator function I as

$$D_{co} = D_c\left(1 - I(\mathbf{x},t)\right). \tag{5.12}$$

The source term in Eq. (5.10) is related to the bulk surfactant concentration by

$$\dot{S}_\Gamma = -D_{co}(\mathbf{n}\cdot\nabla C|_{\text{interface}}). \tag{5.13}$$

The boundary condition at the interface given by Eq. (5.13) is first converted into a source term for the bulk surfactant evolution equation. In this approach, it is assumed that all the mass transfer between the interface and bulk takes place in a thin adsorption layer adjacent to the interface. Thus, the total amount of mass adsorbed on the interface is distributed over the adsorption layer, and added to the bulk concentration evolution equation as a negative source term. Equation (5.11) thus takes the following form:

$$\frac{\partial C}{\partial t} + \nabla \cdot (C\mathbf{u}) = \nabla \cdot (D_{co} \nabla C) + \dot{S}_c, \tag{5.14}$$

where $\dot{S}_c$ is the source term evaluated at the interface and distributed onto the adsorption layer in a conservative manner. The details of this treatment can be found in the paper by Muradoglu et al. [180].

The FENE-P model is adopted as the constitutive equation for the polymeric stress tensor $\boldsymbol{\tau}$ [181, 55]. In this model, the polymer conformation tensor $\mathbf{B}$ evolves by

$$\begin{aligned} \frac{\partial \mathbf{B}}{\partial t} + \nabla \cdot (\mathbf{u}\mathbf{B}) - (\nabla \mathbf{u})^T \cdot \mathbf{B} - \mathbf{B} \cdot \nabla \mathbf{u} &= -\frac{1}{\lambda} \left(F\mathbf{B} - \mathbf{I} \right), \\ F &= \frac{L^2}{L^2 - \mathrm{trace}(\mathbf{B})}, \end{aligned} \tag{5.15}$$

where λ, L, and $\mathbf{I}$ are the polymer relaxation time, the maximum polymer extensibility and the identity tensor, respectively. Once the conformation tensor is obtained from Eq. (5.15), the polymeric stress tensor is computed as

$$\boldsymbol{\tau} = \frac{\mu_p}{\lambda} \left(F\mathbf{B} - \mathbf{I} \right), \tag{5.16}$$

where μ_p is the polymeric viscosity. The viscoelastic constitutive equations are highly non-linear and become extremely stiff at high Weissenberg numbers. Thus, their numerical solution is generally a formidable task and is notoriously difficult especially at high Weissenberg numbers [181, 55]. To overcome the so-called high Weissenberg number problem, the log-conformation method is employed [186] in the present simulations. In this approach, Eq. (5.15) is rewritten in terms of the logarithm of the conformation tensor through eigen decomposition, i.e., $\boldsymbol{\Psi} = \log \mathbf{B}$, which ensures the positive definiteness of the conformation tensor.

The flow equations (Eq. (2.2)) are solved fully coupled with the FENE-P model and the interfacial and bulk surfactant concentration evolution equations. All the field equations are solved on a fixed Eulerian grid with a staggered arrangement where the velocity nodes are located at the cell faces while the material properties,

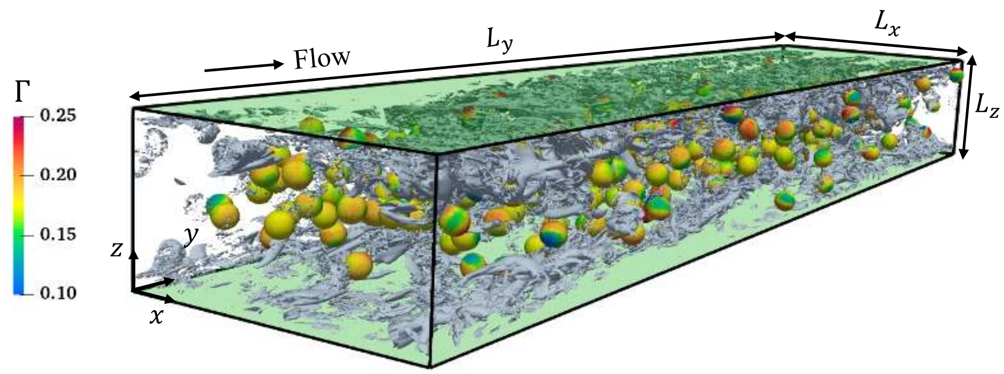

Figure 5.1: The computational domain is shown with $L_x = 4h$, $L_y = 18h$ and $L_z = 2h$ for the HDR cases. For the MDR cases, length of the channel in the streamwise direction is increased to $L_y = 28h$. Constant contours of $Q - criterion$ are shown around the contaminated bubbles at a value of 100 in the HDR regime. The contours on the bubble surface represent interfacial surfactant concentration ($Re_\tau = 180, Wi = 7, Ca = 0.01, \beta = 0.9$).

the pressure, the bulk surfactant concentration and the extra stresses are all located at the cell centers [181]. The interfacial surfactant concentration evolution equation is solved on a separate Lagrangian grid [180]. The spatial derivatives are discretized with second-order central differences for the diffusive terms, while the convective terms are discretized using a QUICK scheme [187] in the momentum equation, and a fifth-order WENO-Z [57] scheme in the viscoelastic and the bulk surfactant concentration equations. The equations are integrated in time with a second-order predictor-corrector method in which the first-order solution (Euler method) serves as a predictor that is then corrected by the trapezoidal rule [20]. Further details of the front-tracking method can be found in the review paper by Tryggvason et al. [20] and in the book by Tryggvason [21].

5.3 Computational Setup

The computational domain is a rectangular channel as shown in Figure 5.1. Periodic boundary conditions are applied in the streamwise (y) and spanwise (x) directions whereas no-slip/no-penetration conditions are applied in the wall-normal (z) direction. The domain size is $4h \times 18h \times 2h$ resolved by $360 \times 1728 \times 288$ grid points in the x, y, and z directions, respectively. As two distinct flow regimes are explored in the present study, the length of the channel is set to $18h$ for the HDR regime whereas the channel length is increased to $28h$ with a streamwise (y) grid resolution of 2592 grid points for the MDR regime. A hyperbolic tangent mapping function is used to slightly stretch the grid in the wall-normal (z) direction, defined as

$$z(k) = 1 + \frac{\tanh\left[\gamma\left(\frac{2k}{N_z} - 1\right)\right]}{\tanh(\gamma)}, \tag{5.17}$$

where the stretching parameter γ is set to 1.43. The resulting inner scaled resolution is $\Delta x^+ = \Delta y^+ = 1.875$ and $\Delta z^+ \leq 0.498$.

The flow is characterized by the following non-dimensional numbers defined as

$$Re = \frac{\rho_o V_o h}{\mu_o},\ Wi = \frac{\lambda V_o}{h},\ Ca = \frac{\mu_o V_o}{\sigma},\ \beta = \frac{\mu_s}{\mu_o}, \tag{5.18}$$

where Re, Wi, Ca are the Reynolds, the Weissenberg and the capillary numbers, respectively. Further, β is the ratio of solvent viscosity to zero shear viscosity of the viscoelastic fluid, ρ_o is the density of the of bulk fluid, V_o is the average velocity in the channel and h is half of the channel width. The value of β is fixed at 0.9, representing a dilute polymer solution. The single-phase turbulent channel flow is generated by initializing the flow field with a streamwise-aligned vortex pair [188], which effectively triggers transition to turbulence. The friction Reynolds number is $Re_\tau = v_\tau h/\nu_o = 180$ ($Re = 2800$). Here, the friction velocity is $v_\tau = \sqrt{\overline{\tau}_{wall}/\rho_o}$, where $\overline{\tau}_{wall}$ is the average total wall shear stress and ν_o is the kinematic viscosity of the liquid. All the multiphase simulations are performed for mono-dispersed bubbles, which are initially distributed randomly in a fully developed viscoelastic turbulent flow. The bubbles are initialized with a spherical shape by setting a very low value of capillary number ($Ca = 0.01$). For all the simulations, the density (ρ_o/ρ_i) and viscosity (μ_o/μ_i) ratios are set to 10. Although in a typical liquid-air system, the density ratio is an order of magnitude higher than the one used here, it has been previously demonstrated ([64], [65]) that the results are not affected significantly at higher ratios for these kind of flows specially under non-buoyant conditions. A smaller property ratio enhances numerical stability, relaxes the time step restrictions and hence reduces the computational cost. The physical parameters governing the flow are listed in Table 5.1.

Table 5.1: Physical and computational parameters governing the flow

Total pressure gradient	$\frac{dp_o}{dy}$	-1
Friction Reynolds Number	Re_τ	180
Weissenberg Number	Wi	0/7/24
Capillary Number	Ca	0.01
Solvent to total viscosity ratio	β	0.9
Maximum extensibility parameter	L_{max}	120
Single-phase average bulk velocity ($Wi = 0$)	V_o	15.55556

The sorption kinetic properties of Triton X-100 surfactant, widely used in experimental studies [189], is considered in the present work. The corresponding physical adsorption (k_a) and desorption (k_d) properties are taken from Takagi et al. [190]. For Triton X-100, $k_a = 50\ m^3\ mol^{-1}\ s^{-1}$ and $k_d = 0.033\ s^{-1}$. Triton X-100 is adsorbed by the interface much faster and is desorbed back into the bulk fluid much slowly, which makes Triton X-100 a very effective surfacant. The non-dimensional numbers related to the surfactant physical properties are listed in Table 5.2. C_{ref} denotes the reference bulk surfactant concentration, taken as the critical micelle concentration and Γ_{max} represents the maximum packing concentration. The C_{ref} values for the Triton X-100 used is 1 ppm. We note that the actual values of the Peclet number are much larger than the values in Table 5.2 but the Peclet number is kept small to avoid thin mass boundary layer at the interface that requires excessive grid resolution.

Table 5.2: Non-dimensional surfactant parameters for Triton X-100

Peclet number	$Pe_c = Pe_s = hV_b/D_c$	777
Biot number	$Bi = hk_d/V_b$	2×10^{-3}
Damkohler number	$Da = \Gamma_{max}/hC_{ref}$	0.456
Langmuir number	$La = k_a C_{ref}/K_d$	2.2
Elasticity number	$\beta_s = RT\Gamma_\infty/\sigma_s$	0.5

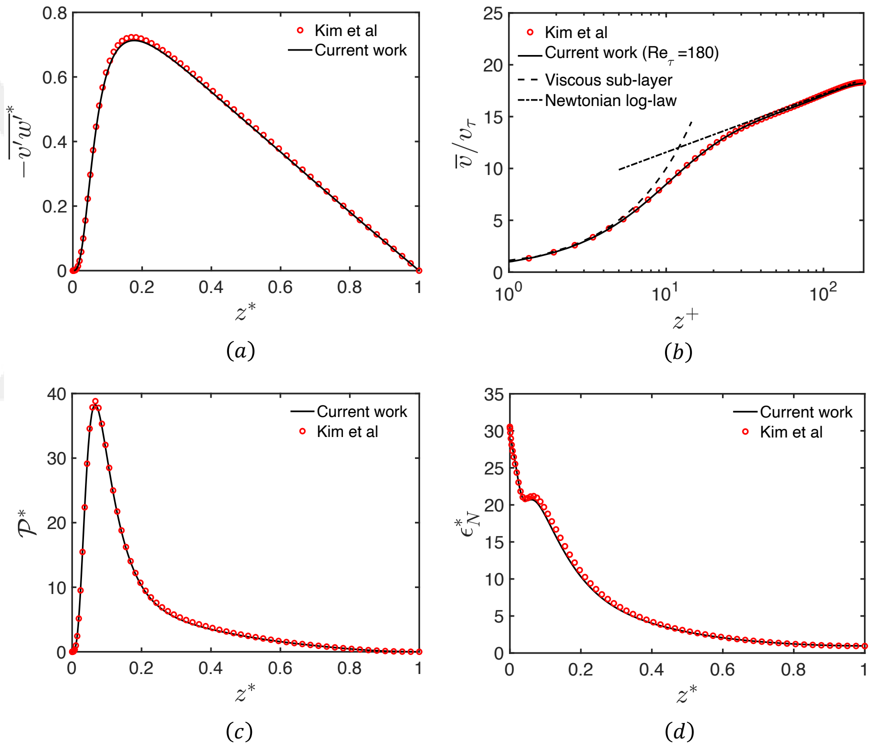

Figure 5.2: (a) Reynolds stress, (b) mean velocity profile, (c) turbulence production and (d) the viscous dissipation in a Newtonian flow compared against the results of Kim et al. [3] at $Re_\tau = 180$

5.4 *Results and Discussion*

Based upon the work of Dallas et al. [151], two different channel lengths are selected in the present study to achieve drag reduction in the limits of HDR ($40\% \leq DR \leq 60\%$) and MDR (DR $> 60\%$) for a single-phase flow. These domains are referred

Table 5.3: Computational parameters of the simulations and the drag reduction achieved in each case

Re_τ	Re	Wi	$\Phi(\%)$	N_b	$L_x \times L_y \times L_z$	$N_x \times N_y \times N_z$	$DR(\%)$
180	2800	0	0	0	$4h \times 18h \times 2h$	$360 \times 1728 \times 288$	0
	3880	7	0	0	$4h \times 18h \times 2h$	$360 \times 1728 \times 288$	49
	3888	7	3	305	$4h \times 18h \times 2h$	$360 \times 1728 \times 288$	50
	4000	7	9	917	$4h \times 18h \times 2h$	$360 \times 1728 \times 288$	52
180	2800	0	0	0	$4h \times 28h \times 2h$	$360 \times 2592 \times 288$	0
	4770	24	0	0	$4h \times 28h \times 2h$	$360 \times 2592 \times 288$	68
	4860	24	3	475	$4h \times 28h \times 2h$	$360 \times 2592 \times 288$	69
	5000	24	9	1426	$4h \times 28h \times 2h$	$360 \times 2592 \times 288$	70

as the HDR domain and the MDR domain in this study. Simulations are started with a Newtonian turbulent flow in both the domains at $Re_\tau = 180$ ($Re = 2800$). The statistics of Newtonian turbulent flow are compared with the results of Kim et al. [3] for validation and a good agreement is observed, as shown in Figure 5.2. Once the Newtoninan turbulent flow reached its statistical steady state, the flow is made viscoelastic and the Weissenberg number is gradually increased until the drag reduction is achieved in the limit of HDR ($40\% \leq DR \leq 60\%$) and MDR (DR $> 60\%$) in the respective domains for a single-phase flow. Subsequently, the contaminated bubbles are injected into these fully developed single-phase viscoelastic flows with two different volume fractions (Φ); 3% and 9%. A dilute polymer solution ($\beta = 0.9$) is used for all these simulations and the capillary number is fixed at a low value of 0.01 for all the multiphase cases to maintain the approximate spherical bubble shapes. The properties of an industrial grade surfactant, Triton X-100 (table 5.2), are used to contaminate the bubbles based upon the observations made in our earlier work [107]. A total of eight simulations are performed for which the computational parameters are provided in table 5.3.

5.4.1 Turbulent statistics of multiphase HDR and MDR regimes

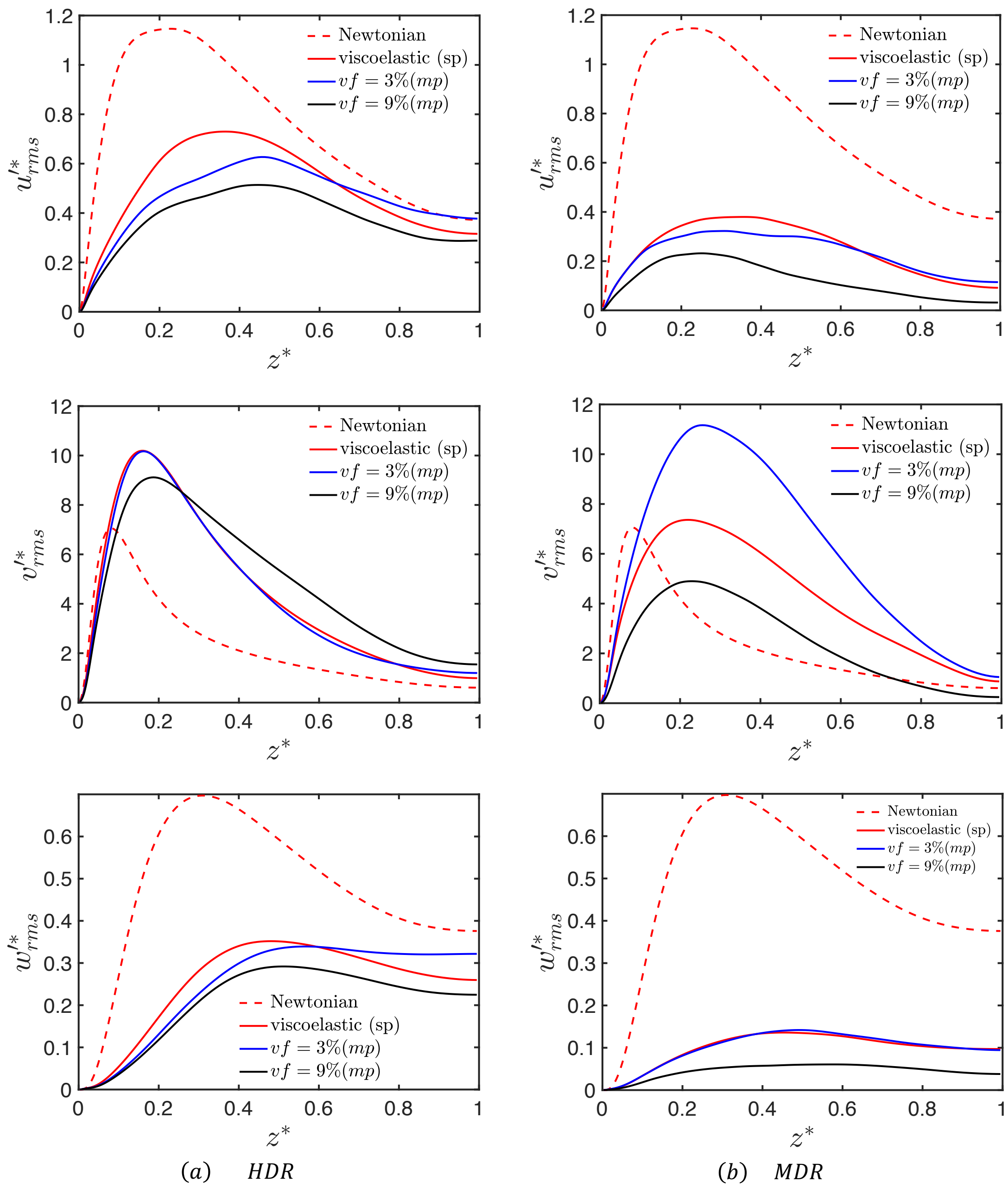

Figure 5.3: Velocity fluctuations normalized by v_τ in the spanwise (u'^{*}_{rms}), streamwise (v'^{*}_{rms}) and wall-normal (w'^{*}_{rms}) directions for the single-phase and multiphase cases in the (a) HDR and (b) MDR flow regimes ($Ca = 0.01, \beta = 0.9$)

In the HDR domain, a maximum drag reduction of 49% is observed for the single-phase viscoelastic flow at $Wi = 7$. The LDR and HDR regimes are primarily differentiated based upon different statistical trends [167]. After the onset of drag reduction, the streamwise velocity fluctuations are enhanced while the spanwise and wall-normal fluctuations are suppressed in both the LDR and HDR regimes as compared to the Newtonian turbulent flow. The same is observed in the HDR domain with $DR = 49\%$ (Fig. 5.3). Once the contaminated bubbles are injected into the flow with a small volume fraction of 3%, the streamwise fluctuations remained the same while the spanwise and streamwise fluctuations are slightly suppressed, except in the central region of the channel where these fluctuations are increased as compared to the single-phase flow. With a higher concentration of bubbles ($\Phi =$ 9%), the spanwise and the wall-normal fluctuations are further suppressed whereas the streamwise fluctuations are found to be increasing towards the central region of the channel. In addition to these interesting trends of velocity fluctuations due to the presence of bubbles, it is found that the the overall drag is not increased once the bubbles are injected into the flow at both the concentrations. Rather, the skin friction drag further reduces to 50% and 52% in this HDR domain with a bubble volume fraction of 3% and 9%, respectively. This trend is opposite to what is observed in case of solid particle suspensions in the LDR regime, as reported by Esteghamatian and Zaki [178, 179]. Since bubbles in the present study have the same spherical shape as particles, this demonstrates the effect of boundary conditions (slip) on the bubble surfaces.

Once the channel length is increased to $28h$ (MDR domain), a maximum drag reduction of 68% is achieved for the single-phase flow at $Wi = 24$. The statistical trends of velocity fluctuations are compared with those of HDR regime in Figure 5.3. Unlike the HDR regime, the streamwise velocity fluctuations are not enhanced and their peak value remains almost similar to single-phase flow. However, the peak of v'_{rms} is slightly shifted towards the channel center. The spanwise and wall-normal fluctuations are significantly suppressed in this single-phase MDR regime. Once bubbles are injected into this MDR regime with a volume fraction of 3%, the streamwise fluctuations are significantly enhanced. This result is in contrast to

HDR regime where streamwise fluctuations were unaffected by bubbles. The wall-normal fluctuations remain at the same level of single-phase flow while the spanwise fluctuations are slightly reduced. Once the bubble concentration is increased to 9% in this MDR regime, the streamwise fluctuations now decrease below the value of single-phase flow, hence showing a non-monotonic trend with bubble concentration in MDR. Meanwhile, the spanwise and wall-normal fluctuations are reduced further. The drag reduction trend continues in this MDR regime as well and instead of increasing with the presence of bubbles, the drag reduces further to 69% & 70% with a volume fraction of 3% and 9%, respectively. The reasons behind this non-monotonic trend in the streamwise fluctuations and drag reduction with the presence of bubbles will be elaborated in the subsequent paragraphs by analyzing some other statistical quantities of these turbulent flow regimes.

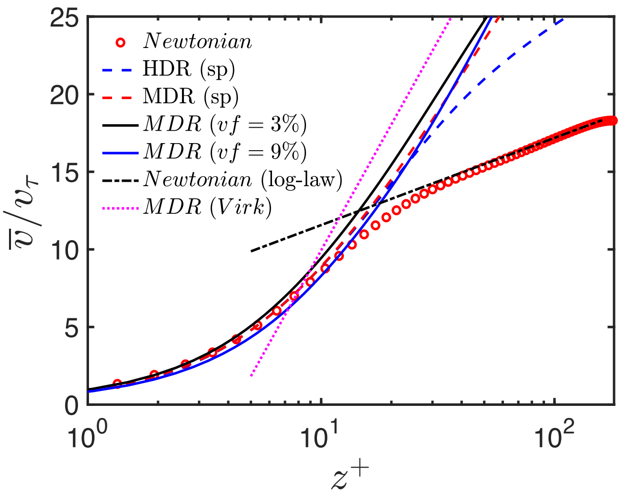

Figure 5.4: Mean velocity profiles in the HDR and MDR regimes compared against the log-law of Newtonian turbulent flow and the maximum asymptote proposed by Virk [4]

The difference between LDR and HDR regimes does not remain limited to different statistical trends in the velocity fluctuations. One of the earlier three layer models proposed by Virk [167] to explain the phenomenon of drag reduction focuses on the buffer layer and the mean velocity profile remains parallel to Newtonian flow in the logarithmic range. This model remains applicable to LDR regime only. In the HDR regime, the drag reduction is governed by different mechanism where the effects of drag reduction are observed beyond the buffer layer as well [191] and the mean velocity profile deviates from the Newtonian log-law, as shown in Fig. 5.4. The slope of mean velocity profile keeps increasing with the reduction in drag and becomes parallel to Virk's profile in the limit of MDR. Once bubbles are injected into the flow, the mean velocity profile gets further closer to MDR asymptote of Virk's due to further reduction in drag. Interestingly, by changing the bubbles concentrations in the MDR regime, the change in velocity profiles is observed in the buffer layer as well due to bubble dynamics and with $\Phi = 9\%$, 70% drag reduction is observed and the slope becomes almost parallel to Virk's. As the near wall structures get coarsened both in the streamwise and spanwise directions with the reduction in drag as compared to the structures in Newtonian flow ([192], [193]), the length of domain size plays a crucial role in the DNS studies of dilute polymer solutions and therefore, the domain size is increased for the MDR simulations [172]. However, as this drag reduction limit is a highly dynamical state which depends upon the domain length, the Weissenberg number, the Reynolds number, concentration of polymers (β), extensibility parameter in the FENE-P model and the time-averaging span used in calculating the turbulent statistics, the profile of mean velocity with 70% drag reduction although becomes parallel to Virk's but does not overlap it perfectly (Fig. 5.4). The overlap can be achieved by changing the extensibility parameter (L) and the polymer concentration β, which are fixed in the present study. For a multiphase viscoelastic channel flow, the average total shear stress of the bulk fluid in the wall-normal direction (z) is given by

$$\underbrace{\overline{\tau}_w(1-z)}_{\overline{\tau}_{yz}} = \underbrace{\overline{\mu_o \frac{\partial v}{\partial z}}}_{\overline{\tau}_N} - \underbrace{\overline{\rho_o v' w'}}_{\overline{\tau}_R} + \overline{\tau}_p + \underbrace{\int_0^z \overline{F}_\sigma \, dz}_{\overline{\tau}_s}, \tag{5.19}$$

$$F_\sigma = \int_A \left[\sigma(\Gamma)\kappa \mathbf{n} + \nabla_s \sigma(\Gamma)\right] \delta(\mathbf{x} - \mathbf{x_f}) dA. \tag{5.20}$$

where $\overline{\tau}_w$ is the average wall shear stress which is composed of viscous stress $\overline{\tau}_N$, the Reynolds stress $\overline{\tau}_R$, the polymeric shear stress $\overline{\tau}_p$ and the shear stress contribution due to the surface tension of bubbles $\overline{\tau}_s$. The surface tension is further dependent upon the surfactant-induced Marangoni stress, as described in equation 5.20. Figure 5.5 shows the distribution of all these components of shear stress in the channel for all the single-phase and multiphase cases of HDR and MDR regimes. In the HDR regime, the trends remain monotonic. With the addition of polymers, the Reynolds stress reduces significantly indicating the laminarization of the flow state with the reduction in drag. The effect of this reduction in the Reynolds stress can be visualized in the buffer layer, where the streaks of streamwise velocity fluctuations are stabilized (aligned & thickened) and the strength of vortices is reduced with the addition of polymers (Fig. 5.5c & d). When the bubbles are injected, the Reynolds stress reduces further with a further decrease in drag. At the wall, the viscous stress also reduces as the overall shear stress balance is augmented by the addition of polymeric stress. It is important to note that although the Reynolds stress is reduced significantly as the polymeric stress starts to rise in the viscoelastic flow, $\overline{\tau}_R$ still remains higher than $\overline{\tau}_p$ in this HDR regime. As the applied pressure gradient is kept constant in this scenario, the mean velocity increases in the channel with the reduction in drag and the viscous stress increases away from the wall as compared to the Newtonian case. This trend remains the same with the addition of bubbles in the HDR regime with an additional contribution of $\overline{\tau}_s$ by the bubbles. As expected, the contaminated bubbles remain away from the channel wall and remain randomly distributed in the entire channel as observed in our earlier study of the LDR regime [107].

In the MDR regime, a further decrease in the Reynolds stress is observed in a single-phase viscoelastic flow indicating a further laminarization of the flow. However, in this MDR regime, polymeric shear stress becomes larger than the Reynolds stress (Fig. 5.5(b)). As described by Xi [177], the turbulent flow regime is mainly governed by the elastic stresses in the limit of MDR. In the buffer layer, the effects remain similar to HDR, *i.e.*, the velocity streaks are stabilized and the quasi-

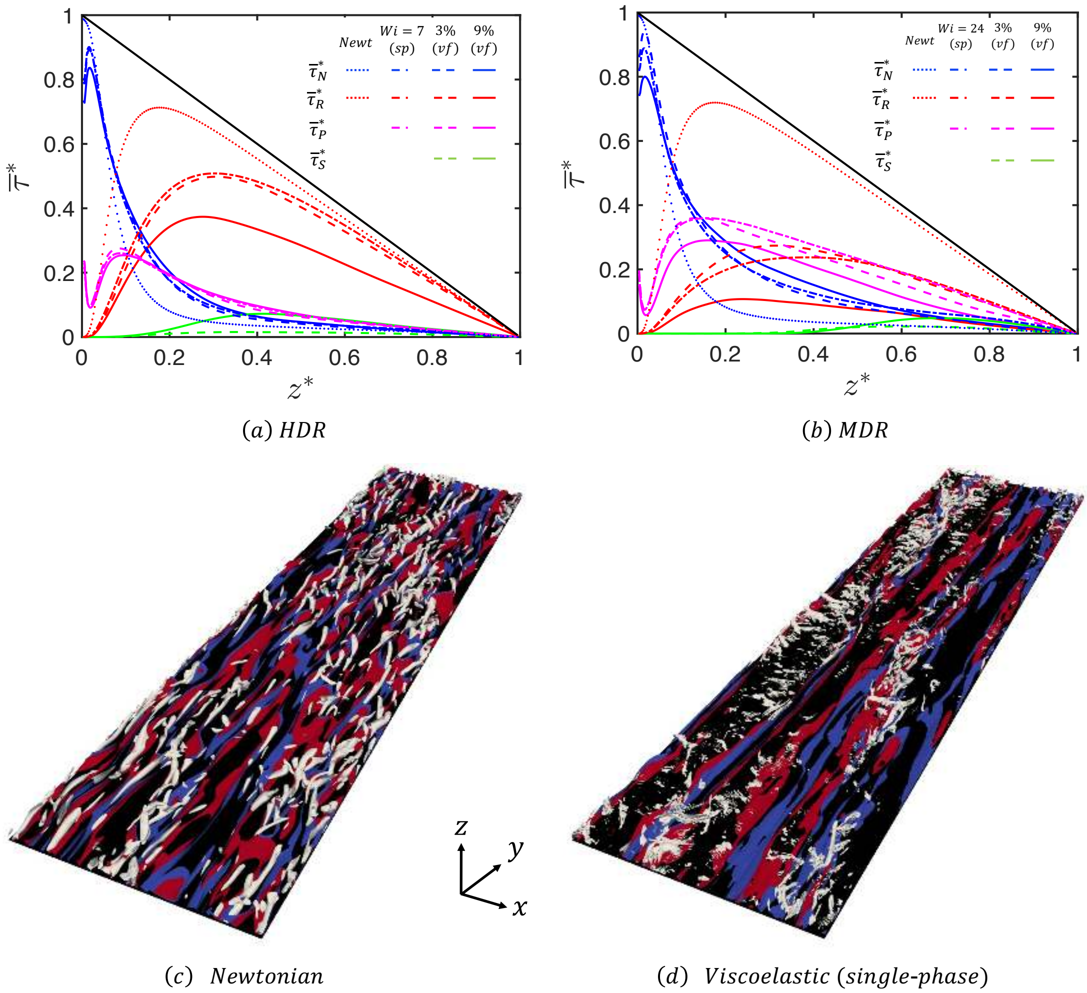

Figure 5.5: The comparison of shear stress balance between single-phase and multi-phase flows with 3 & 9% volume fractions is shown in the (a) HDR and (b) MDR regimes. The streaks of streamwise velocity fluctuations (positive red and negative blue color) and the iso-surfaces of *Q-criterion* (gray color) are shown in the buffer layer ($15 \leq z^+ \leq 30$) at a value of 400 for (c) the Newtonian and for the (c) single-phase viscoelastic flow in the HDR regime. The channel wall is marked with the black color in the background.

streamwise vortices are reduced (not shown here for brevity). The most interesting dynamics are observed with the addition of small concentration of bubbles ($\Phi = 3\%$). Instead of further decrease in the Reynolds stress, a slight increase is observed while the viscous stress also increases slightly at the wall. However, the polymeric stress reduces in the corresponding region away from the wall where the Reynolds stress is increased and the overall DR is not affected. A significant rise in the streamwise velocity fluctuations (Fig. 5.3b) and a rise in $\overline{\tau}_R$ with the addition of 3% bubbles in the limit of MDR indicate an increase in the turbulence intensity of the flow. However, as the flow is mainly dominated by the elastic stresses, this rise in $\overline{\tau}_R$ does not increase the drag again. Once the bubbles volume fraction is increased to 9% ($N_b = 1426$), a non-monotonic trend is observed. The Reynolds stress decreases significantly below the value of single-phase flow along with the viscous and the polymeric stresses and the DR further reduces to 70%. The value of $\overline{\tau}_s$ increases slightly due to higher number of bubbles. These non-monotonic trends will be discussed further in §5.4.2.

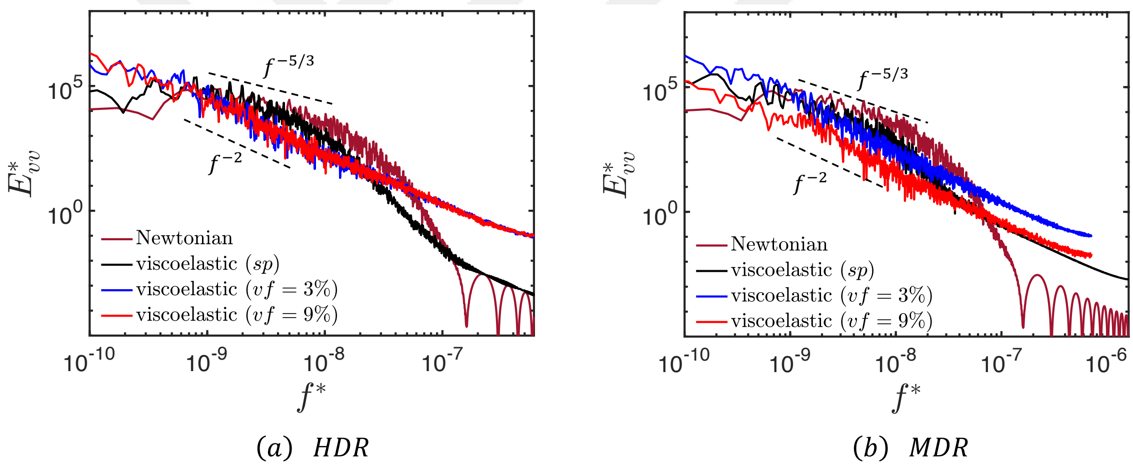

Figure 5.6: 1D energy spectrum of the single-phase and multiphase viscoelastic cases in the (a) HDR and (b) MDR regimes are compared with the Newtonian turbulent flow in their respective domains.

The three components of flow velocity are monitored at each time step at two different locations of each domain. One of these 'numerical probes' is located at the center of the channel ($x^* = h$, $y^* = 9h/14h$, $z^* = h$) and the other at 25% distance ($x^* = h$, $y^* = 9h/14h$, $z^* = 0.5h$) from one of the walls. 1D energy spectra of streamwise velocity component are shown in Fig. 5.6 for the single-phase and multiphase cases of HDR and MDR regimes. For the multiphase cases, the flow velocity inside the bubbles is filtered out from the signal. As the drag reduces with the addition of polymers in the HDR domain, the scaling of kinetic energy spectrum changes from classical $-5/3$ to -2 in the inertial range. At the higher frequencies of inertial turbulence (dissipation range), single-phase viscoelastic flow shows a higher energy content as compared to the Newtonian flow for the same frequency range (Fig. 5.6a). It is due to the fact that the classical energy cascade gets terminated above the Kolmogorov length scale with the addition of polymers and the smallest length scales are now dominated by the elastic effects [161]. Once bubbles are injected into the flow, the energy spectrum shows a scaling of -2 for the entire range. By increasing the bubble concentration, this scaling of energy spectrum does not change indicating a similar flow state. This effect becomes more pronounced in the limit of MDR. In this case, the single-phase viscoelastic flow also shows the scaling of -2 in almost the entire range when compared with the Newtonian turbulent flow (Fig. 5.6b). The non-monotonic trend of Reynolds shear stress by changing the bubbles concentration in the MDR regime is visible in their energy spectra as well. Unlike the HDR regime where the plots of energy spectra for both the bubble concentrations overlap each other, the energy spectrum shows a lower energy content in the MDR regime with $\Phi = 9\%$, due to further decrease in drag and laminarization of the flow. However, its slope still remains -2.

At a statistically steady state, the evolution equation of turbulent kinetic energy for a single-phase viscoelastic channel flow provides a balance between turbulence production
($\mathcal{P} = \overline{u_i'u_j'}(\partial\overline{u_i}/\partial x_j)$), viscous dissipation ($\epsilon_N = \nu_s\overline{(\partial u_i'/\partial x_j)(\partial u_i'/\partial x_j)}$) and the polymer work ($\epsilon_p = (1/\rho_o)\overline{u_i'(\partial\tau_{ij}'/\partial x_j)}$). The prime indicates fluctuation and the symbol 'bar' over any quantity indicates the averaging in space (streamwise and spanwise) and time. In the presence of bubbles, an additional body force term ($\Psi_b = \overline{u_i'f_i'}$) is added to TKE budget, where f' is the fluctuating component of force due to bubble surface tension. Assuming a homogeneous flow in the spanwise (x) and streamwise (y) directions once the flow reaches a statistically steady state, the integration of TKE budget in the wall-normal (z) direction gives

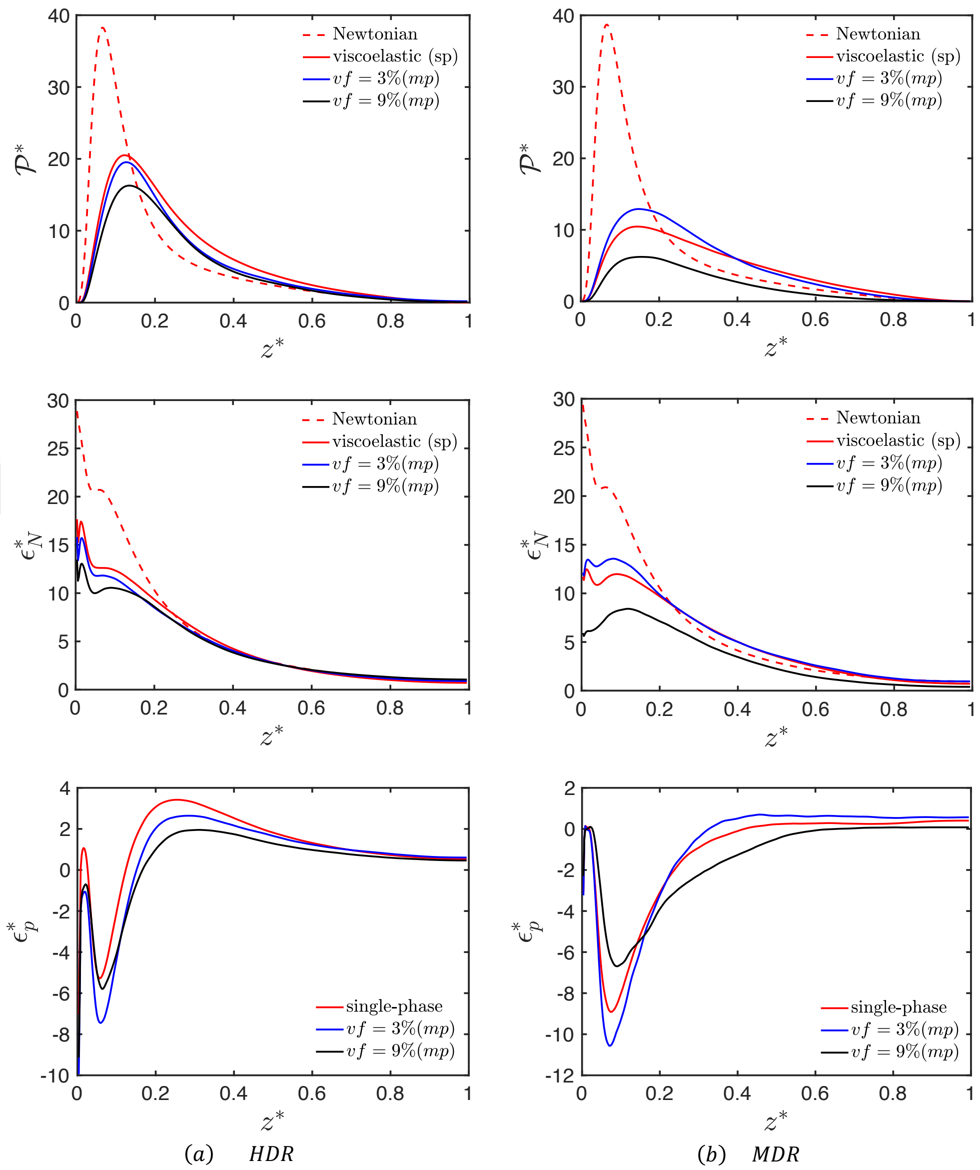

Figure 5.7: Turbulence production ($\mathcal{P}^*$), viscous dissipation (ϵ_N^*) and the viscoelastic work (ϵ_p^*) normalized by v_τ^3/h compared in the (a) HDR and (b) MDR regimes for the single-phase and multiphase cases

$$\int \mathcal{P}\, dz = \int \epsilon_N\, dz + \int \epsilon_p\, dz + \int \Psi_b\, dz. \tag{5.21}$$

The production term serves to exchange kinetic energy between the mean flow and turbulence. This turbulence is dissipated by the fluid viscosity. The polymeric work may contribute towards dissipation or production of TKE depending upon the sign of fluctuating viscoelastic stresses [150]. Figure 5.7 shows the distribution of $\mathcal{P}$, ϵ_N and ϵ_p in the HDR and MDR regimes for all the single-phase and multiphase cases shown in table 5.3. These terms are normalized by v_τ^3/h. In a Newtonian turbulent flow, the turbulence production term reaches its peak value in the buffer layer at the intersection point of Reynolds and the viscous stresses (when $-\overline{v'w'} = \nu_s(\partial\overline{v}/\partial z)$), as shown by [194]. In the HDR and MDR regimes, the peak value of P slightly shifts away from the wall indicating an increase in the thickness of the buffer layer. The injection of bubbles in the HDR regime reduces the production term monotonically with the increase in bubble concentration. However, in the MDR regime, a small bubble concentration increases the peak value of turbulence production but the higher concentration of bubbles reduces it below the value of the single-phase viscoelastic case (Fig. 5.7b). This non-monotonic trend continues to show its effect in the distribution of viscous dissipation as well. The viscoelastic work in the HDR regime of a single-phase flow is positive very close to the wall and then becomes negative in the buffer layer. The negative value of ϵ_p shows its contribution towards turbulence production instead of dissipation. ϵ_p shows a positive peak away from the buffer layer towards the channel center and then gradually decays to a minimum positive value at the channel center. The same trend is observed in the multiphase cases of HDR regime except very close to wall where ϵ_p remains negative as the presence of contaminated bubbles suppresses its peak value. In the MDR regime, with a small bubble concentration of 3%, the negative peak of ϵ_p in the buffer layer increases but the same is reduced with 9% bubble volume fraction. The flow is mainly dominated by the elastic effects and a small bubble concentration increases the contribution of polymer work towards turbulence production. A higher bubble concentration, however, reduces this contribution. At the channel center, it is interesting to note that ϵ_p decays to zero with $\Phi = 9\%$ whereas the single-phase flow and the multiphase case with $\Phi = 3\%$ still remain slightly positive (Fig. 5.7b).

The last term Ψ_b of equation 4.6 is plotted for the multiphase cases of HDR and MDR regimes along with the average volume fractions of bubbles in Fig. 5.8. As

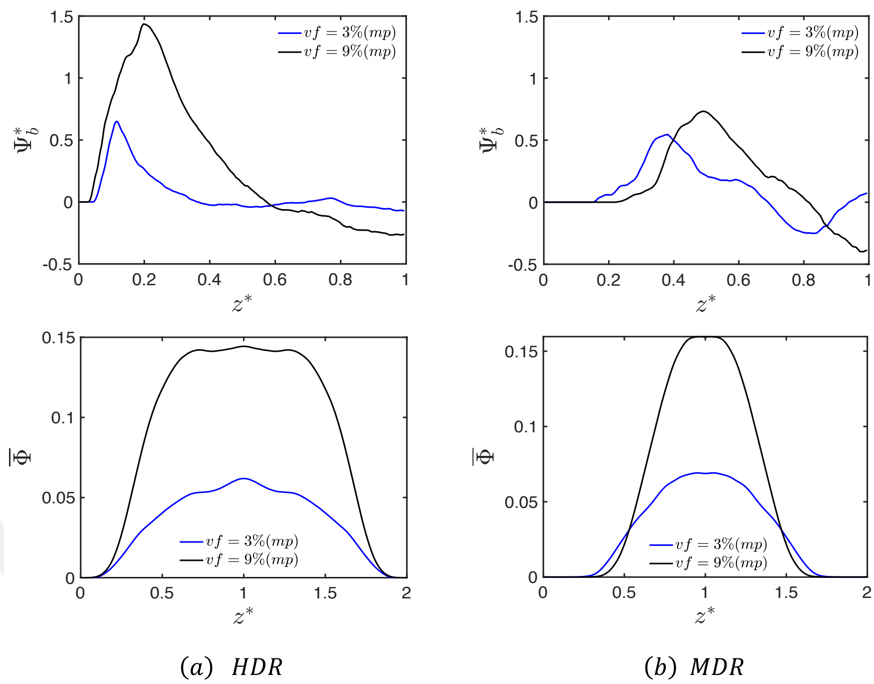

Figure 5.8: Body force term $\Psi_b = \overline{u_i' f_i'}$ normalized by v_τ^3/h and the average void fraction ($\overline{\Phi}$) plotted for the multiphase cases in the (a) HDR and (b) MDR flow regimes

the bubbles are contaminated with Triton X-100, the bubble layers at the channel walls are completely avoided in both the HDR and MDR regimes. However, in the HDR regime, the bubble distribution starts slightly away from the walls while in the MDR regime, the bubbles remain densely concentrated in the core region of the channel. As viscoelasticity promotes migration towards the channel center [141], the shift of bubble's equilibrium position towards the channel center at $Wi = 24$ in the MDR regime is understandable. However, at the higher volume fraction, bubbles accumulate further towards the core compared to the lower volume fraction case. The body force term Ψ_b of equation 4.6 shows its peak value away from the core region in HDR as well as in the MDR regime. When the number of bubbles is increased in HDR, the positive peak of Ψ_b increases significantly and slightly shifts away from the channel wall. At the channel center, where the maximum number of bubbles is aggregated, this body force term in TKE budget reverses its role and becomes negative and contributes towards turbulence production. In the MDR regime, the positive peak of Ψ_b with $\Phi = 9\%$ remains significantly lower than the corresponding case in the HDR regime. As the Reynolds stresses already become very low in the single-phase flow of MDR regime, the body force term cannot dissipate the turbulence beyond a certain point. At the channel center, Ψ_b becomes negative with 9% volume fraction of bubbles while it becomes slightly positive with $\Phi = 3\%$, indicating different roles played by the bubbles with different concentrations in this MDR regime. The complex dynamics of bubbles and the resultant impact on these turbulent flow regimes will be discussed further in §5.4.2.

The distribution of turbulent kinetic energy ($\mathcal{K} = \frac{1}{2}\overline{u_i'u_i'}$) of the flow in the HDR and MDR regimes are shown in Fig. 5.9b. In the HDR regime, its peak value shifts away from the wall with the increase in the thickness of buffer layer, following the trend of turbulence production as shown in Fig. 5.7a. In the MDR regime, the non-monotonic trend with the dilute concentration of bubbles ($\Phi = 3\%$) continues to show its effects in the turbulent kinetic energy (TKE) of the flow as well. Once bubbles with this small concentration start to accumulate away from the walls, a significant rise in the kinetic energy of the flow is observed in the same region. As the mean shear rate decreases towards the channel center (Fig. 5.9a), TKE also decreases and matches with the value of single-phase flow at the channel center. However, with a higher concentration of bubbles ($\Phi = 9\%$), an opposite trend is observed. Once the bubbles are densely aggregated in the core region of the channel, TKE term decreases below the value of single-phase flow. The same trend is observed in the Reynolds shear stress term as well in the wall-normal direction (Fig. 5.9c). An already low value of $-\overline{v'w'}$ in the single-phase MDR regime reduces further in a flow with high concentration of bubbles.

The Reynolds shear stress term in the wall-normal direction ($\overline{v'w'}$) is responsible for the exchange of momentum between the channel center and the walls [195]. This exchange of momentum can be analyzed in the form of ejection and sweep events in the context of quadrant analysis. In a channel flow, these near-wall events can be identified based on the signs of streamwise and wall-normal velocity fluctuations,

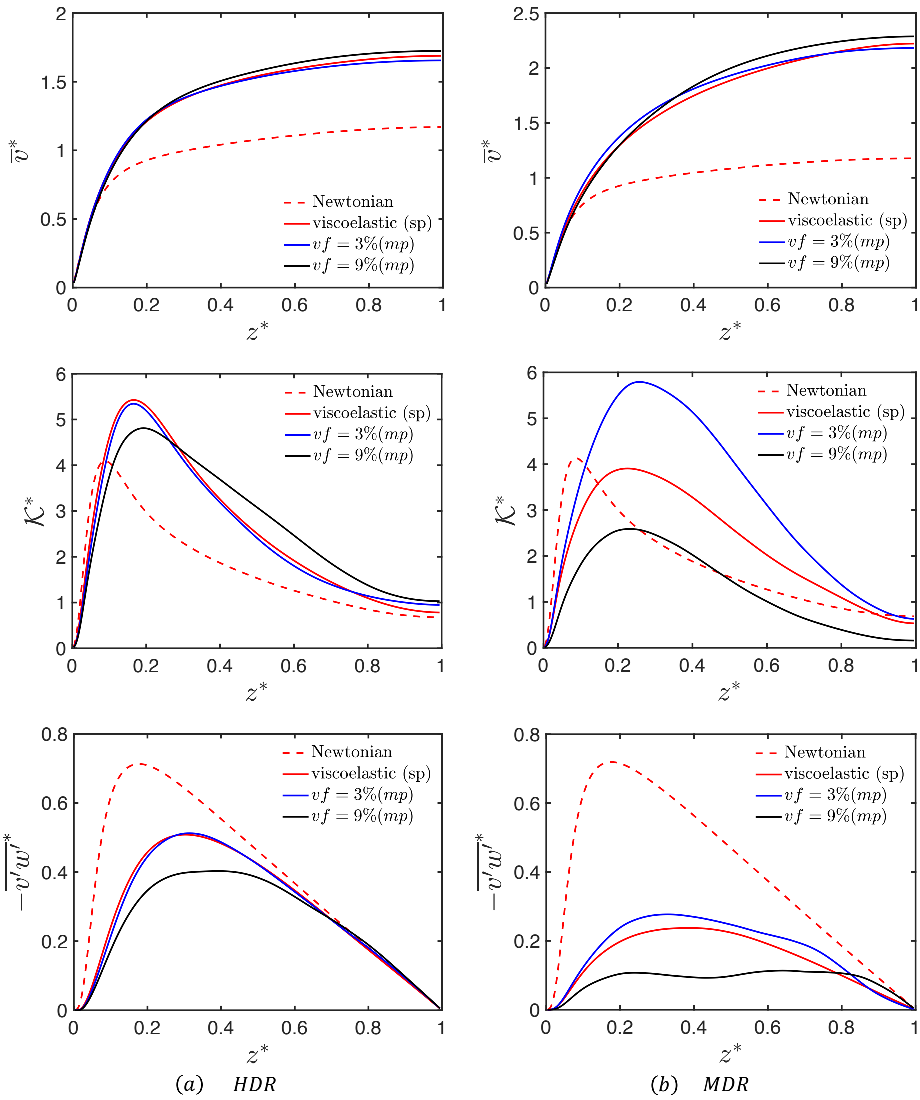

Figure 5.9: Mean flow velocity ($\overline{v}^*$) normalized by the average flow velocity of the Newtonian flow in the same channel, turbulent kinetic energy ($\mathcal{K}^*$) normalized by v_τ^2 and (c) the Reynolds shear stress ($\overline{v'w'}^*$) normalized by $\overline{\tau}_w$ are compared in the (a) HDR and (b) MDR regimes

as summarized in table 5.4. The contours of streamwise (v') and wall-normal (w') velocity fluctuations are shown in a vertical cutting xz-plane at the center of the channel for the different cases of MDR regime in Fig. 5.10. Although these events are highly dynamic in nature, the snapshots of v' and w' at a fixed streamwise location after the flow reaches its statistically steady state provides a useful insight of how elasticity and the presence of bubbles modify these events. In a Newtonian flow, frequent ejection (Q2) and sweep (Q4) structures can be observed closer to wall (Fig. 5.10a). Once the drag is significantly reduced with the addition of polymers in the single-phase MDR regime, the Reynolds stress is reduced and a significantly lower number of sweep and ejection structures are observed near the walls (Fig. 5.10b). A small concentration of bubbles in the MDR regime increases the turbulent kinetic energy of the flow and the Reynolds stress. However, these phenomena remain restricted to the core region of the channel where the bubbles are accumulated. The near wall structures of v' and w' remain largely unmodified (Fig. 5.10c) and hence the drag reduction remains almost similar to the single-phase flow. Similarly, with a higher bubble concentration, although the Reynolds stress decreases significantly as compared to dilute bubble concentration, the near-wall structures of v' are not modified and the DR reduces further to 70%.

Table 5.4: Quadrant analysis

Quadrant	v'	w'	Explanation
Q1	> 0	> 0	Wall-to-center transport of high momentum fluid.
Q2-ejection	< 0	> 0	Wall-to-center transport of low momentum fluid.
Q3	< 0	< 0	Center-to-wall transport of low momentum fluid.
Q4-sweep	> 0	< 0	Center-to-wall transport of high momentum fluid.

5.4.2 Polymer conformation tensor and the transient dynamics of bubbles

The complex interaction of elastic stress with the turbulent flow field at the smallest length and time scales has been an open question in the study of viscoelastic flows. In a turbulent flow field, the polymers are stretched by the velocity gradients and the resultant elastic stress affects the velocity field. The trace of conformation tensor, denoted by tr($\mathbf{B}$) in the present work, is commonly used to describe the average elongation of polymer molecules [196] as it represents the sum of its principal stretches. The conformation tensor evolves by equation 2.4 and is related to polymer

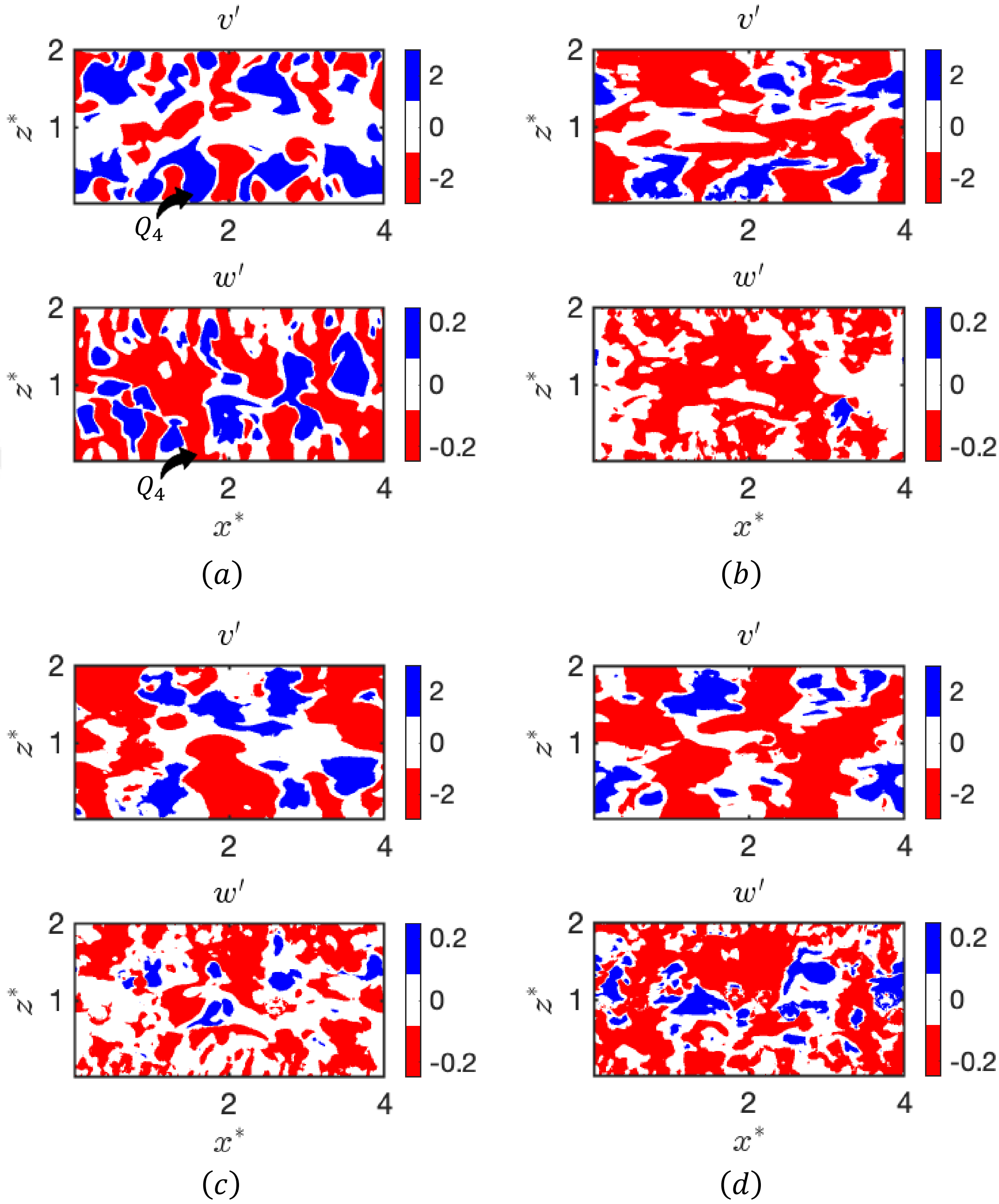

Figure 5.10: The streamwise (v') and wall-normal (w') velocity fluctuations are shown in a vertical cutting xz-plane at the center of the channel for the (a) Newtonian, (b) single-phase viscoelastic, (c) multiphase viscoelastic with $\Phi = 3\%$ and for (d) $\Phi = 9\%$ cases in the MDR regime.

stress by equation 2.5 for the FENE-P model. It is a second-order positive definite tensor that represents the history of polymer deformation. It is derived by averaging the dyad formed by the polymer's end-to-end vector across molecular realizations [197]. As tr($\mathbf{B}$) is directly proportional to the elastic energy of the polymers [169] for most of the viscoelastic models, it is frequently used to analyze the stretching of polymers. However, despite its widespread utilization in the studies of viscoelastic turbulent flows, the tr($\mathbf{B}$) does not completely describe the polymer deformations. The polymers may undergo volumetric deformation even with a constant tr($\mathbf{B}$). In fact, the mean momentum balance in a turbulent flow is linked with different components of conformation tensor through a dynamic coupling which cannot be captured by tr($\mathbf{B}$) only [198].

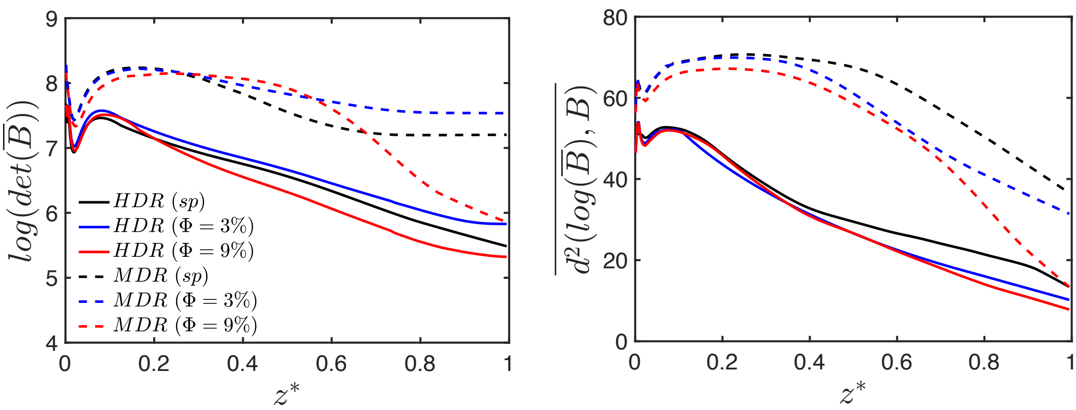

(a) (b)

Figure 5.11: (a) Logarithmic volume ratio of mean conformation tensor and (b) the mean squared geodesic distance of instantaneous conformation tensor from its log-Euclidean mean are shown for the different cases of HDR and MDR regimes.

Hameduddin et al. [199] introduced a new mathematical framework that can capture the polymer deformations in a more realistic way. In this relatively recent approach, the conformation tensor is decomposed in such a way that the fluctuating tensor field remains positive definite and thus retains the physical meaning of the tensor. Under this framework, the squared geodesic distance between $\mathbf{B}$ and $\overline{\mathbf{B}}$ and the logarithmic volume ratio $\log(\det(\mathbf{B}))/\det(\overline{\mathbf{B}}))$ are calculated to characterize the conformation tensor and its perturbations[179]. The squared geodesic distance between two positive-definite matrices, $\mathbf{A}$ and $\mathbf{B}$, is given by

$$d^2(\mathbf{A},\mathbf{B}) = tr(log^2(\mathbf{A}^{-1/2}\cdot\mathbf{B}\cdot\mathbf{A}^{-1/2})). \tag{5.22}$$

Figure 5.11a shows the logarithmic volume ratio of mean conformation tensor for the different cases of HDR and MDR regimes, which compares the volume of $\overline{\mathbf{B}}$ against a reference which is taken as the identity tensor ($\mathbf{I}$) in this case. The choice of identity tensor as a reference facilitates comparison between different flow configurations and shows the departure of $\overline{\mathbf{B}}$ from its isotropic equilibrium state. For the HDR cases ($Wi = 7$), $log(det(\overline{\mathbf{B}}))$ decays away from the wall towards the channel center. As the maximum turbulence is produced in the buffer layer (Fig. 5.7), the polymers relax quickly away from it due to comparatively shorter relaxation time. A small variation in this volumetric ratio is observed between the single-phase and the multiphase cases of the HDR regime at the channel center. In case of single-phase flow in the MDR regime, the polymer deformations are very well transported all across the channel due to long relaxation time at $Wi = 24$ and thus the profile of $log(det(\overline{\mathbf{B}}))$ almost remain constant at the channel center. Once bubbles are injected into the flow in this MDR regime, the polymer perturbations are enhanced towards the central region of the channel with a small concentration of bubbles ($\Phi = 3\%$). As the bubbles agitate the flow away from the wall, the streamwise velocity fluctuations are enhanced (Fig. 5.3), and the same effect is depicted in the deformation of polymers, which stays constant in the core region and is slightly increased as compared to single-phase flow (Fig. 5.11a). However, with a higher bubble concentration ($\Phi = 9\%$), when the bubbles are densely aggregated in the core region, a decrease in the volumetric deformation of polymers is observed towards the channel center. This results in decreased Reynolds stress and the turbulent kinetic energy of the flow.

The mean squared geodesic distance of instantaneous conformation tensor from its log-Euclidean mean is shown in Fig. 5.11b for the different cases of HDR and MDR regime. This quantity is a measure of the intensity of the polymer perturbations from its mean. An increase in this quantity is observed with the increase in Wi and the peak value is shifted away from the wall with the an increase in polymer relaxation time. The polymer fluctuations away from their log-Euclidean mean are significantly decreased towards the central region of the channel and this decay is enhanced with the injection of bubbles into the flow. It is interesting to note that while a small concentration of bubbles in the MDR regime increases the mean volumetric deformation of polymers, the perturbation intensity of the polymers is not increased for the same case.

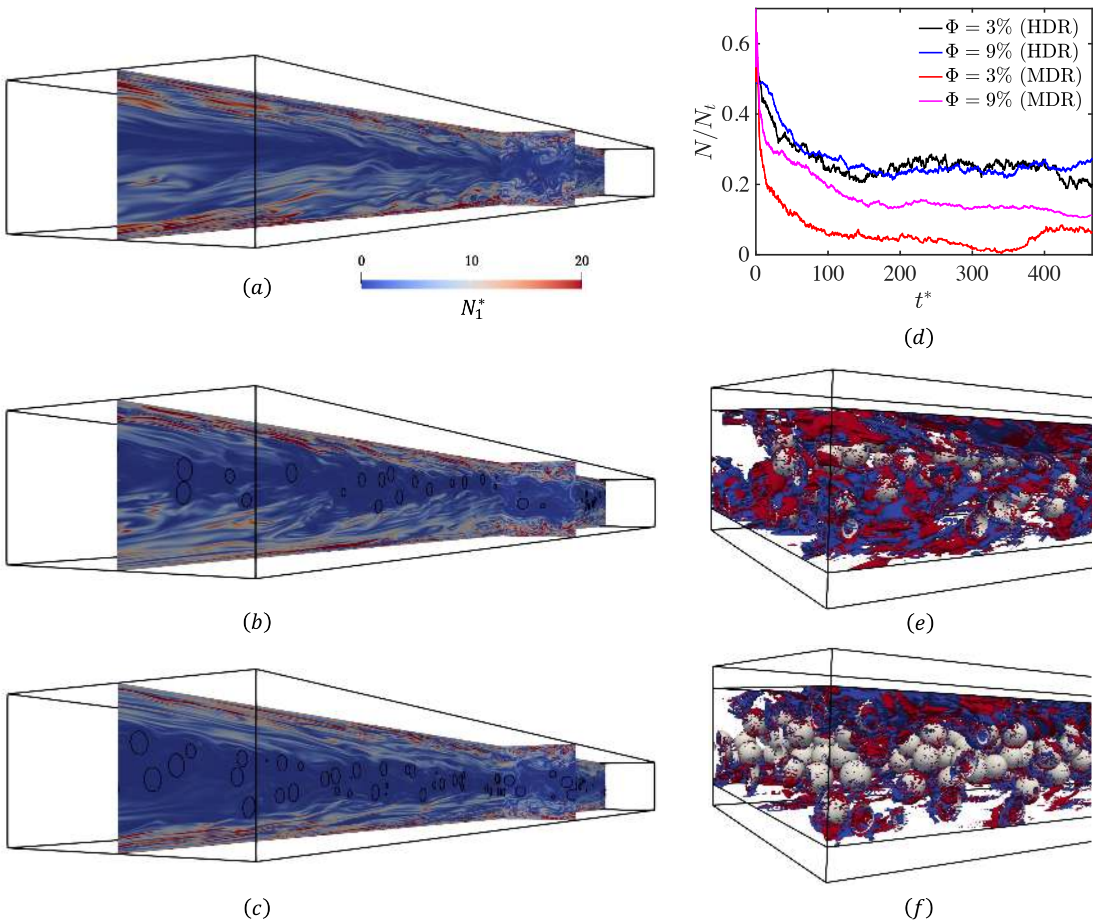

Figure 5.12: The constant contours of first normal stress difference (N_1) are shown in a vertical cutting yz-plane at the center of the channel for (a) single-phase, (b) $\Phi = 3\%$ and (c) $\Phi = 9\%$ in the MDR regime. (d) The number of bubbles outside the core region of the channel ($1.5 \leq z^* \leq 0.5$) are shown for different volume fractions in the HDR and MDR regimes. The iso-surfaces of *Q-criterion* are shown around the bubbles in the core region ($0.5 \leq z^* \leq 1.5$) of the channel at $+100$ (red) and -100 (blue) for (e) $\Phi = 3\%$ and (f) $\Phi = 9\%$ in the MDR regime.

In a viscoelastic channel flow, elasticity promotes migration of the bubbles towards the central region of the channel while inertia of the flow pulls them towards the wall [141, 83]. These competing effects determine the final equilibrium position of the bubbles in the channel. As the bubbles are contaminated with surfactant and the capillary number is kept very low ($Ca = 0.01$), the bubbles maintain an almost spherical shape and migrate towards the channel center in both the HDR and MDR regimes under the influence of elasticity. Figure 5.12d shows the time evolution of bubbles outside the central region of the channel. The central region is defined as $0.5 \leq z^* \leq 1.5$ in the wall-normal direction. Initially ($t = 0$), the bubbles are randomly distributed in the whole domain. The contaminated bubbles quickly move away from the walls and migrate towards the core region of the channel. At the steady state, almost 20% bubbles in the HDR regime ($Wi = 7$) are left outside the core region. Once the Weissenberg number is increased to $Wi = 24$ in the MDR regime, the bubbles are clustered further in the core region and only 10% bubbles are left outside the core region. This clustering of bubbles away from the channel walls affects the distribution of first normal stress difference ($N_1 = \tau_{yy} - \tau_{zz}$) in the channel. Figure 5.12(a), (b), & (c) show the distribution of N_1 in the channel with its constant contours plotted at a central plane for the single-phase and multiphase cases with different concentration of bubbles in the MDR regime. The first normal stress difference is maximum at the walls due to maximum stretching of polymers and decays to a minimum value at the channel center. The long elongated structures of N_1 in the MDR regime at this high $Wi = 24$ are the reason of requiring such a long domain length. Once the bubbles are injected into the flow with a small volume fraction of 3%, the volumetric deformation of polymers is slightly increased in the core region of the channel and almost remain constant, as seen in Fig. 5.11a. As a result, the distribution of N_1 remains largely unaffected in the channel (Fig. 5.12b). However, bubbles with a higher concentration decrease the volumetric deformation of polymers in the core region and as a result, the core area of the channel with minimum N_1 expands, as shown in Fig. 5.12c. This results into a decreased TKE (Fig. 5.9b), decreased Reynolds stress (Fig. 5.9c) and decreased polymeric work(Fig. 5.7c). This reduction in the turbulent intensity of the flow is better visualized in Fig. 5.12(e) & (f). The constant contours of *Q-criterion* (second invariant of velocity gradient tensor) are shown around the bubbles in the core region of the channel for the two multiphase cases of MDR regime. When the bubbles concentration is small (Fig. 5.12e), the presence of bubbles in the core region agitates the flow further and the volumetric deformation of polymers is increased. When the bubbles concentration is high, fewer structures of *Q-criterion* (Fig. 5.12f) show a reduced turbulent intensity of the flow. However, this phenomenon of increase or decrease in the TKE of the flow remain restricted to core region and the skin friction drag at the walls remain largely unaffected.

5.5 Conclusions

Direct numerical simulations of multiphase viscoelastic turbulent channel flow are performed by using a high fidelity front tracking code. FENE-P model is used to solve the constitutive equations of dilute polymer solution while the bubbles are contaminated with an industrial grade surfactant Triton X-100. Simulations are performed in two different domains by varying the channel lengths in the streamwise direction to achieve high drag reduction ($40\% < DR \leq 60\%$) and the maximum drag reduction ($DR > 60\%$) regimes in a single-phase viscoelastic flow. Subsequently, bubbles are injected into these fully developed viscoelastic flows with two different volume fractions (3% and 9%) and the effect of bubbles on the turbulent dynamics of the flow in these regimes are examined in detail.

It is observed that the Reynolds stress is reduced in a single-phase flow in the HDR regime with a drag reduction of 49% but still remains higher than the polymer stress. The addition of bubbles reduces the Reynolds stress even further and the drag is not increased like the solid suspension of particles in the LDR regime. The Reynolds stress in the single-phase flow of MDR regime reduces below the value of polymer stress with a drag reduction of 68% and the flow is dominated by the elastic effects. The injection of bubbles in this MDR regime produces non-monotonic effect. A small concentration of contaminated bubbles increases the Reynolds stress, turbulence production by the mean flow and the turbulent kinetic energy whereas a higher concentration of bubbles in the MDR regime reduces all these quantities. However, these effects remain restricted to core region of the channel and do not increase the drag.

It is found that the kinetic energy shows a scaling of -2 in both the HDR and MDR regimes and this scaling is not changed with the injection of bubbles. The quadrant analysis of Reynolds stress shows a reduction in the ejection and sweep events at the walls by the addition of polymers. These events remain largely unmodified with the addition of bubbles in both these regimes.

It is demonstrated that as the contaminated bubbles are accumulated in the core region of the channel and the volumetric deformation of polymers is significantly changed with a higher bubble concentration in the MDR regime. The deviation of instantaneous conformation tensor from its log-Euclidean mean decreases for the same case. As a result, the distribution of first normal stress difference (N_1) is changed and the turbulent intensity decreases in the core region of the channel. The opposite happens with a dilute concentration of bubbles. The polymer perturbations are still decreased but the volumetric deformation is increased. The bubbles agitate the flow and the Reynolds stresses are increased.

Unlike the solid particles, the absence of no-slip condition on the surface of bubbles and the modification of bubbles' surface tension due to the presence of surfactant accumulate the bubbles in the core region of the channel. A small concentration of bubbles in an MDR regime increases the turbulent kinetic energy of the flow without increasing the drag. This can have potential implications for all those processes where mixing, heat transfer or other transport phenomena are of primary importance. The effects of bubble deformability, polymer concentration, buoyancy, variable surfactant concentration and different sizes of the bubbles on these dynamics are still open questions.

Chapter 6

CONCLUSIONS

Interface-resolved direct numerical simulations of multiphase viscoelastic fluid flows have been performed by using a high fidelity finite-difference/front-tracking method to investigate the effects of viscoelasticity on multiphase flows for a range of conditions of practical importance. The study spans dynamics of a single bubble to complex interactions of thousands of bubbles. The range of the problems studied under this frame work include buoyancy driven two bubbles in a viscoelastic fluid, pressure-driven viscoelastic laminar and turbulent bubbly flows, a new type of transition to elasto-inertial turbulent regime and finally the polymer drag reduction in a turbulent bubbly channel flow in the presence of a soluble surfactant.

It is found that, when a pair of two parallel bubbles rise in a quiescent viscoelastic fluid under buoyancy, the bubbles and their wakes interact strongly as they rise and long tails form behind the bubbles due to viscoelastic stress difference at the interface. The bubble shapes are markedly different in the two bubble system compared to that in the single bubble case. In addition to the formation of long tails that tilt towards each other, the lateral symmetry is also broken in the two bubble system. The rise velocity of the parallel bubbles remains slightly smaller than that of the single bubble due to the bubble-bubble interactions. The symmetry observed in the case of the parallel bubble pairs is broken when the bubbles are initialized by an initial offset in the vertical direction. It is found that equal-sized bubble pairs maintain their initial orientation. In the case of unequal-sized bubble pairs, the larger bubble moves faster leaving the smaller one behind and then maintain their orientation regardless of an initial offset in the vertical direction.

Lateral migration of a bubble determines void fraction distribution in a bubbly pressure-driven channel flow. It is observed that, in a pressure driven viscoelastic laminar flow, the forces induced by fluid inertia push a bubble towards the wall while elasticity and deformability pull it towards the channel center. This interplay between fluid inertia, elasticity, and bubble deformability determines the orientation of bubble migration in the channel and its final equilibrium position. As shear-thinning increases the relative importance of the fluid inertia, it is found to promote migration towards a wall. At a high Weissenberg number, elastic instability occurs due to the curvature of streamlines across the bubble interface. It is shown that the secondary flow velocity induced by a bubble migrating towards the wall is an order of magnitude higher than the one induced by a solid particle under similar flow conditions. This behavior is attributed to the slip condition on the bubble surface. For all the situations where the bubble migrates towards the center, the secondary flow velocity becomes negligible due to the symmetric flow pattern above and below the bubble when viewed in its migrating plane.

Elastic instability observed in the study of lateral migration of a single bubble motivated an examination of a novel mechanism of achieving the EIT state by injecting the bubbles into a pressure-driven viscoelastic flow under the conditions for which a single-phase flow remains laminar. This is tested and verified at a Reynolds number as low as 10 and a Weissenberg number as low as 5. The curved streamlines across the bubbles interfaces provide the necessary condition to trigger an instability even when the viscoelastic stresses are not very high and the single-phase flow remains completely laminar. The energy spectra shows a scaling of -2 for this low Wi multiphase EIT regime. It is concluded that the scaling of energy spectra varies from -4 to $-5/3$ depending upon the relative dominance of inertia and elasticity, i.e, -4 for a purely elastic turbulence and $-5/3$ for a purely inertial turbulence. All the other values of energy scaling would fall in between these two limits depending upon the relative strength of inertia (Re) and elasticity (Wi). It is also observed that the drag increases for all the situations where the laminar viscoelastic flow is fully transitioned to a turbulent state by injecting the bubbles into the flow. However, at the lower values of $Re = 10$ & 100, this higher value of skin friction drag of the EIT regime still remains lower than the corresponding laminar Newtonian flow for the same Reynolds number. Once the inertia and the elasticity are both low, the bubbles are aligned in the core region of the duct forming a string-shaped pattern ($Re = 10$, $Wi = 1$) or clusters ($Re = 100$, $Wi = 1$), and the flow remains laminar in the wall region. For these cases, the friction drag reduces even further instead of increasing in this highly intermittent chaotic flow. Unlike the solid particles, it is found that a higher shear-thinning effect breaks down the alignment of bubbles.

Finally, in a pressure-driven Newtonian turbulent flow at $Re = 2800$ ($Re_\tau = 180$), once the flow is made viscoelastic, a high-drag-reduction regime is achieved with a drag reduction of 49%. It is found that the Reynolds stress is reduced in this HDR regime but still remains higher than the polymer stress. The addition of contaminated bubbles reduces the Reynolds stress even further and the drag is not increased like the solid suspension of particles in the LDR regime. The Reynolds stress in the single-phase flow of MDR regime reduces below the value of polymer stress with a drag reduction of 68% and the flow is dominated by the elastic effects. The injection of bubbles in this MDR regime produces non-monotonic effect. A small concentration of contaminated bubbles increases the Reynolds stress, turbulence production by the mean flow and the turbulent kinetic energy whereas a higher concentration of bubbles in the MDR regime reduces all these quantities. However, these effects remain restricted to core region of the channel and do not increase the drag. It is found that the kinetic energy shows a scaling of -2 in both the HDR and MDR regimes and this scaling is not changed with the injection of bubbles. The quadrant analysis of Reynolds stress shows a reduction in the ejection and sweep events at the walls by the addition of polymers. These events remain largely unmodified with the addition of bubbles in both these regimes. It is demonstrated that as the contaminated bubbles are accumulated in the core region of the channel and the volumetric deformation of polymers is significantly changed with a higher bubble concentration in the MDR regime. The deviation of instantaneous conformation tensor from its log-Euclidean mean decreases for the same case. As a result, the distribution of first normal stress difference (N_1) is changed and the turbulent intensity decreases in the core region of the channel. The opposite happens with a dilute concentration of bubbles. The polymer perturbations are still decreased but the volumetric deformation is increased. The bubbles agitate the flow and the Reynolds stresses are increased. Unlike the solid particles, the absence of no-slip condition on the surface of bubbles and the modification of bubbles' surface tension due to the presence of surfactant accumulate the bubbles in the core region of the channel. A small concentration of bubbles in an MDR regime increases the turbulent kinetic energy of the flow without increasing the drag. This can have potential implications for all those processes where mixing, heat transfer or other transport phenomena are of primary importance.

BIBLIOGRAPHY

[1] W. Yuan, M. Zhang, B. C. Khoo, and N. Phan-Thien, “Dynamics and deformation of a three-dimensional bubble rising in viscoelastic fluids,” *Journal of Non-Newtonian Fluid Mechanics*, vol. 285, p. 104408, 2020.

[2] G. Li, G. H. McKinley, and A. M. Ardekani, “Dynamics of particle migration in channel flow of viscoelastic fluids,” *Journal of Fluid Mechanics*, vol. 785, pp. 486–505, 2015.

[3] J. Kim, P. Moin, and R. Moser, “Turbulence statistics in fully developed channel flow at low reynolds number,” *Journal of Fluid Mechanics*, vol. 177, p. 133–166, 1987.

[4] P. Virk, H. S. Mickley, and K. Smith, “The ultimate asymptote and mean flow structure in toms’ phenomenon,” *Journal of Applied Mechanics, Transactions ASME*, vol. 37, no. 2, pp. 488–493, 1970.

[5] S. S. Datta, A. M. Ardekani, P. E. Arratia, A. N. Beris, I. Bischofberger, G. H. McKinley, J. G. Eggers, J. E. López-Aguilar, S. M. Fielding, A. Frishman, *et al.*, “Perspectives on viscoelastic flow instabilities and elastic turbulence,” *Physical Review Fluids*, vol. 7, no. 8, p. 080701, 2022.

[6] B. Wei, L. Romero-Zerón, and D. Rodrigue, “Oil displacement mechanisms of viscoelastic polymers in enhanced oil recovery (eor): a review,” *Journal of Petroleum Exploration and Production Technology*, vol. 4, pp. 113–121, 2014.

[7] J. F. Steffe, *Rheological methods in food process engineering.* Freeman press, 1996.

[8] J. Aho, S. Hvidt, and S. Baldursdottir, "Rheology in pharmaceutical sciences," *Analytical Techniques in the Pharmaceutical Sciences*, pp. 719–750, 2016.

[9] R. G. Larson, A. K. Van Dyk, T. Chatterjee, and V. V. Ginzburg, "Associative thickeners for waterborne paints: Structure, characterization, rheology, and modeling," *Progress in Polymer Science*, vol. 129, p. 101546, 2022.

[10] N. Huang, "Rheological characterization of pharmaceutical and cosmetic formulations for cutaneous applications," *Current pharmaceutical design*, vol. 25, no. 21, pp. 2349–2363, 2019.

[11] M. Anand and K. Rajagopal, "A shear-thinning viscoelastic fluid model for describing the flow of blood," *International Journal of Cardiovascular Medicine and Science*, vol. 4, no. 2, pp. 59–68, 2004.

[12] F. Romano, M. Muradoglu, H. Fujioka, and J. Grotberg, "The effect of viscoelasticity in an airway closure model," *Journal of fluid mechanics*, vol. 913, p. A31, 2021.

[13] J. Gomez and G. Thurston, "Comparisons of the oscillatory shear viscoelasticity and composition of pathological synovial fluids," *Biorheology*, vol. 30, no. 5-6, pp. 409–427, 1993.

[14] X. Lan, A. Adesida, and Y. Boluk, "Rheological and viscoelastic properties of collagens and their role in bioprinting by micro-extrusion," *Biomedical Materials*, vol. 17, no. 6, p. 062005, 2022.

[15] E. Moeendarbary and A. R. Harris, "Cell mechanics: principles, practices, and prospects," *Wiley Interdisciplinary Reviews: Systems Biology and Medicine*, vol. 6, no. 5, pp. 371–388, 2014.

[16] K. Kim, X. Liu, Y. Zhang, J. Cheng, X. Yu Wu, and Y. Sun, "Elastic and viscoelastic characterization of microcapsules for drug delivery using a force-

feedback mems microgripper," *Biomedical microdevices*, vol. 11, pp. 421–427, 2009.

[17] C. W. Hirt and B. D. Nichols, "Volume of fluid (vof) method for the dynamics of free boundaries," *Journal of computational physics*, vol. 39, no. 1, pp. 201–225, 1981.

[18] M. Sussman, P. Smereka, and S. Osher, "A level set approach for computing solutions to incompressible two-phase flow," *Journal of Computational physics*, vol. 114, no. 1, pp. 146–159, 1994.

[19] D. Jacqmin, "Calculation of two-phase navier–stokes flows using phase-field modeling," *Journal of computational physics*, vol. 155, no. 1, pp. 96–127, 1999.

[20] G. Tryggvason, B. Bunner, A. Esmaeeli, D. Juric, N. Al-Rawahi, W. Tauber, J. Han, S. Nas, and Y.-J. Jan, "A front-tracking method for the computations of multiphase flow," *Journal of Computational Physics*, vol. 169, no. 2, pp. 708 – 759, 2001.

[21] G. Tryggvason, R. Scardovelli, and S. Zaleski, *Direct Numerical Simulations of Gas-Liquid Multiphase Flows.* Cambridge University Press, Cambridge, UK, 2011.

[22] M. Muradoglu and G. Tryggvason, "A front-tracking method for computation of interfacial flows with soluble surfactants," *Journal of computational physics*, vol. 227, no. 4, pp. 2238–2262, 2008.

[23] A. Morozov and S. E. Spagnolie, "Introduction to complex fluids," *Complex fluids in biological systems: experiment, theory, and computation*, pp. 3–52, 2015.

[24] M. M. Denn, C. J. Petrie, and P. Avenas, "Mechanics of steady spinning of a viscoelastic liquid," *AIChE Journal*, vol. 21, no. 4, pp. 791–799, 1975.

[25] J. G. Oldroyd, "On the formulation of rheological equations of state," *Proceedings of the Royal Society of London. Series A. Mathematical and Physical Sciences*, vol. 200, no. 1063, pp. 523–541, 1950.

[26] H. Giesekus, "A simple constitutive equation for polymer fluids based on the concept of deformation-dependent tensorial mobility," *Journal of Non-Newtonian Fluid Mechanics*, vol. 11, no. 1-2, pp. 69–109, 1982.

[27] K. Ferrara, R. Pollard, and M. Borden, "Ultrasound microbubble contrast agents: fundamentals and application to gene and drug delivery," *Annu. Rev. Biomed. Eng.*, vol. 9, pp. 415–447, 2007.

[28] Y. Shah, B. Kelkar, S. Godbole, and W. Deckwer, "Design parameters column reactors," *AICHE Journal*, vol. 28 (3), pp. 353–379, 1982.

[29] N. Kantarci, F. Borak, and K. Ulgen, "Bubble column reactors," *Process Biochemistry*, vol. 40, pp. 2263–2283, 2005.

[30] K. Terasaka, A. Hirabayashi, T. Nishino, S. Fujioka, and D. Kobayashi, "Development of microbubble aerator for waste water treatment using aerobic activated sludge," *Chemical Engineering Science*, vol. 66, no. 14, pp. 3172–3179, 2011.

[31] G. Astarita and G. Apuzzo, "Motion of gas bubbles in non-newtonian liquids," *AIChE Journal*, vol. 11, no. 5, pp. 815–820, 1965.

[32] R. S. Rivlin, "The hydrodynamics of non-newtonian fluids. i," *Proceedings of the Royal Society of London. Series A. Mathematical and Physical Sciences*, vol. 193, no. 1033, pp. 260–281, 1948.

[33] C. Stewart, "Bubble interaction in low-viscosity liquids," *International journal of multiphase flow*, vol. 21, no. 6, pp. 1037–1046, 1995.

[34] T. Maxworthy, C. Gnann, M. Kürten, and F. Durst, "Experiments on the rise of air bubbles in clean viscous liquids," *Journal of fluid mechanics*, vol. 321, pp. 421–441, 1996.

[35] M. Niethammer, G. Brenn, H. Marschall, and D. Bothe, "An extended volume of fluid method and its application to single bubbles rising in a viscoelastic liquid," *Journal of Computational Physics*, vol. 387, pp. 326–355, 2019.

[36] W. Yuan, M. Zhang, B. C. Khoo, and N. Phan-Thien, "On peculiar behaviours at critical volumes of a three-dimensional bubble rising in viscoelastic fluids," *Journal of Non-Newtonian Fluid Mechanics*, vol. 293, p. 104568, 2021.

[37] R. Zenit and J. Feng, "Hydrodynamic interactions among bubbles, drops, and particles in non-newtonian liquids," *Annual Review of Fluid Mechanics*, vol. 50, no. 1, pp. 505–534, 2018.

[38] S. B. Pillapakkam, P. Singh, D. Blackmore, and N. Aubry, "Transient and steady state of a rising bubble in a viscoelastic fluid," *Journal of Fluid Mechanics*, vol. 589, pp. 215–252, 2007.

[39] O. Hassager, "Negative wake behind bubbles in non-newtonian liquids," *Nature*, vol. 279, no. 5712, pp. 402–403, 1979.

[40] F. Carril-Naranjo, B. Mena, D. Samayoa, A. Guerrero, and B. Figueroa-Espinoza, "The influence of the negative wake on the deformation and breakup of viscoelastic droplets," *Korea-Australia Rheology Journal*, vol. 33, no. 3, pp. 283–291, 2021.

[41] D. Funfschilling and H. Z. Li, "Flow of non-newtonian fluids around bubbles: Piv measurements and birefringence visualisation," *Chemical Engineering Science*, vol. 56, no. 3, pp. 1137–1141, 2001.

[42] D. Fraggedakis, M. Pavlidis, Y. Dimakopoulos, and J. Tsamopoulos, "On the velocity discontinuity at a critical volume of a bubble rising in a viscoelastic fluid," *Journal of Fluid Mechanics*, vol. 789, pp. 310–346, 2016.

[43] Y. Imaizumi, T. Kunugi, T. Yokomine, and Z. Kawara, "Viscoelastic fluid behaviors around a rising bubble via a new method of mesh deformation tracking," *Chemical Engineering Science*, vol. 120, pp. 167–173, 2014.

[44] C. Pilz and G. Brenn, "On the critical bubble volume at the rise velocity jump discontinuity in viscoelastic liquids," *Journal of non-newtonian fluid mechanics*, vol. 145, no. 2-3, pp. 124–138, 2007.

[45] D. Bothe, M. Niethammer, C. Pilz, and G. Brenn, "On the molecular mechanism behind the bubble rise velocity jump discontinuity in viscoelastic liquids," *Journal of Non-Newtonian Fluid Mechanics*, p. 104748, 2022.

[46] W. B. Zimmerman, B. N. Hewakandamby, V. Tesař, H. H. Bandulasena, and O. A. Omotowa, "On the design and simulation of an airlift loop bioreactor with microbubble generation by fluidic oscillation," *Food and Bioproducts Processing*, vol. 87, no. 3, pp. 215–227, 2009.

[47] D. Legendre, J. Magnaudet, and G. Mougin, "Hydrodynamic interactions between two spherical bubbles rising side by side in a viscous liquid," *Journal of Fluid Mechanics*, vol. 497, pp. 133–166, 2003.

[48] B. Bunner and G. Tryggvason, "Effect of bubble deformation on the properties of bubbly flows," *Journal of Fluid Mechanics*, vol. 495, pp. 77–118, 2003.

[49] J. Zhang, L. Chen, and M.-J. Ni, "Vortex interactions between a pair of bubbles rising side by side in ordinary viscous liquids," *Physical Review Fluids*, vol. 4, no. 4, p. 043604, 2019.

[50] D. De Kee, R. Chhabra, and A. Dajan, “Motion and coalescense of gas bubbles in non-newtonian polymer solutions,” *Journal of Non-Newtonian Fluid Mechanics*, vol. 37, no. 1, pp. 1–18, 1990.

[51] F. Wenyuan, M. Youguang, L. Xiaolei, and L. Huaizhi, “Study on the flow field around two parallel moving bubbles and interaction between bubbles rising in cmc solutions by piv,” *Chinese Journal of Chemical Engineering*, vol. 17, no. 6, pp. 904–913, 2009.

[52] H. Z. Li, X. Frank, D. Funfschilling, and Y. Mouline, “Towards the understanding of bubble interactions and coalescence in non-newtonian fluids: a cognitive approach,” *Chemical Engineering Science*, vol. 56, no. 21-22, pp. 6419–6425, 2001.

[53] X. Frank, H. Li, and D. Funfschilling, “An analytical approach to the rise velocity of periodic bubble trains in non-newtonian fluids,” *The European Physical Journal E*, vol. 16, no. 1, pp. 29–35, 2005.

[54] W. Yuan, M. Zhang, B. C. Khoo, and N. Phan-Thien, “Hydrodynamic interaction and coalescence of two inline bubbles rising in a viscoelastic liquid,” *Physics of Fluids*, vol. 33, no. 8, p. 083102, 2021.

[55] D. Izbassarov, M. E. Rosti, M. N. Ardekani, M. Sarabian, S. Hormozi, L. Brandt, and O. Tammisola, “Computational modeling of multiphase viscoelastic and elastoviscoplastic flows,” *International Journal for Numerical Methods in Fluids*, vol. 88, no. 12, pp. 521–543, 2018.

[56] R. Fattal and R. Kupferman, “Time-dependent simulation of viscoelastic flows at high weissenberg number using the log-conformation representation,” *Journal of Non-Newtonian Fluid Mechanics*, vol. 126, no. 1, pp. 23–37, 2005.

[57] R. Borges, M. Carmona, B. Costa, and W. S. Don, “An improved weighted

essentially non-oscillatory scheme for hyperbolic conservation laws," *Journal of Computational Physics*, vol. 227, no. 6, pp. 3191 – 3211, 2008.

[58] S. Dong and J. Shen, "A time-stepping scheme involving constant coefficient matrices for phase-field incompressible flows with large density ratios," *Journal of Computational Physics*, vol. 231, pp. 5788–5804, 2012.

[59] M. S. Dodd and A. Ferrante, "A fast pressure-correction method for incompressible two-fluid flows," *Journal of Computational Physics*, vol. 273, pp. 416–434, 2014.

[60] D. Izbassarov and M. Muradoglu, "Effects of viscoelasticity on drop impact and spreading on a solid surface," *Physical Review Fluids*, vol. 1, no. 2, p. 023302, 2016.

[61] H. Zolfaghari, D. Izbassarov, and M. Muradoglu, "Simulations of viscoelastic two-phase flows in complex geometries," *Computers & Fluids*, vol. 156, pp. 548–561, 2017.

[62] Z. Ahmed, D. Izbassarov, P. Costa, M. Muradoglu, and O. Tammisola, "Turbulent bubbly channel flows: Effects of soluble surfactant and viscoelasticity," *Computers & Fluids*, vol. 212, p. 104717, 2020.

[63] M. K. Tripathi, K. C. Sahu, and R. Govindarajan, "Dynamics of an initially spherical bubble rising in quiescent liquid," *Nature communications*, vol. 6, no. 1, pp. 1–9, 2015.

[64] S. Tasoglu, G. Kaynak, A. J. Szeri, U. Demirci, and M. Muradoglu, "Impact of a compound droplet on a flat surface: A model for single cell epitaxy," *Physics of Fluids*, vol. 22, no. 8, p. 082103, 2010.

[65] U. Olgac, D. Izbassarov, and M. Muradoglu, "Direct numerical simulation of an oscillating droplet in partial contact with a substrate," *Computers & Fluids*, vol. 77, pp. 152–158, 2013.

[66] R. Bird, P. Dotson, and N. Johnson, "Polymer solution rheology based on a finitely extensible bead-spring chain model," *J.Non-Newtonian Fluid Mech.*, vol. 7, pp. 213—-235, 1980.

[67] S. L. Ortiz, J. S. Lee, B. Figueroa-Espinoza, and B. Mena, "An experimental note on the deformation and breakup of viscoelastic droplets rising in non-newtonian fluids," *Rheologica Acta*, vol. 55, no. 11, pp. 879–887, 2016.

[68] M. A. Shannon, P. W. Bohn, M. Elimelech, J. G. Georgiadis, B. J. Marinas, and A. M. Mayes, "Science and technology for water purification in the coming decades," *Nature*, vol. 452, no. 7185, pp. 301–310, 2008.

[69] R. D. Vidic, S. L. Brantley, J. M. Vandenbossche, D. Yoxtheimer, and J. D. Abad, "Impact of shale gas development on regional water quality," *science*, vol. 340, no. 6134, p. 1235009, 2013.

[70] S. Nagrath, L. V. Sequist, S. Maheswaran, D. W. Bell, D. Irimia, L. Ulkus, M. R. Smith, E. L. Kwak, S. Digumarthy, A. Muzikansky, *et al.*, "Isolation of rare circulating tumour cells in cancer patients by microchip technology," *Nature*, vol. 450, no. 7173, pp. 1235–1239, 2007.

[71] X. Xuan, J. Zhu, and C. Church, "Particle focusing in microfluidic devices," *Microfluidics and nanofluidics*, vol. 9, pp. 1–16, 2010.

[72] H. Amini, W. Lee, and D. Di Carlo, "Inertial microfluidic physics," *Lab on a Chip*, vol. 14, no. 15, pp. 2739–2761, 2014.

[73] N. Hidman, H. Ström, S. Sasic, and G. Sardina, "The lift force on deformable and freely moving bubbles in linear shear flows," *Journal of Fluid Mechanics*, vol. 952, p. A34, 2022.

[74] G. Segre and A. Silberberg, "Radial particle displacements in poiseuille flow of suspensions," *Nature*, vol. 189, pp. 209–210, 1961.

[75] A. Karnis and S. Mason, "Particle motions in sheared suspensions. xix. viscoelastic media," *Transactions of the Society of Rheology*, vol. 10, no. 2, pp. 571–592, 1966.

[76] J.-P. Matas, J. F. Morris, and É. Guazzelli, "Inertial migration of rigid spherical particles in poiseuille flow," *Journal of fluid mechanics*, vol. 515, pp. 171–195, 2004.

[77] J. Feng, H. H. Hu, and D. D. Joseph, "Direct simulation of initial value problems for the motion of solid bodies in a newtonian fluid. part 2. couette and poiseuille flows," *Journal of fluid mechanics*, vol. 277, pp. 271–301, 1994.

[78] B. H. Yang, J. Wang, D. D. Joseph, H. H. Hu, T.-W. Pan, and R. Glowinski, "Migration of a sphere in tube flow," *Journal of Fluid mechanics*, vol. 540, pp. 109–131, 2005.

[79] M. Frank, D. Anderson, E. R. Weeks, and J. F. Morris, "Particle migration in pressure-driven flow of a brownian suspension," *Journal of Fluid Mechanics*, vol. 493, pp. 363–378, 2003.

[80] F. Del Giudice, G. Romeo, G. D'Avino, F. Greco, P. A. Netti, and P. L. Maffettone, "Particle alignment in a viscoelastic liquid flowing in a square-shaped microchannel," *Lab on a Chip*, vol. 13, no. 21, pp. 4263–4271, 2013.

[81] P. Wang, Z. Yu, and J. Lin, "Numerical simulations of particle migration in rectangular channel flow of giesekus viscoelastic fluids," *Journal of Non-Newtonian Fluid Mechanics*, vol. 262, pp. 142–148, 2018.

[82] D. Yuan, Q. Zhao, S. Yan, S.-Y. Tang, G. Alici, J. Zhang, and W. Li, "Recent progress of particle migration in viscoelastic fluids," *Lab on a Chip*, vol. 18, no. 4, pp. 551–567, 2018.

[83] K. W. Seo, Y. J. Kang, and S. J. Lee, "Lateral migration and focusing of microspheres in a microchannel flow of viscoelastic fluids," *Physics of Fluids*, vol. 26, no. 6, p. 063301, 2014.

[84] M. Villone, G. D'Avino, M. Hulsen, F. Greco, and P. Maffettone, "Particle motion in square channel flow of a viscoelastic liquid: Migration vs. secondary flows," *Journal of Non-Newtonian Fluid Mechanics*, vol. 195, pp. 1–8, 2013.

[85] G. D'Avino, F. Greco, and P. L. Maffettone, "Particle migration due to viscoelasticity of the suspending liquid and its relevance in microfluidic devices," *Annual Review of Fluid Mechanics*, vol. 49, pp. 341–360, 2017.

[86] P. G. Saffman, "The lift on a small sphere in a slow shear flow," *Journal of fluid mechanics*, vol. 22, no. 2, pp. 385–400, 1965.

[87] P. Shi, R. Rzehak, D. Lucas, and J. Magnaudet, "Hydrodynamic forces on a clean spherical bubble translating in a wall-bounded linear shear flow," *Physical Review Fluids*, vol. 5, 06 2020.

[88] A. H. Raffiee, S. Dabiri, and A. M. Ardekani, "Elasto-inertial migration of deformable capsules in a microchannel," *Biomicrofluidics*, vol. 11, no. 6, 2017.

[89] M. Villone, G. D'Avino, M. Hulsen, F. Greco, and P. Maffettone, "Simulations of viscoelasticity-induced focusing of particles in pressure-driven micro-slit flow," *Journal of non-newtonian fluid mechanics*, vol. 166, no. 23-24, pp. 1396–1405, 2011.

[90] Z. Yu, P. Wang, J. Lin, and H. H. Hu, "Equilibrium positions of the elasto-inertial particle migration in rectangular channel flow of oldroyd-b viscoelastic fluids," *Journal of Fluid Mechanics*, vol. 868, pp. 316–340, 2019.

[91] B. Debbaut, T. Avalosse, J. Dooley, and K. Hughes, "On the development of secondary motions in straight channels induced by the second normal stress

difference: experiments and simulations," *Journal of Non-Newtonian Fluid Mechanics*, vol. 69, no. 2-3, pp. 255–271, 1997.

[92] J. Matas, J. Morris, and E. Guazzelli, "Lateral forces on a sphere," *Oil & gas science and technology*, vol. 59, no. 1, pp. 59–70, 2004.

[93] E. Michaelides, *Particles, bubbles & drops: their motion, heat and mass transfer*. World Scientific, 2006.

[94] S. I. Rubinow and J. B. Keller, "The transverse force on a spinning sphere moving in a viscous fluid," *Journal of Fluid Mechanics*, vol. 11, no. 3, pp. 447–459, 1961.

[95] P.-H. Chan and L. Leal, "The motion of a deformable drop in a second-order fluid," *Journal of fluid mechanics*, vol. 92, no. 1, pp. 131–170, 1979.

[96] D. Di Carlo, "Inertial microfluidics," *Lab on a Chip*, vol. 9, no. 21, pp. 3038–3046, 2009.

[97] E. J. Lim, T. J. Ober, J. F. Edd, S. P. Desai, D. Neal, K. W. Bong, P. S. Doyle, G. H. McKinley, and M. Toner, "Inertio-elastic focusing of bioparticles in microchannels at high throughput," *Nature communications*, vol. 5, no. 1, pp. 1–9, 2014.

[98] S. Mortazavi and G. Tryggvason, "A numerical study of the motion of drops in poiseuille flow. part 1. lateral migration of one drop," *Journal of Fluid Mechanics*, vol. 411, pp. 325–350, 2000.

[99] J. Nam, B. Namgung, C. T. Lim, J.-E. Bae, H. L. Leo, K. S. Cho, and S. Kim, "Microfluidic device for sheathless particle focusing and separation using a viscoelastic fluid," *Journal of Chromatography A*, vol. 1406, pp. 244–250, 2015.

[100] S. Hazra, S. Mitra, and A. Sen, "Cross-stream migration of droplets in a confined shear-thinning viscoelastic flow: Role of shear-thinning induced lift," *Physics of Fluids*, vol. 32, no. 9, 2020.

[101] S. Mukherjee and K. Sarkar, "Lateral migration of a viscoelastic drop in a newtonian fluid in a shear flow near a wall," *Physics of fluids*, vol. 26, no. 10, 2014.

[102] M. Muradoglu and G. Tryggvason, "Simulations of soluble surfactants in 3d multiphase flow," *Journal of computational physics*, vol. 274, pp. 737–757, 2014.

[103] Z. Ahmed, D. Izbassarov, J. Lu, G. Tryggvason, M. Muradoglu, and O. Tammisola, "Effects of soluble surfactant on lateral migration of a bubble in a pressure driven channel flow," *International Journal of Multiphase Flow*, vol. 126, p. 103251, 2020.

[104] G. Tryggvason, B. Bunner, A. Esmaeeli, D. Juric, N. Al-Rawahi, W. Tauber, J. Han, S. Nas, and Y.-J. Jan, "A front-tracking mackethod for the computations of multiphase flow," *Journal of computational physics*, vol. 169, no. 2, pp. 708–759, 2001.

[105] C. Fetecau and C. Fetecau, "Unsteady flows of oldroyd-b fluids in a channel of rectangular cross-section," *International Journal of Non-Linear Mechanics*, vol. 40, no. 9, pp. 1214–1219, 2005.

[106] G. Tryggvason, R. Scardovelli, and S. Zaleski, *Direct numerical simulations of gas–liquid multiphase flows.* Cambridge university press, 2011.

[107] D. Izbassarov, Z. Ahmed, P. Costa, V. Vuorinen, O. Tammisola, and M. Muradoglu, "Polymer drag reduction in surfactant-contaminated turbulent bubbly channel flows," *Physical Review Fluids*, vol. 6, no. 10, p. 104302, 2021.

[108] D. Izbassarov and M. Muradoglu, “A front-tracking method for computational modeling of viscoelastic two-phase flow systems,” *Journal of Non-Newtonian Fluid Mechanics*, vol. 223, pp. 122–140, 2015.

[109] G. Schleiniger and R. Weinacht, “A remark on the giesekus viscoelastic fluid,” *Journal of Rheology*, vol. 35, no. 6, pp. 1157–1170, 1991.

[110] R. Borges, M. Carmona, and B. Costa, “Wai sun don,” *An improved weighted essentially non-oscillatory scheme for hyperbolic conservation laws*, vol. 227, pp. 3191–3211, 2008.

[111] S. Dong and J. Shen, “A time-stepping scheme involving constant coefficient matrices for phase-field simulations of two-phase incompressible flows with large density ratios,” *Journal of Computational Physics*, vol. 231, no. 17, pp. 5788–5804, 2012.

[112] B. Ho and L. Leal, “Migration of rigid spheres in a two-dimensional unidirectional shear flow of a second-order fluid,” *Journal of Fluid Mechanics*, vol. 76, no. 4, pp. 783–799, 1976.

[113] H. U. Naseer, Z. Ahmed, D. Izbassarov, and M. Muradoglu, “Dynamics and interactions of parallel bubbles rising in a viscoelastic fluid under buoyancy,” *Journal of Non-Newtonian Fluid Mechanics*, vol. 313, p. 105000, 2023.

[114] R. Zenit and J. Magnaudet, “Path instability of rising spheroidal air bubbles: a shape-controlled process,” *Physics of Fluids*, vol. 20, no. 6, p. 061702, 2008.

[115] W. L. Shew and J.-F. Pinton, “Viscoelastic effects on the dynamics of a rising bubble,” *Journal of Statistical Mechanics: Theory and Experiment*, vol. 2006, no. 01, p. P01009, 2006.

[116] G. H. McKinley, P. Pakdel, and A. Öztekin, “Rheological and geometric scaling of purely elastic flow instabilities,” *Journal of Non-Newtonian Fluid Mechanics*, vol. 67, pp. 19–47, 1996.

[117] D. Legendre, R. Zenit, and J. R. Velez-Cordero, "On the deformation of gas bubbles in liquids," *Physics of Fluids*, vol. 24, no. 4, p. 043303, 2012.

[118] J. Lu, S. Biswas, and G. Tryggvason, "A dns study of laminar bubbly flows in a vertical channel," *International Journal of Multiphase Flow*, vol. 32, no. 6, pp. 643–660, 2006.

[119] W. L. Haberman and R. Morton, *An experimental investigation of the drag and shape of air bubbles rising in various liquids.* David W. Taylor Model Basin Washington, DC, 1953.

[120] E. Kelley and M. Wu, "Path instabilities of rising air bubbles in a hele-shaw cell," *Physical review letters*, vol. 79, no. 7, p. 1265, 1997.

[121] P. K. Ray and T. A. Zaki, "Absolute instability in viscoelastic mixing layers," *Physics of Fluids*, vol. 26, no. 1, 2014.

[122] A. Duarte, A. I. Miranda, and P. J. Oliveira, "Numerical and analytical modeling of unsteady viscoelastic flows: The start-up and pulsating test case problems," *Journal of Non-Newtonian Fluid Mechanics*, vol. 154, no. 2-3, pp. 153–169, 2008.

[123] D. Rajagopalan, M. Arigo, and G. H. McKinley, "The sedimentation of a sphere through an elastic fluid part 2. transient motion," *Journal of non-newtonian fluid mechanics*, vol. 65, no. 1, pp. 17–46, 1996.

[124] N. Goyal and J. Derksen, "Direct simulations of spherical particles sedimenting in viscoelastic fluids," *Journal of Non-Newtonian Fluid Mechanics*, vol. 183, pp. 1–13, 2012.

[125] A. Groisman and V. Steinberg, "Elastic turbulence in a polymer solution flow," *Nature*, vol. 405, no. 6782, pp. 53–55, 2000.

[126] V. Steinberg, "Elastic turbulence: An experimental view on inertialess random flow," *Annual Review of Fluid Mechanics*, vol. 53, pp. 27–58, 2021.

[127] R. K. Singh, P. Perlekar, D. Mitra, and M. E. Rosti, "Intermittency in the not-so-smooth elastic turbulence," *Nature Communications*, vol. 15, no. 1, p. 4070, 2024.

[128] A. N. Morozov and W. van Saarloos, "Subcritical finite-amplitude solutions for plane couette flow of viscoelastic fluids," *Physical review letters*, vol. 95, no. 2, p. 024501, 2005.

[129] A. Morozov and W. Van Saarloos, "Subcritical instabilities in plane poiseuille flow of an oldroyd-b fluid," *Journal of Statistical Physics*, vol. 175, pp. 554–577, 2019.

[130] Y. Dubief, V. E. Terrapon, and B. Hof, "Elasto-inertial turbulence," *Annual Review of Fluid Mechanics*, vol. 55, pp. 675–705, 2023.

[131] D. Samanta, Y. Dubief, M. Holzner, C. Schäfer, A. N. Morozov, C. Wagner, and B. Hof, "Elasto-inertial turbulence," *Proceedings of the National Academy of Sciences*, vol. 110, no. 26, pp. 10557–10562, 2013.

[132] G. Foggi Rota, C. Amor, S. Le Clainche, and M. E. Rosti, "Unified view of elastic and elasto-inertial turbulence in channel flows at low and moderate reynolds numbers," *Physical Review Fluids*, vol. 9, no. 12, p. L122602, 2024.

[133] P. Garg, I. Chaudhary, M. Khalid, V. Shankar, and G. Subramanian, "Viscoelastic pipe flow is linearly unstable," *Physical review letters*, vol. 121, no. 2, p. 024502, 2018.

[134] M. Beneitez, J. Page, Y. Dubief, and R. R. Kerswell, "Multistability of elasto-inertial two-dimensional channel flow," *Journal of Fluid Mechanics*, vol. 981, p. A30, 2024.

[135] S. Sid, V. Terrapon, and Y. Dubief, "Two-dimensional dynamics of elasto-inertial turbulence and its role in polymer drag reduction," *Physical Review Fluids*, vol. 3, no. 1, p. 011301, 2018.

[136] Y. Dubief, J. Page, R. R. Kerswell, V. E. Terrapon, and V. Steinberg, "First coherent structure in elasto-inertial turbulence," *Physical Review Fluids*, vol. 7, no. 7, p. 073301, 2022.

[137] Y. Dubief, C. M. White, E. S. Shaqfeh, and V. E. Terrapon, "Polymer maximum drag reduction: A unique transitional state," *arXiv preprint arXiv:1106.4482*, 2011.

[138] Y. Dubief, V. E. Terrapon, and J. Soria, "On the mechanism of elasto-inertial turbulence," *Physics of Fluids*, vol. 25, no. 11, 2013.

[139] S. O. Unverdi and G. Tryggvason, "A front-tracking method for viscous, incompressible, multi-fluid flows," *Journal of computational physics*, vol. 100, no. 1, pp. 25–37, 1992.

[140] D. Izbassarov and M. Muradoglu, "A computational study of two-phase viscoelastic systems in a capillary tube with a sudden contraction/expansion," *Physics of Fluids*, vol. 28, no. 1, p. 012110, 2016.

[141] H. U. Naseer, D. Izbassarov, Z. Ahmed, and M. Muradoglu, "Lateral migration of a deformable fluid particle in a square channel flow of viscoelastic fluid," *Journal of Fluid Mechanics*, vol. 996, p. A31, 2024.

[142] S. Varchanis, S. J. Haward, C. C. Hopkins, J. Tsamopoulos, and A. Q. Shen, "Evaluation of constitutive models for shear-banding wormlike micellar solutions in simple and complex flows," *Journal of Non-Newtonian Fluid Mechanics*, vol. 307, p. 104855, 2022.

[143] D. Izbassarov, M. E. Rosti, M. N. Ardekani, M. Sarabian, S. Hormozi, L. Brandt, and O. Tammisola, "Computational modeling of multiphase viscoelastic and elastoviscoplastic flows," *International Journal for Numerical Methods in Fluids*, vol. 88, no. 12, pp. 521–543, 2018.

[144] S. R. Yerasi, J. R. Picardo, A. Gupta, and D. Vincenzi, "Preserving large-scale features in simulations of elastic turbulence," *Journal of Fluid Mechanics*, vol. 1000, p. A37, 2024.

[145] B. E. Owolabi, R. J. Poole, and D. J. Dennis, "Experiments on low-reynolds-number turbulent flow through a square duct," *Journal of Fluid mechanics*, vol. 798, pp. 398–410, 2016.

[146] B. Bunner and G. Tryggvason, "Dynamics of homogeneous bubbly flows part 1. rise velocity and microstructure of the bubbles," *Journal of Fluid Mechanics*, vol. 466, pp. 17–52, 2002.

[147] S. Mukherjee, R. K. Singh, M. James, and S. S. Ray, "Intermittency, fluctuations and maximal chaos in an emergent universal state of active turbulence," *Nature Physics*, vol. 19, no. 6, pp. 891–897, 2023.

[148] G. Buza, J. Page, and R. R. Kerswell, "Weakly nonlinear analysis of the viscoelastic instability in channel flow for finite and vanishing reynolds numbers," *Journal of Fluid Mechanics*, vol. 940, p. A11, 2022.

[149] D. Wan, G. Sun, and M. Zhang, "Subcritical and supercritical bifurcations in axisymmetric viscoelastic pipe flows," *Journal of Fluid Mechanics*, vol. 929, p. A16, 2021.

[150] P. Ptasinski, F. Nieuwstadt, B. Van Den Brule, and M. Hulsen, "Experiments in turbulent pipe flow with polymer additives at maximum drag reduction," *Flow, Turbulence and Combustion*, vol. 66, pp. 159–182, 2001.

[151] V. Dallas, J. C. Vassilicos, and G. F. Hewitt, "Strong polymer-turbulence interactions in viscoelastic turbulent channel flow," *Physical Review E*, vol. 82, no. 6, p. 066303, 2010.

[152] A. Shahmardi, S. Zade, M. N. Ardekani, R. J. Poole, F. Lundell, M. E. Rosti, and L. Brandt, "Turbulent duct flow with polymers," *Journal of Fluid Mechanics*, vol. 859, p. 1057–1083, 2019.

[153] D. Won and C. Kim, "Alignment and aggregation of spherical particles in viscoelastic fluid under shear flow," *Journal of non-newtonian fluid mechanics*, vol. 117, no. 2-3, pp. 141–146, 2004.

[154] J. Yoo and H. C. Choi, "On the steady simple shear flows of the one-mode giesekus fluid," *Rheologica acta*, vol. 28, pp. 13–24, 1989.

[155] M. Lellep, M. Linkmann, and A. Morozov, "Purely elastic turbulence in pressure-driven channel flows," *Proceedings of the National Academy of Sciences*, vol. 121, no. 9, p. e2318851121, 2024.

[156] D. Izbassarov, M. E. Rosti, L. Brandt, and O. Tammisola, "Effect of finite weissenberg number on turbulent channel flows of an elastoviscoplastic fluid," *Journal of Fluid Mechanics*, vol. 927, p. A45, 2021.

[157] B. A. Toms, "Some observations on the flow of linear polymersolutions through straight tubes at large reynolds numbers," in *Proc. 1st Intl Congr. Rheol.*, vol. 2, pp. 135–141, 1949.

[158] J. L. Lumley, "Drag reduction in turbulent flow by polymer additives," *Journal of Polymer Science: Macromolecular Reviews*, vol. 7, no. 1, pp. 263–290, 1973.

[159] G. Ryskin, "Turbulent drag reduction by polymers: a quantitative theory," *Physical review letters*, vol. 59, no. 18, p. 2059, 1987.

[160] M. Tabor and P. De Gennes, “A cascade theory of drag reduction,” *EPL (Europhysics Letters)*, vol. 2, no. 7, p. 519, 1986.

[161] K. R. Sreenivasan and C. M. White, “The onset of drag reduction by dilute polymer additives, and the maximum drag reduction asymptote,” *Journal of Fluid Mechanics*, vol. 409, pp. 149–164, 2000.

[162] H. Kim, S. Kline, and W. Reynolds, “The production of turbulence near a smooth wall in a turbulent boundary layer,” *Journal of Fluid Mechanics*, vol. 50, no. 1, pp. 133–160, 1971.

[163] J. D. Swearingen and R. F. Blackwelder, “The growth and breakdown of streamwise vortices in the presence of a wall,” *Journal of Fluid Mechanics*, vol. 182, pp. 255–290, 1987.

[164] F.-C. Li, Y. Kawaguchi, and K. Hishida, “Investigation on the characteristics of turbulence transport for momentum and heat in a drag-reducing surfactant solution flow,” *Physics of Fluids*, vol. 16, no. 9, pp. 3281–3295, 2004.

[165] Y. Dubief, V. E. Terrapon, C. M. White, E. S. Shaqfeh, P. Moin, and S. K. Lele, “New answers on the interaction between polymers and vortices in turbulent flows,” *Flow, turbulence and combustion*, vol. 74, pp. 311–329, 2005.

[166] M. D. Warholic, G. M. Schmidt, and T. J. Hanratty, “The influence of a drag-reducing surfactant on a turbulent velocity field,” *Journal of Fluid Mechanics*, vol. 388, pp. 1–20, 1999.

[167] P. S. Virk, “Drag reduction fundamentals,” *AIChE Journal*, vol. 21, no. 4, pp. 625–656, 1975.

[168] C. D. Dimitropoulos, R. Sureshkumar, and A. N. Beris, “Direct numerical simulation of viscoelastic turbulent channel flow exhibiting drag reduction:

effect of the variation of rheological parameters," *Journal of Non-Newtonian Fluid Mechanics*, vol. 79, no. 2-3, pp. 433–468, 1998.

[169] T. Min, J. Y. Yoo, H. Choi, and D. D. Joseph, "Drag reduction by polymer additives in a turbulent channel flow," *Journal of Fluid Mechanics*, vol. 486, pp. 213–238, 2003.

[170] Y. Dubief, C. M. White, V. E. Terrapon, E. S. Shaqfeh, P. Moin, and S. K. Lele, "On the coherent drag-reducing and turbulence-enhancing behaviour of polymers in wall flows," *Journal of Fluid Mechanics*, vol. 514, p. 271, 2004.

[171] C. M. White and M. G. Mungal, "Mechanics and prediction of turbulent drag reduction with polymer additives," *Annu. Rev. Fluid Mech.*, vol. 40, no. 1, pp. 235–256, 2008.

[172] C.-F. Li, R. Sureshkumar, and B. Khomami, "Influence of rheological parameters on polymer induced turbulent drag reduction," *Journal of Non-Newtonian Fluid Mechanics*, vol. 140, no. 1-3, pp. 23–40, 2006.

[173] G. H. Choueiri, J. M. Lopez, and B. Hof, "Exceeding the asymptotic limit of polymer drag reduction," *Physical review letters*, vol. 120, no. 12, p. 124501, 2018.

[174] M. D. Graham, "Drag reduction and the dynamics of turbulence in simple and complex fluids," *Physics of Fluids*, vol. 26, no. 10, 2014.

[175] L. Xi and M. D. Graham, "Turbulent drag reduction and multistage transitions in viscoelastic minimal flow units," *Journal of fluid mechanics*, vol. 647, pp. 421–452, 2010.

[176] L. Xi and M. D. Graham, "Intermittent dynamics of turbulence hibernation in newtonian and viscoelastic minimal channel flows," *Journal of fluid mechanics*, vol. 693, pp. 433–472, 2012.

[177] L. Xi, "Turbulent drag reduction by polymer additives: Fundamentals and recent advances," *Physics of Fluids*, vol. 31, no. 12, 2019.

[178] A. Esteghamatian and T. A. Zaki, "Dilute suspension of neutrally buoyant particles in viscoelastic turbulent channel flow," *Journal of Fluid Mechanics*, vol. 875, pp. 286–320, 2019.

[179] A. Esteghamatian and T. A. Zaki, "Viscoelasticity and the dynamics of concentrated particle suspension in channel flow," *Journal of Fluid Mechanics*, vol. 901, p. A25, 2020.

[180] M. Muradoglu and G. Tryggvason, "Simulations of soluble surfactants in 3d multiphase flow," *Journal of Computational Physics*, vol. 274, pp. 737 – 757, 2014.

[181] D. Izbassarov and M. Muradoglu, "A front-tracking method for computational modeling of viscoelastic two-phase flow systems," *Journal of Non-Newtonian Fluid Mechanics*, vol. 223, pp. 122 – 140, 2015.

[182] U. Olgac and M. Muradoglu, "Computational modeling of unsteady surfactant-laden liquid plug propagation in neonatal airways," *Physics of Fluids*, vol. 25, no. 7, p. 071901, 2013.

[183] S. Tasoglu, D. Utkan, and M. Muradoglu, "The effect of soluble surfactant on the transient motion of a buoyancy-driven bubble," *Physics of Fluids*, vol. 20, no. 4, p. 040805, 2008.

[184] V. G. Levich, *Physicochemical Hydrodynamics.* Prentice Hall, 1962.

[185] H. A. Stone, "A simple derivation of the time-dependent convective-diffusion equation for surfactant transport along a deforming interface," *Physics of Fluids A: Fluid Dynamics*, vol. 2, no. 1, pp. 111–112, 1990.

[186] R. Fattal and R. Kupferman, "Time-dependent simulation of viscoelastic flows at high weissenberg number using the log-conformation representation," *Journal of Non-Newtonian Fluid Mechanics*, vol. 126, no. 1, pp. 23 – 37, 2005.

[187] B. Leonard, "A stable and accurate convective modelling procedure based on quadratic upstream interpolation," *Computer Methods in Applied Mechanics and Engineering*, vol. 19, no. 1, pp. 59 – 98, 1979.

[188] D. S. Henningson and J. Kim, "On turbulent spots in plane poiseuille flow," *Journal of Fluid Mechanics*, vol. 228, p. 183–205, 1991.

[189] S. Takagi and Y. Matsumoto, "Surfactant effects on bubble motion and bubbly flows," *Annual Review of Fluid Mechanics*, vol. 43, pp. 615–636, 2011.

[190] S. Takagi, T. Ogasawara, and Y. Matsumoto, "The effects of surfactant on the multiscale structure of bubbly flows," *Philosophical Transactions of the Royal Society A: Mathematical, Physical and Engineering Sciences*, vol. 366, no. 1873, pp. 2117–2129, 2008.

[191] L. Zhu, H. Schrobsdorff, T. M. Schneider, and L. Xi, "Distinct transition in flow statistics and vortex dynamics between low-and high-extent turbulent drag reduction in polymer fluids," *Journal of Non-Newtonian Fluid Mechanics*, vol. 262, pp. 115–130, 2018.

[192] G. Hetsroni, J. Zakin, and A. Mosyak, "Low-speed streaks in drag-reduced turbulent flow," *Physics of Fluids*, vol. 9, no. 8, pp. 2397–2404, 1997.

[193] C. White, V. Somandepalli, and M. Mungal, "The turbulence structure of drag-reduced boundary layer flow," *Experiments in fluids*, vol. 36, pp. 62–69, 2004.

[194] S. Cant, "Sb pope, turbulent flows, cambridge university press, cambridge, uk, 2000, 771 pp.," *Combustion and Flame*, vol. 125, no. 4, pp. 1361–1362, 2001.

[195] J. M. Wallace, H. Eckelmann, and R. S. Brodkey, "The wall region in turbulent shear flow," *Journal of Fluid Mechanics*, vol. 54, no. 1, pp. 39–48, 1972.

[196] R. Sureshkumar, A. N. Beris, and R. A. Handler, "Direct numerical simulation of the turbulent channel flow of a polymer solution," *Physics of Fluids*, vol. 9, no. 3, pp. 743–755, 1997.

[197] R. B. Bird, R. C. Armstrong, and O. Hassager, "Dynamics of polymeric liquids. vol. 1: Fluid mechanics," 1987.

[198] K. D. Housiadas and A. N. Beris, "Polymer-induced drag reduction: Effects of the variations in elasticity and inertia in turbulent viscoelastic channel flow," *Physics of Fluids*, vol. 15, no. 8, pp. 2369–2384, 2003.

[199] I. Hameduddin, C. Meneveau, T. A. Zaki, and D. F. Gayme, "Geometric decomposition of the conformation tensor in viscoelastic turbulence," *Journal of Fluid Mechanics*, vol. 842, pp. 395–427, 2018.